OFFICE OF NAVAL RESEARCH

END-OF THE YEAR REPORT

PUBLICATIONS/PATENTS/PRESENTATIONS/HONORS/STUDENTS REPORT

for

GRANT: N00014-96-1-0045

PR Number 96PR00715

NONLINEAR DYNAMICS OF COUPLED LASER SYSTEMS

Rajarshi Roy
School of Physics
Georgia Institute of Technology
Atlanta GA 30332-0430
September 1997

OFFICE OF NAVAL RESEARCH
PUBLICATIONS/PATENTS/PRESENTATIONS/HONORS/STUDENTS REPORT

PR Number 96PR00715
GRANT: N00014-96-1-0045
Contract/Grant Title: NONLINEAR DYNAMICS OF COUPLED LASER SYSTEMS
Principal Investigator: Rajarshi Roy
Mailing Address: School of Physics, Georgia Institute of Technology, Atlanta GA 30332
Phone number: 404 894 5265
FAX Number: 404 894 9958
E-Mail Address: rajarshi.roy@physics.gatech.edu

a. Number of papers submitted to refereed journals, but not published: 2
b. Number of papers published in refereed journals: 6

[1] "Chaos and Coherence in Coupled Lasers", K.S. Thornburg et al., Phys. Rev. **E55**, 3865 (1997).

[2] "Noise Amplification in a Stochastic Ikeda Model", J. Garcia Ojalvo and R. Roy, Phys. Lett. **A 224**, 51 (1996).

[3] "Intracavity Chaotic Dynamics in ring lasers with an injected signal", J. Garcia Ojalvo and R. Roy, Phys. Lett. **A 229**, 362 (1997).

[4] "Fast Polarization Dynamics of an erbium doped fiber ring laser", Q. Williams and R. Roy Opt. Lett. **21**, 1478 (1996).

[5] "Fast Intracavity polarization dynamics of an erbium doped fiber ring laser: inclusion of stochastic effects", Q. Williams, J. Garcia Ojalvo and R. Roy, Phys. Rev. **A55**, 2376 (1997).

[6] "Influence of Noise on Chaotic Laser Dynamics" C. Liu, Rajarshi Roy, H.D.I. Abarbanel, Z. Gills and K. Nunes, Phys. Rev. **E 55**, 6483-6[illegible] (1997).

c. Number of books or chapters submitted, but not yet published: None
d. Number of book or chapters published: None
e. Number of printed technical reports/non-refereed papers: None
f. Number of patents filed: None
g. Number of patents granted: None
h. Number of invited presentations: 13

Heraeus Foundation Physics and Dynamics Conference, Berlin (1996)
Flucutations, Disorder and Nonlinearity, Crete (1996)
University of Houston (1996)
University of Maryland (1996)
International Conference on Dynamical Systems, Bangalore (1997)
University of Alabama, Birmingham (1997)
Suzhou University, China (1997)
Beijing Normal University (1997)

University of Nice, France(1997)
Control of Chaos Conference, Montecatini (1997)
SIAM Dynamical Systems Conference (1997)
College of William and Mary (1997)
Rensselaer Polytechnic (1997)

i. Number of submitted presentations: 0

j. Honors/Awards/Prizes for grant employees:

Editorial Board of Journal of Semiclassical and Quantum Optics (IOP)
Editorial Board of Nonlinear Science Today (Springer)
Editorial Board of International Journal of Bifurcations and Chaos, Jan. 1998 -
Fellow of the Optical Society of America

k. Total number of Full Time Equivalent Graduate Students and Post-Doctoral Associates supported during this period, under this R&T:

Graduate Students: 2
Post-Doctoral Associates: 1
Including number of
Female Graduate Students: 0
Female Post-Doctoral Associates: 0
Minority Graduate Students: 0
Minority Post-Doctoral Associates: 0
Asian Graduate Students: 0
Asian Post-Doctoral Associates: 0

l. Other funding received this year:

National Science Foundation, "Communication With Synchronized Chaotic Lasers", (1996 - 1999), joint grant of $1,069,000 with Profs. Henry Abarbanel (UCSD) and Steve Strogatz (Cornell). The Georgia Tech part of the contract is $326,337.

Program Objective

To design and build coupled solid state lasers and arrays and develop models to understand and predict coherence and synchronization properties of the light emitted. Also the study of coupled waves in optical fibers, their nonlinear interactions, transport of polarized light.

Significant Results During Last Year

I. Dynamics of Coupled Lasers

Our experimental, numerical and analytic results on the dynamics of two coupled lasers were published in Physical Review E in April [1]. A novel result demonstrated was the possibility of phase synchronization of the lasers even though the amplitudes of the laser fields are unstable and chaotic. Stochastic fluctuations of the detuning between the lasers were accounted for in simulations to reproduce the characteristics of the intensity time traces measured.

A new set of experiments on a linear array of three lasers was initiated. We find the remarkable result that the outer two lasers may be beautifully synchronized with each other though the middle laser is not. We are investigating this phenomenon in the light of recent work on generalized synchronization of nonlinear oscillators [2]. An illustration of the phenomenon is being sent by mail.

Extensive simulations of the correlations of the intensity fluctuation of a nine laser array have been done this past year, and a paper is in preparation, to be submitted to Physical Review E [3]. The conclusion from experimental observations and numerical computations is that the spatial correlations of intensity correlations for the elements of the array can decay sharply or very slowly depending on the coupling strength of the lasers.

II. Nonlinear Dynamics in Optical Fibers

We are about to submit a paper to Physical Review E on an extensive study of nonlinear wave propagation in a single mode optical fiber [4]. It is shown that the evolution of new sidebands in the fiber due to four wave mixing can be significantly affected by phase fluctuations along the fiber length, as well as by fine spectral structure of the pump waves.

Two papers were published in Physics Letters A [5,6], that developed a stochastic version of the Ikeda model. Two papers, one in Optics Letters [7] and one in Physical Review A [8], reported the results of extensive measurements of the polarization dynamics of the laser intensity on nanosecond time scales. A new laser model based on the Ikeda equations was developed and used to explain the formation of sharp pulses, irregular chaotic dynamics, as well as the formation of square waves in this system. These experiments and the corresponding models open a new regime for the investigation of fiber laser dynamics and future applications.

References:

[1] "Chaos and Coherence in Coupled Lasers", K.S. Thornburg et al., Phys. Rev. E55, 3865 (1997).

[2] K.S. Thornburg, G. Van Wiggeren and R. Roy, in preparation for submission, Physical Review E.

[3] "Spatial Correlations in Arrays of Coupled Lasers", K. S. Thornburg, R. Roy and L. Fabiny, in preparation for submission to Phys. Rev. E

[4] "Dynamical Evolution of Multiple Four Wave Mixing Processes along an Optical Fiber", D. L. Hart, A.F. Judy, R. Roy and J.W. Beletic, submitted to Phys. Rev. E.

[5] "Noise Amplification in a Stochastic Ikeda Model", J. Garcia Pjalvo and R. Roy, Phys. Lett. **A 224**, 51 (1996).

[6] "Intracavity Chaotic Dynamics in ring lasers with an injected signal", J. Garcia Ojalvo and R. Roy, Phys. Lett. **A 229** (362 (1997).

[7] "Fast Polarization Dynamics of an erbium doped fiber ring laser", Q. Williams and R. Roy Opt. Lett. **21**, 1478 (1996).

[8] "Fast Intracavity polarization dynamics of an erbium doped fiber ring laser: inclusion of stochastic effects", Q. Williams, J. Garcia Ojalvo and R. Roy, Phys. Rev. **A55**, 2376 (1997).

Chaos and coherence in coupled lasers

K. S. Thornburg, Jr., M. Möller,* and Rajarshi Roy
School of Physics, Georgia Institute of Technology, Atlanta, Georgia 30332

T. W. Carr,† R.-D. Li,‡ and T. Erneux
Université Libre de Bruxelles, Optique Nonlinéaire Théorique, Campus Plaine, C.P. 231, 1050 Bruxelles, Belgium
(Received 5 August 1996)

A fundamental chaotic instability in a system of two coupled lasers is investigated both experimentally and theoretically. The amplitude instability and mutual coherence of the light emitted by the lasers is investigated as a function of the detuning and coupling parameters. A quantitative comparison of the intensity fluctuations is made with numerical simulations that include noise in the laser detuning. [S1063-651X(97)03904-4]

PACS number(s): 05.45.+b, 42.50.Lc, 42.55.Rz

Haken's seminal analogy between fluid dynamics and laser instabilities initiated extensive studies of the Lorenz-like chaotic dynamics of the single mode far-infrared ammonia laser over the last two decades [1,2]. While this is conceptually the simplest chaotic laser system, it is also of great fundamental interest that two single-mode lasers that are stable individually can exhibit a chaotic instability when coupled [3,4]. Such a system provides a beautiful illustration of the rich and complex dynamical behavior of two coupled nonlinear oscillators. Pairs of neurons [5], pacemaker cells [6], chemical oscillators [7], and Josephson junctions [8] provide other examples of coupled nonlinear oscillator systems. It has been theoretically recognized that the amplitudes of the coupled oscillators can display a rich variety of unstable behaviors for certain regimes of coupling strength [9]. However, there are no experiments on physical systems that have quantitatively probed the relationship between the chaotic amplitude instability and phase coherence of coupled nonlinear oscillators. In this paper we report the results of precise measurements of the amplitude dynamics and phase coherence of coupled lasers and make quantitative comparisons with numerical models.

Many studies of coupled lasers have been motivated by the need for high power coherent sources. Coupled semiconductor, solid state, and CO_2 lasers have been studied [4,10–12], but it is the spatial properties of the output radiation that have received the most attention, rather than the dynamical characteristics of the emitted light [13]. Here, we study the chaotic dynamics and mutual coherence [14] of two coupled single-mode Nd:YAG (neodymium doped yttrium aluminum garnet) lasers that are detuned from each other by a very small amount (roughly 1 part in 10^8 of the oscillator frequency) and for which we can vary the coupling strength over many orders of magnitude.

The following equations describe the time evolution of the complex, slowly varying electric field E and gain G of a pair of spatially coupled, single transverse and longitudinal mode class B lasers [15,16]

$$\frac{dE_1}{dt}=\tau_c^{-1}[(G_1-\alpha)E_1-\kappa E_2]+i\omega_1 E_1, \tag{1a}$$

$$\frac{dG_1}{dt}=\tau_f^{-1}(p_1-G_1-G_1|E_1|^2), \tag{1b}$$

$$\frac{dE_2}{dt}=\tau_c^{-1}[(G_2-\alpha_2)E_2-\kappa E_1]+i\omega_2 E_2, \tag{1c}$$

$$\frac{dG_2}{dt}=\tau_f^{-1}(p_2-G_2-G_2|E_2|^2). \tag{1d}$$

In these equations, τ_c is the cavity round trip time ($\approx$450 ps for a cavity of length of 6 cm), τ_f is the fluorescence time of the upper lasing level of the Nd^{3+} ion ($\approx$ 230 μs for the 1064 nm transition), p_1 and p_2 are the pump coefficients, α_1 and α_2 are the cavity loss coefficients, and ω_1 and ω_2 (angular frequencies) are the detunings of the lasers from a common cavity mode, respectively. The lasers are coupled linearly to each other with strength κ, assumed to be small, and the sign of the coupling terms is chosen to account for the observed stale phase-locked state in which the lasers have a phase difference of 180°. For laser beams of Gaussian intensity profile and $1/e^2$ beam radius r the coupling strength, as determined from the overlap integral of the two fields, is defined as $\kappa=\exp(-d^2/2r^2)$. Control parameters are the frequency detuning of the lasers ($\Delta\omega=\omega_2-\omega_1$) and the coupling coefficient κ.

The dependence of the system dynamics on parameters can be numerically investigated by integrating Eqs. (1) using different values of κ and $\Delta\omega$. Figure 1 displays the predicted amplitude instability of the two lasers and its relationship to the coherence of the laser light as a function of both the laser separation d and the detuning $\Delta\omega$. The height of the graph shows the largest intensity value of laser 1 recorded during the 5 ms integration time. The color coding shows the degree of mutual coherence between the two lasers, as measured by

*Permanent address: Westfälische Wilhelms-Universität, Institut für Angewandte Physik, Corrensstrasse 2/4, 48149 Münster, Germany.

†Present address: Naval Research Lab, Code 6700. 3, Special Project in Nonlinear Science, Washington, D.C. 20375-5000.

‡Present address: HGM Medical Lasers Inc., 3959 West 1820 South, Salt Lake City, UT 84104.

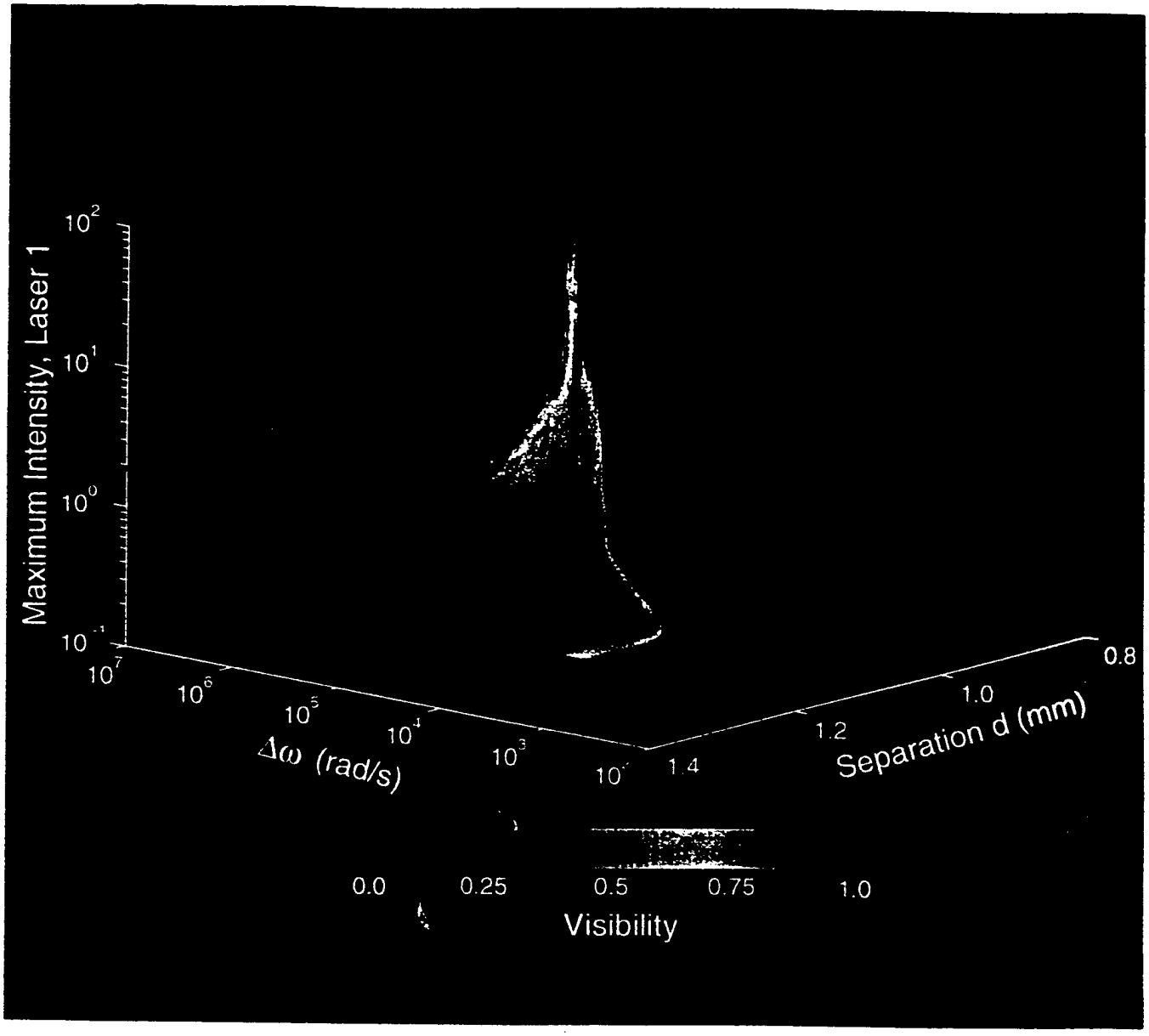

FIG. 1. (Color). Numerically computed parameter space plot of the amplitude instability of two lasers as a function of both the separation d and detuning $\Delta\omega$. Here $p_1=0.053$, $p_2=0.051$, $\alpha_1=\alpha_2=0.04$, and $r=225$ μm. We use pump parameters that differ by a few percent in the simulation to account for the fact that the two lasers may be nonidentical in the experiment. The height of the graph indicates the largest intensity value recorded at a given value of separation and detuning, while the color of the graph denotes the degree of mutual coherence between the two lasers, as indicated by the fringe visibility. Blue colors indicate low visibilities, while red colors indicate visibilities approaching unity, as shown in the legend.

the fringe visibility. The visibility V of the fringe pattern formed by the small angle interference of the laser beams is defined as $V=(I_{max}-I_{min})/(I_{max}+I_{min})$ where I_{max} and I_{min} are adjacent maxima and minima in the fringe profile. The fringe visibility is directly proportional to the absolute value of the complex degree of mutual coherence [14]. Low visibilities, shown as blue colors in this figure, indicate states of low mutual coherence, while reds indicate visibilities approaching one and therefore high degrees of mutual coherence. One can clearly see from Fig. 1 that the area where the intensity instabilities exist occurs just before the onset of phase locking and that significant intensity oscillations appear only around a rather narrow band of detuning values between 10^5 and 10^6 s^{-1}. A single positive Lyapunov exponent was computed in this regime with a typical value of $\approx 10^4$ s^{-1}, demonstrating the chaotic nature of the instability.

Insight into the amplitude instability can be obtained by considering the special case of identical laser parameters and by assuming that the two laser amplitudes and gains are identical. Equations (1) then reduce to

$$\frac{d\mathcal{E}}{dt}=\tau_c^{-1}[G-\alpha-\kappa\cos(\Phi)]\mathcal{E}, \tag{2a}$$

$$\frac{dG}{dt}=\tau_f^{-1}(p-G-G\mathcal{E}^2), \tag{2b}$$

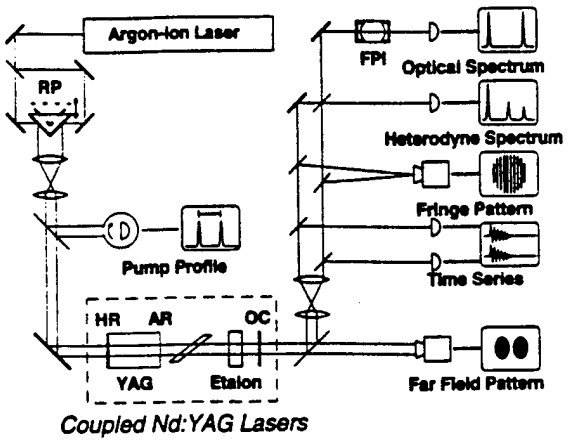

FIG. 2. Experimental system for generating two laterally coupled lasers in a Nd:YAG crystal and observing the amplitude instability. RP is a rectangular prism; translating this device changes the pump beam separation, and thus the infrared beam separation. The Nd:YAG crystal is coated for high reflectivity (HR) on one side and antireflection coated (AR) on the other. The output coupler (OC) is 2% transmissive; both mirrors at flat. FPI is a scanning Fabry-Pérot interferometer, and as used to measure the mode spectrum of both lasers.

$$\frac{d\Phi}{dt} = 2\tau_c^{-1}\kappa \sin(\Phi) + \Delta\omega \tag{2c}$$

for the laser amplitudes $|E_1| = |E_2| = \mathcal{E}$, gains $G_1 = G_2 = G$ and phase difference $\Phi = \phi_2 - \phi_1$, where ϕ_1 is the phase of the field E_i.

Equations (2a)–(2c) are the rate equations describing a single mode class B laser with variable losses. The phase equation can be integrated exactly, and $\Phi(t)$ is an unbounded function of time if the detuning $|\Delta\omega|$ exceeds a critical detuning $\Delta\omega_c$, where

$$\Delta\omega_c \equiv 2\kappa\tau_c^{-1}. \tag{3}$$

This is the critical condition for an amplitude instability [4]; we also note that the lasers are phase locked for detunings smaller than $\Delta\omega_c$ [16]. If condition (3) is obeyed, then the laser equations (2a) and (2b) are periodically modulated by the $\cos[\Phi(t)]$ term. The frequency of these modulations is given by

$$\omega_M \equiv \sqrt{\Delta\omega^2 - \Delta\omega_c^2}. \tag{4}$$

On the other hand, it is known that the laser relaxation oscillation frequency ω_R $(=2\pi\nu_R)$ for small τ_c/τ_f and $\kappa = 0$ is given by

$$\omega_R \equiv \left(\frac{2(p-\alpha)}{\tau_c\tau_f}\right)^{1/2}. \tag{5}$$

This implies the possibility of subharmonic resonance if the ratio of ω_M to ω_R is close to an integer. These resonances then produce branches of subharmonic solutions which explain the destabilization of the laser system [17,18].

We have tested the prediction of the amplitude instability with the experimental system of Fig. 2, which consists of two parallel, laterally separated lasers created by pumping a single Nd:YAG rod of 5 mm length and diameter in a plane parallel cavity. The pump beams are generated from the argon ion laser output ($\lambda = 514.5$ nm) by a system of beam splitters and prisms that ensure parallel propagation at an adjustable separation symmetric with respect to the YAG rod axis. The optical cavity consists of one high reflection coated end face of the rod and of an external planar output coupler with 2% transmittance. A Brewster plate and thick etalon within the cavity ensure linear polarization and single longitudinal mode operation. The lasers were operated at approximately 33% above threshold pump power. For these parameters, the relaxation oscillation frequency, ν_R, is of the order of 100 kHz. The frequency detuning between the two lasers can be adjusted by tilting the output coupler slightly, thereby introducing a minute difference in cavity lengths.

Thermal lensing induced in the YAG crystal by the pump beams of waist radius ~ 20 μm is responsible for generating two stable, separate cavities [16]. The TEM_{00} infrared laser beams have radii (at $1/e^2$ of the maximum intensity of the Gaussian profile) of $r \sim 200$ μm and their overlap may be continuously changed by varying the lateral separation d of the pump beams over a range of 0.5 mm–3 mm. The pump beam separation and profiles are measured directly by a rotating slit technique. In this range, there is no appreciable overlap of the pump beams and coupling is entirely due to the spatial overlap of the infrared laser fields.

The individual output intensity time series are recorded with fast photodetectors and a two channel digital oscilloscope. The optical frequency difference of the lasers is measured with a radio frequency spectrum analyzer after combining the two beams on a photodetector. A scanning Fabry-Pérot interferometer was used to ensure that both lasers oscillated only on a single longitudinal mode.

The change of dynamical behavior of the detuned, coupled system can be seen as the separation of the pump beams is varied. For a large separation ($d \geq 1.20$ mm) the lasers were stable and incoherent. The visibility of the fringes was low ($V \approx 0$), and the heterodyne single was measured to be between 30 and 40 MHz. For a small separation ($d \leq 0.8$ mm), the lasers are stable and phase locked. The fringe visibility was high ($V \sim 1$), and the heterodyne signal was absent since the lasers were frequency locked. Figure 3(a) shows a typical intensity time trace characteristic of the unstable regime. Large bursts of the intensity occur, separated by quiescent periods. Here the lasers were separated by 1.03 mm, which implies $\kappa \approx 2.0 \times 10^{-5}$. Using Eq. (3), we find that the condition for an amplitude instability requires $|\Delta\omega| > 10^5$ s^{-1}, which is verified in our experiments ($\Delta\omega \sim 1$ MHz). The intermediate visibility of $V = 0.20$ signifies the onset of phase locking. The experimentally measured visibilities are in excellent agreement we the numerically computed values represented in Fig. 1.

In the experiment, a substantial amount of fluctuation in the detuning between the two lasers was observed; the beat signal frequency in the unstable regime fluctuated between 0 and 10 MHz. In order to obtain quantitative comparison between measured intensity time series and simulations, we numerically investigated the behavior of Eqs. (1) with a stochastic detuning term, such that $\Delta\omega(t) = \omega_2 - \omega_1$, where $\omega_i = \omega_{0,i} + \delta\omega_i(t)$. Here $\delta\omega_i(t)$ is a colored noise term of

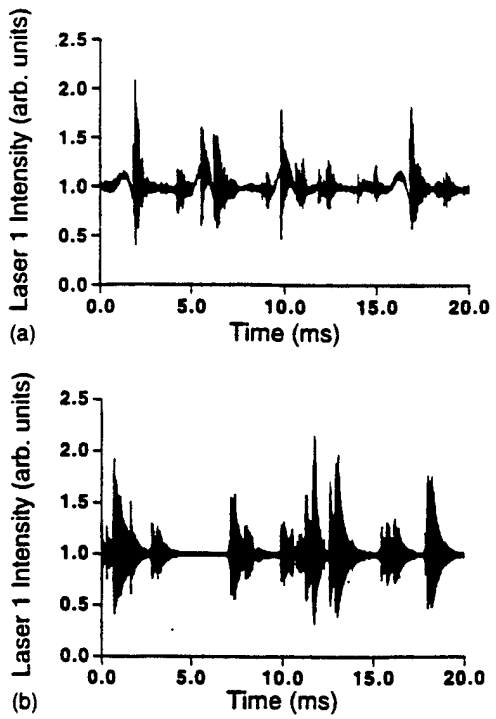

FIG. 3. Intensity time traces of (a) experiment and (b) numerical simulation. The time trace in (a) was measured at a pump separation of $d=1.03$ mm, and illustrates the bursting nature of the amplitude instability. The average interspike interval (ISI) is 1.9 ms, the normalized standard deviation $\sigma_I/\bar{I}=0.10$, and the standard deviation of the detuning $\sigma_{\Delta\omega}\approx 10^6\ \mathrm{s}^{-1}$. (b) The numerically computed time trace of the intensity of laser 1 with an exponentially correlated, stochastic detuning term of strength $D=5\times 10^9\ \mathrm{s}^{-1}$ and correlation time $\lambda^{-1}=3$ ms. The mean detuning $\Delta\omega_0=5\times 10^5\ \mathrm{s}^{-1}$, and the standard deviation of the detuning $\sigma_{\Delta\omega}=1.4\times 10^6\ \mathrm{s}^{-1}$. The average ISI was 1.7 ms, and $\sigma_I/\bar{I}=0.12$. The cavity losses were taken to be 4% and the lasers were pumped one-third above threshold, with a 0.5% asymmetry.

strength D and correlation time λ^{-1}, with the properties $\langle\delta\omega_i(t)\rangle=0$ and $\langle\delta\omega_i(t)\,\delta\omega_j(t+\Delta t)\rangle=\delta_{ij}D\lambda\exp(-\lambda|\Delta t|)$ [19].

We used three different statistical measures to compare the numerically simulated and experimental traces—the normalized standard deviation of the intensity $\sigma_i/\bar{I}$, the average interspike interval (ISI), and the standard deviation of the detuning $\sigma_{\Delta\omega}$. The average ISI is determined by measuring the average time between adjacent bursts whose intensities are greater than some threshold, here defined to be 1.2 times the average intensity. To avoid counting the same burst twice, a "quiescence time" τ_q of 0.8 ms was used such that a new spike would be detected no sooner than τ_q. The standard deviation of the detuning in the experiments was measured to be on the order of 10 MHz or less; numerically, $\sigma_{\Delta\omega}=\sqrt{D\lambda}$. Using these statistical measures, the parameters D and λ were adjusted to give quantitative agreement between the observed experimental results and the numerical simulations. The range of parameters D and λ that gave quantitative agreement with experiment is very limited: $D\sim O(10^9\ \mathrm{s}^{-1})$ and $\lambda^{-1}\sim O(10^{-3}\ \mathrm{s})$. Figure 3(b) shows a good match with the experimental data.

In conclusion, we have demonstrated a fundamental amplitude instability of two coupled lasers and its relationship to the mutual coherence of the total field. Theoretical and numerical predictions, using a dynamical model, of the range of coupling strengths where the instability is expected to occur agree very well with experimental observations. For large separations, both the model and experiment reveal stable intensities and no appreciable coherence. As the separation is decreased to just above the phase-locking point, large amplitude fluctuations are observed, in agreement with numerical predictions. The laser fields exhibit a low degree of mutual coherence for this range of coupling strength. It was necessary to include stochastic detuning fluctuations to achieve quantitative agreement between experimental and simulation in the unstable regime. Finally, for even smaller separations, phase locking is achieved. The lasers are now found to be stable, mutually coherent, and frequency locked. These studies are directly relevant to the design of laser arrays; they also reveal a rich and complex dynamical scenario which should be systematically explored in the future for a variety of different oscillator systems.

We acknowledge support from the Division of Chemical Sciences, Office of Basic Energy Sciences, Office of Energy Research, U.S. Department of Energy, and the Office of Naval Research. M.M. acknowledges support from the Deutsche Forschungsgemeinschaft (DFG, Germany). R.R. thanks Neal Abraham, Edgar Knobloch, and Steve Strogatz for helpful discussions. T.E. acknowledges support from U.S. Air Force Office of Scientific Research Grant AFOSR-93-1-0084, National Science Foundation Grant DMS-9308009, the Fonds National de la Recherche Scientifique (Belgium), and the InterUniversity Attraction Pole of the Belgian government.

[1] H. Haken, Phys. Lett. A **53**, 77 (1975).
[2] C. O. Weiss and R. Vilaseca, *Dynamics of Lasers* (VCH, Weinheim, 1991); A. C. Newell and J. V. Moloney, *Nonlinear Optics* (Addison-Wesley, New York, 1992).
[3] S. S. Wang and H. G. Winful, Appl. Phys. Lett. **52**, 1774 (1988); H. G. Winful and S. S. Wang, *ibid.* **53**, 1894 (1988).
[4] A. V. Bondarenko, A. F. Glova, S. N. Kozlov, F. V. Lebedev, V. V. Likhanskii, A. P. Napartovich, V. D. Pis'mennyi, and V. P. Yartsev, Zh. Eksp. Teor. Fiz. **95**, 807 (1989) [Sov. Phys. JETP **68**, 461 (1989)].
[5] M. Kawato and R. Suzuki, J. Theor. Biol. **86**, 547 (1980).
[6] A. Winfree, *The Geometry of Biological Time* (Springer-Verlag, Berlin, 1990).
[7] K. Bar-Eli, Physica D **14**, 242 (1985).
[8] S. Watanabe, S. H. Strogatz, H. S. J. van der Zant, and T. P. Orlando, Phys. Rev. Lett. **75**, 45 (1995).
[9] D. G. Aronson, G. B. Ermentrout, and N. Kopell, Physica D **41**, 403 (1990).
[10] V. V. Likhanskii and A. P. Napartovich, Usp. Fiz. Nauk **160**, 101 (1990) [Sov. Phys. Usp. **33**, 228 (1990)]; B. Ozygus and

Fast polarization dynamics of an erbium-doped fiber ring laser

Quinton L. Williams and Rajarshi Roy

School of Physics, Georgia Institute of Technology, Atlanta, Georgia 30332-0430

Received May 3, 1996

The polarization dynamics of a unidirectional erbium-doped fiber ring laser has been observed for individual round trips in the cavity. A rich variety of dynamic states, including square-wave pulses and irregular temporal patterns, was observed as operating parameters were changed. A model with coupled delay and differential equations is used to interpret the dynamics. © 1996 Optical Society of America

Rare-earth-doped silica fiber lasers have recently received much attention in the context of long-time-scale polarization resolved dynamics. Phenomena such as antiphase dynamics in orthogonal polarization states,[1] self-pulsing,[2] and polarization switching induced by optical feedback[3] have been reported. Experimental evidence of the quasi-periodic route to chaos in an erbium-doped fiber laser has been published.[4] The previous reports were done on the millisecond time scale, which corresponds to the relaxation oscillation frequency of the fiber laser.

We present some measurements of the fast temporal (on the nanosecond time scale) dynamics of the Er^{3+}-doped fiber ring laser (EDFRL). The fiber laser output beam contains two linearly polarized components. It is within the two groups of orthogonal polarization eigenmodes that the various dynamic states are observed and investigated. Computational results from a model based on coupled delay and differential equations of the Ikeda type[5] provide an explanation of the experimental observations. A similar model was developed by Loh and Tang[6] for polarization dynamics of an external-cavity semiconductor laser.

The EDFRL presents a unique opportunity for the study of laser nonlinear dynamics. The small longitudinal mode spacing and large gain bandwidth make the EDFRL a practical experimental system in which the collective behavior of a large number of globally coupled nonlinear oscillators can be observed. Such models have been studied in the context of physical and biological systems by Strogatz and co-workers[7] and by many others recently.

A schematic of the experimental configuration is shown in Fig. 1. The coherent pump source was the 514.5-nm-wavelength line from an argon-ion laser. A 6-m length of erbium-doped fiber with an ion concentration of ~240 parts in 10^6 was taken as the gain medium. A Faraday optical isolator was included in the laser cavity to ensure unidirectional operation. An output coupler removed 3% of the intracavity power. The polarization controller functioned as a discrete birefringence-inducing element. Overall, the laser cavity was 20 m long, 14 m being passive optical fiber. Free ends of the couplers were placed in index-matching fluid to suppress the small, but parasitic, Fresnel reflections. The output at $\lambda = 1.561\ \mu m$ was sent through a $\lambda/2$ wave plate and a polarization beam splitter cube, where the orthogonal polarization eigenmodes could be observed simultaneously with high-speed photodetectors. Data were recorded by a fast digital oscilloscope with a 1-GHz sample rate. The round-trip time for the cavity was ~100 ns, and it was possible to store 100 data points per round trip.

The EDFRL lases on a broad 3-dB optical gain bandwidth that is $\sim 10^{10}$ Hz. The longitudinal mode separation is 9.8 MHz; the number of active oscillating modes is well over 2000. An optical spectrum analyzer reveals that the modes oscillate within orthogonally polarized mode groups that have been modeled as two supermodes.[1]

While the EDFRL was pumped well above threshold (the threshold pump power was ~175 mW), self-pulsing was observed on the nanosecond time scale. Figures 2(a) and 2(b) are resolved polarization components of the total output intensity. In Fig. 2(a) the distinct sharp pulses are separated by the fundamental cavity round-trip time of ~100 ns. Figure 2(b) shows a highly complex time series that is quasi-periodic or nearly perfectly repeating, with a period of ~7 cavity round trips. Inspection of the irregular waveforms in Fig. 2(b) shows that these patterns repeat for several hundred cavity round trips before eventually evolving into other irregular waveforms. At the higher pump

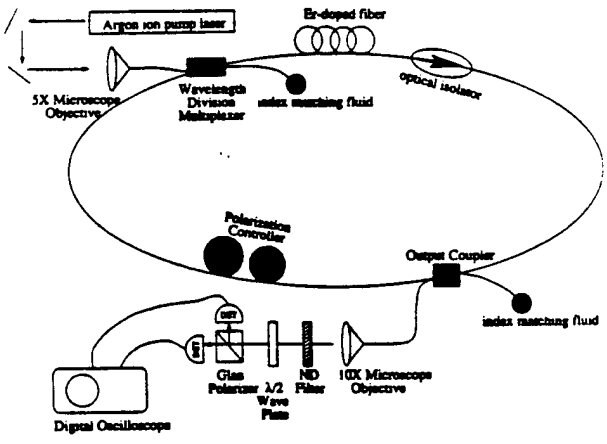

Fig. 1. Experimental arrangement: Ar^+-ion laser, λ_p = 514.5 nm; 514.4–1550 nm wavelength division multiplexer optical coupler; Faraday optical isolator (not shown); 97/3 coupling ratio output coupler; neutral density (ND) filter with 10% transmission at 1.55 μm; $\lambda/2$ wave plate at 1.55 μm; DET's, fast-response InGaAs/p–i–n photodetectors.

0146-9592/96/181478-03$10.00/0

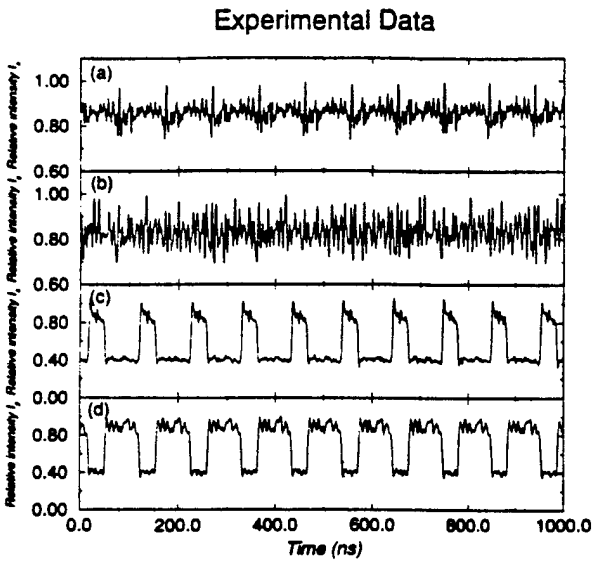

Fig. 2. Experimentally measured polarization resolved traces of (a) self-pulsing at the cavity round-trip time in the x-polarization direction from an EDFRL with 10% output coupling, (b) irregular trace in the y-polarization direction. The EDFRL was pumped four times threshold. (c), (d) Antiphase square pulses in the x- and y-polarization directions, respectively, from an EDFRL with 3% output coupling. The EDFRL was pumped at 3.3 times threshold.

levels (three to four times above threshold), antiphase square pulses were formed in the orthogonal polarization intensities for a narrow range of adjustment of the polarization controller. Figure 2(c) shows 30-ns pulses. This corresponds to the 6-m length of the gain medium. Figure 2(d) shows 70-ns pulses that correspond to the 14-m length of the passive fiber within the laser cavity. Another detail to note is the highly structured intensity fluctuations that ride on top of the square pulses and repeat over many round trips.

A laser model based on an Ikeda-type set of delay-differential equations was used to investigate the dynamical behavior of the EDFRL. Loh and Tang derived a set of difference-differential equations to study ultrahigh-frequency polarization self-modulation in semiconductor lasers.[6] It is in the same spirit that we derive our set of equations from the Maxwell–Bloch equations; they take the form

$$S_1(t) = \frac{R_1^2}{2}\{S_1(t-\tau_R)\exp\{2A_1[W(t)]\}(1+\cos\phi) + S_2(t-\tau_R)\exp\{2A_2[W(t)]\}(1-\cos\phi) - 2[S_1(t-\tau_R)S_2(t-\tau_R)]^{1/2} \times \exp\{A_1[W(t)] + A_2[W(t)]\} \times \sin\{\kappa[W(t)]\}\sin\phi\}, \quad (1)$$

$$S_2(t) = \frac{R_2^2}{2}\{S_1(t-\tau_R)\exp\{2A_1[W(t)]\}(1-\cos\phi) + S_2(t-\tau_R)\exp\{2A_2[W(t)]\}(1+\cos\phi) + 2[S_1(t-\tau_R)S_2(t-\tau_R)]^{1/2} \times \exp\{A_1[W(t)] + A_2[W(t)]\} \times \sin\{\kappa[W(t)]\}\sin\phi\}, \quad (2)$$

$$\frac{dW(t)}{dt} = P - \gamma_{\parallel}[W_T + W(t)] - S_1(t-\tau_R) \times (\exp\{a_1[W(t) - N_0L]\} - 1) - S_2(t-\tau_R)(\exp\{a_2[W(t) - N_0L]\} - 1), \quad (3)$$

where $W(t) = \int_0^L N(z, t + z/v_g)dz$, $\kappa[W(t)] = q_1[W(t)] - q_2[W(t)] - \beta$, $S_{1,2}(t-\tau_R) = |E_{1,2}(t-\tau_R)|^2/\hbar\omega_{1,2}$, $A_{1,2}[W(t)] = (a_{1,2}/2)[W(t) - N_0L]$, $q_{1,2}[W(t)] = \alpha_{1,2}(a_{1,2}/2)[W(t) - W(t=0)]$, and ϕ is the relative phase difference between the polarized fields. The mode detuning factor is defined as $\alpha_m = -\Delta_m/\gamma_\perp$, where $\Delta_m = \omega_m - \omega_0$ and $m = 1, 2$. Other parameters are defined in Table 1.

In this model the gain is taken to be a linear function of the population inversion. S_1 and S_2 are the photon number densities for the x- and y-polarization modes, respectively, and W represents the inversion. The differential equation was integrated with a fourth-order Runge–Kutta routine with a 1-ns integration time step, corresponding to the experimental sampling time for observation of laser dynamics in a single cavity round trip.

In Eqs. (1)–(3) the lumped parameter β is due to the phase shift associated with fiber birefringence over the

Table 1. Parameter Values Used in the Numerical Simulations

Parameter	Value	Unit	Definition
$R_{1,2}$	0.97	–	Return coefficient
L_T	20	m	Total cavity length
L	6	m	Length of active fiber
N_T	10^{25}	m^{-3}	Ion concentration
N_0	10^{20}	m^{-3}	Transparency inversion
τ_R	10^{-7}	s	Cavity round-trip time
$\gamma_\perp$	4.75×10^{14}	s^{-1}	Polarization decay rate
$\gamma_\parallel$	10^2	s^{-1}	Population decay rate
λ_0	1.530×10^{-6}	m	Resonance wavelength
λ_1	1.561×10^{-6}	m	Wavelength of mode 1
σ_e	7.5×10^{-25}	m^2	Emission cross section
$a_{1,2}$	2.03×10^{-23}	m^2	Mode 1, 2 gain factor
$\alpha_{1,2}$	3.52×10^{-2}	–	Mode 1, 2 detuning factor
P	1.44×10^{28}	$m^{-2}\,s^{-1}$	Pump term

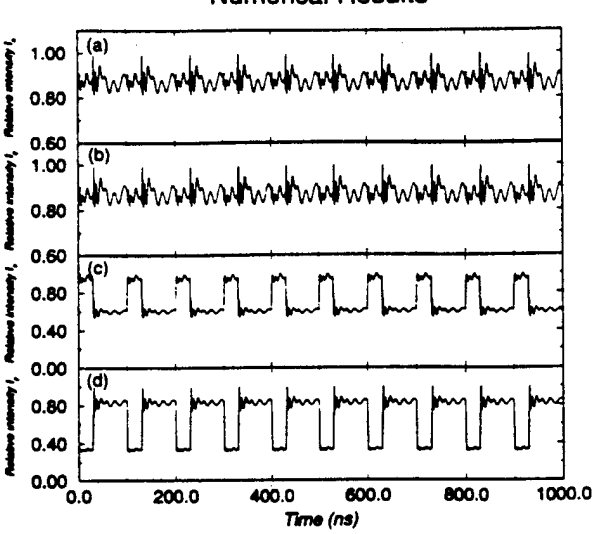

Fig. 3. Numerical simulations of time traces showing self-pulsing at the cavity round-trip time in (a) the x-polarization direction, (b) the y-polarization direction. (c), (d) Antiphase square-wave pulses in the x- and y-polarization directions corresponding to those of Figs. 2(c)–2(d). Parameters for (a) and (b): $\phi_A = 0.027$, $\phi_P = \pi - 0.175$, $\beta = 1.5 \times 10^{-3}$, and $\Delta\lambda = 0.125$ fm. Parameters for (c) and (d): $\phi_A = 0.027$, $\phi_P = \pi - 0.015$, $\beta = 10^{-2}$, and $\Delta\lambda = 4.09$ fm. The pump rate is 3.2 times threshold.

entire cavity. By changing the polarization controller, one introduces a local birefringence by applying stress to the fiber, which appears as a discrete phase shift in the section of passive fiber. We take the phase term ϕ to be ϕ_A in the active region and ϕ_P in the passive region that contains the polarization controller. The value of ϕ_A was taken to be small but nonzero. The small phase shift in the active fiber could be a result of the active fiber's being wound onto a spool. This feature of separate phases in the active and passive fiber portions is necessary for reproducing the observed asymmetric nature of the square-wave pulsations. ϕ_P was taken to be approximately π rad because the polarization controller functions roughly as a $\lambda/2$ wave plate. The birefringence causes the two mode groups to travel at different speeds, ultimately resulting in a mode group detuning $\Delta\lambda = (\lambda_2 - \lambda_1)$.

Typical results from the numerical model showing output intensities in orthogonal polarization directions are displayed in Fig. 3. Table 1 gives values for the physical parameters of the system. These parameters yield a good match between theory and experiment, as seen from Figs. 2 and 3. However, these computations are merely representative of the large variety of waveforms that emerges for different parameter values; they are not meant to provide a detailed reproduction of the experimental waveforms. The sharp pulses are seen to be distinctly separated by the fundamental cavity round-trip time of 100 ns in Figs. 3(a) and 3(b). One sees that the irregular waveforms actually repeat over single cavity round trips for the parameters chosen. Figures 3(c) and 3(d) show antiphase square-wave pulses that form when the parameter value settings of ϕ_A, ϕ_P, β, and $\Delta\lambda$ are in the proper regime.

Essential experimental features captured by the model are the following: (1) the dynamics occur on the nanosecond time scale, (2) self-pulsing at the cavity round-trip time or multiples with repeating irregular waveforms is present, (3) antiphase square-wave pulses form when parameter values are favorable, (4) the dynamics of the system take place with a dc background, (5) highly structured fluctuations are present on the tops of the square pulses, and (6) the time durations of the square pulses correspond to the lengths of active and passive fiber in the ring.

In conclusion, measurements of the fast temporal dynamics during a single cavity round trip have been made for an erbium-doped fiber ring laser. Square-wave pulsing and irregular dynamics that repeat at round-trip times have been observed in the two orthogonal polarization eigenstates. The experimentally observed properties were described by a unified model based on an Ikeda-type delay-differential equation model of the laser. We have shown that fiber birefringence, polarization controller adjustment, and the frequency difference between the orthogonal mode groups influence the nature of the dynamics.

We acknowledge support from the Division of Chemical Sciences, Office of Basic Energy Sciences, Office of Energy Research, U.S. Department of Energy, and from the U.S. Office of Naval Research. It is a pleasure to thank J. Garcia-Ojalvo, R. Hilborn, K. McCoy, and C. Verber for many discussions and help with the experiments. We also thank S. Strogatz for many discussions of coupled nonlinear oscillator models.

References

1. S. Bielawski, D. Derozier, and P. Glorieux, Phys. Rev. A **46,** 2811 (1992); E. Lacot, F. Stoeckel, and M. Chenevier, Phys. Rev. A **49,** 3997 (1994).
2. F. Sanchez, P. Le Boudec, P. L. Francois, and G. Stephan, Phys. Rev. A **48,** 2220 (1993); P. Le Boudec, M. Le Flohic, P. L. Francois, F. Sanchez, and G. Stephan, Opt. Quantum Electron. **25,** 359 (1993).
3. B. Meziane, F. Sanchez, G. Stephan, and P. L. Francois, Opt. Lett. **19,** 1970 (1994).
4. F. Sanchez, M. Le Flohic, G. Stephan, P. Le Boudec, and P. L. Francois, IEEE J. Quantum Electron. **31,** 481 (1995).
5. K. Ikeda, Opt. Commun. **30,** 257 (1979); K. Ikeda, H. Daido, and O. Akimoto, Phys. Rev. Lett. **45,** 709 (1980); K. Ikeda, K. Kondo, and O. Akimoto, Phys. Rev. Lett. **49,** 1467 (1982).
6. W. H. Loh and C. L. Tang, IEEE J. Quantum Electron **27,** 389 (1991); Opt. Commun. **85,** 283 (1991).
7. S. H. Strogatz and I. Stewart, Sci. Am. **269,** 102 (1993); S. H. Strogatz and R. E. Mirollo, J. Stat. Phys. **63,** 613 (1991); S. Watanabe and S. H. Strogatz, Phys. Rev. Lett. **70,** 2391 (1993).

Fast intracavity polarization dynamics of an erbium-doped fiber ring laser: Inclusion of stochastic effects

Q. L. Williams, J. García-Ojalvo,* and R. Roy
School of Physics, Georgia Institute of Technology, Atlanta, Georgia 30332-0430
(Received 5 September 1996; revised manuscript received 31 October 1996)

The dynamics of a unidirectional erbium-doped fiber laser is investigated on a time scale short enough to observe, with good resolution, its behavior for individual round-trips in the laser cavity. With an intracavity polarization controller, a rich variety of nonlinear phenomena, ranging from self-pulsing to square-wave antiphase patterns in two orthogonal states of polarization, are observed. These patterns evolve continuously in time. A stochastic delay-differential equation model is proposed to describe this system. Numerical simulations show that this model satisfactorily accounts for all types of qualitative behavior and reveal that the inclusion of spontaneous-emission noise is necessary to reproduce the observed continuous pattern evolution. Two different, typical types of nonlinear dynamical states are found both numerically and experimentally: a deterministic, low-dimensional regime and a noise-driven high-dimensional motion. [S1050-2947(97)01403-0]

PACS number(s): 42.65.Sf, 42.81.−i

I. INTRODUCTION

The idea of doping glass to obtain amplifying optical fibers is very attractive from both a technological and a fundamental point of view. Technologically, fiber amplifiers are very promising useful devices in all-optical telecommunication schemes, through their use to replace repeaters in fiber-optic transmission lines, for instance. When these materials are complemented with a cavity resonator and a pumping scheme, laser emission can be obtained. Such systems are used for the generation of ultrashort pulses and solitons.

Besides their evident practical applications, fiber lasers are very interesting from a basic physics perspective. The conjunction of the inherent nonlinear character of both the optical fiber and the light amplification process makes this type of laser specially suited for investigations of nonlinear dynamics in optical systems. Furthermore, because of the amorphous character of the glass host, fiber lasers are the ideal counterpart of the more extended and well-known doped-crystal solid-state lasers.

Due to the optical-guiding characteristics of their amplifying medium, fiber lasers can have cavity lengths of the order of tens of meters, orders of magnitude higher than in most other lasers. This fact, along with the broad gain profile of doped fibers, ensures that a large number of longitudinal modes experience gain and coexist inside the cavity, coupled through gain sharing. Hence fiber lasers usually operate in a strongly multimode regime. The dynamics of multimode lasers is very rich, including antiphase behavior and self-organized collective oscillations [1]. Previous experiments in fiber lasers [2,3] have shown this kind of phenomenon in the dynamics of two orthogonal states of polarization, which suggest a description of this system in terms of two supermodes associated with two different polarization eigenstates of the field. Another dynamical feature that is usually observed in experiments is self-pulsing [4], which has recently been related to an absorption effect due to interaction between dopant ions [5]. All the previous experiments have been done in the millisecond to microsecond time scale, which corresponds to the relaxation-oscillation frequency of the laser. But this system, due to its large cavity length and thus long round-trip time, gives us a unique chance to observe its dynamics for individual round-trips inside the cavity. This work aims at the characterization of this fast polarization dynamics in the regimes previously mentioned.

We report experimental observations of the intracavity dynamics of an erbium-doped fiber laser. A polarization-controlling device has been included in the cavity and, as a result, a fast polarization-switching effect, on a time scale of the order of nanoseconds, has been observed. This kind of effect is known to occur in semiconductor lasers [6] when a wave plate is inserted in the laser cavity. Recently, optical feedback has been found to induce this effect also in Nd-doped fiber lasers [7], but on a much slower time scale (on the order of microseconds). A model is proposed to explain the behavior observed. Most models used so far in doped-fiber lasers to account for antiphase [2], self-pulsing [3], and polarization-switching [7] behavior are based on semiclassical rate equations for each of the two polarization supermodes, which are coupled to one another through cross saturation and gain sharing. In some cases, the need of explicitly taking into account the dependence of the system variables on the propagation direction has been stressed [3]. This consideration, which is, in general, advisable in this system due to its long cavity, is in our case unavoidable given the time scale in which the observations are made. Following Loh and Tang [8,9] in their modeling of fast polarization self-modulation in semiconductor lasers, we develop a delay-differential equation model that accounts for all kinds of features observed. The inclusion of spontaneous-emission noise is seen to be necessary to obtain a more complete agreement. Indeed, the importance of spontaneous emission in the dynamics of guided lasers is a well-established fact [2]. Finally,

*Permanent address: Departament de Física i Enginyeria Nuclear, Escola Tècnica Superior d'Enginyers Industrials de Terrassa, Universitat Politècnica de Catalunya, Colom 11, E-08222 Terrassa, Spain.

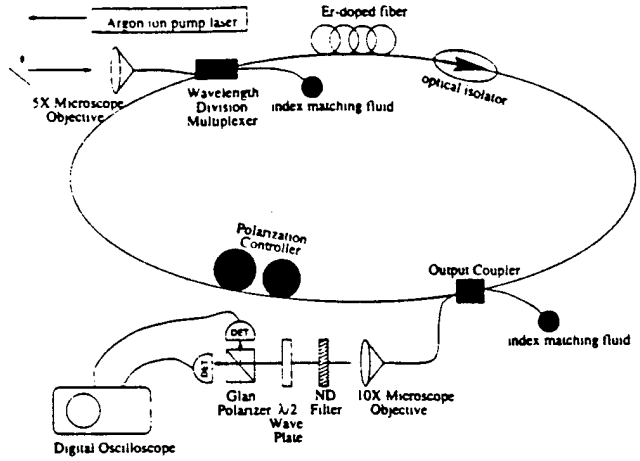

FIG. 1. Experimental setup.

in order to simplify the modeling of the system, a ring-cavity configuration is used. Preliminary results of this investigation have been reported elsewhere [10].

The outline of the paper is the following. Section II contains a description of the experimental apparatus and a report of the behavior observed. Section III establishes a theoretical model that reproduces this behavior, as shown by numerical simulations. Finally, some conclusions and comments are made in Sec. IV.

II. EXPERIMENTAL FEATURES

A. Experimental setup

Several wavelengths can be used to optically pump an erbium-doped fiber amplifier in order to obtain laser emission. In our case the pump wavelength is fixed at 514.5 nm and is provided by an Ar^+-ion laser. Under these conditions, the lasing frequency lies in the near infrared, at 1.561μm. The experimental setup is shown in Fig. 1. The amplifying medium is a 6-m-long erbium-doped fiber, with an ion concentration of approximately 240 ppm (corresponding to 4.98×10^{25} ions/m^3). The total cavity length is made to be 20 m long with the addition of 14 m of passive optical fiber. The fiber is closed on itself in order to form a ring cavity. To ensure unidirectional operation, an optical isolator is placed inside the cavity. The optical isolator is based on the Faraday effect and is polarization insensitive. The pump light coming from the argon laser is launched into the ring fiber through a wavelength division multiplexer (WDM), while an output coupler removes part of the light that circulates inside the cavity. In both cases, fiber ends were placed in an index-matching fluid to prevent possible parasitic Fresnel reflections, as shown in Fig. 1. Two different output couplers have been used, with coupling ratios 90/10 (10%) and 97/3 (3%), respectively. A 5× microscope objective is used to optimize the coupling of the pump light into the input port of the WDM. The output emission is passed through a 10% transmission neutral density (ND) filter and a half-wave plate to a polarization beam splitter, which separates the light into its two orthogonal polarization components. These components are measured with two high-speed photodetectors connected to the two input channels of a fast digital oscilloscope with a 1-GHz sampling rate. This setup allows us to measure the intensity with 100 data points per cavity round-trip.

In order to modify the polarization state of the light traveling inside the fiber, a polarization controller is used. Polarization controllers produce a phase shift by introducing a local birefringence into a portion of the fiber. This is accomplished by winding the fiber around mandrels of the proper diameter. It is very important to correctly choose both the diameter of the mandrels and the number of turns of the fiber around them: if the diameter is too small, the bending loss of the device becomes too high; too few turns would undesirably reduce the phase shift. We found that, for wavelengths of the circulating light, a diameter of 38 mm and three turns of fiber around each mandrel was a good choice to produce a small loss and a retardation effect similar to that of a half-wave plate.

B. Characterization of the system

A measurement of the total output power as a function of pumping is the first standard procedure used to characterize this laser system. Such a procedure shows that the lasing threshold is ~150 mW. When the the output light is separated into its two orthogonal polarization components, one can see that the two states have slightly different thresholds and very different output vs pump slopes in the lasing regime. This is a first indication of the well-known two-mode-like behavior of doped-fiber lasers [2,3]. By suitably modifying the state of the polarization controller, it is possible to separate the two main groups of modes that are amplified inside the cavity. The optical spectra in two orthogonal polarization directions, as obtained from an optical spectrum analyzer, show that the two mode groups are indeed orthogonal and linearly polarized, with spectral peaks centered around ~1.560 52 μm and ~1.561 05 μm, respectively.

The behavior of output vs pump power in the lasing regime is observed to be linear, which is a characteristic of most lasers. Nevertheless, at high pump powers, an increase of output power fluctuations occurs while making the measurements. In order to quantify this effect, one can measure the standard deviation of these fluctuations as a function of the mean light intensity and pump power. The results are shown in Fig. 2 for the case of 10% output coupling. For the sake of clarity, we should remark at this point that the pump power that appears in this figure is just the recorded output of the pump laser; it does not correspond exactly to the actual power that is being injected into the fiber laser, due to the imperfect launching of pump light into the cavity through the WDM. In any case, an analysis of this figure reveals a steady increase of the fluctuations as both pump level and output power are raised. This phenomenon is rather unexpected: in most single mode lasers, fluctuations produced by spontaneous emission are independent of pump level once lasing has been achieved. This is so because the spontaneous-emission rate is proportional to the population inversion in the amplifying medium, and this is constant beyond threshold, as can be seen from any rate-equation model [11]. In multimode lasers, these fluctuations may be deterministic and originate in the nonlinear dynamics of modes coupled through sharing of the population inversion.

We can calculate the number of modes inside the cavity by measuring the optical spectrum of the output light. The ratio of its full width at half maximum to the free spectral

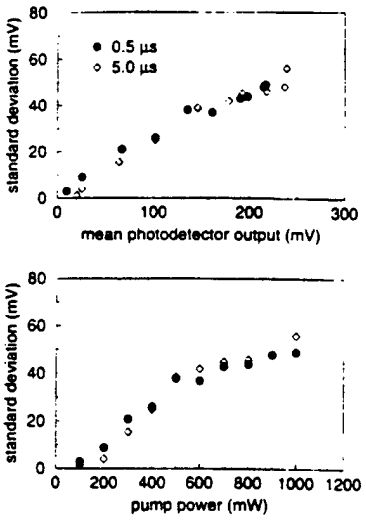

FIG. 2. Standard deviation of the output intensity fluctuations vs the mean output level and pump power. Two different sample times (shown in the legend) have been used. The pump power shown in the lower figure does not correspond to the power that is actually injected into the fiber.

range of the cavity (longitudinal mode spacing) gives us an estimate of this quantity. We observe a pronounced spectral narrowing and a corresponding sharp decrease in the number of modes (from $\sim 3\times 10^5$ to $\sim 2\times 10^3$) as the lasing threshold is crossed. Note, however, that even in the lasing regime the number of amplified modes is very large. This fact shows the strongly multimode character of fiber lasers.

C. Dynamical behavior

1. Self-pulsing

A characteristic time trace of the total output intensity extracted by the output coupler in the higher loss case (10% coupling) is shown in Fig. 3 for a pump rate well above threshold. Self-pulsing is observed with a periodicity of ~100 ns. This corresponds to the cavity round-trip time of our system, which is estimated as L/v, where $L=20$ m is the cavity length and $v=c/n$ is the speed of light in the fiber. The index of refraction of erbium-doped fiber is $n=1.46$.

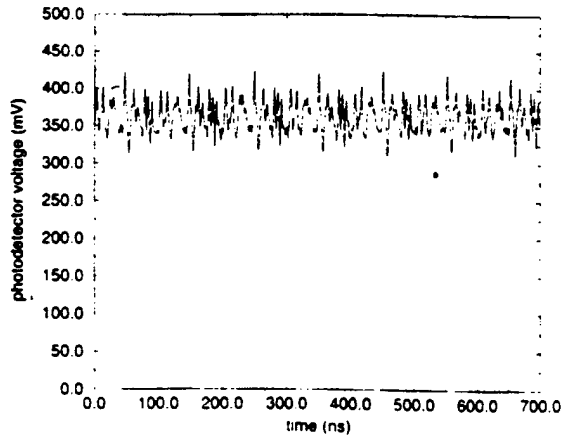

FIG. 3. Total output intensity time trace showing self-pulsing with 10% output coupler. The pump power is 400 mW.

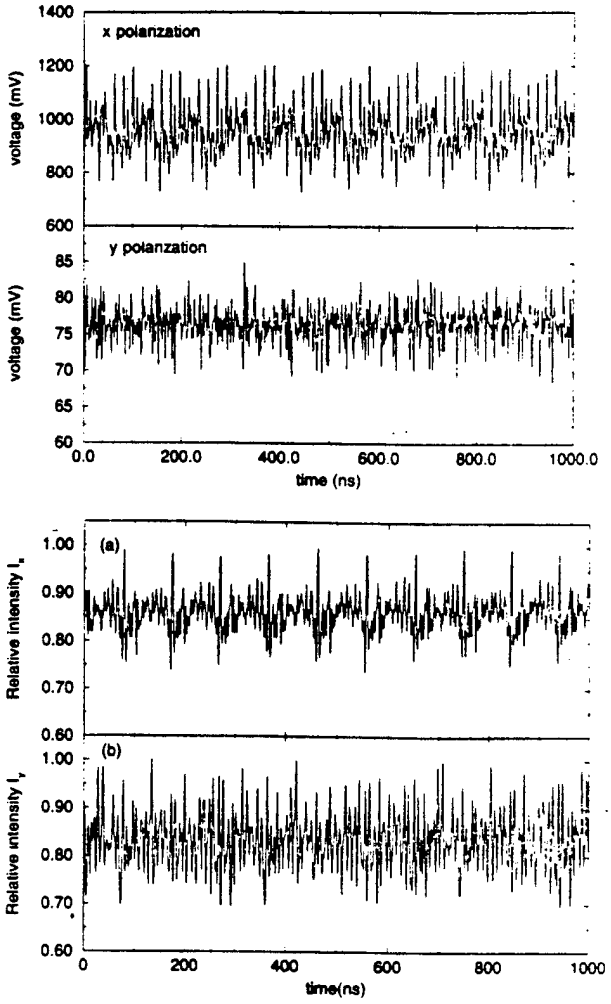

FIG. 4. Two different polarization-resolved time traces. Both polarization directions are shown in each case.

One can now resolve the output in terms of its orthogonal linear polarization components. These components, although coupled, may exhibit very different dynamics. Figure 4(a) shows quasiperiodic behavior in one polarization direction and random evolution in the other, also for 10% output coupling. In other experimental situations, one can observe different quasiperiodic evolution in the two modes. Figure 4(b) corresponds to a case with period-1 behavior in one direction and period-7 in the other. The 3% output coupler has been used in this case.

2. Influence of the polarization controller

Another way of establishing the distinct character of the polarization-resolved intensity time traces compared to those of the total output intensity is through their power spectrum. In the latter case, a typical spectrum shows peaks separated by the fundamental cavity frequency of 9.8 MHz. However, when the signal used comes from a single polarization direction, sideband peaks appear between the main ones. These sidebands can be tuned by manipulating the polarization controller and eventually can be made to overlap. When this happens and losses are small enough (i.e., the light intensity inside the cavity is high enough), the pulsed behavior disappears and square pulses develop in the output intensity of the

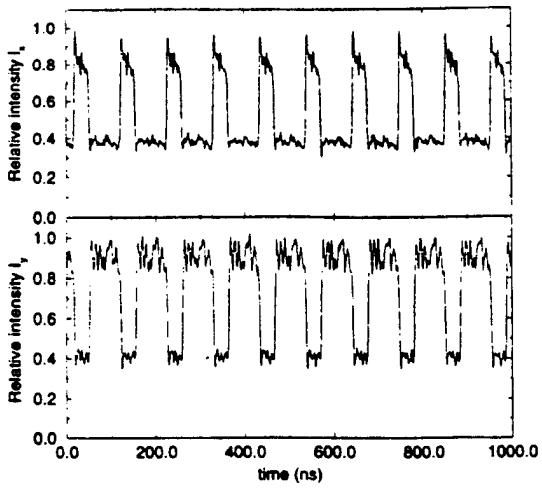

FIG. 5. Antiphase square pulsing in the two orthogonal polarization components of the output light for a given setting of the polarization controller and a 3% output coupling. The pump power is 600 mW.

orthogonal polarization states. This behavior is antiphase in the two states and is periodic at the cavity round-trip time, as shown in Fig. 5. The requirement that losses have to be low for this effect to occur is reflected in the fact that square pulses are observed when the 3% output coupler is used, but not in the 10% case. It is also worth noting that the time durations of the plateaus correspond to the lengths of the active and passive part of the fiber. In other words, the 70-ns upper part of the pulse in the y-polarization trace of Fig. 5 corresponds to the 14 m of passive fiber, whereas the 30-ns lower part is related to the 6 m of active erbium-doped fiber. A threshold pump power is typically observed for the onset of square pulsing. For the measurements shown, square pulses formed at a pump power ~ 2.2 times above threshold. In addition to square pulses, other antiphase pulse patterns have been observed. One of them is shown in Fig. 6. A final remark on this behavior is that the irregular intensity patterns superimposed on the plateaus of the square waves evolve continuously and slowly in time.

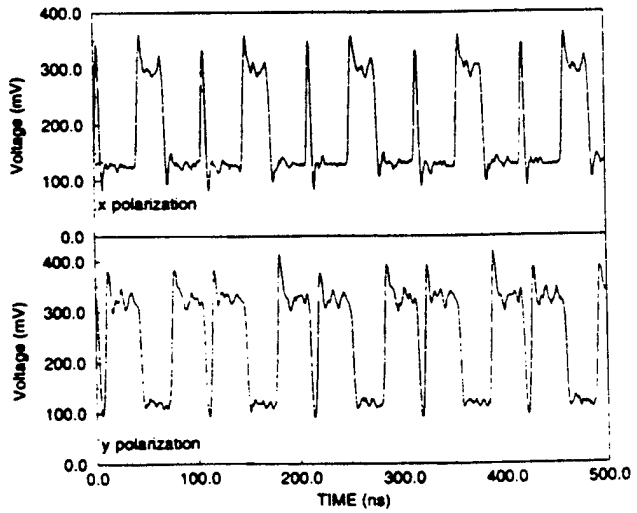

FIG. 6. Another antiphase pattern observed. Here the pump power is here 700 mW.

D. Nonlinear analysis

We have observed so far that this system has a wide variety of nonlinear attractors: regular or irregular temporal patterns in which the dynamics are trapped. Which specific attractor occurs depends on many factors: the state of the polarization controller, the pump power, the output losses, etc. We are now interested in dynamical characteristics of these attractors.

The state space of a dynamical system can be reconstructed from the information obtained through a scalar measurement (the intensity of one of the polarization eigenstates, for instance) by means of time-delay vectors [12]. If we denote as $x(n) \equiv x(t_0 + n\Delta)$ a scalar set of measurements sampled at equally spaced time intervals Δ, one can construct d-dimensional vectors

$$\mathbf{y}(n) = (x(n), x(n+T), \ldots, x(n+[d-1]T)). \quad (1)$$

The evolution of these time-delayed vectors in state space describes an attractor. There exists a minimum value of d for this attractor to properly represent the dynamical behavior of the system. This value is called the *embedding dimension* of the system. Both the embedding dimension and the time lag T have to be chosen carefully if one wants this state space reconstruction to be really useful.

To obtain a reasonable value of the time delay T, one has to reach a compromise between the high correlation between vector components that would arise if T is chosen too small [$x(n+iT)$ and $x(n+(i-1)T)$ would be nearly identical] and their statistical independence if T is too large. All these features are reflected in the so-called *average mutual information function*, which can be interpreted as a nonlinear correlation function between the time series $x(n)$ and $x(n+\Delta t)$ as a function of the time lag Δt. Its definition is

$$M(\Delta t) = \sum_{n=1}^{N} P(s(n), s(n+\Delta t)) \times \log_2 \left[\frac{P(s(n), s(n+\Delta t))}{P(s(n)) P(s(n+\Delta t))} \right], \quad (2)$$

where $P(s(n))$ is the probability density of the process $s(n)$ and $P(s(n), s(n+\Delta t))$ is the joint probability of the two time-shifted series. A high value of this function represents a high correlation between the series and a low value corresponds to a high degree of independence. A suitable value of T will be intermediate between these two regimes. A reasonable prescription that is frequently used [13] is to choose T as the first minimum of $M(\Delta t)$.

We can compute the average mutual information function (2) for the time series measurements obtained from our experiment. A typical result is shown in Fig. 7, corresponding to the intensity for a single polarization direction. The behavior is roughly the same for the other polarization direction and for the total output and also for the other different dynamical regimes investigated. The results suggest that an adequate value for the time delay is $T = 3$.

Once the time delay has been chosen, one needs to determine the embedding dimension. To do so, we use a method proposed in Ref. [14]. This procedure determines the minimum useful embedding dimension as that for which the per-

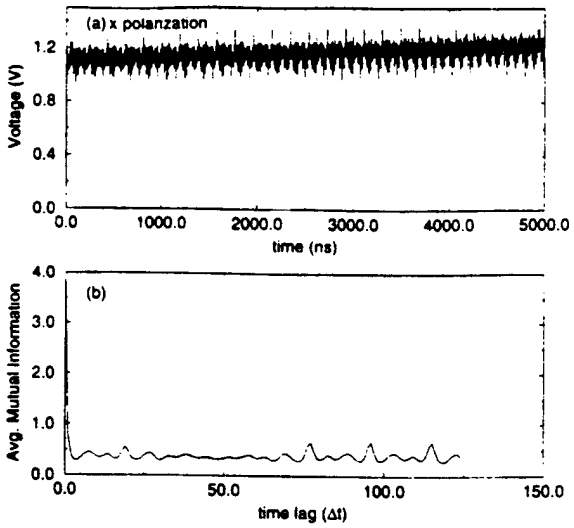

FIG. 7. Self-pulsing time series for the intensity output in one of the polarization directions and its corresponding average mutual information function. The pulse separation is $2\tau_R$ and the pump power is 1000 mW.

centage of *false nearest neighbors* (FNNs) in the attractor drops to zero. Two points of the attractor are said to be FNNs when they seem to be close only because the attractor is embedded in a dimension that is too low, but they are actually separated from one another. They can be identified by measuring the distance between them in two consecutive dimensions. When this distance is very small in the lowest-dimensional space and much larger in the highest-dimensional space, the two points are FNNs. The procedure consists of computing the percentage of FNNs for increasing dimensions. The embedding dimension is then determined as that dimension for which this percentage drops to a very small number. Figure 8 presents the result of this method for two different time series exhibiting very different dynamical behaviors. Figure 8(a) corresponds to a quasiperiodic low-dimensional regime with an embedding dimension $d_E=4$. Figure 8(b), on the other hand, shows a nonperiodic time series whose percentage of FNNs does not go to zero as the embedding dimension increases. This indicates that the dynamics in this case is high dimensional and hence noise driven. A similar coexistence of deterministic and stochastic behavior in the same dynamical system has recently been observed in a Nd:YAG laser (where YAG denotes yttrium aluminum garnet) exhibiting deterministic chaos [15].

III. MODELING

A. A delay-differential equation model

To develop a theoretical model that reproduces the observations made so far, several important characteristics of this system have to be taken into account.

(i) Even though many longitudinal modes are being amplified inside the cavity, the dynamics of the system can be described in terms of two supermodes corresponding to two orthogonal polarization states of the emitted light [2,3,7].

(ii) A description in terms of two-level rate equations is not suitable because of the long cavity of fiber lasers [3]. Variations in the direction of propagation of laser light have

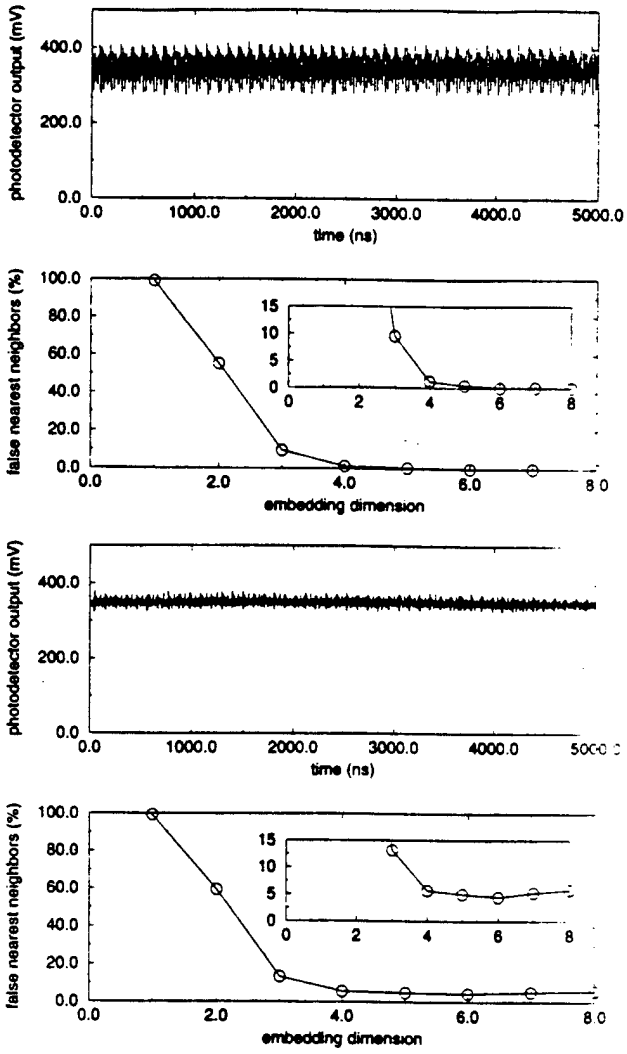

FI Experimental time traces and the corresponding percentage of nearest neighbors vs dimension for the (a) quasiperiodic case and (b) nonperiodic case. The insets in the lower plots show a zoom of the relevant regions of the graph.

to be taken into account. This requirement is completely unavoidable in our case since we are observing the dynamics *within* individual cavity round-trips.

(iii) The polarization controller is acting as an imperfect half-wave plate that almost completely switches polarizations once every cavity round-trip.

(iv) Only part of the total cavity length is active medium Hence this system has two different characteristic lengths which are reflected in the experimental results (see Sec II C 2) and must appear also in the theoretical model.

(v) Spontaneous-emission noise is known to have an important influence on the behavior of guided lasers such as the one we are dealing with in this experiment [2]. It thus seems necessary to include it in any realistic model of fiber lasers.

The first three points in the previous list have already been faced by Loh and Tang [8,9] in their description of ultrafast polarization self-modulation in semiconductor lasers. In this study, they developed a delay-differential equation model similar in approach to that used by Ikeda and co-workers [16,17] to analyze instabilities in the absorption of light by a passive medium placed inside a ring cavity and

by Otsuka and Iwamura [18] to model the dynamics of semiconductor laser amplifiers. We will follow the spirit of Loh and Tang's study to derive a model for our system.

Let $E_1(t,z)$ and $E_2(t,z)$ be the complex field envelopes of the two polarization modes of the amplified radiation. The following set of equations can be derived for their time evolution after adiabatically eliminating the polarization of the medium from the corresponding Maxwell-Bloch equations [8]:

$$\frac{\partial E_1(t,z)}{\partial z}+\frac{1}{v_g}\frac{\partial E_1(t,z)}{\partial t}=\frac{a_1}{2}(1-i\alpha_1)[N-N_0]E_1(t,z)+\mu_1(t,z), \tag{3}$$

$$\frac{\partial E_2(t,z)}{\partial z}+\frac{1}{v_g}\frac{\partial E_2(t,z)}{\partial t}=\frac{a_2}{2}t(1-i\alpha_2)[N-N_0]E_2(t,z)+\mu_2(t,z), \tag{4}$$

$$\frac{\partial N(t,z)}{\partial t}=P-\gamma_{\|}[N(t,z)+N_t]-a_1[N(t,z)-N_0]\frac{|E_1|^2}{\hbar\omega_1}-a_2[N(t,z)-N_0]\frac{|E_2|^2}{\hbar\omega_2}. \tag{5}$$

It can be seen that the two modes are coupled through $N(t,z)$, the population inversion of the medium. N_0 is the population inversion necessary for transparency (i.e., for zero gain) and N_t the density of erbium ions in the fiber. The quantity N_t has to be taken into account because erbium-doped fiber, when pumped at 514.5 nm, behaves as a three-level medium with incoherent pumping [11]. a_1 and a_2 are gain coefficients, α_1 and α_2 represent the detuning between the corresponding mode frequency ω_i and the resonance frequency of the cavity ω_0 [$\alpha_i=(\omega_0-\omega_i)/\gamma_\perp$, where $\gamma_\perp$ is the decay rate of the polarization of the medium], v_g is the velocity of light in the medium (assumed equal for the two modes), and P is the pump rate. These parameters have been defined in Ref. [10]. z is the direction of propagation of the light inside the cavity. $\mu_1(t,z)$ and $\mu_2(t,z)$ are spatiotemporal Gaussian and white stochastic processes that account for spontaneous emission. They have zero mean and correlation given by

$$\langle\mu_i(t,z)\mu_j^*(t',z')\rangle=2D_i\delta_{ij}\delta(t-t')\delta(z-z'). \tag{6}$$

We are now going to map the spatial dependence of the system into time by making use of the boundary conditions that have to be fulfilled by the fields E_1 and E_2 inside the cavity. These boundary conditions are

$$E_1(t,0)=\frac{1}{2}R_1e^{ik_1L}\left[E_1\left(t-\frac{l_P}{v_g},l_A\right)(e^{i\varphi}+1)+E_2\left(t-\frac{l_P}{v_g},l_A\right)(e^{i\varphi}-1)e^{-i\beta}\right], \tag{7}$$

$$E_2(t,0)=\frac{1}{2}R_2e^{ik_2L}\left[E_1\left(t-\frac{l_P}{v_g},l_A\right)(e^{i\varphi}-1)+E_2\left(t-\frac{l_P}{v_g},l_A\right)(e^{i\varphi}+1)e^{-i\beta}\right]. \tag{8}$$

Here l_A and l_P are the lengths of the active and passive parts of the fiber, respectively, and $L=l_A+l_P$ is the total fiber length. The reference frame is chosen in such a way that $z=0$ corresponds to one end of the active fiber. R_1 and R_2 are the return coefficients of the output coupler for each one of the modes. The parameter φ represents the phase shift caused by the polarization controller. In the perfect half-wave case ($\varphi=\pi$) it can be seen that the previous boundary conditions merely represent an exchange of polarizations every round-trip. We shall consider φ near, but not equal to, its perfect half-wave value. Finally, the parameter β represents the birefringence of the fiber, which causes different phase shifts in the two polarization modes. These different phase shifts are produced by the different velocities that the two modes actually have when traveling through the fiber, which can be modeled satisfactorily by including the parameter β while keeping v_g equal in both modes [9].

The previous boundary conditions can be used in combination with an integration of Eqs. (3)–(5) with respect to z to obtain the difference-differential model [9,19]

$$\psi_1(t)=\frac{1}{2}R_1\Lambda_1\left\{\left[\psi_1(t-\tau_R)\exp\left(\frac{\Gamma_1}{2}(1-i\alpha_1)[\phi(t)-1]\right)+\eta_1(t)\right](e^{i\varphi}+1)\times\left[\psi_2(t-\tau_R)\exp\left(\frac{\Gamma_2}{2}(1-i\alpha_2)[\phi(t)-1]\right)+\eta_2(t)\right](e^{i\varphi}-1)e^{-i\beta}\right\}, \tag{9}$$

$$\psi_2(t)=\frac{1}{2}R_2\Lambda_2\left\{\left[\psi_1(t-\tau_R)\exp\left(\frac{\Gamma_1}{2}(1-i\alpha_1)[\phi(t)-1]\right)+\eta_1(t)\right](e^{i\varphi}-1)\times\left[\psi_2(t-\tau_R)\exp\left(\frac{\Gamma_2}{2}(1-i\alpha_2)[\phi(t)-1]\right)+\eta_2(t)\right](e^{i\varphi}+1)e^{-i\beta}\right\}, \tag{10}$$

$$\frac{\partial\phi}{\partial t}=q-\phi(t)-|\psi_1(t-\tau_R)|^2(\exp\{\Gamma_1[\phi(t)-1]\}-1)-\mathrm{Re}[\psi_1(t-\tau_R)\xi_1(t)]-|\psi_2(t-\tau_R)|^2(\exp\{\Gamma_2[\phi(t)-1]\}-1)-\mathrm{Re}[\psi_2(t-\tau_R)\xi_2(t)], \tag{11}$$

where new dimensionless variables have been defined. ψ_1 and ψ_2 are related to the electric field envelopes at $z=0$,

$$\psi_i(t) \equiv \frac{E_i(t,0)}{\sqrt{\hbar \omega l_A \gamma_{\parallel} N_0}} \tag{12}$$

and ϕ is the dimensionless total population inversion in the active fiber,

$$\phi(t) \equiv \frac{W(t-\tau_R, l_A)}{l_A N_0} = \frac{1}{l_A N_0} \int_0^{l_A} N(t-\tau_R, z)\, dz. \tag{13}$$

Time is now measured in units of $\gamma_{\parallel}^{-1}$. τ_R is the cavity round-trip time, also measured in units of $\gamma_{\parallel}^{-1}$ ($\tau_R = L/v_g \gamma_{\parallel}$). We have defined a dimensionless gain parameter and an effective pump rate as

$$\Gamma_i = a_i l_A N_0, \quad q \equiv \frac{P}{\gamma_{\parallel} N_0} - \frac{N_t}{N_0}. \tag{14}$$

Λ_1 and Λ_2 are phase-shift coefficients that can be evaluated as [9]

$$\Lambda_i \equiv e^{ik_i L} = \exp\left[i\alpha_i \frac{\Gamma_i}{2} [\phi(0) - 1] \right]. \tag{15}$$

An inspection of the delay-differential model (9)–(11) shows that the original spontaneous emission noise sources $\mu_i(t,z)$, $i=\{1,2\}$, have given rise to new noise terms $\eta_i(t)$ and $\xi_i(t)$ in all three equations for the electric fields and the population inversion. The stochastic processes $\eta_i(t)$ come from the formal integration of the spontaneous-emission noise sources $\mu_i(t,z)$ over the space variable z, whereas $\xi_i(t)$ appear through the introduction of the result of this integration into Eq. (5). It is worth noting that these new stochastic processes are no longer space dependent; this is true of all the other quantities of the model as well. Note also that in the population inversion equation the noise terms are *multiplicative* [19]. They are all Gaussian distributed with zero mean, and we will denote their variances by D_i^{η} and D_i^{ξ}. We will treat these noise strengths as adjustable parameters for our studies; they can be related to the physical properties of the system as [19]

$$D_i^{\eta} = \frac{D_i}{\hbar \omega_i N_0},$$

$$D_i^{\xi} = 4\, a_i^2 (N_{SS} - N_0)^2 l_A^2 \frac{D_i}{\hbar \omega_i N_0}, \tag{16}$$

where N_{SS} is the steady-state value of the population inversion.

In summary, we have obtained a delay-differential equation model that translates the space dependence on the propagation direction z (and hence its infinite-dimensional character) into a dependence on time-delayed quantities. The model also includes the influence of intrinsic noise sources. We have performed extensive numerical computations with this model, and the results obtained will be described in the following subsections.

The simulations are performed as follows. Each cavity round-trip time is divided into equal-size time intervals (or, equivalently, the cavity is discretized in a number of equal cells). The evolution of the fields ψ_1 and ψ_2 depends on their values one round-trip earlier [Eqs. (9) and (10)] and the total inversion ϕ evolves according to the differential equation (11), which is discretized in the equally spaced time intervals defined above (or in the one-dimensional spatial lattice in which the cavity has been divided). Since in our case the cavity round-trip time is much smaller than the population inversion decay time, the integration time steps resulting from a not very dense cavity subdivision are small enough to ensure numerical stability in the algorithm that integrates the differential equation. We will usually choose a subdivision of the cavity in 100 parts and use a Heun algorithm (a stochastic version of a second-order Runge-Kutta scheme) [20] to simulate that equation. The multiplicative noise terms are treated according to a Stratonovich interpretation.

A distinction has to be made at this point between the active and the passive fiber. Since the polarization controller is located in the passive part of the cavity and the delay differential model maps time into space, the value of the phase shift φ will be close to π only in the time instants corresponding to the passive part of the fiber. The rest of the time φ will be near zero (not exactly zero because any small winding in the active fiber may also have a small phase-shifting effect). Hence we will take φ to be equal to φ_A (small) in the active region and to φ_P (close to π) in the passive part.

Several of the parameters of the model will be fixed by physical requirements of the active medium and the experimental setup, whereas others will be used as adjustable parameters. Among the former, we have the gain coefficients a_1 and a_2, which will be taken to be coincident and equal to 2.03×10^{-23} m^2. The detuning factors α_1 and α_2 will also be taken to be the same and equal to 3.52×10^{-2}. The population decay rate $\gamma_{\parallel}$ is 10^2 s^{-1} and its inverse is the time unit we use throughout this section. The lengths of the active and passive fibers are the ones used in the experiment (6 m and 14 m, respectively), with a total cavity length of $L=20$ m, which gives a round-trip time equal to $\tau_R = nL/c\gamma_{\parallel} = 10^{-5}$ dimensionless time units. The dopant ion concentration is $N_t = 4.98 \times 10^{25}$ m^{-3} and the transparency inversion is $N_0 \approx 10^{20}$ m^{-3}. The return coefficient of the output coupler will be taken to be, according to the experimental setup, $R_1 = R_2 = 0.97$, equal for both polarization modes. The noise strengths are chosen to be $D_1^{\eta} = D_2^{\eta} = D_1^{\xi} = D_2^{\xi} = 10^{-5}$. To put these noise source variances in perspective, we should remark at this point that the magnitude of the light intensity in the lasing regime is, in our dimensionless units, of the order of 10^6. The pump rate will take several values for the different regimes. The phase shifts φ_A and φ_P and the birefringence coefficient β will be adjustable parameters. A summary of the previous values is shown in Table I.

B. Characterization of the model

A first comparison between the numerical model that has just been derived and the experimental observations shown previously is made by computing how the laser output

TABLE I. Parameters used in the delay-differential model.

Parameter	Value	Units	Description
$a_{1,2}$	2.03×10^{-23}	m^2	gain coefficients
$\alpha_{1,2}$	3.52×10^{-2}		detuning factors
$\gamma_{\parallel}$	10^2	s^{-1}	population decay rate
l_A	6	m	length of active fiber
L	20	m	total cavity length
τ_R	10^{-7}	s	cavity round-trip time
N_0	10^{20}	m^{-3}	transparency inversion
N_t	4.98×10^{25}	m^{-3}	dopant ion concentration
$R_{1,2}$	0.97		output coupler return
$D^{\eta}_{1,2}$	10^{-5}		coefficients
$D^{\xi}_{1,2}$	10^{-5}		electric-field noise strength
			population inversion noise strength

changes with increasing pump power. A sudden jump in photon number (over nine orders of magnitude) is observed and represents the transition from a spontaneous emission (no lasing) to a stimulated emission regime (lasing). Linear behavior is observed in the lasing regime. The estimated value of the lasing threshold ($\sim5\times10^5$ in dimensionless units) is in qualitative agreement with the experimental result.

It has also been found that this model reproduces the striking experimental observation of an increase in intensity fluctuations for higher pumping and output power. The results are shown in Fig. 9 and should be compared with their experimental counterpart presented in Fig. 4. The fact that this behavior persists even in the absence of stochastic terms in the simulations indicates that these intensity fluctuations are of deterministic origin. They are related to spiking and pulsing phenomena occurring in the time evolution of the light intensity and may be caused by the coupling dynamics between the many modes that are undergoing amplification, as mentioned in Sec. III A.

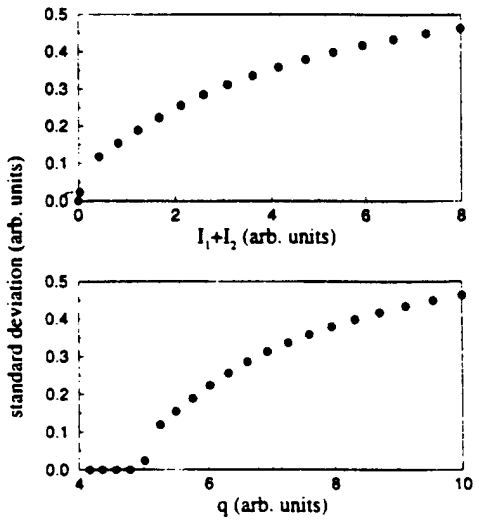

FIG. 9. Standard deviation of the total intensity output vs total output power I_1+I_2 and pump rate q.

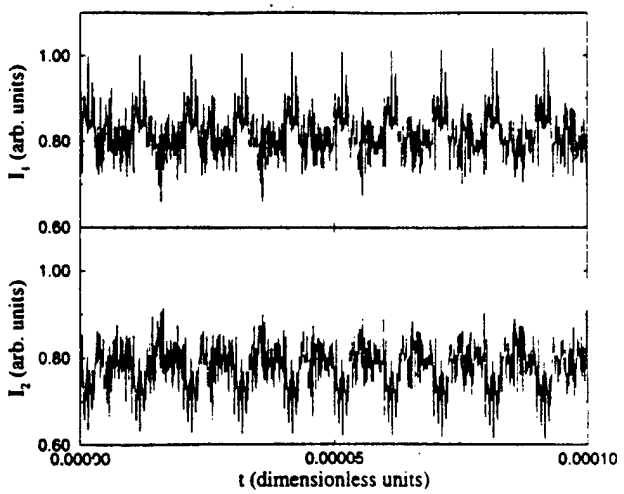

FIG. 10. Polarization-resolved quasiperiodic self-pulsing time traces. A periodicity equal to one cavity round-trip time is observed. The pump rate is $q=2\times10^6$ dimensionless units, roughly 5 times above threshold.

C. Dynamical behavior

1. Self-pulsing

Typical time traces of the output intensity $I_i=|\psi_i|^2$, as obtained from our delay-differential model, are shown in Figs. 10 and 11. Self-pulsing behavior is clearly observed, with different overall characteristics depending on the values of the parameters. Figure 10 presents antiphase quasiperiodic self-pulses at a periodicity of one cavity round-trip time. Figure 11 shows period-2 behavior. The difference between both cases lies only in the value of the birefringence factor, equal to 0.0015 in the first case and taken to be exactly zero in the second. The values chosen for the phase shifts are 0.027 in the active fiber and $\pi-0.175$ in the passive fiber. All the other parameters are those of Table I. It is worth noting that in all cases we obtain antiphase motion for the two polarization modes. The structures immersed in this self-pulsing behavior are observed to drift slowly as time

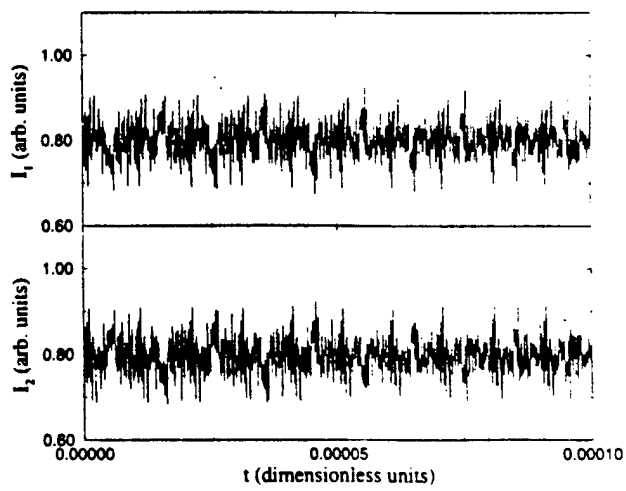

FIG. 11. Polarization-resolved quasiperiodic self-pulsing time traces with a period equal to $2\tau_R$. The pump rate is the same as in Fig. 10.

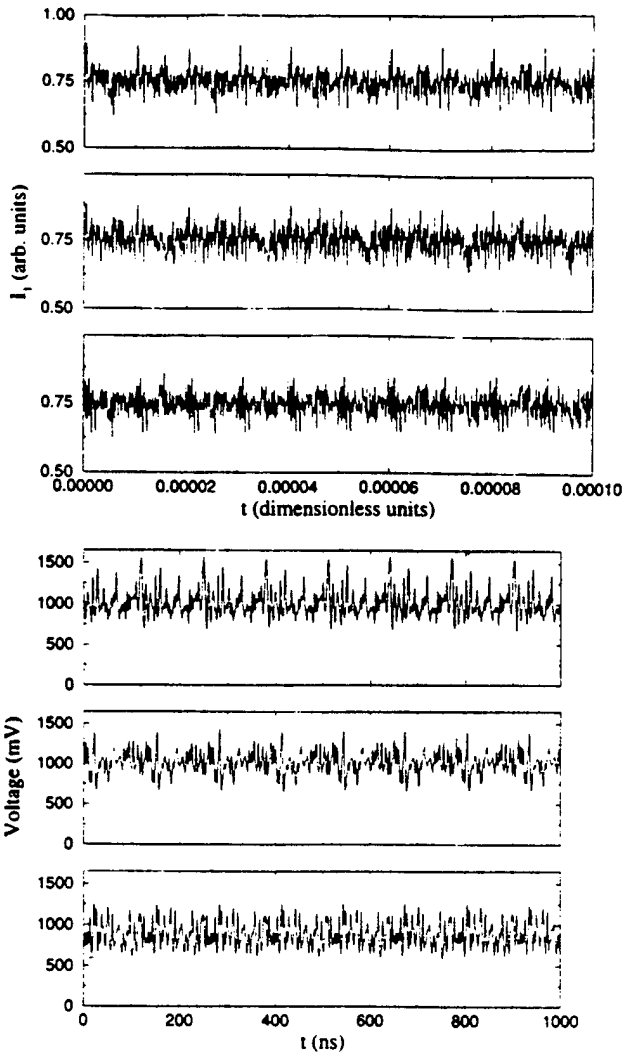

FIG. 12. Three snapshots of the self-pulsing behavior of one polarization mode, showing the slow drift of temporal patterns due to the effect of stochastic noise sources. These snapshots are separated in time by several hundred round-trips. (a) Numerical simulation (parameters are the same as in the previous figures) and (b) experimental behavior (in this case the cavity round-trip time is ~130 ns).

evolves, as observed in the experiments (see Fig. 12). This pattern evolution does not occur if the noise sources are neglected in the model, which indicates the importance of spontaneous emission in this system.

2. *Influence of the phase shifts*

The value of φ_P used in the previous simulations corresponds to an imperfect half-wave plate. By taking a value of this phase shift closer to π (which amounts to properly tuning the polarization-controller mandrels in the experiment), we can reproduce the square-wave behavior observed in the real system. Figure 13 is the result of making $\varphi_P = \pi - 0.015$ and $\beta = 0.020$. As in the experimental output, these square waves are antiphase in both polarization components, with a period equal to the cavity round-trip time, and a relation between the lengths of the upper and lower plateau equal to that between the lengths of the active and passive part of the cavity. Also, as in the experiment, the

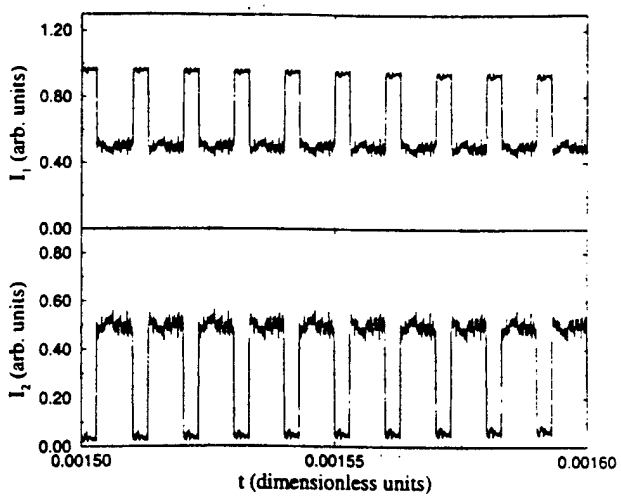

FIG. 13. Antiphase square pulses generated by the delay-differential model by properly tuning the value of φ_P. The pump rate is the same as in the previous figures.

patterns on top of the square pulses change continuously and slowly with time, as shown in Fig. 14, where three series of ten cavity round-trip times occurring at different instants of the same dynamical evolution are compared. Again, this behavior is not obtained if the spontaneous-emission noise is not taken into account.

D. Nonlinear analysis

To complete our comparison between the results given by the delay-differential model that has been derived in this section and the results obtained from the experimental system, we will analyze the numerical time traces from a nonlinear dynamics point of view. We can compute the average mutual information function of a polarization-resolved output time trace. Figure 15 shows the typical behavior of this function [which in this case corresponds specifically to the time trace shown in Fig. 16(a)]. We conclude that a reasonable value

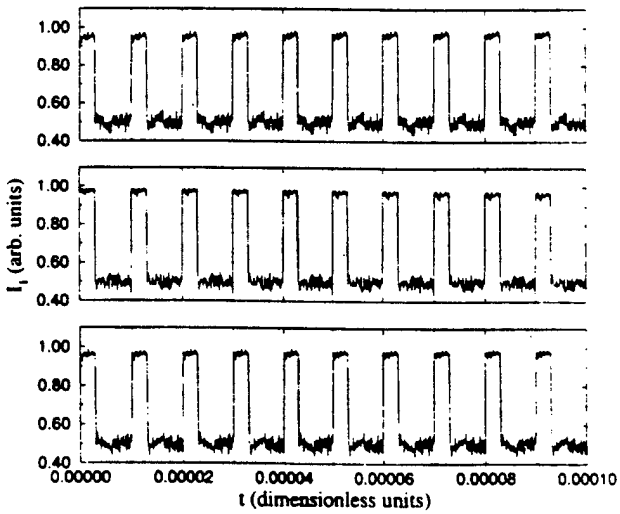

FIG. 14. Three snapshots of the numerically simulated behavior of one polarization mode, showing that the detailed structure of the square-wave patterns evolves slowly in time. The parameters are the same as in the previous figures.

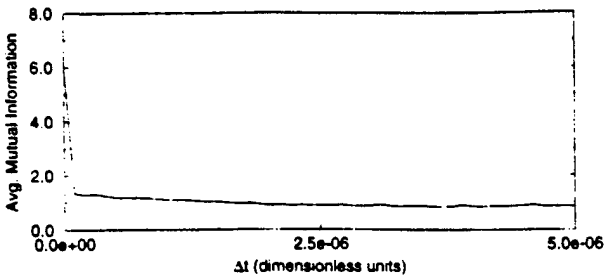

FIG. 15. Typical example of the average mutual information function obtained numerically. The actual time trace from which this function has been derived is shown in Fig. 16(a).

for the time lag to be used in phase-space reconstruction is $\Delta t = 10^{-7}$ dimensionless units, which corresponds to one time interval in the cavity subdivision we have chosen throughout this work. We now compute the percentage of false nearest neighbors for different dimensions in two different regimes. Figure 16(a) shows a time trace exhibiting a high degree of periodicity and its corresponding false-nearest-neighbor percentage vs embedding dimension. This result shows that the behavior of the system in this regime is low-dimensional and deterministic, with an embedding dimension $d_E = 4$. Figure 16(b), on the other hand, shows a nonperiodic time trace and a false-nearest-neighbor percentage that does *not* go to zero for increasing dimension, implying that the behavior in this case is high dimensional and noise driven. We remind the reader that these two different regimes have also been obtained experimentally (Fig. 8). We regard this agreement as a significant indication of the success of our model in capturing the dynamical behavior of the laser system.

IV. CONCLUSION

We have analyzed the fast, intracavity dynamics of an erbium-doped fiber laser in a ring cavity. Since it is well known that this kind of system presents interesting polarization dynamics, we have introduced a polarization controller inside the laser cavity. Self-pulsing has been observed in a very broad range of system configurations, both in the total output intensity of the laser and in the polarization-resolved dynamics, in periods of the order of the cavity round-trip time. In this regime the two different polarization modes can behave independently, i.e., one may show quasiperiodic dynamics and the other chaotic behavior, for instance. Due to the long cavity and fast detection devices, we have been able to sample the behavior inside a cavity round-trip. By carefully tuning the polarization controller, the self-pulsing behavior can be transformed into square-wave dynamics. In this case, the behavior of the two polarization modes is usually antiphase, as predicted for lasers with a strong multimode character. All these features can be reproduced by a stochastic delay-differential equation model, which takes into account the fact that a mean-field approximation in the propagation direction is misleading in this kind of long-cavity laser. Spontaneous emission is introduced via a noise term in the original Maxwell-Bloch equations and leads to a nontrivial stochastic contribution to the delay-differential model. This model is able to reproduce both the self-pulsing

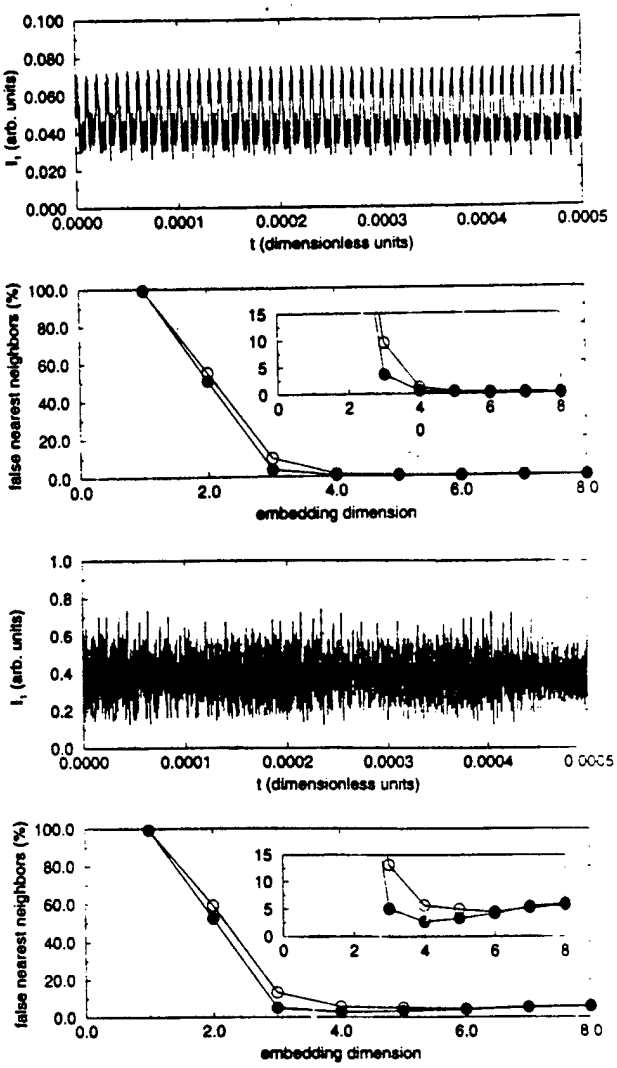

FIG. 16. Quasiperiodic time trace and its percentage of false nearest neighbors vs dimension. Full circles represent the numerical result, which corresponds to a pump rate of $q = 6 \times 10^5$ dimensionless units, ~1.1 times above threshold. Empty circles are the experimental result of Fig. 8(a). (b) Nonperiodic time trace and its percentage of false nearest neighbors vs dimension, which displays a residual percentage of FNNs, implying random dynamics. Full circles represent the numerical result, which corresponds to a pump rate of $q = 1 \times 10^6$ dimensionless units, ~2 times above threshold. In this case, the noise source strengths have been increased to a value of 1.2×10^{-4} dimensionless units to obtain better agreement with the experiments, which are represented by empty circles [from Fig. 8(b)].

and the square-wave behavior. Spontaneous-emission noise is necessary to obtain the observed slow time drift of the patterns underlying the square-pulse structure. However, even though spontaneous emission (and hence the noise sources in the model) is always present in the laser operation, we observe, numerically and experimentally, both a deterministic and a noise-driven regime for slightly different values of the system parameters. The first situation corresponds to a quasiperiodic, low-dimensional motion and the second to a random, high-dimensional behavior. The coexistence of these two types of behavior in the same nonlinear dynamical system is a remarkable feature that deserves further study.

ACKNOWLEDGMENTS

We gratefully thank H. Abarbanel and C. Liu for making available to us the software on the false-nearest-neighbor method. We also acknowledge support from the Division of Chemical Sciences, Office of Basic Energy Sciences, Office of Energy Research, U.S. Department of Energy and the Office of Naval Research. J.G.O. acknowledges support from the Dirección General de Investigación Científica y Técnica (Spain).

[1] K. Otsuka, P. Mandel, S. Bielawski, D. Derozier, and P. Glorieux, Phys. Rev. A **46**, 1692 (1992).
[2] S. Bielawski, D. Derozier, and P. Glorieux, Phys. Rev. A **46**, 2811 (1992).
[3] E. Lacot, F. Stoeckel, and M. Chenevier, Phys. Rev. A **49**, 3997 (1994).
[4] P. Le Boudec, M. Le Flohic, P.L. François, F. Sanchez, and G. Stephan, Opt. Quantum Electron. **25**, 359 (1993).
[5] F. Sanchez, P. Le Boudec, P.L. François, and G. Stephan, Phys. Rev. A **48**, 2220 (1993).
[6] W.H. Loh, Y. Ozeki, and C.L. Tang, Appl. Phys. Lett. **56**, 2613 (1990).
[7] B. Meziane, F. Sanchez, G.M. Stephan, and P.L. François, Opt. Lett. **19**, 1970 (1994).
[8] W.H. Loh and C.L. Tang, IEEE J. Quantum Electron. **27**, 389 (1991).
[9] W.H. Loh and C.L. Tang, Opt. Commun. **85**, 283 (1991).
[10] Q.L. Williams and R. Roy, Opt. Lett. **21**, 1478 (1996).
[11] O. Svelto, *Principles of Lasers*, 3rd ed. (Plenum, New York, 1989).
[12] H.D.I. Abarbanel, R. Brown, J.J. Sidorowich, and L.S. Tsimring, Rev. Mod. Phys. **65**, 1331 (1993).
[13] A.M. Fraser and H.L. Swinney, Phys. Rev. A **33**, 1134 (1986).
[14] M.B. Kennel, R. Brown, and H.D.I. Abarbanel, Phys. Rev. A **45**, 3403 (1992).
[15] H.D.I. Abarbanel, Z. Gills, C. Liu, and R. Roy, Phys. Rev. A **53**, 440 (1996).
[16] K. Ikeda, Opt. Commun. **30**, 257 (1979).
[17] K. Ikeda, H. Daido, and O. Akimoto, Phys. Rev. Lett. **45**, 709 (1980).
[18] K. Otsuka and H. Iwamura, Phys. Rev. A **28**, 3153 (1983).
[19] J. García-Ojalvo and R. Roy, Phys. Lett. A (to be published).
[20] T.C. Gard, *Introduction to Stochastic Differential Equations* (Dekker, New York, 1987).

PHYSICS LETTERS A

Physics Letters A 224 (1996) 51–56

Noise amplification in a stochastic Ikeda model

J. García-Ojalvo [1], R. Roy
School of Physics, Georgia Institute of Technology, Atlanta, GA 30332-0430, USA

Received 3 July 1996; revised manuscript received 15 September 1996; accepted for publication 14 October 1996
Communicated by C.R. Doering

ELSEVIER

30 December 1996

PHYSICS LETTERS A

ELSEVIER

Physics Letters A 224 (1996) 51–56

Noise amplification in a stochastic Ikeda model

J. García-Ojalvo [1], R. Roy

School of Physics, Georgia Institute of Technology, Atlanta, GA 30332-0430, USA

Received 3 July 1996; revised manuscript received 15 September 1996; accepted for publication 14 October 1996
Communicated by C.R. Doering

Abstract

The effect of spontaneous emission noise on the light circulating in a ring cavity with a nonlinear absorbing medium is studied by means of a set of stochastic delay-differential equations based on the deterministic Ikeda model. Noise fluctuations are found to be amplified as the first bifurcation from the steady state of the system is approached.

1. Introduction

Delay-differential equations are frequently used to model nonlinear dynamical systems. Among them, the so-called *Ikeda model* is particularly well known in the analysis of the dynamical behavior of nonlinear optical media. Since its introduction by Ikeda and coworkers [1,2] in the investigation of the light transmission process by a nonlinear absorber contained in a ring cavity, it has increasingly been applied to the study of the interaction of light with either passive [3–5] or active [6,7] media. Also, due to its highly complex multistable behavior, the model eventually leads to chaos through a rich variety of routes [8]. Hence, its simplified map version has become a paradigm in the analysis of chaotic systems [9–12]. It is therefore of interest to investigate the influence of spontaneous emission noise on the dynamics of this system. It is particularly important to consider the physical origin of the noise source; here we begin with the Maxwell–Bloch equations and outline the inclusion of spontaneous emission noise in a physically meaningful way, leading to a stochastic version of the deterministic Ikeda model.

2. Derivation of the stochastic Ikeda model

Let us consider the simple situation, originally analysed by Ikeda in his seminal paper [1], of a nonlinear absorbing medium placed in a ring cavity. This medium shall be assumed to be a set of homogeneously broadened two-level atoms, whose interaction with an incident light beam can be described by the following equations,

$$\frac{\partial E}{\partial z} = (\alpha + i\beta)(N - N_0)E + \mu, \tag{1}$$

$$\frac{\partial N}{\partial \tau} = -\gamma N - \Omega(N - N_0)|E|^2, \tag{2}$$

where $E(\tau, z)$ is the complex envelope of the electric field which propagates in the absorber, $N(\tau, z)$ is the population inversion ($N < 0$ for an absorber) and $\mu(\tau, z)$ is a Gaussian and spatio-temporal white stochastic process accounting for spontaneous emis-

[1] On leave from: Dept. de Física i Enginyeria Nuclear, E.T.S. d'Enginyers Industrials de Terrassa, Univ. Politècnica de Catalunya, Colom 11, E-08222 Terrassa, Spain.

PII S0375-9601(96)00802-X

sion processes. This noise term is chosen to have zero mean and correlation equal to

$$\langle \mu(\tau, z)\mu^*(\tau', z')\rangle = 2D\delta(\tau - \tau')\delta(z - z'). \quad (3)$$

It should be noted that the white character of this noise source is a mathematical idealization of the spontaneous emission process, which actually has correlations in time and space that are very small in comparison to all other time and length scales of the system.

Eqs. (1), (2) can be obtained in a straightforward way from the standard Maxwell–Bloch equations which describe the propagation of the electric field inside the absorber by adiabatically eliminating the polarization of the medium, whose relaxation rate is much larger that those of N and E. The space variable z corresponds to the direction of light propagation (transverse effects which might appear in the directions perpendicular to propagation [13,14] are not considered here). The time variable τ is written in a reference frame which moves with the velocity v_g of light in the medium, $\tau = t - z/v_g$. α (>0) is the absorption coefficient of the medium, β is a parameter depending on the detuning between the cavity and the transition resonance frequencies, and γ is the population decay rate. The coefficient Ω of the nonlinear term in (2) depends on the dipole moment of the transition. N_0 is the value of N corresponding to transparency.

Let L denote the length of the absorbing medium, $\mathcal{L}$ that of the whole cavity and $l = \mathcal{L} - L$. Then, the relation between the incident field E_I and the field propagating inside the cavity is given by the following boundary condition,

$$E(t,0) = \sqrt{T}\,E_I + R\exp(ik\mathcal{L})E\left(t - \frac{l}{v_g}, L\right) \quad (4)$$

where T is the transmission coefficient of the input mirror M1 and $R = 1 - T$ is the reflexion coefficient of both the input and output mirrors M1 and M2 (see Fig. 1). Mirrors M3 and M4 are assumed to be perfectly reflecting. k is the light wavenumber.

The space dependence of the previous equations can be removed by using this boundary condition. First, we formally integrate Eq. (1) with respect to z and introduce the result into Eq. (2). As a result, the originally additive noise μ generates a *multiplicative* noise term in the equation for the population inversion,

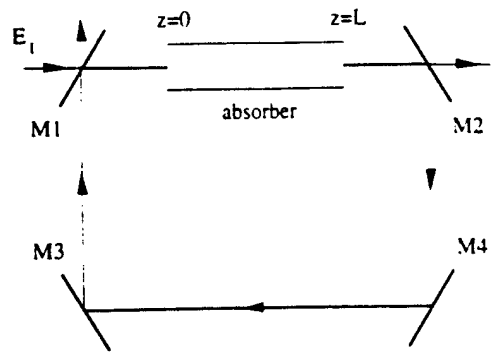

Fig. 1. Scheme of the ring cavity containing the absorber.

$$E\left(\tau + \frac{z}{v_g}, z\right) = E(\tau,0)\exp\left[(\alpha + i\beta)(W - N_0 z)\right] + \Gamma(\tau, z) \quad (5)$$

$$\frac{\partial W(\tau,z)}{\partial \tau} = -\gamma W + \frac{\Omega}{2\alpha}\{\exp[2\alpha(W - N_0 z)] - 1\}|E(\tau,0)|^2 + 2\Omega(N_s - N_0)\mathrm{Re}(E(\tau,0)\chi(\tau,z)), \quad (6)$$

where $W(\tau, z)$ is defined as

$$W(\tau,z) = \int_0^z dz'\, N\left(\tau + \frac{z'}{v_g}, z'\right). \quad (7)$$

To obtain the evolution equation for $W(\tau, z)$ (1 (6)), the variations of the population inversion in (5) have been assumed to be negligible. Numeri simulations show that the variations in this quan are a very small fraction of its average value N_s (Fig. 2). Also, two new stochastic processes have b defined, which are also Gaussian with zero mean correlations,

$$\langle \Gamma(\tau,z)\Gamma^*(\tau',z)\rangle = 2Dz\delta(\tau - \tau'), \quad (8)$$

$$\langle \chi(\tau,z)\chi^*(\tau',z)\rangle = 2Dz^3\delta(\tau - \tau'), \quad (9)$$

$$\langle \chi(\tau,z)\Gamma(\tau',z)\rangle = 2Dz^2\delta(\tau - \tau'). \quad (10)$$

These noise sources arise from the application of tegral operators to the original spontaneous emiss noise. In order to obtain the simple expressions sh above for the variances, the population inversion been assumed again to be constant. Notice also the cross-correlation between $\chi(\tau, z)$ and $\Gamma(\tau, z$

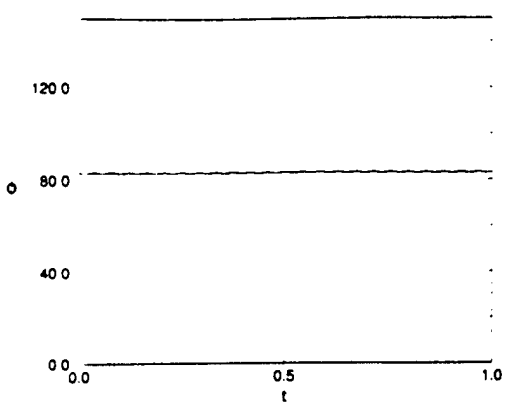

Fig. 2. Typical evolution of the total population inversion, coming from a simulation of Eqs. (11) and (12), with parameters: $A = 9.90$, $B = 0.60$, $\phi_0 = 0.0$, $\tau_R = 0.01$, and $D_\eta = D_\xi = 0.0$.

non-zero. Nevertheless, the influence of this cross-correlation in the dynamics of the system was found negligible in numerical simulations, and it has not been considered in what follows. It should also be noted that, in deriving Eq. (6), a contribution proportional to $|\Gamma|^2$ has been discarded, due to the small strength of this noise source.

Introduction of Eq. (5) into boundary condition (4) and use of the population inversion Eq. (6) at point $z = L$ leads to the following difference–differential equations,

$$\psi(t) = A + B\psi(t-\tau_R)\exp\left\{i\left[\phi(t)+\phi_0\right]\right\} + \eta(t), \tag{11}$$

$$\frac{d\phi}{dt} = -\phi + |\psi(t-\tau_R)|^2 + 2\mathrm{Re}\left[\psi(t-\tau_R)\xi(t)\right]. \tag{12}$$

Time t is now measured in units of γ^{-1} and the following dimensionless variables have been defined,

$$\psi(t) \equiv E(t,0)\exp(\alpha W_0)\sqrt{\frac{\Omega\beta}{2\alpha\gamma}}, \tag{13}$$

$$\phi(t) \equiv \beta W(t-\tau_R, L), \tag{14}$$

where $W_0 = N_0 L$.

The noise sources $\eta(t)$ and $\xi(t)$ are dimensionless and space-independent versions of Γ and χ. It can easily be seen that its variances D_η and D_ξ are related to the original physical parameters by

$$D_\eta = DR^2 e^{2\alpha W_0}\Omega L\beta/2\alpha, \tag{15}$$

$$D_\xi = De^{-2\alpha W_0}\Omega L^3\beta 2\alpha(N_s - N_0). \tag{16}$$

A remark should be made at this point in relation to the difference equation (11). This equation makes no sense mathematically if the stochastic process $\eta(t)$ is taken to be white. This interpretation problem can be avoided by recalling that the original spontaneous emission noise has a very small, but non-negligible, correlation time. In this case the parameter D corresponds to the (finite) value of the correlation function of the noise at equal times.

Besides these two noise strengths, this model has four other independent parameters: the dimensionless incident field $A = \sqrt{T}E_1\exp(\alpha W_0)\sqrt{\Omega\beta/2\alpha\gamma}$, the dissipation $B = R\exp(-\alpha W_0)$, the phase shift due to propagation $\phi_0 = k\mathcal{L} - \beta N_0 L$ and the dimensionless cavity round-trip time $\tau_R = \gamma\mathcal{L}/v_g$.

Eqs. (11) and (12) define the stochastic version of the standard Ikeda model, which includes the existence of spontaneous emission processes of the two-level atoms forming the absorber. It is worth noting that what is initially an additive noise in the original partial-differential equation scheme has become multiplicative in the difference-differential equation model. This may be considered as an indication of the non-trivial influence of the spontaneous emission process.

3. Influence of noise on dynamics

As stated above, the dynamical properties of even the deterministic version of the Ikeda model lead to a highly complex behavior of the model. In particular, the steady state solution of the model, which can be seen to obey the following transcendental equation,

$$|\psi_s|^2\left[1 + B^2 - 2B\cos\left(|\psi_s|^2 + \phi_0\right)\right] = A^2, \tag{17}$$

is a multivalued function of the input parameter A (see Fig. 3). This means that even in the cases in which the system evolves towards a fixed-point attractor, it faces a high degree of multistability. The effects of this fact can immediately be seen by looking at the bifurcation diagram of the light intensity extrema $|\psi|^2_e$ versus the input parameter A (Fig. 4). The step-like appearance of this diagram is a clear indication of the multistable character of the attractor structure of the system, each step corresponding to a jump between two equally stable states. The position of the jumps

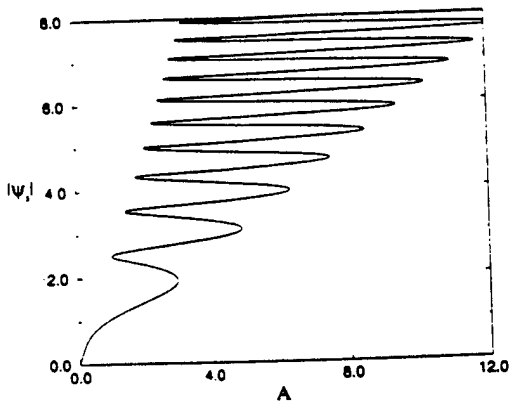

Fig. 3. Steady state solution of the deterministic Ikeda map. Parameters are $B = 0.60$, $\phi_0 = 0.0$ and $\tau_R = 0.01$.

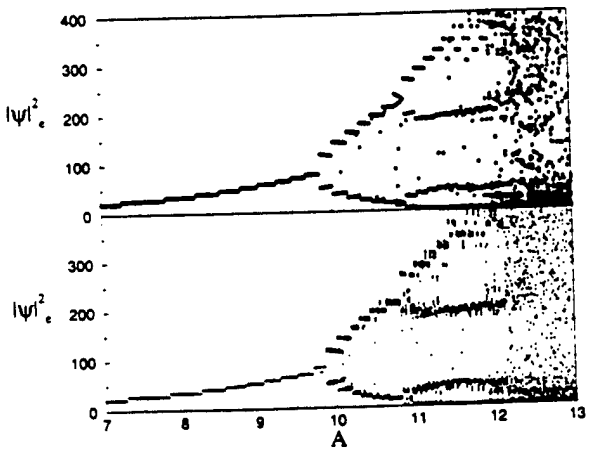

Fig. 4. Bifurcation diagram of the deterministic (above) and the stochastic (below) Ikeda model. Parameters are those of Fig. 3. In the stochastic case $D_\eta = D_\xi = 10^{-4}$.

is slightly affected by the choice of initial conditions, suggesting that the role of spontaneous emission noise might be relevant as well.

In order to analyse the influence of noise in the behavior of the system, we will first compare how the transition to chaos is produced in the deterministic and the stochastic cases. The algorithm used to integrate the differential equation appearing in the stochastic model is a standard Heun algorithm [15], where the integration time step is the one imposed by the discrete equation for ψ and the number of subdivisions made within one cavity round-trip time (100 in our calculations). The Stratonovich interpretation is used to derive the integration algorithm including the influence of noise sources.

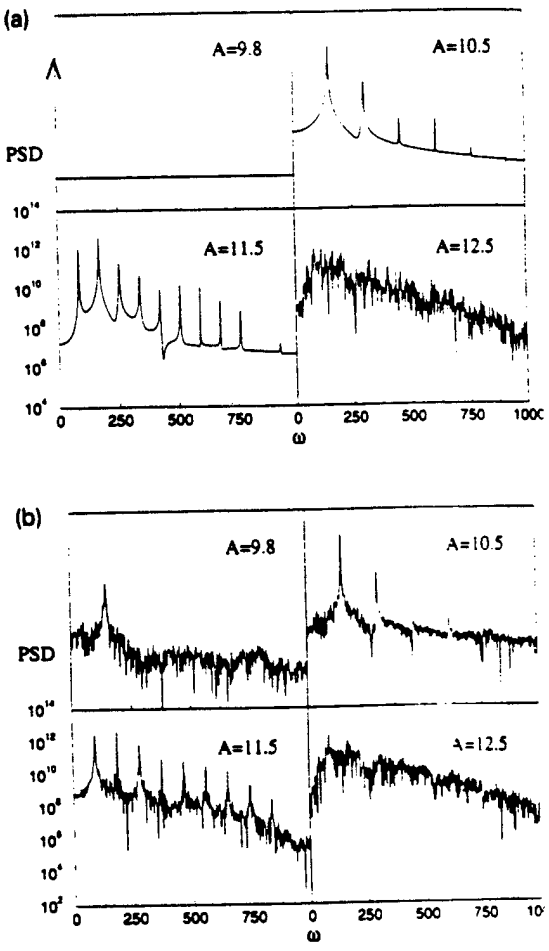

Fig. 5. Power spectral density of ψ for different values of A in deterministic (a) and stochastic (b) cases. Parameters are those of Fig. 4. The vertical scale is the same for all graphs, except the steady-state case (first graph in Fig. 5a), where the zero is explicitly shown. In this last case, an arrow in the vertical indicates the existence of a Dirac delta function at $\omega = 0$.

Fig. 5a shows the power spectral density of the tensity time signal for increasing values of A in deterministic case ($D_\eta = D_\xi = 0$). A period-doub route to chaos is found. As can be seen by compa this figure with the previous one, the smaller valu A ($A = 9.8$) corresponds to a steady-state situa (power spectrum is a Dirac delta function centere $\omega = 0$, whereas only non-zero frequencies are sh in the plot). For the largest value of A ($A = 12$ the broadband spectrum of a chaotic trajectory is tained.

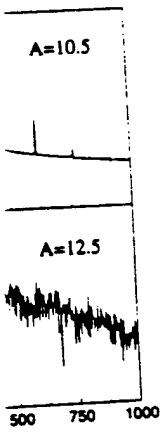

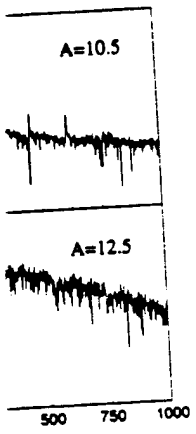

rent values of A in the . Parameters are those or all graphs, except in .), where the zero level row in the vertical axis nction at $\omega = 0$.

al density of the in- values of A in the . A period-doubling e seen by comparing the smaller value of teady-state situation function centered at equencies are shown ue of A ($A = 12.5$), iotic trajectory is ob-

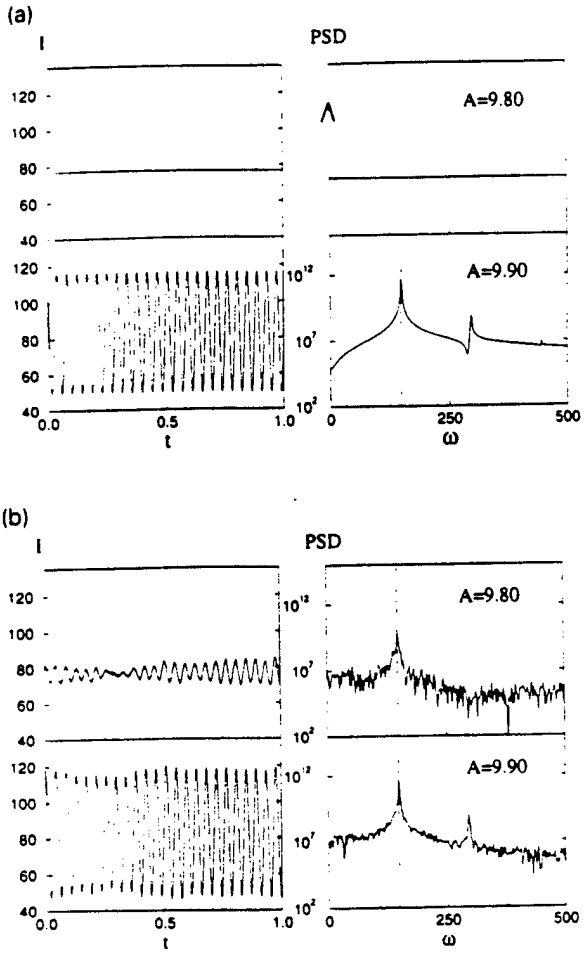

Fig. 6. Comparison of the time evolution of the intensity and its power spectrum short before and after the first bifurcation in the deterministic (a) and stochastic (b) cases. Parameters are those of Fig. 4.

The existence of a small noise source (Fig. 5b), does not substantially modify the period-doubling scenario after the first bifurcation has taken place ($A > A_c$, $A_c \sim 9.85$ for the parameters chosen, corresponding to the last three plots in each of Figs. 5a and 5b). A noisy background superimposed on the deterministic spectral density appears, as expected. On the other hand, the situation before the first bifurcation is reached (first plot in each of Figs. 5a and 5b) shows a radical change. A distinct peak in the power spectrum can be observed for a non-zero finite frequency in the stochastic case, in contrast to the delta function of the deterministic case. This frequency is seen

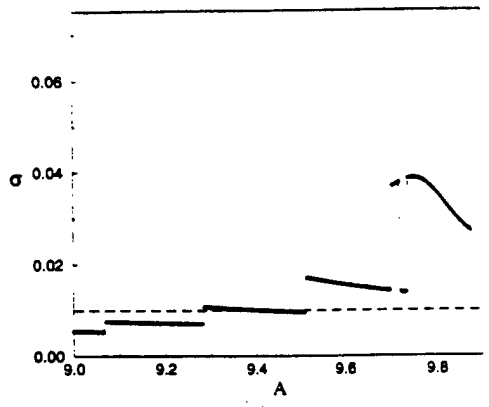

Fig. 7. Standard deviation of the intensity time series against control parameter A. The final jump corresponds to the first bifurcation in Fig. 3. A horizontal dashed line indicates the standard deviation of the noise source. Parameters are those of Fig. 5b.

to be the same as that of the periodic attractor which appears after the bifurcation. Fig. 6 demonstrates this fact, by means of a comparison between the light intensity time series and its power spectrum for the deterministic (Fig. 6a) and noisy (Fig. 6b) cases. The main peak in both spectra coincide, as seen in Fig. 6b. The oscillation amplitudes are however very different. The fact that the oscillations are much smaller in the first case ($A = 9.80$) than in the second ($A = 9.90$) proves that this is not a mere advance of the bifurcation caused by the noise. However, the amplitude in the pre-bifurcation case is much larger than the noise source variance would have us expect. We are hence observing an amplification of noise fluctuations, which takes place at the natural frequency selected by the dynamics of the system. We note that the fluctuation-enhanced peak observed here is of the same shape and occurs at the same frequency as that which appears after the bifurcation; this behavior seems different from that of the "noisy precursors" studied by Wiesenfeld and others (see Ref. [16], and references therein).

A clear picture of the amplification of noise fluctuations can be obtained by computing the standard deviation of the intensity time series as the first bifurcation is approached. This is shown in Fig. 7, where a horizontal dashed line indicates the value that is to be expected from the real noise intensity which is being handled. The amplification effect is plainly revealed.

4. Conclusion

The main objective of this paper was to systematically derive the equations for the stochastic Ikeda model of a ring cavity with a nonlinear absorber. Spontaneous emission noise has been found to significantly influence the dynamical behavior of the system. We observe substantial amplification of noise fluctuations before the steady state loses stability; this amplification occurs at a natural frequency of the system.

Acknowledgement

J.G.O. acknowledges financial support from the Dirección General de Investigación Científica y Técnica (Spain). R.R. acknowledges support from the Office of Naval Research.

References

[1] K. Ikeda, Opt. Commun. 30 (1979) 257.
[2] K. Ikeda, H. Daido and O. Akimoto, Phys. Rev. Lett. 4 (1980) 709.
[3] S.M. Hammel, C.K.R.T. Jones and J.V. Moloney, J. Op Soc. Am. B 2 (1985) 552.
[4] W.J. Firth and W.J. Sinclair, J. Mod. Opt. (UK) 35 (198 431.
[5] M. Haelterman and M.D. Tolley, Opt. Commun. 108 (199 165.
[6] W.H. Loh and C.L. Tang, IEEE J. Quantum Electron. (1991) 389.
[7] Q.L. Williams and R. Roy, Fast polarization dynamics of erbium-doped fiber ring laser, preprint.
[8] Ch. Häger and F. Kaiser, Appl. Phys. B 55 (1992) 132.
[9] P. Bryant, R. Brown and H.D.I. Abarbanel, Phys. Rev. Le 65 (1990) 1523.
[10] D.B. Murray, Physica D 68 (1993) 318.
[11] P. So and E. Ott, Phys. Rev. E 51 (1995) 2955.
[12] J.A.C. Gallas, Appl. Phys. B 60 (1995) S203.
[13] D.W. McLaughlin, J.V. Moloney and A.C. Newell, Phy Rev. Lett. 54 (1985) 681.
[14] M. Sauer and F. Kaiser, Appl. Phys. B 55 (1992) 138.
[15] T.C. Gard, Introduction to stochastic differential equatic (Marcel Dekker, New York, 1987).
[16] K. Wiesenfeld, in: Noise in nonlinear dynamical syster Vol. 2, Ch. 7, eds. F. Moss and P.V.E. McClintc (Cambridge Univ. Press, Cambridge, 1989).

Instructions to Authors (short version)

(A more detailed version of these instructions is published in the preliminary pages to each volume.)

Submission of papers

Contributions in triplicate should be sent to the editor whose expertise covers the research reported and with whom the author can communicate efficiently. Editorial Board, addresses and primary interests are given on page 2 of the cover. In case of doubt, contributions can be submitted directly to the Publisher at the address below. However, it should be realized that such papers will have to be forwarded to one of the Editors, which will result in some delay.

Original material. By submitting a paper for publication in Physics Letters A the authors imply that the material has not been published previously nor has been submitted for publication elsewhere and that the authors have obtained the necessary authority for publication.

Refereeing. All contributions will be refereed. The Editors reserve the right to edit contributions, whenever necessary, and to refuse papers which in their opinion do not satisfy conditions as to standard or contents. Linguistic corrections not affecting the meaning will be carried out by the Publisher.

Types of contributions

The *length* of the papers is not formally limited, but expedient and compact formulation, appropriate to a letters journal, is expected. The Editor may require the removal of figures, lengthy introductions, derivations, descriptions of apparatus or speculations if these are not essential for the efficient and clear communication of important new results. An *abstract* of less than 50 words is required.

Manuscript preparation

All manuscripts should be written in good English. The paper copies of the text should be prepared with double line spacing and wide margins, on numbered sheets. See notes opposite on electronic versions of manuscripts.

Structure. Please adhere to the following order of presentation: Article title, Author(s), Affiliation(s), Abstract, PACS codes and keywords, Main text, Acknowledgements, Appendices, References, Figure captions, Tables.

Corresponding author. The name, complete postal address, telephone and fax numbers and the e-mail address of the corresponding author should be given on the first page of the manuscript.

Classification codes/keywords. Please supply one to four classification codes (PACS and/or MSC) and up to six keywords of your own choice that describe the content of your article in more detail.

References. References to other work should be consecutively numbered in the text using square brackets and listed by number in the Reference list. Please refer to the more detailed instructions for examples.

Illustrations

Illustrations should also be submitted in triplicate: one master set and two sets of copies. The *line drawings* in the master set should be original laser printer or plotter output or drawn in black india ink, with careful lettering, large enough (3–5 mm) to remain legible after reduction for printing. The *photographs* should be originals, with somewhat more contrast than is required in the printe version. They should be unmounted unless part of a composite fig ure. Any scale markers should be inserted on the photograph, nc drawn below it.

Colour plates. Figures may be published in colour, if this is judge essential by the Editor. The Publisher and the author will each be part of the extra costs involved. Further information is availabl from the Publisher.

After acceptance

Notification. You will be notified by the Editor of the journal c the acceptance of your article and invited to send an electronic ve sion of the accepted text to the Publisher.

Copyright transfer. You will be asked to transfer the copyright c the article to the Publisher. This transfer will ensure the wide possible dissemination of information.

No proofs. In order to speed up publication, all proofreading wi be done by the Publisher and proofs are *not* sent to the author(s).

Electronic manuscripts

The Publisher welcomes the receipt of an electronic version c your accepted manuscript (preferably encoded in LaTeX). If yo have not already supplied the final, revised version of your artic (on diskette) to the Journal Editor, you are requested herewith send a file with the text of the accepted manuscript directly to th Publisher by e-mail or on diskette (allowed formats 3.5" or 5.2 MS-DOS, or 3.5" Macintosh) at the address given below. Plea note that no deviations from the version accepted by the Editor c the journal are permissible without the prior and explicit approv by the Editor. Such changes should be clearly indicated on a accompanying printout of the file.

Author benefits

No page charges. Publishing in Physics Letters A is free.

Free offprints. The corresponding author will receive 50 offprin free of charge. An offprint order form will be supplied by th Publisher for ordering any additional paid offprints.

Discount. Contributors to Elsevier Science journals are entitled a 30% discount on all Elsevier Science books.

Contents Alert. Physics Letters A is included in Elsevier's pr publication service Contents Alert and CoDaS.

Further information (after acceptance)

Elsevier Science B.V., Physics Letters A
Issue Management Physics and Materials Science
P.O. Box 2759, 1000 CT Amsterdam
The Netherlands
Tel.: +31 20 4852638
Fax: + 31 20 4852319
E-mail: NHPDESKED@ELSEVIER.NL

Printed in The Netherlands

North-Holland, an imprint of Elsevier Scienc

PHYSICS LETTERS A

Physics Letters A 229 (1997) 362–366

Intracavity chaotic dynamics in ring lasers with an injected signal

J. García-Ojalvo [1], R. Roy

School of Physics, Georgia Institute of Technology, Atlanta, GA 30332-0430, USA

Received 19 December 1996; revised manuscript received 24 February 1997; accepted for publication 24 February 1997
Communicated by C.R. Doering

ELSEVIER

ELSEVIER

2 June 1997

PHYSICS LETTERS A

Physics Letters A 229 (1997) 362–366

Intracavity chaotic dynamics in ring lasers with an injected signal

J. García-Ojalvo [1], R. Roy

School of Physics, Georgia Institute of Technology, Atlanta, GA 30332-0430, USA

Received 19 December 1996; revised manuscript received 24 February 1997; accepted for publication 24 February 1997
Communicated by C.R. Doering

Abstract

The intracavity dynamics of optically injected ring lasers is studied by means of an extended delay-differential Ikeda model. The behavior of this kind of lasers is, in some aspects, strikingly different from that of a nonlinear absorber placed in a ring cavity, for which the Ikeda model was originally derived. In particular, chaotic behavior in the laser case is seen to occur on much faster time scales than for the absorber. The scenario in which the transition to chaos occurs is also different.

Injection of coherent light into laser systems has been a common practice since the early years of the laser era. The reasons for using such a technique are diverse. At high injection levels, the laser locks its frequency and phase to those of the injected signal; this is called the *injection-locking* regime, and is very useful for obtaining a stable and narrow-band laser output at a desired frequency. On the other hand, if the injected signal is not strong enough, locking is not possible and a competition arises between the two coherent signals which coexist inside the laser resonator, giving rise to a wide and interesting variety of dynamical behavior (see Ref. [1] for a general review on the subject).

In the present work, we are interested in the chaotic regimes that frequently appear in a laser with an injected signal, and in the transitions and instabilities leading to them. Much attention has been paid to this problem in the past years [2–6], and evidence of chaos has been obtained from both an experimental and a theoretical point of view. Nevertheless, similarly to almost all investigations of laser dynamics, these studies were done on time scales longer than the cavity round-trip time of the laser. For "typical" laser systems, such as semiconductor, gas, or Nd:YAG solid-state lasers, this quantity usually takes values in the range ~ 10 ps–1 ns, which places the analysis of intracavity phenomena beyond the reach of standard measurement devices. The recent development of optical fiber lasers, mainly for communication purposes [7], has changed this situation. In such lasers, the amplifying medium is an optical fiber that has been doped with rare-earth ions.

The waveguiding properties of optical fibers enable the construction of lasers with very large (even of the order of km) cavities, and hence with round-trip times long enough (of the order of μs) to be able to observe their behavior inside the cavity [8]. The question of analysing the intracavity dynamics of

[1] Present address: Dept. de Física i Enginyeria Nuclear, E.T.S. d'Enginyers Industrials de Terrassa, Univ. Politècnica de Catalunya, Colom 11, E-08222 Terrassa, Spain.

0375-9601/97/$17.00
PII S0375-9601(97)00198-9

lasers with an injected signal when operating in a chaotic regime naturally arises. It is interesting to investigate, for instance, if chaos occurs in time scales faster than the cavity round-trip time, and if this is the case, whether these time scales can be fast enough to be interesting for encoding purposes [9,10] in all-optical communication systems.

The intracavity dynamics of long-cavity erbium-doped fiber lasers has been recently analysed by means of a system of delay-differential equations of the Ikeda type [8,11]. This model was first introduced by Ikeda to study the absorption of light by a nonlinear medium placed in a ring cavity [12], and predicted the existence of chaotic behavior in this system. This prediction was first tested in a passive optical fiber ring [13], and became one of the first examples of optical chaos. The Ikeda model has also been occassionally used in a laser context by several authors. In the few years following its appearance, Otsuka and coworkers used it to describe the nonlinear dynamics of a semiconductor laser amplifier with delayed feedback [14,15]. Several years later, Loh and Tang derived a delay-differential model, following Ikeda, to analyse ultrafast polarization modulation in semiconductor lasers [16,17]. Again, these studies were done on time scales larger than the cavity round-trip time of the system. It is our aim here to compare the dynamical behavior of these two versions of the Ikeda model, namely that corresponding to a nonlinear absorber and the one used to analyse laser systems. As we will show in what follows, the time scales in which the second model evolves correspond to nontrivial intracavity dynamics.

The Ikeda delay-differential model can be written in dimensionless form as follows,

$$E(t) = \sqrt{T}E_i + RE(t-\tau_R) \times \exp[a(1+i\alpha)(\phi-1)], \quad (1)$$

$$\frac{d\phi(t)}{dt} = q - \phi - |E(t-\tau_R)|^2 \times \{\exp[2a(\phi-1)] - 1\}. \quad (2)$$

These equations describe the interaction between light and a nonlinear medium (absorbing or amplifying) placed in a ring cavity. $E(t)$ is the complex envelope of the electric field, measured at a given reference point inside the cavity. ϕ is the total population inversion between the two energy levels of the nonlinear medium which interact with the propagating light. Time is measured in units of τ_f^{-1}, where τ_f is the decay time of the atomic transition. The delay τ_R is the dimensionless cavity round-trip time, i.e. the time the light takes to travel once around the cavity, in units of the inverse of the transition decay time τ_f. E_i is the amplitude of the injected field, assumed constant. R is the return coefficient of the ring (fraction of light that remains in the cavity after one round-trip), and $T = 1 - R$. The parameter α is the dimensionless detuning between the atomic transition frequency and the light frequency. The coefficient a represents either absorption or gain, depending on whether we are studying a nonlinear absorber or a laser, respectively [2]. In this last case, the amplifying medium has to be pumped, which is represented by the dimensionless pump rate q.

In the absorbing case ($q = 0$), this model has been extensively studied both numerically and analytically [18–21]. In particular, Kaiser and coworkers [19,21] numerically obtained the bifurcation structure of the system for several sets of parameters, displaying different routes to chaos for round-trip times of the order of the transition decay time (i.e. for τ_R of order 1). Otsuka used similar time scales in his study of semiconductor lasers with optical feedback [15]. We, on the other hand, are interested in another region of parameter space, where the round-trip time is several orders of magnitude smaller than the transition decay time (in fiber lasers, the difference can be of 5 orders of magnitude [11]). Throughout this paper, we will consider $\tau_R = 0.01$.

We have numerically integrated Eqs. (1), (2) to obtain the bifurcation structure of the Ikeda model with and without pumping in the (a, α) space. The result is shown in Fig. 1, for $R = 0.95$, $\tau_R = 0.01$ and $E_i = 5.0$. The pump rate is $q = 0$ in Fig. 1a and $q = 5$ in Fig. 1b. The influence of pumping is evident. When $q = 0$, the situation is qualitatively similar to that reported in Ref. [21], with islands of

[2] We choose a to be always positive, so that it is the sign of the population inversion ϕ what makes the medium absorbing or amplifying.

periodic behavior embedded in a chaotic background. When $q \neq 0$, on the other side, this scenario changes drastically. First, the fixed point loses stability at smaller values of the detuning (compare the x-axis scales in Figs. 1a and 1b). Second, the instability threshold is virtually independent of the gain, and leads almost immediately to the chaotic regime, so that the transition to chaos is much sharper now. Third, there are no islands of periodic behavior in the chaotic regime. A comparison between typical routes to chaos in both cases is presented in Fig. 2. The system parameters are the same as in the previous figure. Fig. 2a corresponds to a slice of Fig. 1a at $a = 3.5$ for increasing values of α, starting shortly after the fixed point loses stability, and clearly shows a period-doubling sequence leading to a chaotic attractor of annular shape. The situation is again very

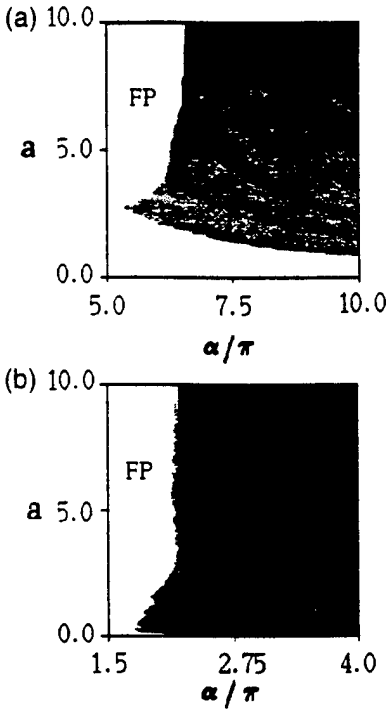

Fig. 1. Phase diagram of the delay-differential model presented in Eqs. (1), (2). The parameters are: $E_i = 5.0$, $R = 0.95$ and $\tau_R = 0.01$. (a) $q = 0$, (b) $q = 5.0$. White regions correspond to fixed-point dynamics, black regions to chaotic behavior, and the different grey areas represent periodic motions with different repetition rates. The period of the motion is represented by the numbers shown in the figure. Different superscripts correspond to qualitatively different periodic orbits.

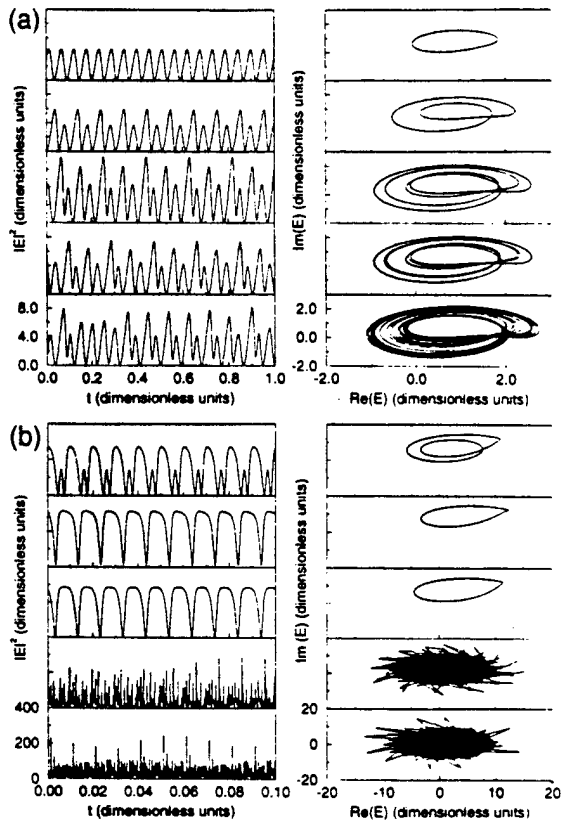

Fig. 2. Time series (left) and attractor in complex-E space (right) for different values of α as the system goes from a fixed-point to chaos without (a) and with (b) pumping. Parameters are those on the previous figure and $a = 3.5$. The values of α/π are, from top to bottom: (a) 6.25, 7.00, 8.00, 8.05, and 8.50; (b) 2.29, 2.31, 2.34, 3.00, and 6.00.

different in the presence of pumping (Fig. 2b), with periodic behavior in a very narrow band of α values separating regions of fixed-point and chaotic behavior. In the periodic regime, the attractor is similar in shape to that of the absorbing case, whereas in the chaotic region, the attractor fills all the space inside its boundaries, and covers a much larger region of phase space. It should also be noted that the time scale for the chaotic dynamics is much faster in the laser case than it is in the absorber case. Taking into account that the round-trip time is 0.01 in both cases, it can be seen from Fig. 2 that the system exhibits intracavity chaos for $q \neq 0$, but not for $q = 0$, where variations in the intensity, although chaotic, occur in a time interval larger than τ_R.

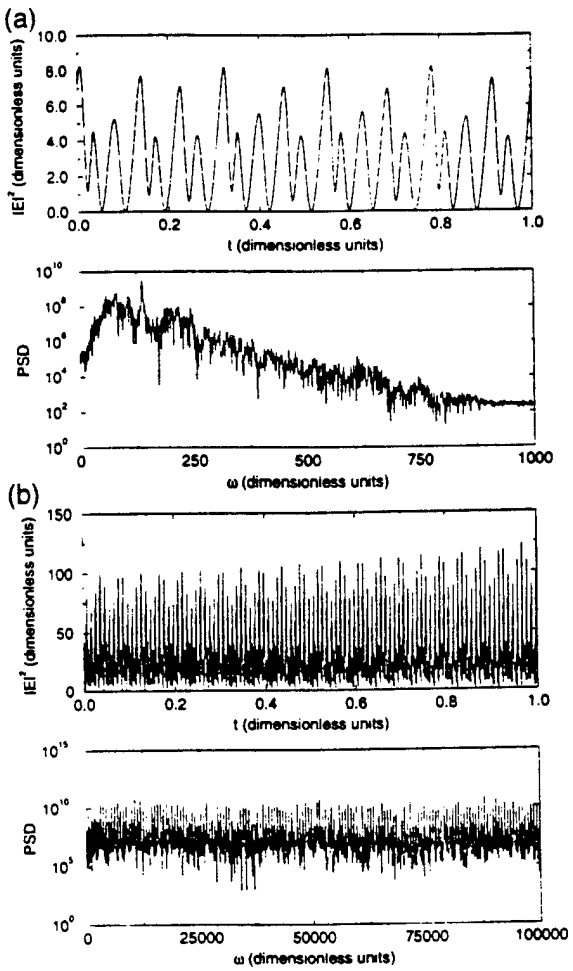

Fig. 3. Two time series (top) and their corresponding power spectral densities (bottom) with and without pumping. Parameters are those of the previous figure, and $\alpha/\pi = 8.60$. (a) $q = 0.0$; (b) $q = 5.0$.

In order to further investigate and corroborate the existence of different time scales in the two different chaotic dynamics observed so far, it is also useful to analyze their respective power spectral densities (PSD). A comparison between these functions for typical time traces in the two chaotic regimes (with and without pumping) is shown in Fig. 3. The existence of much higher frequencies in the laser case (Fig. 3b) as compared with the absorber case (Fig. 3a), can be easily observed in the time-domain representations (upper plots), and is quantitatively described in the frequency domain (lower plots). The PSD is seen to be much broader for $q \neq 0$. This difference corresponds to several orders of magnitude (cf. the scales of the frequency axis in both cases).

Finally, we now address the question of whether the faster dynamics observed in the laser case corresponds to a higher dimensional motion. This seems to be suggested by the differences in the chaotic attractors shown in Fig. 2. We can estimate the dynamical dimension of the two systems by using a phase-space reconstruction method [22] and computing the percentage of false nearest neighbors as we increase the dimension of the space in which the intensity time series is embedded. To perform this calculation we make use of a method developed in Ref. [23]. False nearest neighbors are points in phase space which seem to be nearby only because the dynamics has been embedded in a space of too low dimension. They can be revealed by increasing the dimension of the space in which the dynamics is trying to be reconstructed. In this way, when the percentage of false nearest neighbors (with respect to all points in the attractor) drops to zero beyond a given dimension, we can expect that the phase space has been correctly reconstructed. The minimum dimension for which this happens constitutes a measure of the dynamical dimension of the system. Fig. 4 shows the percentage of false nearest neighbors vs. increasing dimension of the embedding space for the Ikeda model, both with and without pumping. As can be observed in the inset, the embedding dimension in the pumped case (circles) is equal to 4, and coincides with that of the "classical" Ikeda model for an absorber, i.e. for no pumping (diamonds).

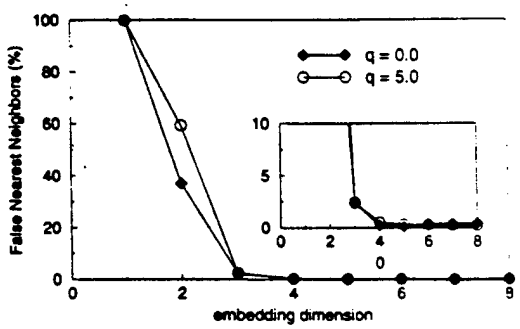

Fig. 4. Percentage of false nearest neighbors versus embedding dimension for the time traces shown in Fig. 3.

In summary, we have analysed and compared the dynamics of the delay-differential Ikeda model for an absorber and a laser with long cavity. The phase diagrams of the two systems display fixed-point, periodic and chaotic behaviors, and in the periodic regime the time scale seems to be similar in both systems. This is not the case in the chaotic regime; here, the time scale for intensity fluctuations is still long for the absorber, but much faster for the laser. In this last situation, the dynamics is chaotic within a single cavity round trip. In spite of the different frequencies involved in the two cases, both systems seem to have equal dimensionality, as shown by a false nearest neighbor analysis. The transition between the regions of "slow" and "fast" dynamics can be seen not to be discontinuous at $q = 0$. On the contrary, the standard, "slow" behavior can be observed for a finite range of q values up to a given threshold, beyond which the fast regime appears. This bifurcation might correspond to a jump towards a higher branch of the multistable system. Further research, both numerical and analytical, is needed in order to clarify this point. The existence of intracavity chaotic dynamics for lasers with a long cavity, such as optical fiber lasers, might be important for chaotic encoding of information at frequencies in the GHz–THz range, in all-optical communication systems. In this sense, it would be of interest to analyse how a time variation of the injected signal (the message to be encoded, for instance) would affect the scenario presented here.

We thank Henry Abarbanel for making available to us the software on the false nearest neighbors method. J.G.O. acknowledges financial support from the Dirección General de Investigación Científica y Técnica (Spain) and the Office of Naval Research (USA). R.R. acknowledges support from the Office of Naval Research and the National Science Foundation (USA).

References

[1] C.O. Weiss and R. Vilaseca, Dynamics of lasers (VCH, Weinheim, 1991).
[2] J.R. Tredicce, F.T. Arecchi, G.L. Lippi and G.P. Puccioni, J. Opt. Soc. Am. B 2 (1985) 173.
[3] D.J. Jones and D.K. Bandy, J. Opt. Soc. Am. B 7 (1990) 2119.
[4] J. Sacher, D. Baums, P. Panknin, W. Elsässer, and E.O. Göbel, Phys. Rev. A 45 (1992) 1893.
[5] M. Haelterman, S. Trillo and S. Wabnitz, Phys. Rev. A 47 (1993) 2344.
[6] V. Kovanis, A. Gavrielides, T.B. Simpson, and J.M. Liu, Appl. Phys. Lett. 67 (1995) 2780.
[7] G.P. Agrawal, Nonlinear fiber optics (Academic Press, New York, 1995).
[8] Q.L. Williams and R. Roy, Opt. Lett. 21 (1996) 1478.
[9] P. Colet and R. Roy, Opt. Lett. 19 (1994) 2056.
[10] C.R. Mirasso, P. Colet and P. García-Fernández, IEEE Photon. Technol. Lett. 8 (1996) 299.
[11] Q.L. Williams, J. García-Ojalvo and R. Roy, Phys. Rev. A, to appear, (March 1997).
[12] K. Ikeda, Opt. Comm. 30 (1979) 257.
[13] H. Nakatsuka, S. Asaka, H. Itoh, K. Ikeda and M. Matsuoka, Phys. Rev. Lett. 50 (1983) 109.
[14] K. Otsuka and H. Iwamura, Phys. Rev. A 28 (1983) 3153.
[15] K. Otsuka, J. Opt. Soc. Am. B 2 (1985) 168.
[16] W.H. Loh and C.L. Tang, IEEE J. Quantum Electron. 27 (1991) 389.
[17] W.H. Loh and C.L. Tang, Opt. Commun. 85 (1991) 283.
[18] M. Le Berre, E. Ressayre, A. Tallet, H.M. Gibbs, D.L. Kaplan and M.H. Rose, Phys. Rev. A 35 (1987) 4020.
[19] F. Kaiser and D. Merkle, Phys. Lett. A 139 A (1989) 133.
[20] D. Merkle and F. Kaiser, Phys. Lett. A 153 A (1991) 95.
[21] Ch. Häger and F. Kaiser, Appl. Phys. B 55 (1992) 132.
[22] H.D.I. Abarbanel, R. Brown, J.J. Sidorowich and L.S. Tsimring, Rev. Mod. Phys. 65 (1993) 1331.
[23] M.B. Kennel, R. Brown and H.D.I. Abarbanel, Phys. Rev. A 45 (1992) 3403.

Influence of noise on chaotic laser dynamics

Clif Liu,[1] Rajarshi Roy,[2] Henry D. I. Abarbanel,[1,3] Zelda Gills,[2] and Ken Nunes[1,4]
[1]*Department of Physics and Institute for Nonlinear Science, University of California, San Diego, La Jolla, California 92093*
[2]*School of Physics, Georgia Institute of Technology, Atlanta, Georgia 30332*
[3]*Marine Physical Laboratory, Scripps Institution of Oceanography, University of California, San Diego, La Jolla, California 92093*
[4]*Department of Physics, University of California, Santa Cruz, California 95064*
(Received 7 August 1996; revised manuscript received 6 December 1996)

The Nd:YAG laser with an intracavity second harmonic generating crystal is a versatile test bed for concepts of nonlinear time series analysis as well as for techniques that have been developed for control of chaotic systems. Quantitative comparisons of experimentally measured time series of the infrared light intensity are made with numerically computed time series from a model derived here from basic principles. These comparisons utilize measures that help to distinguish between low and high dimensional dynamics and thus enhance our understanding of the influence of noise sources on the emitted laser light.
[S1063-651X(97)10805-4]

PACS number(s): 05.45.+b, 42.50.Lc, 42.65.Sf

I. INTRODUCTION

The Nd:YAG (neodymium doped yttrium aluminum garnet) laser with an intracavity KTP (potassium titanyl phosphate) crystal is a chaotic dynamical system for which it is possible to directly compare statistical aspects of measured time series with predictions from a numerical model that has been derived from basic theory. When operated with three or more longitudinal cavity modes, this laser is known to display chaos, and attempts have previously been made to write dynamical equations that could capture certain aspects of observed behavior [1–3]. These models have successfully predicted the existence of antiphase dynamical states, energy sharing of chaotic polarization modes of the laser, and also the possibility of obtaining stable operation through rotational orientation of the KTP and YAG crystals. The laser system has also served as an example of which algorithms for the control of chaotic lasers have been successfully applied, both experimentally and in numerical simulations [4–7].

It was, however, the observation that simple control algorithms failed in certain operating regimes that motivated us in a previous paper to apply methods of nonlinear time series to experimentally recorded intensity time series with the goal of discovering qualitative and quantitative differences in the operating regimes. The laser was thus operated specifically in three longitudinal modes in two polarization configurations by careful adjustment of crystal orientations in the cavity. In the first configuration, all three longitudinal modes were polarized parallel to each other. In the second, one mode was polarized orthogonal to the other two. All other parameters of the laser system such as the cavity loss, pump level, etc. were maintained constant, and the instrumentation for the measurements was operated with exactly the same sampling times and other settings.

The dynamics observed in these two polarization configurations were labeled type I and type II. Nonlinear time series analysis allowed us to determine the dimensionality of the chaotic attractors for the two cases and estimate the Lyapunov exponents in the two cases. A major conclusion of our previous study was that while the type I behavior was established to be low dimensional, there was clear evidence that the type II behavior was significantly influenced by noise, indicating the presence of high dimensional dynamics as well. At the end of that paper we sketched the outline of a theoretical approach to the derivation of a model that would allow us to simulate intensity time series and apply the nonlinear analysis techniques to make a direct comparison with the experimental results.

In this paper we present the derivation outlined in [8], and obtain the equations that describe the dynamics of a three mode laser with an intracavity KTP crystal. Previous models [1–3] were found not to reproduce type I dynamical behavior after conducting extensive searches in parameter space. It is shown here that the inclusion of nondegenerate four wave mixing, which leads to a model that includes the phase dynamics of the electric fields, overcomes this difficulty. Type II behavior of the infrared light has very different characteristics, and is accompanied by emission of substantial amounts of green light, in contrast to type I dynamics. Degenerate four wave mixing is the dominant process in this case. A major purpose of the research reported here is to include noise sources appropriately in the numerical equations and to explore their influence on type I and type II deterministic chaotic dynamics.

The next section reviews the main aspects of type I and type II chaotic dynamics of the laser. The experimentally observed differences (time series behavior, controllability, mode structure, and green output power) are summarized. We describe a noise measurement method called false nearest neighbors, an algorithm normally used to find the embedding dimension of a chaotic time series. We demonstrate that the two types of dynamics differ significantly in the amount of high dimensional (noisy) dynamics of the laser. Section II provides the basis for comparison with numerical computations that are the focus of this paper.

Section III contains a derivation of the model equations of motion from a Hamiltonian. Three infrared cavity modes are modeled as harmonic oscillators coupled to heat baths. A mode that represents green light generated by the KTP crys-

tal is also included. It is nonlinearly coupled to the infrared modes so as to model the interaction in the KTP crystal. The cavity loss for the green light is very high compared to that for the infrared modes, hence it is sufficient to just consider a single mode of green light and to eliminate its dynamics from the final set of equations that describe the evolution of the field amplitudes of the infrared modes and of the population inversion of the two level atoms that drive them.

In Sec. IV we describe the results from numerically integrating the equations of motion derived in Sec. III. There is a qualitative match between the wave forms of the model and experimental data in both chaos regimes. We also present the false neighbors results when noise is added to the system and find that the resulting noise in the output intensity differs in the two chaotic regimes for the same input noise, leading us to conclude that the susceptibility of the dynamics to noise differs for the two chaotic behaviors.

Section V attempts to locate the source of noise that is seen in the laser time series. Four intrinsic quantum fluctuation sources (cavity loss of infrared light, cavity loss of green light, intrinsic conversion noise, and spontaneous emission) are analyzed for their expected noise levels. These noise sources are all too weak by many orders of magnitude to contribute the amount of noise evidenced in the laser dynamics. We also consider and eliminate extrinsic pumping fluctuations as the noise source.

II. TYPE I AND TYPE II BEHAVIOR

The basic elements of the laser system are a diode laser pumped Nd:YAG crystal and an intracavity KTP crystal with an output mirror that is highly reflecting at the 1.064 μm line of the Nd:YAG crystal but highly transmitting for the green light [1]. It has been shown that this laser can be configured so that few modes ($\approx 3-10$) are present in the cavity; each mode can have one of two polarizations.

Using the methods of nonlinear time series analysis [8] we are able to distinguish between chaotic behavior where the noise level is very low and situations where the output is still chaotic but substantial noise is also present. The former we call type I chaos; it is observed when all three modes all polarized parallel to each other. The latter we label type II chaos; it is observed when one of the three modes is polarized perpendicular to the other two. Very little green light is generated for type I behavior, which is demonstrably low dimensional chaos, and is controllable by the method of occasional proportional feedback (OPF) [4,5]. Type II chaos is accompanied by the generation of a substantial amount of green light and a clear signature of noise is evident in its chaotic dynamics. It is typically not controlled by OPF.

The laser system displays chaotic intensity output when operated with three or more longitudinal modes. In the present experiments the system parameters were adjusted to obtain three mode operation in the two distinct polarization configurations. An appropriate orientation of the crystal axes allowed us to select these configurations. The pump level, set to about twice the threshold pump power, was similar for the two configurations. The total intensity (the sum of the intensities of each individual mode) was observed with a photodiode having a rise time of less than 1 ns and was sampled using a 100 MHz eight bit digital oscilloscope capable of storing 10^6 samples. In Fig. 1(a) we show the total intensity when all three modes are polarized parallel to each other (type I chaos). In Fig. 1(b) we show the total intensity with one mode polarized perpendicular to the other two (type II chaos).

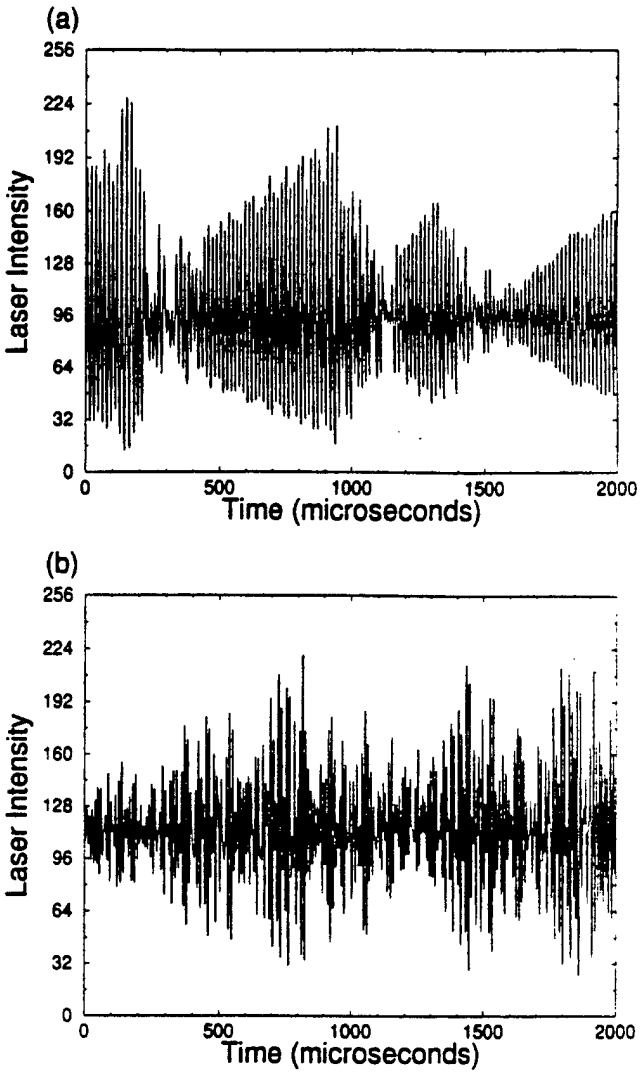

FIG. 1. (a) Fluctuations of the total infrared intensity for three mode Nd:YAG laser operation with all modes polarized parallel to each other. Relaxation oscillations of period ~ 16 μs are evident with irregular modulations of the envelope, typical of type I dynamics. (b) Fluctuations of the total infrared intensity for three mode Nd:YAG laser operation with two modes polarized parallel to each other and one polarized perpendicular to the other two (type II). The relaxation oscillations are still visible.

In the time traces we can see the distinction between these two operating regimes. Type I consists of long "bursts" of relaxation oscillations, while type II appears far more irregular. During type I operation very little green light, less than 1 μW, was observed, while more than 25 μW of power in green light accompanied type II activity.

We use the total laser intensity $I(n)=I(t_0+n\tau_s)$, with the sampling time $\tau_s=100$ ns, and its time delayed values to reconstruct the system phase space [9–12] by forming vectors

$$\mathbf{y}(n)=(I(n),I(n+T),\ldots,I(n+(d_E-1)T)), \quad (1)$$

$$\mathbf{y}(n+1)=(I(n+1),I(n+1+T),\ldots,I(n+(d_E-1)T+1))$$

$$\vdots \qquad (2)$$

where d_E is the integer embedding dimension of the reconstructed phase space and T is the integer time lag in units of τ_s. Our ability to use this phase space reconstruction for extracting physical properties from the observations rests on a proper choice of the time delay T and the embedding dimension d_E. For T we use the first minimum of the average mutual information [9,10,13] between $I(n)$ and $I(n+T)$ evaluated as a function of T.

d_E is chosen by using the false nearest neighbors algorithm [14,9,10]. This relies on the property of autonomous dynamical systems that their trajectories in phase space do not cross each other unless the system is observed in a space with too low a dimension. To determine the d_E necessary to unfold the trajectories using time delay coordinates we observe each point along the trajectory $\mathbf{y}(n)$ and its nearest neighbor as the dimension of the space is increased from d_E to d_E+1. If the point and its nearest neighbor move sufficiently far from each other as the dimension is increased, we conclude they were falsely seen to be nearest neighbors because of projection from a higher dimensional object, the attractor. When the percentage of false nearest neighbors drops to zero, we have established the value of d_E. Here, we use the property of the algorithm that in the presence of noise [9,10], a residual percentage of false nearest neighbors is observed. The amount of residual is a measure of the noise level.

The original data sets of 10^6 points were oversampled. These were down sampled by a factor of 8, resulting in 125 000 data points. Using the time delay suggested by the average mutual information, we evaluated the percentage of false nearest neighbors for types I and II chaos. This percentage averaged over five type I data traces is shown in Fig. 2(a) (solid line) and enlarged in Fig. 2(b). We see that $d_E=5$ where the percentage of false nearest neighbors drops well below 0.5%. The dotted lines in Figs. 2(a) and 2(b) represent the corresponding average over four type II data sets. In these data it is clear that there is a residual number of false neighbors that is not eliminated by going to higher embedding dimensions. We have consistently observed this much larger fraction of residual false nearest neighbors for type II dynamics compared to type I dynamics in the many time series of total intensity from our laser system. In fact, the mean type II residual is ≈ 40 times the mean type I residual at $d_E=6$.

Table I contains a summary of the differences between type I and type II chaos as found from experimental measurements and from the nonlinear analysis of the data.

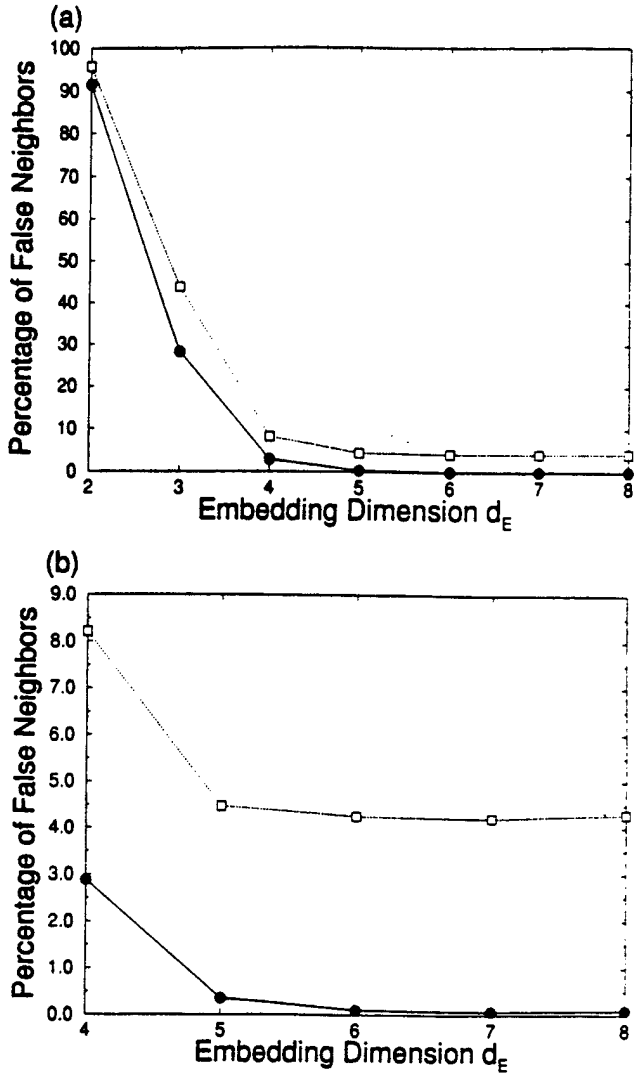

FIG. 2. (a) The percentage of false nearest neighbors (FNN) vs the embedding dimension d_E averaged over five type I chaotic data sets (solid line) and four type II chaotic data sets (broken line). (b) An enlargement of (a) showing that the percentage of type I FNN drops to 0.1% and stays there as d_E increases but the percentage of type II FNN does not drop below 4%.

III. MODEL OF THE PROCESS

The laser is modeled using three interacting components: the infrared cavity modes, a green cavity mode, and a two level active medium. We write the whole Hamiltonian as

$$H=H_{\mathrm{IR}}+H_{\mathrm{green}}+H_{\mathrm{conv}}+H_{\mathrm{2\,level}}+H_{\mathrm{driving}}. \qquad (3)$$

H_{conv} models the conversion of IR to green and vice versa that occurs in the KTP crystal, and H_{driving} models the interaction of the two level system with the infrared cavity modes.

The longitudinal infrared normal modes in the laser are represented by the annihilation and creation operators a_n and $a_n^\dagger$, respectively. These satisfy the usual equal time Bose commutation relations

TABLE I. Type I and type II chaos summary.

Characteristic	Type I	Type II
Time series	Bursting	Irregular
Green output	$<1\ \mu$W	$\geq 25\ \mu$W
Mode configuration	3-0	2-1
OPF controllable	Yes	No
Embedding dimension	≈ 5	≈ 5
False neighbors residual	$<1\%$	$\approx 5\%$

$$[a_n, a_m^\dagger] = \delta_{mn}, \quad n,m = 1,2,\ldots,M. \tag{4}$$

For us, $M = 3$.

Each mode is coupled to independent heat baths or reservoirs which are represented by boson operators b_{ik} for the kth reservoir mode of infrared mode i. This harmonic oscillator has a frequency of Ω_{ik}. We assume that all of the reservoir modes are independent of each other and the infrared modes (except through the coupling), that is

$$[b_{qn}, b_{pm}^\dagger] = \delta_{mn}\delta_{pq} \tag{5}$$

and

$$[b_{pn}, a_m^\dagger] = 0. \tag{6}$$

The reservoir modes are bilinearly coupled to the infrared modes with real coupling constants Γ_{ik}, which leads to

$$H_{\mathrm{IR}} = \sum_{i=1}^{M} \hbar\omega_i a_i^\dagger a_i + \sum_{i=1}^{M}\sum_k [\hbar\Omega_{ik} b_{ik}^\dagger b_{ik} + i\hbar\Gamma_{ik}(b_{ik}a_i^\dagger - a_i b_{ik}^\dagger)]. \tag{7}$$

There is a single green mode represented by annihilation and creation operators g and $g^\dagger$ that satisfies

$$[g, g^\dagger] = 1 \tag{8}$$

and

$$[g, a_m^\dagger] = 0. \tag{9}$$

It is bilinearly coupled (via real coupling constants Γ_{gk}) to a reservoir that is independent of the infrared mode reservoirs. The kth reservoir mode of the green mode is represented as b_{gk} and has a frequency of Ω_{gk}. The green mode Hamiltonian is

$$H_{\mathrm{green}} = \hbar\omega_g g^\dagger g + \sum_k [\hbar\Omega_{gk} b_{gk}^\dagger b_{gk} + i\hbar\Gamma_{gk}(b_{gk}g^\dagger - g b_{gk}^\dagger)]. \tag{10}$$

In the KTP frequency conversion process, modeled by H_{conv}, conversion occurs when two infrared photons are destroyed to create a green photon and when one green photon is destroyed to create two infrared photons. We assume the coupling tensor κ_{ij} is real and symmetric:

$$H_{\mathrm{conv}} = i\hbar \sum_{i,j=1}^{M} \kappa_{ij}(a_i^\dagger a_j^\dagger g - g^\dagger a_j a_i). \tag{11}$$

The laser driving system is represented by a distribution of spin-1/2 systems along the z axis over the length of the laser cavity. The Pauli spin operators $S_3(z,t)$ and $S_\pm(z,t)$ are used to represent the two level systems and satisfy

$$[S_3(z), S_\pm(z')] = \pm 2 S_\pm(z)\delta(z-z') \tag{12}$$

and

$$[S_+(z), S_-(z')] = S_3(z)\delta(z-z'). \tag{13}$$

In addition, it can be shown that

$$S_\pm(z)S_3(z') = \mp S_\pm(z)\delta(z-z'),$$

$$S_+(z)S_-(z') = \tfrac{1}{2}[I + S_3(z)]\delta(z-z'). \tag{14}$$

The two level system is damped by a cavity mode reservoir represented by boson operators b_{sk} and $b_{sk}^\dagger$. The Hamiltonian is

$$H_{2\,\mathrm{level}} = \int_0^L \left\{ \frac{\hbar\omega_s}{2} S_3(z) + \sum_k [i\hbar\Gamma_{sk}(z)S_+(z)b_{sk} - i\hbar\Gamma_{sk}^*(z)b_{sk}^\dagger S_-(z)] \right\} dz + \sum_k \hbar\Omega_{sk} b_{sk}^\dagger b_{sk}. \tag{15}$$

The coupling between the medium and the cavity modes is bilinear and the driving efficiency σ_i is assumed to be real:

$$H_{\mathrm{driving}} = \int_0^L i\hbar \sum_{i=1}^{M} \sigma_i [S_+(z)a_i \sin(K_i z) - a_i^\dagger S_-(z)\sin(K_i z)]dz. \tag{16}$$

A derivation of the equations of motion for this system can be found in the Appendix. Here we give an overview of the physics of the model and the approximations that are made in the derivation.

First we use the Hamiltonian to determine the standard Heisenberg equations of motion for the system. The reservoir model allows us to apply the Wigner-Weisskopf approximation (see Appendix and Chap. 19.2 of [15]) to write a Langevin equation for the green mode:

$$\frac{dg}{dt} = -(\gamma_g + i\omega_g)g - \sum_{l,m=1}^{M} \kappa_{lm}^* a_l a_m - \sum_k \Gamma_{gk} b_{gk}(0) e^{-i\Omega_{gk}t}, \tag{17}$$

where γ_g represents the damping rate and the last term is a fluctuation or noise term. Integrating this equation and taking advantage of the fact that the decay rate γ_g ($\sim 10^{10}$ Hz) is much faster than the characteristic rate at which g fluctuates (10^5 Hz), we can find an equation for the green mode:

$$g = -\frac{1}{\gamma_g} \sum_{l,m=1}^{M} \kappa_{lm} a_l a_m + \eta_g, \tag{18}$$

where η_g is a dimensionless fluctuation term

$$\eta_g = -\sum_k \frac{\Gamma_{gk} b_{gk}(0)}{\gamma_g + i(\omega_g - \Omega_{gk})} e^{-i\Omega_{gk}t}. \tag{19}$$

The green mode is seen here to be "slaved" to the infrared dynamics; namely, $g(t)$ is determined solely in terms of the infrared modes and fluctuations associated with its coupling to the external world. The use of a single green mode operator is justified as the green light escapes from the laser cavity

and its dynamics is not observed. In what follows, we shall see it acts as a damping factor, and the detailed mode structure is not important.

We do the same with the infrared reservoir and infrared equations of motion and substitute in the green evolution equation to get

$$\frac{dA_i}{dt} = -\gamma_i A_i - \frac{2}{\gamma_g}\sum_{j,l,m=1}^{M} \kappa_{ij}\kappa_{lm}A_j^\dagger A_l A_m + 2\sum_{j=1}^{M} A_j^\dagger \eta_g e^{i(\omega_i+\omega_j)t} + \eta_i e^{i\omega_i t} - \int_0^L \sigma_i^* e^{i\omega_i t} S_-(z)\sin(K_i z)dz. \tag{20}$$

The noise (η_i and η_g) and damping (γ_i and γ_g) can be related through a fluctuation-dissipation relation, which we derive in a later section.

Now we turn to the two level system equations of motion. Although the Nd:YAG laser is actually a four level system, this model works well for determining the equations of motion. It fails when computing the spontaneous emission noise power, so we compute this power in another way. In the meanwhile we will ignore all noise contributions from the two level system.

The equations of motion are found again, and we formally integrate the reservoir operators, substitute them into the $S_+(z)$ equation of motion, and make the Langevin approximation to get

$$\frac{dS_+(z)}{dt} = (-\gamma_p + i\omega_s)S_+(z) + \eta_s(z)S_3(z) - \sum_{i=1}^{M} \sigma_i^* a_i^\dagger S_3(z)\sin(K_i z). \tag{21}$$

At this point, we note that the Nd:YAG laser is a class B laser and its polarization decay rate is much higher than γ_s because the polarization of the active medium is affected by the surrounding crystal lattice. For Nd:YAG, γ_s^{-1} is approximately 240 μs. The actual polarization decay time γ_p^{-1} is on the order of 10^{-11} s.

So we substitute the faster decay rate γ_p for γ_s and ignore the associated fluctuations.

In the interaction frame moving at the driving frequency ω_d we find that the driving terms are slaved to the population inversion $S_3(z)$ due to the high polarization decay rate. In a way similar to the method used to determine the green mode equation of motion we determine the driving terms to be

$$S_+(z) = -\frac{1}{\gamma_p}\sum_{i=1}^{M} \sigma_i a_i^\dagger e^{-i\omega_d t}\sin(K_i z)S_3(z), \tag{22}$$

$$S_-(z) = -\frac{S_3(z)}{\gamma_p}\sum_{i=1}^{M} \sigma_i a_i e^{i\omega_d t}\sin(K_i z). \tag{23}$$

We now take the $S_3(z)$ equation, substitute the reservoir solutions, and perform the Langevin approximations.

$$\frac{dS_3(z)}{dt} = 2\Lambda - 2\gamma_s[I+S_3(z)] - 2[S_+(z)\eta_s^\dagger(z) - \eta_s(z)S_-(z)] + 2\sum_{i=1}^{M} \sigma_i[S_+(z)a_i + a_i^\dagger S_-(z)]\sin(K_i z). \tag{24}$$

A constant population inversion 2Λ has been added to account for optical pumping. Further manipulations and associating the operator $S_3(z)$ with the population inversion $n(z)$, we find and equation for the population inversion of the laser,

$$\frac{dn(z)}{dt} = -\frac{1}{\tau_f}[n(z)-\bar{n}] - n(z)\sum_{i=1}^{M} 4\frac{\sigma_i^2}{\gamma_p}A_i^\dagger A_i \sin^2(K_i z), \tag{25}$$

where τ_f is the fluorescence decay time of the Nd:YAG medium (240 μs) and $\bar{n}$ is the mean population inversion.

After substituting the driving terms into the field equation we get

$$\frac{dA_i}{dt} = -\gamma_i A_i - \frac{2}{\gamma_g}\sum_{j,l,m=1}^{M} \kappa_{ij}\kappa_{lm}A_j^\dagger A_l A_m + 2\sum_{j=1}^{M} A_j^\dagger \eta_g e^{i(\omega_i+\omega_j)t} + \eta_i e^{i\omega_i t} + \frac{\sigma_i^2}{N\gamma_p}\int_0^L \sin^2(K_i z)n(z)dz A_i. \tag{26}$$

We have identified $n(z)$ here. At this point we recall that the number of photons in the cavity is large (10^9) and treat the quantum mechanical operators A_i and $A_i^\dagger$ as if they are c numbers.

Since we now have a partial differential equation for $n(z)$, we break this equation into the component normal modes as described in detail in [3]. To do this, we define a mode gain G_i as

$$G_i = \frac{2|\sigma_i|^2\tau_c}{N\gamma_p}\int_0^L n(z)\sin^2(K_i z)dz, \tag{27}$$

where τ_c is the round trip cavity time of the laser (0.2 ns). Assuming that $n(z,t)$ separate into time and space components we can write down equations for the mode gains instead of the population inversion. After rescaling the equations so that the electric field has measurable units we obtain

$$\frac{dE_i}{dt} = \frac{1}{2\tau_c}\left[(G_i-\alpha_i)E_i - \epsilon\sum_{j,k,l=1}^{M} \zeta_{ij}\zeta_{lm}E_j^* E_l E_m\right] + 2\kappa\sum_{j=1}^{M} \zeta_{ij}E_j^* \eta_g e^{i(\omega_i+\omega_j)t} + \sqrt{\frac{\hbar\omega_d}{\tau_c}}\eta_i e^{i\omega_i t}. \tag{28}$$

$$\frac{dG_i}{dt} = \frac{1}{\tau_f}\left[\rho_i - G_i\left(1+\sum_{j=1}^{M} \beta_{ij}|E_j|^2\right)\right]. \tag{29}$$

At this point we make use of an earlier model of the laser [3]:

$$2\tau_c \frac{dE_i}{dt} = (G_i - \alpha_i)E_i - \epsilon g |E_i|^2 E_i - 2\epsilon \sum_{j \neq i} \mu_{ij} |E_j|^2 E_i , \tag{30}$$

$$\tau_f \frac{dG_i}{dt} = \rho_i - G_i \left(1 + \sum_{j=1}^{M} \beta_{ij} |E_j|^2 \right). \tag{31}$$

where $\mu_{ij} = g_c$ if the modes are parallel polarized and $\mu_{ij} = (1 - g_c)$ if the modes are orthogonally polarized. These values of μ_{ij} have been determined in [3] after consideration of the phase-matching conditions for the intracavity KTP crystal in the presence of the polarized modes of the laser field. Notice that Eq. (30) is a special case of Eq. (28) having the terms where $i = k$ and $j = l$ (or $i = l$ and $j = k$). This is called degenerate four wave mixing. Matching coefficients in the degenerate case, we find that $\zeta_{ij} = \sqrt{g_c}$ when modes i and j are parallel polarized and $\zeta_{ij} = \sqrt{1 - g_c}$ when they are perpendicularly polarized.

We expect that the degenerate and nondegenerate four wave mixing rates differ in the different laser configurations. Type I chaos exhibits nondegenerate four wave mixing with little, if any, degenerate four wave mixing. This implies that the green photons never have a chance to leave the cavity before being downconverted to infrared again. The opposite is true for type II chaos where the green photons immediately leave the cavity. In order to separate these two cases, it is necessary to define a four wave mixing tensor ϵ_{ijkl} where

$$\epsilon_{ijkl} \begin{cases} \epsilon_d \zeta_{ij} \zeta_{kl} & \text{if } i = k \text{ and } j = l \\ \epsilon_d \zeta_{ij} \zeta_{kl} & \text{if } i = l \text{ and } j = k \\ \epsilon_n \zeta_{ij} \zeta_{kl} & \text{otherwise.} \end{cases} \tag{32}$$

Here, ϵ_d is the degenerate four wave mixing rate and ϵ_n is the nondegenerate four wave mixing rate. We see that Eq. (28) is a special case where the two rates are identical while Eq. (30) is the case when there is only degenerate four wave mixing and no nondegenerate four wave mixing.

The equations we numerically integrate are

$$\frac{dE_i}{dt} = \frac{1}{2\tau_c} \left[(G_i - \alpha_i)E_i - \sum_{j,k,l=1}^{M} \epsilon_{ijkl} E_j^* E_k E_l \right] + \eta_i' , \tag{33}$$

$$\frac{dG_i}{dt} = \frac{1}{\tau_f} \left[\rho_i - G_i \left(1 + \sum_{j=1}^{M} \beta_{ij} |E_j|^2 \right) \right]. \tag{34}$$

In these equations $i = 1, 2, \ldots, M$. We have lumped all of the noise terms into the single additive noise term η_i'. This is possible because the multiplicative noise in Eq. (28) is much smaller than the additive noise (see below).

We use the parameters shown in Table II. ϵ_{ijkl} is the four wave mixing efficiency in inverse watts and has a magnitude on the order of 10^{-5} W^{-1}. It depends on the mode configuration and the relative orientations of the Nd:YAG and KTP crystals. β_{ij} is the cross saturation parameter between modes i and j in units of inverse watts. These values are different for type I and type II chaos and are discussed below.

TABLE II. Model parameters.

Parameter	Value	Description
τ_c	0.2 ns	Round trip cavity time
τ_f	240 μs	Fluorescence decay time of Nd:YAG
α	0.01	Cavity loss factor
ϵ_{ijkl}	See Tables III and Tables IV	Four wave mixing efficiency
ρ_i	0.02	Pumping power
β_{ij}	See Tables III and IV	Cross saturation parameter

IV. NUMERICAL INTEGRATION RESULTS

These model equations were numerically integrated using a standard stiff integrator from the Los Alamos CLAMS library with a time step of 100 ns. The reservoir noise η_i was simulated by adding a complex Gaussian offset with a variance of 10^{-4} W to the electric field of each mode between integration steps.

Type I behavior is obtained in numerical integration when all modes are polarized in the same direction and no nondegenerate four wave mixing is present, as shown in Table III.

The absence of degenerate four wave mixing is consistent with the experimental absence of measurable green output. Figure 3(a) shows a type I time trace obtained by numerical integration of the equations. The bursting behavior and the relaxation oscillation period echo the experimental type I data in Fig. 1(a).

An approximation to type II behavior is obtained when degenerate four-wave mixing dominates over nondegenerate four-wave mixing as shown in Table IV.

Note that the factors ζ_{ij} in (32) are all equal regardless of whether mode i and mode j are parallel or perpendicular. The predominance of degenerate four wave mixing is consistent with experiment; with type II behavior we observe a high amount of green output. An example of a type II time trace obtained from numerical integration is shown in Fig. 3(b).

A. Data preparation

In our previous paper [8] we discussed the digital signal processing methods we used to extract more resolution from

TABLE III. Type I model parameters.

Parameter	Type I chaos Condition	Value
ϵ_{ijkl}	$i = k$ and $j = l$	0 W^{-1}
	$i = l$ and $j = k$	0 W^{-1}
	Otherwise	2.1×10^{-6} W^{-1}
β_{ij}	$i = j$	1.0 W^{-1}
	$i \neq j$	0.6 W^{-1}

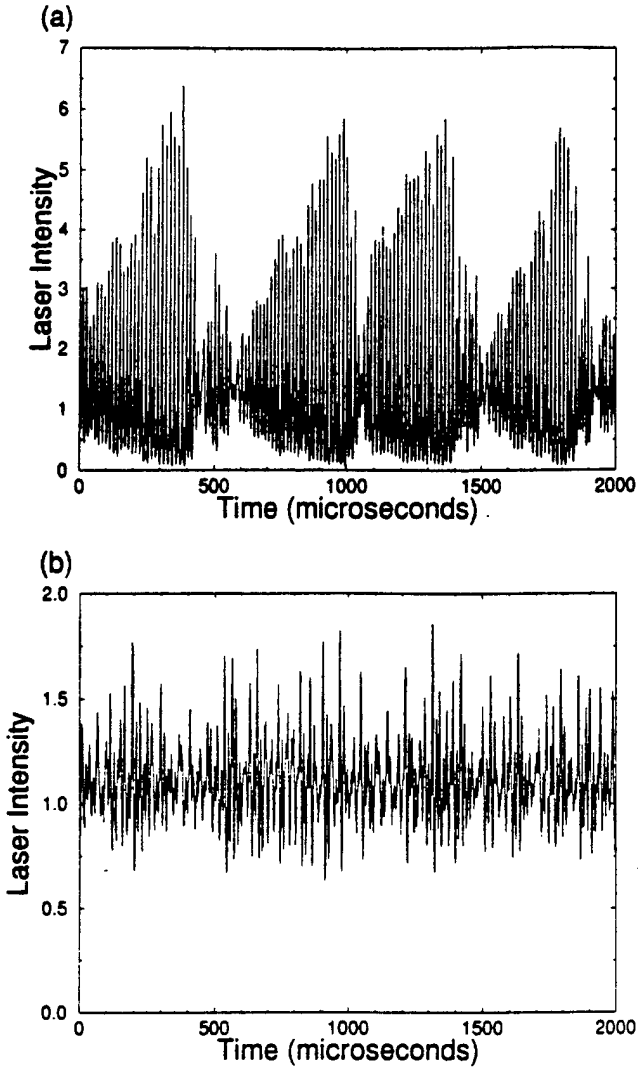

FIG. 3. (a) Numerically integrated type I intensity time series with all modes polarized parallel to each other and no degenerate four-wave mixing. (b) Numerically integrated type II intensity time series with two modes polarized parallel to each other and one polarized perpendicular to the other two and no nondegenerate four wave mixing.

our data acquired using an eight bit sampling oscilloscope. The resolution affects the local false neighbors and the Lyapunov exponent calculations so in order to use these tools to compare the experimental data and the numerical model, it was necessary to perform the same manipulations. In summary, the numerical model was integrated for 10^6 points with a time step of 100 ns, matching the maximum storage capacity and the sampling time of the oscilloscope. The data were then quantized to eight bits. For the false nearest neighbors test and the average mutual information calculation, the data were down sampled by a factor of eight, that is, seven out of every eight samples were thrown out. This leaves 125 000 points at a sampling rate of 1.25 MHz (τ_s=800 ns). The down sampling preserves the broadband noise level.

For the local false nearest neighbors test and the Lyapunov exponents, the quantized data were interpolated using a digital linear filter. This filter is designed to remove frequencies from 500 kHz to the Nyquist frequency $f_s/2$=5 MHz and pass all frequencies below 500 kHz. This was needed to get higher resolution from the experimental data traces. In order to match our results, we did this with the numerical traces as well. After performing the interpolation, the data were also down sampled by a factor of 8, leaving 125 000 points at a sampling rate of 1.25 MHz (800 ns).

TABLE IV. Type II model parameters.

Parameter	Type II chaos Condition	Value
ϵ_{ijkl}	$i=k$ and $j=l$	10^{-5} W^{-1}
	$i=l$ and $j=k$	10^{-5} W^{-1}
	Otherwise	0 W^{-1}
β_{ij}	$i=j$	1.0 W^{-1}
	$i\neq j$	0.85 W^{-1}

B. Power spectrum

When we compare the power spectra of the numerical results and the experimental data, we find similarities. Figure 4 shows the power spectra for the experimental data [Fig. 4(a)] and the numerical data [Fig. 4(b)] for type I chaos. The peaks and their structure are very similar. Figure 5 shows the same information for type II chaos. Here, it is not clear from the spectra whether the type II chaos is well modeled.

C. Average mutual information

The average mutual information of the model is strikingly similar to the experimental data. Figure 6(b) is the average mutual information as a function of time lag for the numerically integrated model for type I chaos, and has essentially the same shape as the average mutual information function of the experimental data [Fig. 6(a)]. Note that the relaxation oscillation time is slightly different between the model and the data, however, this can be adjusted with a small change in the pump power.

The average mutual information function for type II chaos is also very similar between model and experiment as shown in Fig. 7. Again, the relaxation oscillation time can be refined by changing the pumping power.

D. False nearest neighbors

When we examine how the model dynamics respond to noise using the false nearest neighbors algorithm, we find that the type I dynamics tend to suppress noise while the type II dynamics do not. Figure 8 shows the false nearest neighbors results for the numerically integrated time traces (125 000 points) for both types of dynamics, with and without reservoir noise. It is clear, especially in Fig. 8(b) that when no noise is present, both type I and type II dynamics exhibit low-dimensional behavior with almost no residual.

When Gaussian noise ($\sigma=0.01|\mathcal{E}_{\text{nominal}}|$) is added to the electric field for every integration time step of 100 ns, we find that type I dynamics have no residual, or in other words, the reservoir noise has been suppressed by the dynamics. However, in the type II dynamics, the residual is around 5%, which indicates that the dynamics have been significantly

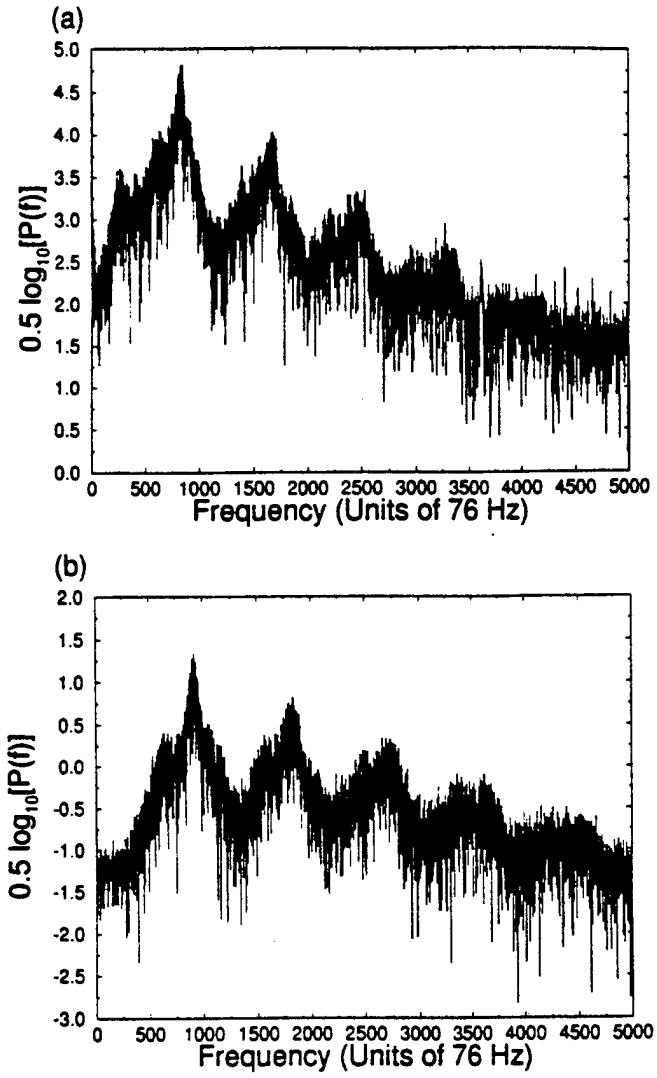

FIG. 4. (a) The power spectrum of the type I experimental data shown in Fig. 1(a). (b) The power spectrum of the numerically integrated time series shown in Fig. 3(a) (type I chaos).

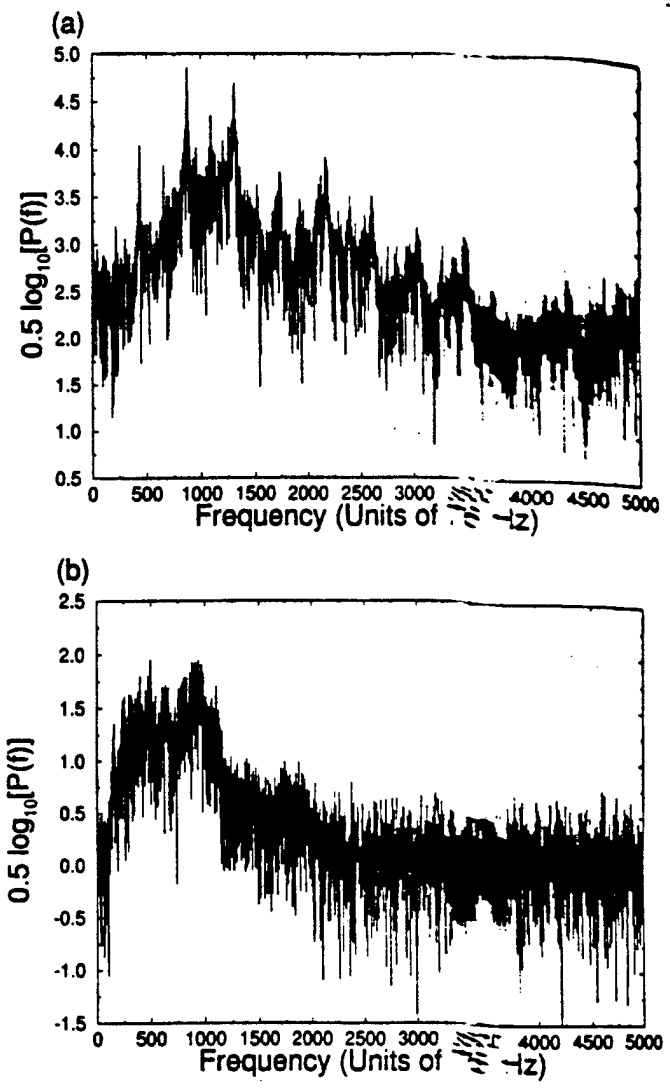

FIG. 5. (a) The power spectrum of the type I experimental data shown in Fig. 1(a). (b) The power spectrum of the numerically integrated time series shown in Fig. 3(b) (type I chaos).

affected by the reservoir noise. These findings are numerically consistent with our observations. When we normalize the noise levels using the maximum amplitude of the type I and type II time series, we find that type II is three times more susceptible to noise than type I.

E. Local false nearest neighbors

We also performed a test called local false nearest neighbors on the numerical data [8]. This is used to find the local dimension, or number of equations of motion of the system that generated the data. The results for type I chaos are shown in Fig. 9. For the experimental data [Fig. 9(a)] the predictability of the data has become independent of the number of neighbors and the embedding dimension. We find that numerical results [Fig. 9(b)] match well; both sets have a local dimension $d_L \approx 6$ and the same fraction of poor predictions. For type II chaos (Fig. 10) the match is not so good—the fraction of poor predictions is different by a factor of 2 and the local dimension appears substantially smaller for the model than for the experiment.

F. Average local Lyapunov exponents

The average local Lyapunov exponents matched well between the model and experimental type I traces. These are computed using the methods described in [8]. Figure 11 shows the average local Lyapunov exponents for the experimental type I data [Fig. 11(a)] and numerical model type I data [Fig. 11(b)] using $d_E=7$ and $d_L=7$. Figure 12 shows a closeup of these graphs. Note that in both cases, there are two positive Lyapunov exponents and a zero exponent. The negative Lyapunov exponents are slightly larger for the model dynamics. It is likely that a small parameter change can improve the match.

For the type II data, the match is not as good. Figure 13 shows the average local Lyapunov exponents for the experimental type II data [Figure 13(a)] and the numerical model type II data [Fig. 13(b)] using $d_E=7$ and $d_L=7$. Figure 14 is a closeup of these graphs. The experimental data have three positive Lyapunov exponents while the numerical model has 2. The largest Lyapunov exponent from the experimental data exceeds that of the model by a factor of two. We conclude that the model of type II dynamics does not match the experiment well.

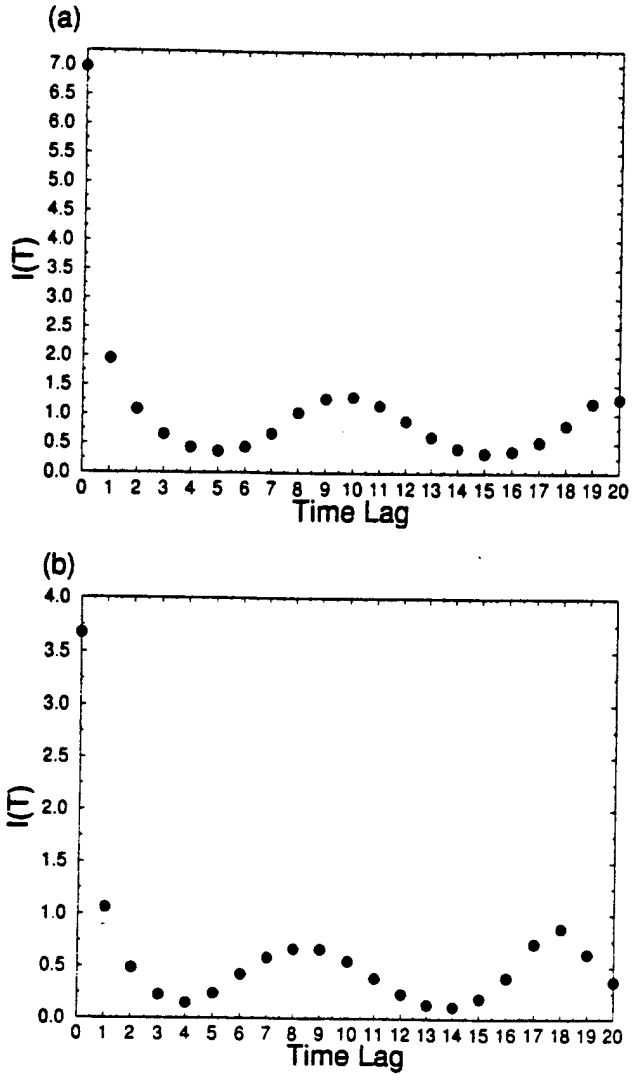

FIG. 6. (a) The average mutual information as a function of time lag for the experimental time series shown in Fig 1(a) (type I chaos). The time lag is given in units of 8/100 MHz or 800 ns. (b) The average mutual information as a function of time lag for the numerically integrated time series shown in Fig. 3(a) (type I chaos).

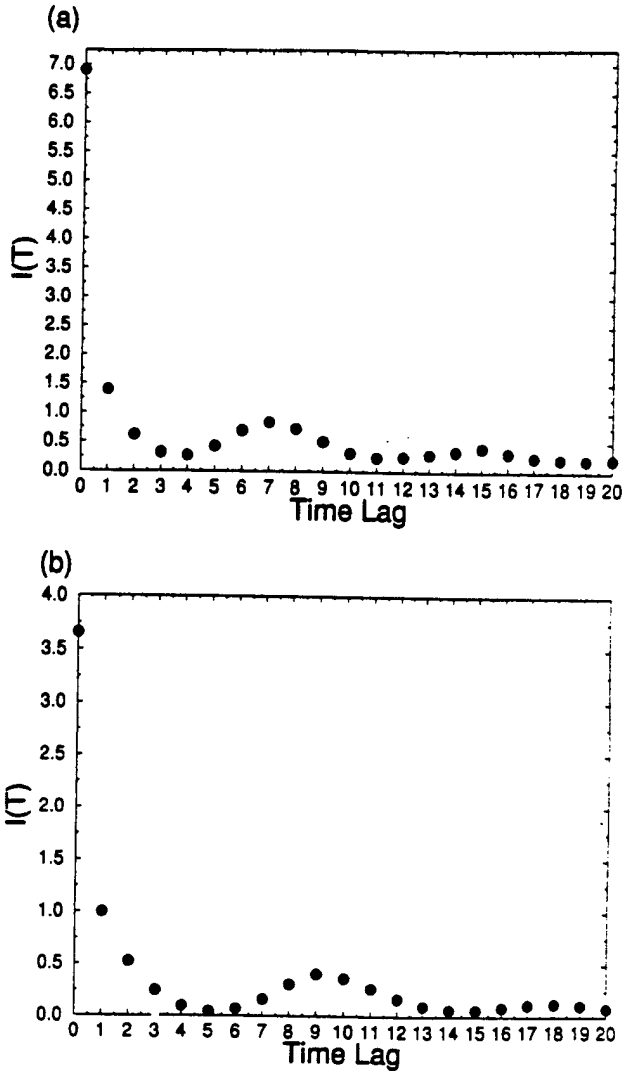

FIG. 7. (a) The average mutual information as a function of time lag for the experimental time series shown in Fig. 1(b) (type II chaos). The time lag is given in units of 8/100 MHz or 800 ns. (b) The average mutual information as a function of time lag for the numerically integrated time series shown in Fig. 3(b) (type II chaos).

Table V gives the average Lyapunov exponent values for $L=2048$, which is a good approximation of the global Lyapunov exponents for the experimental data and the model data. From these numbers, it is clear that type I chaos is modeled well, while type II chaos is not.

V. NOISE SOURCES

In an attempt to determine the source of the noise in the equations, we discuss four sources of intrinsic quantum fluctuations: fluctuations due to cavity damping of the infrared, fluctuations due to the green light leaving the cavity, fluctuations due to spontaneous emission, and fluctuations inherent in the conversion process. We also examined the possibility of fluctuations in the pumping power, and concluded that these could not cause the noise in the output intensity.

We choose to compute the noise levels in photons/s, so we abandon our current units and go back to using the c numbers associated with the creation and annihilation operators $A_i^\dagger$ and A_i. $A_i^\dagger A_i$ is simply the number of photons in mode i and we call this quantity N_{IR}. We repeat the differential equation governing A_i using a generic source of noise $\eta(t)$:

$$\frac{dA_i}{dt} = -\gamma_i A_i - \frac{2}{\gamma_g}\sum_{j,l,m=1}^{M} \kappa_{ij}\kappa_{lm} A_j^\dagger A_l A_m + \sqrt{D}\,\eta, \quad (35)$$

where $\eta(t)$ satisfies

$$\langle \eta^\dagger(t')\,\eta(t)\rangle = \delta(t-t') \quad (36)$$

and D is the noise variance or strength in units of s^{-1}.

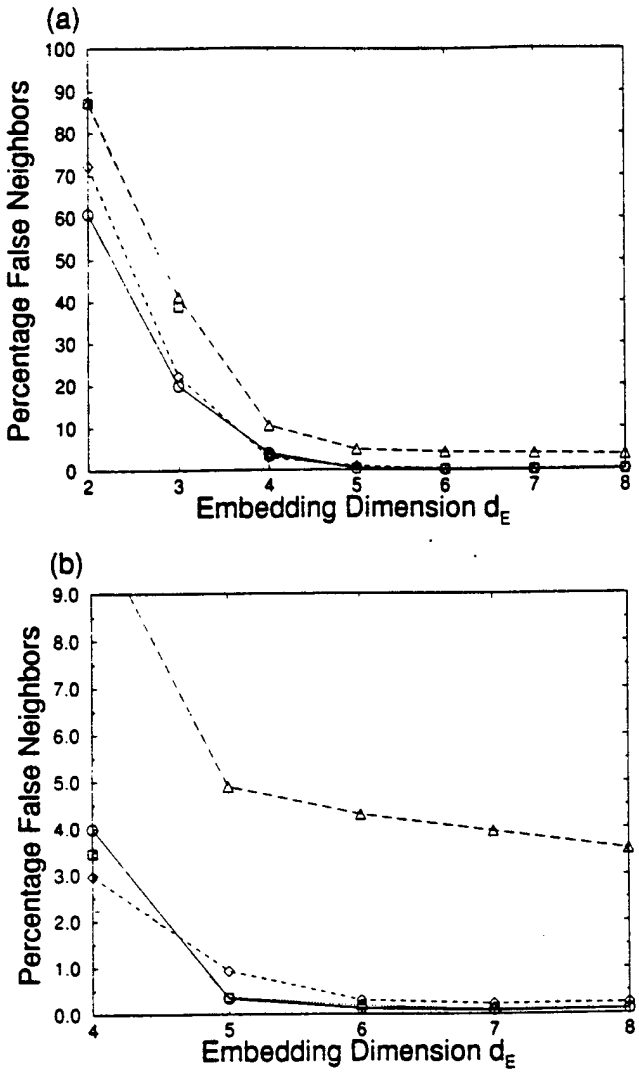

FIG. 8. (a) The percentage of false nearest neighbors (FNN) vs the embedding dimension d_E for the numerically integrated model. The graphs depict type I with no noise (circles), type II with no noise (squares), type I with reservoir noise ($\sigma^2 = 10^{-4}$, diamonds) and type II with the same reservoir noise (triangle). (b) An enlargement of (a) showing that the percentage of FNN drops to 0.1% and stays there as d_E increases for both types of dynamics with no noise added, and type I dynamics with noise. However, the percentage of type II FNN when noise is added is much higher, around 3% .

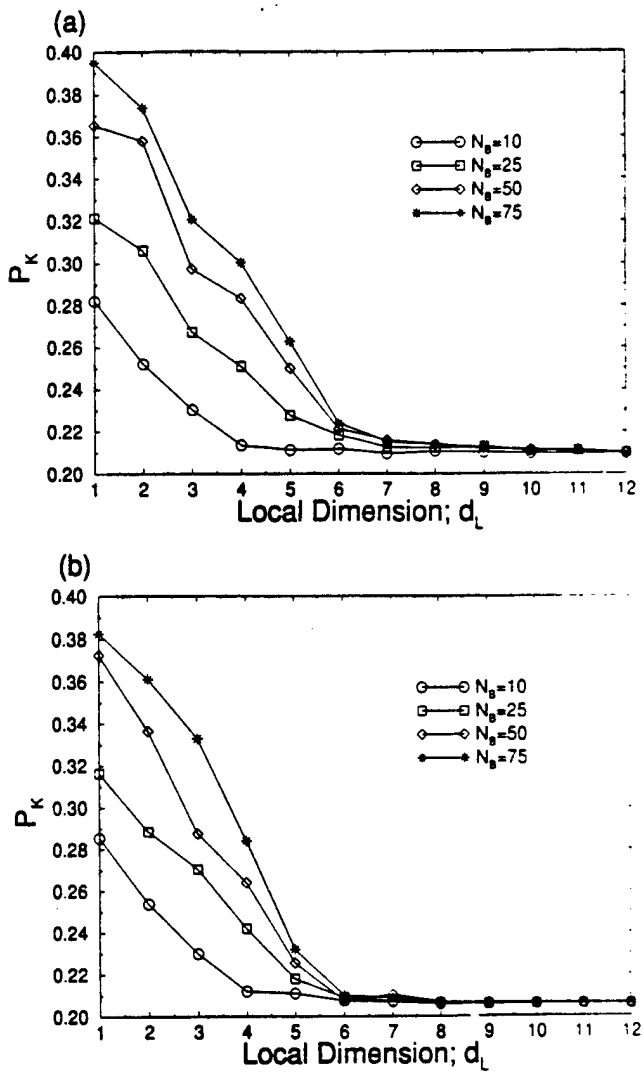

FIG. 9. (a) Local false nearest neighbors for the experimental type I time series shown in Fig. 1(a). (b) Local false nearest neighbors for the numerically integrated type I time series.

The noise power in units of photons/s that is added to each mode can be computed using the number equation:

$$\frac{dA_i^\dagger A_i}{dt} = -2\gamma_i A_i^\dagger A_i - \frac{2}{\gamma_g}\sum_{j,l,m=1}^{M} \kappa_{ij}\kappa_{lm} A_i^\dagger A_j^\dagger A_l A_m + A_i^\dagger \sqrt{D}\,\eta - \frac{2}{\gamma_g}\sum_{j,l,m=1}^{M} \kappa_{ij}\kappa_{lm} A_j A_l^\dagger A_m^\dagger A_i + \sqrt{D}\,\eta^\dagger A_i . \tag{37}$$

The amount of noise added to the numerical integration in these units can be determined by converting the noise term in the above equation to real units E where $|E|^2$ is in watts.

$$\frac{dE_i}{dt} = -\gamma_i E_i - \frac{2\tau_c}{\gamma_g \hbar \omega_{dj,l,m=1}}\sum^{M} \kappa_{ij}\kappa_{lm} E_j^* E_l E_m + \sqrt{\frac{\hbar\omega_d}{\tau_c}}\sqrt{D}\,\eta. \tag{38}$$

The noise strength in the simulation is 10^3 W/s. Thus, $D = 10^{21}$ s^{-1}. Using Eq. (37) we find that the noise in photons/s is

$$N_{num} \approx 2\sqrt{N_i}\sqrt{D}\,\frac{1}{s^{-1/2}}, \tag{39}$$

where N_i is the number of IR photons in mode i. The strange units in Eq. (39) occur because the units of η are the units of a square root of a δ function in time.

From the experiment we find that about 1 mW of infrared light is output from the laser. Given a transmission loss of $\approx 0.1\%$, this means that there is approximately 1 W of infrared power inside the cavity. Since each photon has an energy of $\hbar\omega_d = 2\times 10^{-19}$ J and the round trip cavity time is

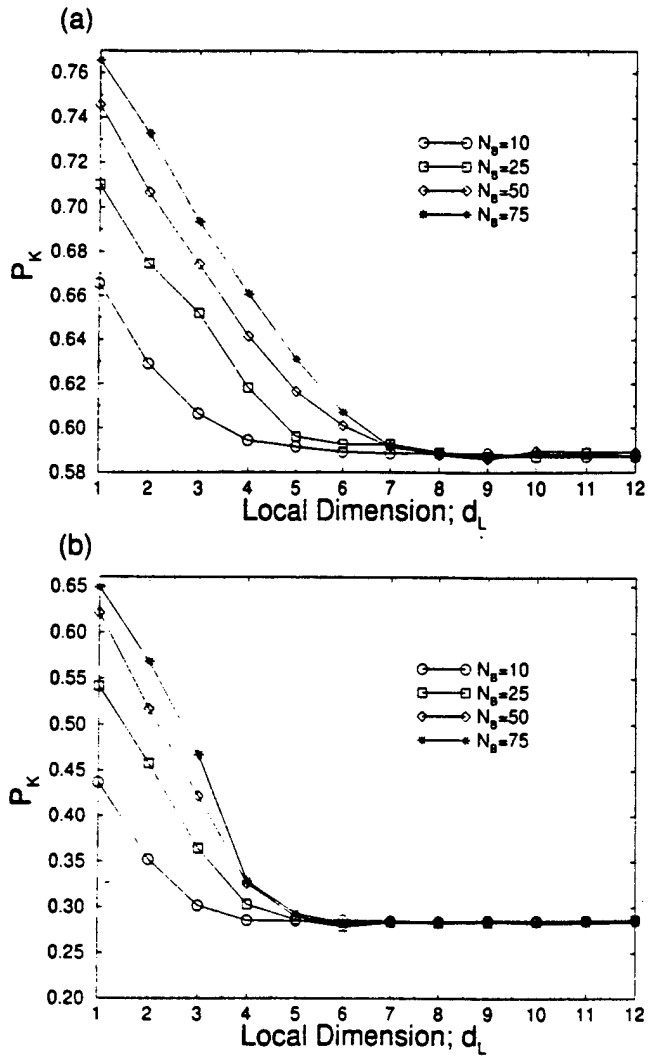

FIG. 10. (a) Local false nearest neighbors for the experimental type II time series shown in Fig. 1(b). (b) Local false nearest neighbors for the numerically integrated type II time series shown in Fig. 3(b).

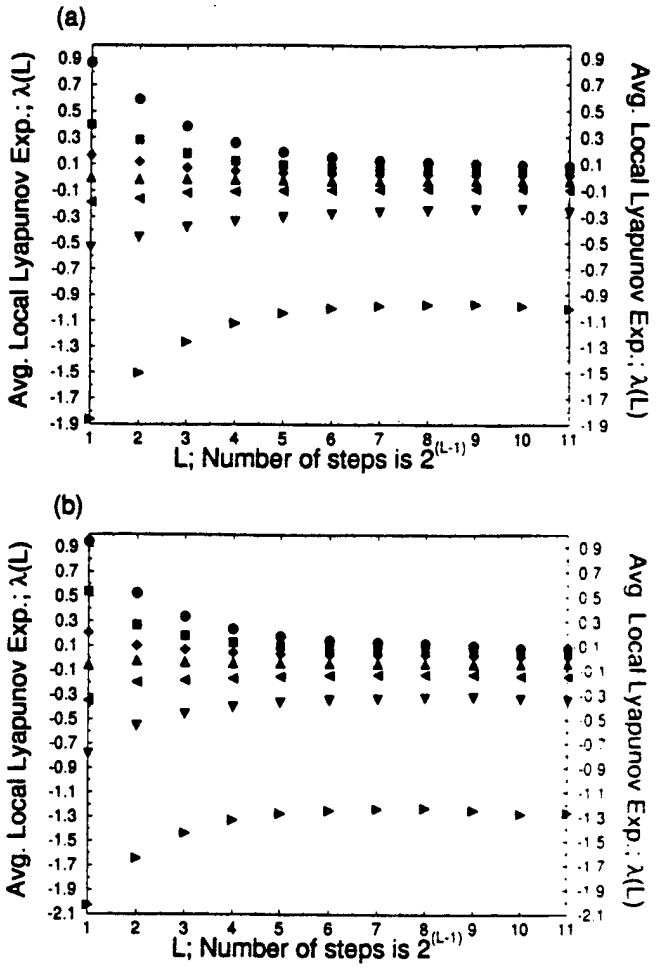

FIG. 11. (a) The average local Lyapunov exponents for the experimental type I time series shown in Fig. 1(a). (b) The average local Lyapunov exponents for the numerically integrated type I time series shown in Fig. 3(a).

$\tau_c = 2\times 10^{-10}$ s, we find that $N_i \approx 10^9$. This puts the numerical integration noise at 2×10^{15} photons/s.

Similarly, the output green power of 100 μW with a fully transmitting cavity implies that the number of green photons in the cavity N_g is about 10^5.

A. Damping fluctuations

First we wish to find the noise power due to damping of infrared light. We compute the noise strength D_{ii}.

$$\langle \eta_i^\dagger(t)\,\eta_i(t')\rangle = D_{ii}\delta(t-t'). \tag{40}$$

Based on Chap. 19-2 in [15] we find that

$$N_i^{\mathrm{IR}} = \gamma_i\langle n(\omega_i)\rangle = \frac{\alpha}{\tau_c}\langle n(\omega_i)\rangle, \tag{41}$$

where $\langle n(\omega_i)\rangle$ is the mean occupation number of bosons and

$$\langle n(\omega_i)\rangle = \frac{1}{e^{\hbar\omega_i/kT}-1}. \tag{42}$$

Here, k is Boltzmann's constant and T is the temperature of the reservoir, which we take to be the cold cavity temperature of 300 K. The energy of an infrared photon is 1.2 eV while kT at room temperature is about 0.026 eV. Thus $\langle n(\omega)\rangle$ is 10^{-20}. The noise strength is $10^{-13}\ \mathrm{s}^{-1}$. The noise added to each mode due to IR damping is approximately

$$N_{\mathrm{IR}} \approx 2\sqrt{N_i}\sqrt{D_{ii}} = 0.02 \text{ photons/s}. \tag{43}$$

Similarly, the green noise strength is

$$\langle \eta_g^\dagger(t)\,\eta_g(t')\rangle = D_g\delta(t-t') = \frac{\langle n(\omega_g)\rangle}{\gamma_g}\delta(t-t'). \tag{44}$$

The noise power in infrared mode i due to green cavity damping fluctuations from Eq. (A47) is

$$N_i^{\mathrm{green}} = 2\sum_{j=1}^{M}\kappa_j A_i^\dagger A_j^\dagger\sqrt{D_g}\,\eta + 2\sum_{j=1}^{M}\kappa_j A_j^\dagger A_i^\dagger\sqrt{D_g}\,\eta^*. \tag{45}$$

which we approximate as

$$N_i^{\mathrm{green}} = 4\kappa N_i\sqrt{\frac{\langle n(2\omega_d)\rangle}{\gamma_g}}. \tag{46}$$

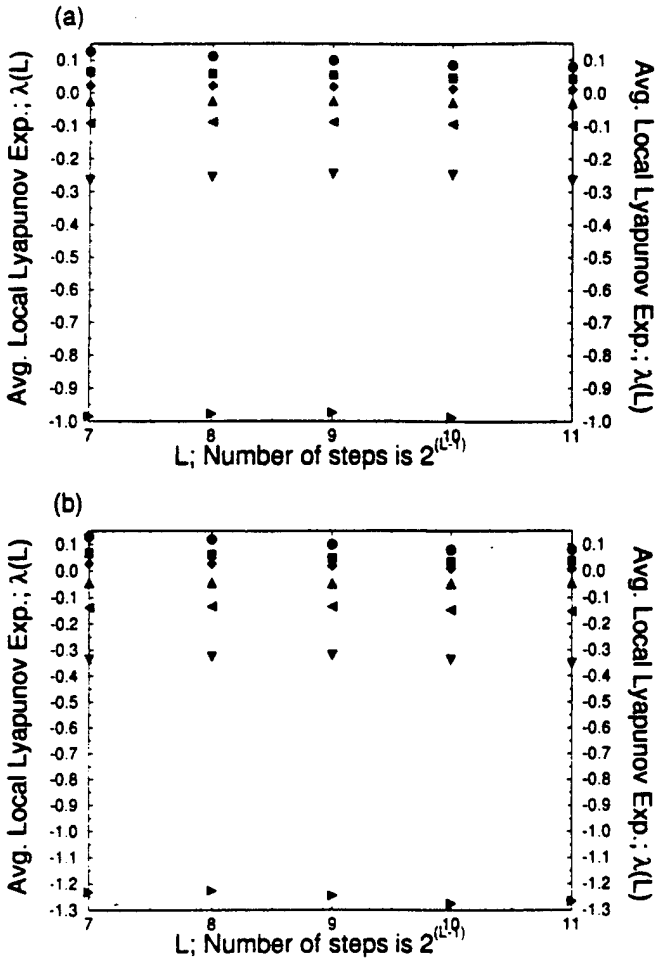

FIG. 12. (a) A closeup of Fig. 11(a). (b) A closeup of Fig. 11(b).

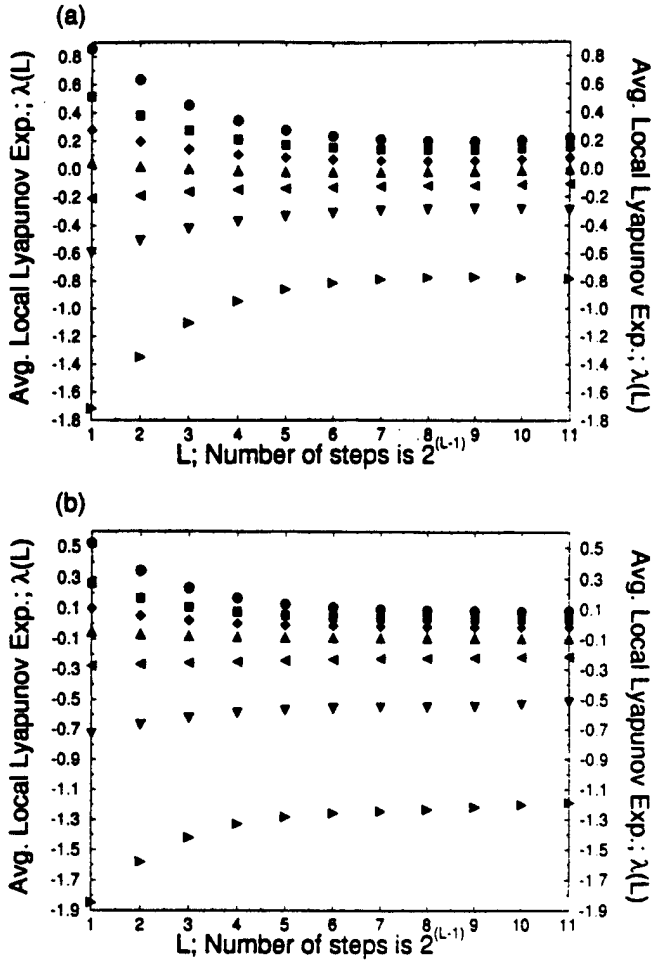

FIG. 13. (a) The average local Lyapunov exponents for the experimental type II time series shown in Fig. 1(b). (b) The average local Lyapunov exponents for the numerically integrated type II time series shown in Fig. 3(b).

Since we know the value of ϵ,

$$\epsilon = \frac{4\tau_c^2\kappa^2}{\hbar\omega_d\gamma_g} \approx 10^{-5}\ \mathrm{W}^{-1}, \tag{47}$$

we find $\kappa \approx 500\ \mathrm{s}^{-1}$. We assume that the decay time of the green is one cavity round trip time, or $1/\tau_c$, which leads to a noise power of 2×10^{-12} photons/s, which is so tiny that it can be ignored.

B. Spontaneous emission noise

The spontaneous emission power can be determined in a similar way to the infrared and green contributions shown above. A simpler method following [16] is used instead.

The Nd:YAG medium has a spontaneous emission spectrum with a Lorentzian shape of width γ_p or 6 cm^{-1} (180 GHz). Knowing the density of photon modes in a cavity with volume V,

$$\frac{dN}{df} = \frac{8\pi V f^2}{c^3}, \tag{48}$$

and assuming a cavity volume of 0.25 cm^3 we find that the number of modes in the spontaneous emission width df is $p = 3\times10^9$.

The total spontaneous emission power in photons/s into a single mode is simply

$$N_i^{\mathrm{spont}} = \frac{N_2}{p\tau_f}, \tag{49}$$

where N_2 is the population of the second level. We can determine this population at threshold especially easily for an Nd:YAG laser because it is a four level laser where $N_2 >> N_1$. According to [16], just below threshold,

$$(N_2 - N_1)_{\mathrm{threshold}} = \frac{p\tau_f}{\tau_p} \approx N_2, \tag{50}$$

where τ_p is the cavity decay time or, using our constants, $\tau_p = \tau_c/\alpha$. What this says is that no net stimulated emission occurs, and the entire population inversion fluoresces at the same rate as the resulting photons leak away. In our laser the population inversion is about 3×10^{15} at threshold.

Substituting the expression for population inversion into the power equation, we find that at threshold,

$$N_i^{\mathrm{spont}} = \frac{\alpha}{\tau_c} = 5\times10^7\ \text{photons/s}. \tag{51}$$

This is still 7 orders of magnitude lower than the levels we expect from numerical integration.

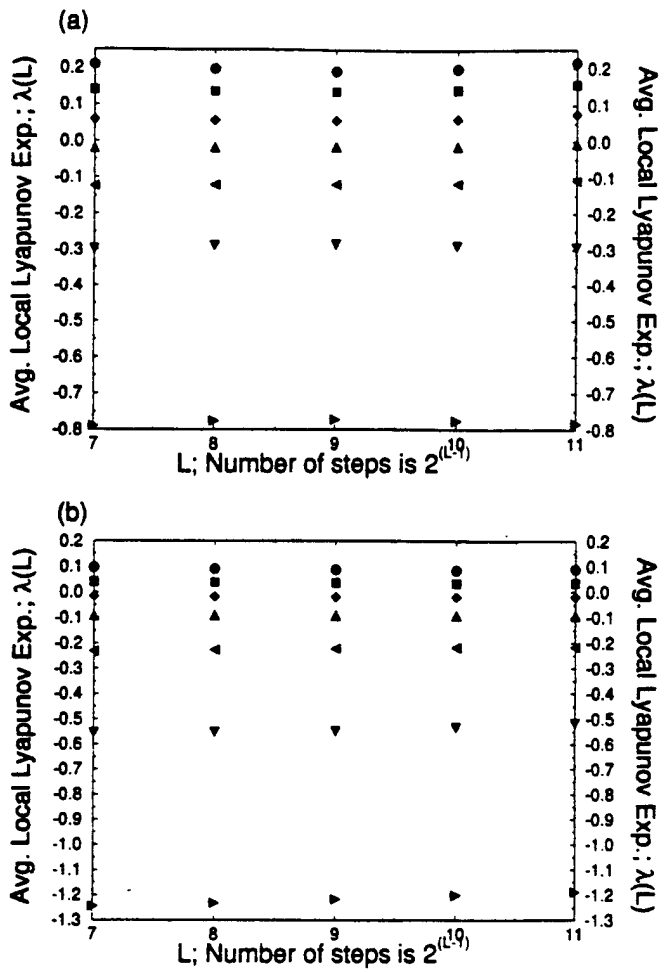

FIG. 14. (a) A closeup of Fig. 13(a). (b) A closeup of Fig. 13(b).

C. Conversion noise

Quantum fluctuations also occur in the conversion of infrared to green and vice versa. This noise must be determined with a different method than used in the above derivation [17,18]. In this calculation, a differential equation is written for the evolution of the density matrix of the system (master equation), a coherent state basis is used to convert the master equation into a Fokker-Planck equation, and finally, the Fokker-Planck equation is converted to a Langevin equation much like Eq. (A47). In the process, a new noise appears, which is related to the diffusion of probability that occurs with nonlinear terms in the Hamiltonian. Since our derivation of this noise term follows [17] almost exactly, we will simply present the results.

TABLE V. Lyapunov exponents of experimental data and model.

Average Lyapunov exponents			
$L = 2048$; $d_E = 7$; $d_L = 7$			
Type 1 chaos		Type 2 Chaos	
Experiment	Model	Experiment	Model
0.080	0.080	0.244	0.088
0.041	0.038	0.172	0.034
0.008	0.009	0.091	−0.019
−0.033	−0.044	0.007	−0.091
−0.102	−0.152	−0.104	−0.216
−0.278	−0.338	−0.298	−0.518
−1.017	−1.266	−0.788	−1.188

Starting with the perturbation related to the KTP conversion process,

$$V = i\hbar \sum_{i,j=1}^{M} \kappa_{ij}(a_i^\dagger a_j^\dagger g - g^\dagger a_j a_i), \tag{52}$$

we find that the terms due to this perturbation in the differential equations are

$$\frac{d}{dt}\begin{bmatrix} \mathcal{A}_1 \\ \mathcal{A}_1^\dagger \\ \mathcal{A}_2 \\ \mathcal{A}_2^\dagger \\ \mathcal{A}_3 \\ \mathcal{A}_3^\dagger \end{bmatrix} = \begin{bmatrix} -2\sum_{j=1}^{3} \kappa_{1j}\mathcal{A}_j^\dagger \mathcal{G} \\ -2\sum_{j=1}^{3} \kappa_{1j}\mathcal{A}_j \mathcal{G}^\dagger \\ -2\sum_{j=1}^{3} \kappa_{2j}\mathcal{A}_j^\dagger \mathcal{G} \\ -2\sum_{j=1}^{3} \kappa_{2j}\mathcal{A}_j \mathcal{G}^\dagger \\ -2\sum_{j=1}^{3} \kappa_{3j}\mathcal{A}_j^\dagger \mathcal{G} \\ -2\sum_{j=1}^{3} \kappa_{3j}\mathcal{A}_j \mathcal{G}^\dagger \end{bmatrix} + \mathbf{B}\begin{bmatrix} \eta_1 \\ \eta_1^\dagger \\ \eta_2 \\ \eta_2^\dagger \\ \eta_3 \\ \eta_3^\dagger \end{bmatrix}, \tag{53}$$

$$\frac{d}{dt}\begin{bmatrix} \mathcal{G} \\ \mathcal{G}^\dagger \end{bmatrix} = \sum_{i,j=1}^{M} \kappa_{ij}\begin{bmatrix} \mathcal{A}_i\mathcal{A}_j \\ \mathcal{A}_i^\dagger \mathcal{A}_j^\dagger \end{bmatrix}. \tag{54}$$

Here, $\mathcal{A}_i$ is a c number similar to (and can be considered to be equivalent to) a_i used earlier. The noise matrix $\mathbf{B}$ is defined by

$$\mathbf{B}\mathbf{B}^T = \begin{bmatrix} \kappa_{11}\mathcal{G} & 0 & \kappa_{12}\mathcal{G} & 0 & \kappa_{13}\mathcal{G} & 0 \\ 0 & \kappa_{11}\mathcal{G}^\dagger & 0 & \kappa_{12}\mathcal{G}^\dagger & 0 & \kappa_{13}\mathcal{G}^\dagger \\ \kappa_{12}\mathcal{G} & 0 & \kappa_{22}\mathcal{G} & 0 & \kappa_{23}\mathcal{G} & 0 \\ 0 & \kappa_{12}\mathcal{G}^\dagger & 0 & \kappa_{22}\mathcal{G}^\dagger & 0 & \kappa_{23}\mathcal{G}^\dagger \\ \kappa_{13}\mathcal{G} & 0 & \kappa_{23}\mathcal{G} & 0 & \kappa_{33}\mathcal{G} & 0 \\ 0 & \kappa_{13}\mathcal{G}^\dagger & 0 & \kappa_{23}\mathcal{G}^\dagger & 0 & \kappa_{33}\mathcal{G}^\dagger \end{bmatrix} \tag{55}$$

and the η terms are zero-mean fluctuation terms satisfying

$$\langle \eta_i^\dagger(t)\eta_j^\dagger(t')\rangle = \delta_{ij}\delta(t-t'). \tag{56}$$

Other than the noise term, the four wave mixing perturbations are the same as what were derived earlier. The multiplicative noise term is much larger than the one derived previously. A rough estimate of the number of noise photons added to the IR mode every second is

TABLE VI. Noise power estimates.

Name	Expression	Power	Description
N_i^{green}	$4\kappa N_i\sqrt{\frac{1}{\gamma_g(e^{\hbar\omega_d/kT}-1)}}$	2×10^{-12}/s	Cavity damping of green light
N_i^{IR}	$2\sqrt{N_i}\sqrt{\frac{\alpha}{\tau_c}\frac{1}{e^{\hbar\omega_d/kT}-1}}$	2×10^{-2}/s	Cavity damping of infrared light
N_i^{conv}	$2\sqrt{N_i\kappa N_g}$	10^7/s	KTP frequency conversion
N_i^{spont}	$\frac{\alpha}{\tau_c}$	10^8/s	Spontaneous emission
N_i^{expt}		2×10^{15}/s	Noise power from experiment

$$N_i^{\text{conv}}\approx 2\sqrt{N_i}\sqrt{\kappa N_g} \tag{57}$$

or 10^7 photons/s. This answer can be arrived at by other means. According to Eq. (37) the green production rate is approximately $4\kappa^2 N_i^2/\gamma_g$, which is 2×10^{14} photons/s. This is the mean value of a process whose standard deviation we would expect to be the noise added to the infrared mode. Since the green mode is a coherent state and therefore has a Poisson distribution in the number states, we would expect the standard deviation to be the square root of the mean. Thus, the noise added to the infrared mode should be around 10^7 photons/s. Table VI summarizes the power estimates in photons/s for the noise sources described above.

It appears that there must be another source of noise in our system that contributes much more than these quantum mechanical sources. Pumping fluctuations were considered. To determine if this were the noise source, we substituted

$$\rho_i \Leftarrow \rho_i[1+\sigma\eta(t)] \tag{58}$$

into Eq. (34) where $\eta(t)$ is a zero mean unit variance random number. We found that in order to reproduce the noise levels of the integrated time series with the experimental time series using the false nearest neighbors algorithm, we had to set $\sigma=0.05$ or 5% fluctuation in ρ_i. This level is unrealistically high for pumping fluctuations. In addition, the fluctuations seen in the experimental data have a characteristic frequency that is much higher than the relaxation oscillation rate, which is impossible to attain through pumping fluctuations because of the slow time constant in Eq. (34).

VI. SUMMARY AND CONCLUSIONS

In summary, we have developed a model that captures key features of the intensity dynamics of the three-mode Nd:YAG laser with an intracavity KTP crystal. This model consists of three equations for each infrared mode: two describe the complex electric field and one describes the gain. The inclusion of both degenerate and nondegenerate four wave mixing are features not found in previous models of the laser. Both qualitative and quantitative behaviors found in the experimental system are captured by this model, which is especially successful in its description of the type I case. The distinction between type I and type II chaos is seen as a difference in structure of the four wave mixing tensor, which also leads to a difference in the noise susceptibility of the equations of motion.

Type I chaos occurs when all modes are parallel polarized and is controllable by the OPF chaos control algorithm. The model contains the bursting behavior found in the time traces. Extremely low levels of green light are measured in type I output, which is described by the model as a predominance of nondegenerate four wave mixing in the laser cavity. Low noise levels are measured in the intensity dynamics, which agrees with the suppression of noise in the type I model dynamics. The local false nearest neighbors test and the Lyapunov exponents match between model and experiment.

Type II chaos occurs when one mode is polarized perpendicular to the other two and is not controllable by the OPF scheme. The spiking, highly irregular time series behavior is captured in the model. The large amount of green light produced by the laser is due to a large amount of degenerate four wave mixing in the laser cavity. The high noise levels found in the intensity dynamics agree with the model's tendency to not suppress reservoir noise but to amplify it instead. However, the local false nearest neighbors test and the Lyapunov exponents do not match well between the model and the experiment, leading us to believe that type II chaos is not fully modeled. We have found that the parameter space of the model is quite complex, especially when degenerate four wave mixing is present. It is possible that additional noise sources remain to be identified and included in the model.

Nonlinear time series analysis has aided this investigation by revealing the link between the high noise levels in the data and the large green light output. A more sophisticated model that reproduces type I behavior almost perfectly and approximates type II behavior is the major result of this paper. Time series analysis allows us to make a quantitative comparison of the model with the experiment. This is the first case we know of where chaotic time series analysis has significantly aided the development of a more complete physical model of the dynamics. This system and model provide a means to study the influence of noise on chaotic systems.

ACKNOWLEDGMENTS

Z.G. and R.R. thank R. Fox, B. Kennedy, and K. Wiesenfeld for many helpful discussions on the material discussed here. Z.G. was financially supported by AT&T. R.R. acknowledges support from NSF Grant No. ECS-9114232. C.L. and H.D.I.A. thank the members of INLS for numerous discussions on this subject. Their work was supported in part by the U.S. Department of Energy, Office of Basic Energy Sciences, Division of Engineering and Geosciences, under Contract No. DE-FG03-90ER14138, and in part by the Office of Naval Research (Contract No. N00014-91-C-0125).

APPENDIX

We reiterate the Hamiltonian:

$$H=\sum_{i=1}^{M}\hbar\omega_i a_i^\dagger a_i+\hbar\omega_g g^\dagger g+i\hbar\sum_{i,j=1}^{M}\kappa_{ij}(a_i^\dagger a_j^\dagger g-g^\dagger a_j a_i)+\sum_{i=1}^{M}\sum_k[\hbar\Omega_{ik}b_{ik}^\dagger b_{ik}+i\hbar\Gamma_{ik}(b_{ik}a_i^\dagger-a_i b_{ik}^\dagger)]+\sum_k[\hbar\Omega_{gk}b_{gk}^\dagger b_{gk}+i\hbar\Gamma_{gk}(b_{gk}g^\dagger$$
$$-gb_{gk}^\dagger)]+\int_0^L\left\{\frac{\hbar\omega_s}{2}S_3(z)+i\hbar\sum_{i=1}^{M}[\sigma_i S_+(z)a_i\sin(K_i z)-\sigma_i^* a_i^\dagger S_-(z)\sin(K_i z)]+\sum_k[i\hbar\Gamma_{sk}(z)S_+(z)b_{sk}-i\hbar\Gamma_{sk}^*(z)b_{sk}^\dagger S_-(z)]\right\}dz$$
$$+\sum_k\hbar\Omega_{sk}b_{sk}^\dagger b_{sk}. \tag{A1}$$

Using this Hamiltonian and the standard Heisenberg equations of motion

$$i\hbar\frac{d\cdot}{dt}=[\cdot,H], \tag{A2}$$

we arrive at the equations of motion governing the system.

$$\frac{da_i}{dt}=-i\omega_i a_i+2\sum_{j=1}^{M}\kappa_{ij}a_j^\dagger g+\sum_k\Gamma_{ik}b_{ik}$$
$$-\int_0^L\sigma_i^* S_-(z)\sin(K_i z)dz, \tag{A3}$$

$$\frac{dg}{dt}=-i\omega_g g-\sum_{l,m=1}^{M}\kappa_{lm}a_l a_m+\sum_k\Gamma_{gk}b_{gk}, \tag{A4}$$

$$\frac{db_{ik}}{dt}=-\Gamma_{ik}a_i-i\Omega_{ik}b_{ik}, \tag{A5}$$

$$\frac{db_{gk}}{dt}=-\Gamma_{gk}g-i\Omega_{gk}b_{gk}. \tag{A6}$$

The green reservoir equation (A6) is linear in $b_{gk}(t)$ so we can integrate it:

$$b_{gk}=-b_{gk}(0)e^{-i\Omega_{gk}t}-\Gamma_{gk}\int_0^t g(t')e^{-i\Omega_{gk}(t-t')}dt'. \tag{A7}$$

Substituting this into (A4) we arrive at

$$\frac{dg}{dt}=-i\omega_g g-\sum_{l,m=1}^{M}\kappa_{lm}a_l a_m+\sum_k\Gamma_{gk}\left[-b_{gk}(0)e^{-i\Omega_{gk}t}\right.$$
$$\left.-\Gamma_{gk}\int_0^t g(t')e^{-i\Omega_{gk}(t-t')}dt'\right]. \tag{A8}$$

The fourth term can be approximated by a damping term using the Wigner-Weisskopf approximation where the modes are assumed to form a continuous spectrum and the interference time of sum on $g(t)$ is assumed to be much smaller than the characteristic time scale of the equation. This approximation is discussed in detail in Sec. 19-2 of [15] and will not be elaborated further here. This leads us to

$$\frac{dg}{dt}=-(\gamma_g+i\omega_g)g-\sum_{lm=1}^{M}\kappa_{lm}^* a_l a_m-\sum_k\Gamma_{gk}b_{gk}(0)e^{-i\Omega_{gk}t}. \tag{A9}$$

where γ_g represents the damping rate.

Since this equation is linear in $g(t)$, we can integrate it to find

$$g=-g(0)e^{-(\gamma_g+i\omega_g)t}$$
$$-\int_0^t\sum_{l,m=1}^{M}\kappa_{lm}a_l(t')a_m(t')e^{-(\gamma_g+i\omega_g)(t-t')}dt'$$
$$-\sum_k\frac{\Gamma_{gk}b_{gk}(0)}{\gamma_g+i(\omega_g-\Omega_{gk})}(e^{(\gamma_g+i\omega_g-i\Omega_{gk})t}-1). \tag{A10}$$

In the integral, we replace the rapidly varying infrared operators $a_i(t)$ with the more slowly varying interaction representation forms $A_i(t)$ in the rotating coordinate system where

$$a_i(t)=e^{-i\omega_i t}A_i(t), \tag{A11}$$

then we perform the integrations by removing the slowly varying operators from under the integral. This method assumes that the damping rate γ_g ($\sim 10^{10}$ Hz) is much higher than the characteristic time scale of the evolution of the slowing varying interaction form of the green operator. We find through experimental observation that the green intensity varies at the same 100 kHz rate as the infrared operator. For times large compared to γ_g^{-1} we can ignore the decaying transients. Thus we find

$$g(t)=-\sum_{l,m=1}^{M}\frac{\kappa_{lm}a_l a_m}{\gamma_g+i(\omega_g-\omega_l-\omega_m)}$$
$$-\sum_k\frac{\Gamma_{gk}b_{gk}(0)}{\gamma_g+i(\omega_g-\Omega_{gk})}e^{-i\Omega_{gk}t}. \tag{A12}$$

This expression is further simplfied if we assume that in order for significant infrared-green conversion to occur, $\omega_g=\omega_l+\omega_m$.

$$g=-\frac{1}{\gamma_g}\sum_{l,m=1}^{M}\kappa_{lm}a_l a_m+\eta_g, \tag{A13}$$

where η_g is a dimensionless fluctuation term

$$\eta_g = -\sum_k \frac{\Gamma_{gk} b_{gk}(0)}{\gamma_g + i(\omega_g - \Omega_{gk})} e^{-i\Omega_{gk}t}. \tag{A14}$$

The green mode is seen here to be "slaved" to the infrared dynamics; namely, $g(t)$ is determined solely in terms of the infrared modes and fluctuations associated with its coupling to the external world. The use of a single green mode operator is justified as the green light escapes from the laser cavity and its dynamics is not observed. In what follows, we shall see it acts as a damping factor, and the detailed mode structure is not important.

Performing the same operations on the infrared equations (without the final integration) we arrive at the equations of motion for the M infrared modes.

$$\frac{da_i}{dt} = -(\gamma_i + i\omega_i)a_i + \eta_i - \sum_{j=1}^{M} 2\kappa_{ij} a_j^\dagger g - \int_0^L \sigma_i^* S_-(z)\sin(K_i z)\,dz, \tag{A15}$$

where

$$\gamma_i = \pi |\Gamma_i(\omega_i)|^2 \mathcal{D}(\omega_i) \tag{A16}$$

$$\eta_i = -\sum_k \Gamma_{ik} b_{ik}(0) e^{-i\Omega_{ik}t}. \tag{A17}$$

$M = 3$ in our problem.

Next we substitute g into this equation, move to a coordinate system rotating with frequency ω_i by substituting

$$A_i = e^{i\omega_i t} a_i, \tag{A18}$$

and assume that in order for significant four wave mixing to occur, $\omega_i + \omega_j = \omega_l + \omega_m$:

$$\frac{dA_i}{dt} = -\gamma_i A_i - \frac{2}{\gamma_g} \sum_{j,l,m=1}^{M} \kappa_{ij}\kappa_{lm} A_j^\dagger A_l A_m + 2\sum_{j=1}^{M} A_j^\dagger \eta_g e^{i(\omega_i+\omega_j)t} + \eta_i e^{i\omega_i t} - \int_0^L \sigma_i^* e^{i\omega_i t} S_-(z)\sin(K_i z)\,dz. \tag{A19}$$

Now we turn to the two level system equations of motion. Although the Nd:YAG laser is actually a four level system, this model works well for determining the equations of motion. It fails when computing the spontaneous emission noise power, so we compute this power in another way. In the meanwhile we will ignore all noise contributions from the two level system.

The pertinent equations of motion are

$$\frac{dS_3(z)}{dt} = 2\sum_{i=1}^{M} \sigma_i [S_-(z)a_i + a_i^\dagger S_-(z)]\sin(K_i z) + 2\sum_k [\Gamma_{sk}(z)S_+(z)b_{sk} + \Gamma_{sk}^*(z)b_{sk}^\dagger S_-(z)] + 2\Lambda, \tag{A20}$$

$$\frac{dS_-(z)}{dt} = i\omega_s S_+(z) - \sum_k \Gamma_{sk}^*(z) b_{sk}^\dagger S_3(z) - \sum_{i=1}^{M} \sigma_i a_i^\dagger S_3(z)\sin(K_i z), \tag{A21}$$

$$\frac{dS_-(z)}{dt} = -i\omega_s S_-(z) - \sum_k \Gamma_{sk}(z) S_3(z) b_{sk} - \sum_{i=1}^{M} \sigma_i S_3(z) a_i \sin(K_i z), \tag{A22}$$

$$\frac{db_{sk}}{dt} = -i\Omega_{sk} b_{sk} - \int_0^L \Gamma_{sk}^*(z) S_-(z)\,dz, \tag{A23}$$

$$\frac{db_{sk}^\dagger}{dt} = i\Omega_{sk} b_{sk}^\dagger - \int_0^L \Gamma_{sk}(z) S_+(z)\,dz. \tag{A24}$$

Note that we have added a constant 2Λ to the S_3 equation to account for the steady-state population inversion due to optical pumping. Λ is a pumping rate density and has units of 1/(length × time).

Formally integrating the reservoir operators, substituting them into the $S_+(z)$ equation of motion, and making the Langevin approximation we get

$$\frac{dS_+(z)}{dt} = (-\gamma_p + i\omega_s)S_+(z) + \eta_s(z)S_3(z) - \sum_{i=1}^{M} \sigma_i^* a_i^\dagger S_3(z)\sin(K_i z). \tag{A25}$$

At this point, we need to note that the Nd:YAG laser is a class B laser and its polarization decay rate is much higher than γ_s because the polarization of the active medium is affected by the surrounding crystal lattice. For Nd:YAG, γ_s^{-1} is approximately 240 μs. The actual polarization decay time γ_p^{-1} is on the order of 10^{-11} s. So we substitute the faster decay rate γ_p for γ_s and ignore the associated fluctuations.

Now we transform the $S_+(z)$ equation to a rotating frame with the driving term frequency ω_d by substituting

$$S_+(z) = e^{-i\omega_d t} S_+(z), \tag{A26}$$

$$\frac{dS_+(z)}{dt} = [-\gamma_p + i(\omega_s - \omega_d)]S_+(z) - \sum_{i=1}^{M} \sigma_i a_i^\dagger e^{-i\omega_d t} S_3(z)\sin(K_i z). \tag{A27}$$

Since the polarization decay rate is so high, the $S_-(z)$ equation is slaved to the population $S_3(z)$ and the field $a_i e^{i\omega_s t}$. So we adiabatically eliminate this equation by setting

$$\frac{dS_+(z)}{dt}=0. \tag{A28}$$

We also assume $\gamma_p >> \omega_s-\omega_d$, which is equivalent to saying that the modes that lase are very near the peak of the Lorentzian line shape of the transition. The $S_-(z)$ equation is similar.

$$S_+(z)=-\frac{1}{\gamma_p}\sum_{i=1}^{M}\sigma_i a_i^\dagger e^{-i\omega_d t}\sin(K_i z)S_3(z), \tag{A29}$$

$$S_-(z)=-\frac{S_3(z)}{\gamma_p}\sum_{i=1}^{M}\sigma_i a_i e^{i\omega_d t}\sin(K_i z). \tag{A30}$$

We now take the $S_3(z)$ equation, substitute the reservoir solutions, and perform the Langevin approximations:

$$\frac{dS_3(z)}{dt}=2\Lambda-2\gamma_s[I+S_3(z)]-2[S_+(z)\eta_s^\dagger(z)-\eta_s(z)S_-(z)]+2\sum_{i=1}^{M}\sigma_i[S_+(z)a_i+a_i^\dagger S_-(z)]\sin(K_i z). \tag{A31}$$

For simplicity, we ignore the noise contribution term $\eta_s(z)$. Substituting $S_\pm(z)e^{\mp i\omega_d t}$ for $S_\pm(z)$, assuming $S_3(z)$ commutes with a_i, and ignoring cross terms we have

$$\frac{dS_3(z)}{dt}=2\Lambda-2\gamma_s[I+S_3(z)]-\frac{1}{\gamma_p}S_3(z)\times\sum_{i=1}^{M}\sigma_i^2 a_i^\dagger a_i\sin^2(K_i z). \tag{A32}$$

We substitute in A_i and multiply the entire equation by N, the total number of atoms.

$$\frac{dNS_3(z)}{dt}=2N\Lambda-2\gamma_s[NI+NS_3(z)]-\frac{4}{\gamma_p}NS_3(z)\times\sum_{i=1}^{M}\sigma_i^2 A_i^\dagger A_i\sin^2(K_i z). \tag{A33}$$

Associating the operator $NS_3(z)$ with the population inversion $n(z)$, we find that NI must be the density of two level systems in the medium N/L. We also define

$$\tau_f\equiv(2\gamma_s)^{-1}, \tag{A34}$$

$$\bar{n}\equiv\left[\frac{N\Lambda}{\gamma_s}-\frac{N}{L}\right], \tag{A35}$$

to get

$$\frac{dn(z)}{dt}=-\frac{1}{\tau_f}(n(z)-\bar{n})-n(z)\sum_{i=1}^{M}4\frac{\sigma_i^2}{\gamma_p}A_i^\dagger A_i\sin^2(K_i z), \tag{A36}$$

where τ_f is the fluorescence decay time of the Nd:YAG medium (240 μs) and $\bar{n}$ is the mean population inversion.

Now we return to the field equation and substitute $S_-(z)e^{-i\omega_d t}$ for $S_-(z)$ and take advantage of the orthogonality condition of the normal modes

$$\int_0^L\sin(K_i z)\sin(K_j z)dz=\delta_{ij} \tag{A37}$$

to get

$$\frac{dA_i}{dt}=-\gamma_i A_i-\frac{2}{\gamma_g}\sum_{j,l,m=1}^{M}\kappa_{ij}\kappa_{lm}A_j^\dagger A_l A_m+2\sum_{j=1}^{M}A_j^\dagger\eta_g e^{i(\omega_i+\omega_j)t}+\eta_i e^{i\omega_i t}+\frac{\sigma_i^2}{N\gamma_p}\int_0^L\sin^2(K_i z)n(z)dz A_i. \tag{A38}$$

We have identified $n(z)$ here. At this point we recall that the number of photons in the cavity is large (10^9) and treat the quantum mechanical operators A_i and $A_i^\dagger$ as if they are c numbers.

We break the population equation into the component normal modes as described in detail in [3]. To do this, we define a mode gain G_i as

$$G_i=\frac{2|\sigma_i|^2\tau_c}{N\gamma_p}\int_0^L n(z)\sin^2(K_i z)dz, \tag{A39}$$

where τ_c is the round trip cavity time of the laser (0.2 ns). Then

$$=\frac{2\sigma_i^2\tau_c}{N\gamma_p}\int_0^L\left[-\frac{1}{\tau_f}[n(z)-\bar{n}]-n(z)\sum_{j=1}^{M}\frac{4|\sigma_j|^2}{\gamma_p}|A_j|^2\sin^2(K_j z)\right]\sin^2(K_i z)\,dz. \tag{A40}$$

We integrate the first two terms on the right hand side and substitute the pumping power

$$\rho_i=\frac{\sigma_i^2\bar{n}L\tau_c}{N\gamma_p}, \tag{A41}$$

$$\frac{dG_i}{dt}=\frac{1}{\tau_f}(\rho_i-G_i)-\frac{2\sigma_i^2\tau_c}{N\gamma_p}\sum_{j=1}^{M}2\frac{|\sigma_j|^2}{\gamma_p}A_j|^2\times\int_0^L n(z)\sin^2(K_i z)dz+\frac{2\sigma_i^2\tau_c}{N\gamma_p}\sum_{j=1}^{M}2\frac{\sigma_i^2}{\gamma_p}|A_j|^2\times\int_0^L n(z)\cos(2K_j z)\left(\frac{1-\cos(2K_i z)}{2}\right)dz. \tag{A42}$$

We define the mode coupling constant ξ_{ij}:

$$\xi_{ij}=\frac{\int_0^L n(z)\cos(2K_j z)[1-\cos(2K_i z)]dz}{\int_0^L n(z)[1-\cos(2K_i z)]dz}$$

$$= \frac{\int_0^L n(z)\cos(2K_j z)[1-\cos(2K_i z)]dz}{2G_i(N\gamma_p/2\sigma_i^2\tau_c)} \quad \text{(A43)}$$

This coefficient is truly a constant if $n(z,t)$ factors into separate time and space dependent components; this is probably a good assumption for a standing wave cavity. Thus

$$\frac{dG_i}{dt} = \frac{1}{\tau_f}(\rho_i - G_i) - G_i \sum_{j=1}^{M} \frac{2|\sigma_j|^2}{\gamma_p}|A_j|^2 + G_i \sum_{j=1}^{M} \frac{2|\sigma_j|^2}{\gamma_p}|A_j|^2 \xi_{ij} \quad \text{(A44)}$$

$$= \frac{1}{\tau_f}\left[\rho_i - G_i\left(1 + \sum_{j=1}^{M} \beta'_{ij}|A_j|^2\right)\right], \quad \text{(A45)}$$

where

$$\beta'_{ij} = \frac{2\sigma_i^2}{\gamma_p}\tau_f(1-\xi_{ij}). \quad \text{(A46)}$$

The field equation is simplified.

$$\frac{dA_i}{dt} = \left(\frac{G_i}{2\tau_c} - \gamma_i\right)A_i - \frac{2}{\gamma_g}\sum_{j,l,m=1}^{M} \kappa_{ij}\kappa_{lm}A_j^\dagger A_l A_m + 2\sum_{j=1}^{M} \kappa_j A_j^\dagger \eta_g e^{i(\omega_i+\omega_j)t} + \eta_i e^{i\omega_i t}. \quad \text{(A47)}$$

We rescale the field equation so that it has measurable units. We define the electric field E so that $I=|E|^2$ has units of watts. That is,

$$|E_i|^2 = |A_i|^2 \frac{\hbar\omega_d}{\tau_c} \quad \text{(A48)}$$

since $|A_i|^2$ is simply the number of photons in mode i. We also substitute $\alpha_i = 2\gamma_i\tau_c$ and assume the κ_{ij} are real:

$$\frac{dE_i}{dt} = \frac{1}{2\tau_c}\left[(G_i-\alpha_i)E_i - \frac{4\tau_c^2}{\hbar\omega_d\gamma_g}\sum_{j,l,m=1}^{M} \kappa_{ij}\kappa_{lm}E_j^* E_l E_m\right] + 2\sum_{j=1}^{M} \kappa_{ij}E_j^* \eta_g e^{i(\omega_i+\omega_j)t} + \sqrt{\frac{\hbar\omega_d}{\tau_c}}\eta_i e^{i\omega_i t}. \quad \text{(A49)}$$

Now we define κ and ζ_{ij} so that $\kappa\zeta_{ij}=\kappa_{ij}$ and ζ_{ij} is unitless and of order unity and define

$$\epsilon = \frac{4\tau_c^2\kappa^2}{\hbar\omega_d\gamma_g}, \quad \text{(A50)}$$

which has units of inverse watts. We also define

$$\beta_{ij} = \beta'_{ij}\frac{\hbar\omega_d}{\tau_c} = \frac{2|\sigma_i|^2\hbar\omega_d\tau_f}{\gamma_p\tau_c}(1-\xi_{ij}) \quad \text{(A51)}$$

which has units of inverse watts. The resulting equations are

$$\frac{dE_i}{dt} = \frac{1}{2\tau_c}\left[(G_i-\alpha_i)E_i - \epsilon\sum_{j,k,l=1}^{M} \zeta_{ij}\zeta_{lm}E_j^* E_l E_m\right] + 2\kappa\sum_{j=1}^{M} \zeta_{ij}E_j^* \eta_g e^{i(\omega_i+\omega_j)t} + \sqrt{\frac{\hbar\omega_d}{\tau_c}}\eta_i e^{i\omega_i t}, \quad \text{(A52)}$$

$$\frac{dG_i}{dt} = \frac{1}{\tau_f}\left[\rho_i - G_i\left(1 + \sum_{j=1}^{M} \beta_{ij}|E_j|^2\right)\right]. \quad \text{(A53)}$$

[1] T. Baer, J. Opt. Soc. Am. B **3**, 1175 (1986).

[2] C. Bracikowski, and R. Roy, Chaos **1**, 49 (1991).

[3] R. Roy, C. Bracikowski, and G.E. James, in *Proceedings of the International Conference on Int. Conf. Quantum Optics*, edited by R. Inguva and G. S. Agarwal (Plenum Press, New York, 1992).

[4] R. Roy, T. W. Murphy, Jr., T. D. Maier, Z. Gills, and E. R. Hunt, Phys. Rev. Lett. **68**, 1259 (1992).

[5] Z. Gills, C. Iwata, R. Roy, I. B. Schwartz, and I. Triandaf, Phys. Rev. Lett. **69**, 3169 (1992).

[6] P. Colet, R. Roy, and K. Wiesenfeld, Phys. Rev. E **50**, 3453 (1994).

[7] T. W. Carr and I. B. Schwartz, Phys. Rev. E **51**, 5109 (1995).

[8] H. D. I. Abarbanel, Z. Gills, C. Liu, and R. Roy, Phys. Rev. A **53**, 440 (1996).

[9] H. D. I. Abarbanel, R. Brown, J. J. Sidorowich, and Lev Sh. Tsimring, Rev. Mod. Phys. **65**, 1331 (1993).

[10] H. D. I. Abarbanel, *Analysis of Observed Chaotic Data* (Springer, New York, 1996).

[11] R. Mañé, in *Dynamical Systems and Turbulence, Warwick 1980*, edited by D. Rand and L. S. Young, Lecture Notes in Mathematics Vol. 898 (Springer, Berlin, 1981), p. 230.

[12] F. Takens, in *Dynamical Systems and Turbulence, Warwick 1980*, edited by D. Rand and L. S. Young, Lecture Notes in Mathematics Vol. 898 (Springer, Berlin, 1981), p. 366.

[13] (a) A. M. Fraser and H. L. Swinney, Phys. Rev. A **33**, 1134 (1986); (b) A. M. Fraser, IEEE Trans. Inf. Theory **35**, 245 (1989).

[14] Matthew B. Kennel, R. Brown, and H. D. I. Abarbanel, Phys. Rev. A **45**, 3403 (1992).

[15] M. Sargent III, M. O. Scully, and W. E. Lamb, Jr., *Laser Physics* (Addison-Wesley, Reading, MA, 1974).

[16] A. Yariv, *Quantum Electronics*, 3rd ed. (Wiley, New York, 1989).

[17] P. D. Drummond, K. J. McNiel, and D. F. Walls, Opt. Acta **28**, 211 (1981).

[18] D. F. Walls and G. J. Milburn, *Quantum Optics* (Springer, Berlin, 1994).

Encoding and decoding messages with chaotic lasers

P. M. Alsing*
High Performance Computing Center, University of New Mexico, 1601 Central NE, Albuquerque, New Mexico 87131

A. Gavrielides† and V. Kovanis‡
Nonlinear Optics Center, Phillips Laboratory, 3550 Aberdeen Avenue SE, Kirtland Air Force Base, New Mexico 87117-5776

R. Roy and K. S. Thornburg, Jr.
School of Physics, Georgia Institute of Technology, Atlanta, Georgia 30332-0430
(Received 5 August 1996)

We investigate the structure of the strange attractor of a chaotic loss-modulated solid-state laser utilizing return maps based on a combination of intensity maxima and interspike intervals, as opposed to those utilizing Poincaré sections defined by the intensity maxima of the laser ($\dot{I}=0,\ddot{I}<0$) alone. We find both experimentally and numerically that a simple, intrinsic relationship exists between an intensity maximum and the pair of preceding and succeeding interspike intervals. In addition, we numerically investigate encoding messages on the output of a chaotic transmitter laser and its subsequent decoding by a similar receiver laser. By exploiting the relationship between the intensity maxima and the interspike intervals, we demonstrate that the method utilized to encode the message is vital to the system's ability to hide the signal from unwanted deciphering. In this work alternative methods are studied in order to encode messages by modulating the magnitude of pumping of the transmitter laser and also by driving its loss modulation with more than one frequency. [S1063-651X(97)01808-4]

PACS number(s): 05.40+j, 42.50.Lc

I. INTRODUCTION

There has been great interest in the use of chaotic signals as the carriers of analog and digital information over the last few years, initiated by the work of Pecora and Carroll [1], who suggested that synchronized chaotic systems could be employed to encode and decode messages in real time. Recent experiments have demonstrated that using chaos to communicate is practically feasible with electronic circuits [2,3]. The typical frequencies of the chaotic carrier wave forms in these circuits is of the order of 10 kHz, and even with the prospects of speeding up these circuits by several orders of magnitude, it is still of interest to consider communication with chaotic optical signals which have the potential for even higher information transmission and reception rates.

Two groups have experimentally demonstrated that chaotic lasers can be synchronized. Roy and Thornburg [4] showed that synchronization could be achieved in a pair of pump-modulated Nd:YAG (yttrium gallium garnet) lasers by altering the mutual evanescent coupling between the lasers. Sugawara *et al.* [5] demonstrated synchronization of two CO_2 lasers by injecting the output of a master laser into a receiver laser with a saturable absorber. Colet and Roy [6] have suggested a scheme involving the synchronization of a chaotic Nd:YAG carrier laser to a receiving laser, and the subsequent decoding of the hidden message in real time by subtraction of the receiver input from its output. The sharp pulses generated by loss modulation of the laser serve as a natural background for encoding and camouflaging digital information. The authors demonstrated the validity of their proposed scheme in numerical simulations. This idea has been extended to a model of synchronized chaotic semiconductor lasers by Mirasso *et al.*, who have included the effects of a fiber optic channel on the information processing [7].

In this paper we explore issues related to the communication scheme as proposed in [6]. In Sec. II the loss-modulated Nd:YAG laser model is introduced along with techniques for encoding and decoding of messages. Next, in Sec. III we present an analysis of numerical and experimental time series via return maps based upon interspike intervals. We find that a simple relationship exists between an intensity peak and interspike intervals that precede and follow the peak. The consequences of this relationship on the issue of deciphering the message encrypted in the chaotic carrier is explored in Sec. IV. Two schemes for encoding information are then introduced that make it more difficult to decipher the message. These consist of laser parameter modulation of the transmitter to encode the message and the use of quasiperiodic parameter modulation in both transmitter and receiver, so that the interspike interval return maps become ineffectual as deciphering tools, while the receiver's ability to decode the message is retained. The main results of the paper are summarized in Sec. V, and conclusions are drawn.

II. SCHEME FOR COMMUNICATING WITH SYNCHRONIZED CHAOTIC LASERS

The scheme proposed by Colet and Roy [6] for communicating signals via chaotic synchronized lasers is composed of a pair of loss-modulated Nd:YAG lasers operated in the chaotic regime. The hidden signal is decoded by subtraction

*Electronic address: alsing@arc.unm.edu
†Electronic address: toni@photon.plk.af.mil
‡Electronic address: kovanis@xaos.plk.af.mil

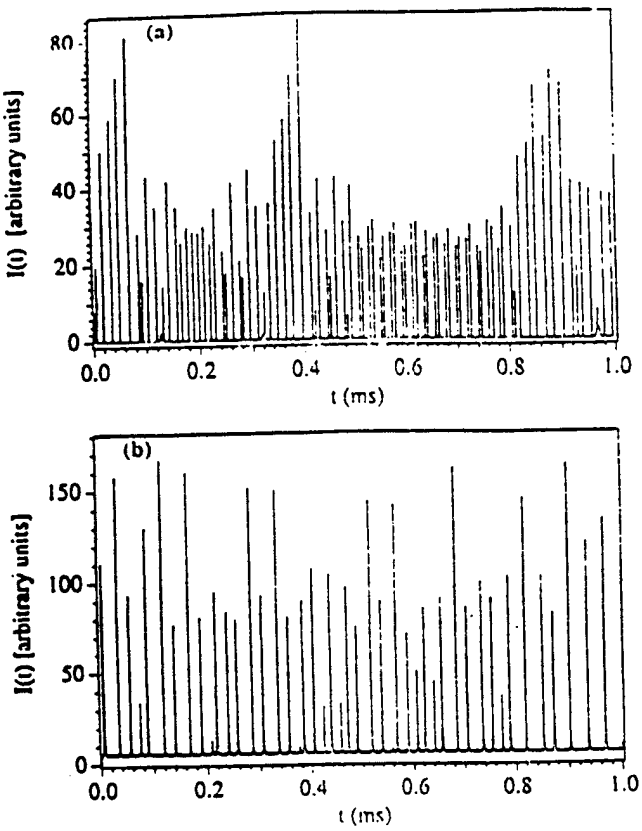

FIG. 1. (a) Numerical simulation of the loss-modulated Nd:YAG chaotic laser, Eqs. (2.1). $\alpha_{0T}=\alpha_{0R}=0.01$, $\alpha_1=2.0\times10^{-4}$, $\Omega=541.6$ ms^{-1}, $P_T=P_R=0.03$, $\epsilon_T=\epsilon_R=8.33\times10^{-9}$ s^{-1}, $\omega_R-\omega_T=50\,000$ rad/s and $\kappa=10^{-4}$; (b) Experimental data from a loss-modulated Nd:YAG chaotic laser operated one-third above threshold with parameters as in (a) except for $\tau_c=1/\gamma_c=0.45$ ns.

of the receiver and transmitter intensities.

The model for the transmitting laser is described by [6,9]

$$\frac{dE_T}{dt}=\gamma_c(G_T-\alpha_{0T}-\alpha_1\cos\Omega t)E_T+i\omega_T E_T+\sqrt{\epsilon_T}\eta_T, \tag{2.1a}$$

$$\frac{dG_T}{dt}=\gamma_f[P_T-G_T(1+|E_T|^2)], \tag{2.1b}$$

where E_T is the complex, slowly varying amplitude of the electric field, G_T is the gain of the active medium, $\tau_c=1/\gamma_c=450$ ps is the cavity round-trip time, $\tau_f=1/\gamma_f=240$ μs is the decay time of the upper lasing level, ω_T is the detuning of the laser frequency from the nearest empty cavity mode, P_T is the pump parameter, ϵ_T is the spontaneous emission noise strength, and η_T is a complex Gaussian white noise term of zero mean and correlation $\langle\eta_T(t)\,\eta_T^*(t')\rangle=2\,\delta(t-t')$. The loss modulation is given by $\alpha_T(t)=\alpha_{0T}+\alpha_1\cos(\Omega t)$ where $\alpha_1/\alpha_{0T}\ll1$. The modulation frequency Ω is chosen to be close to a submultiple of the relaxation frequency $\omega_r=\sqrt{2\gamma_c\gamma_f(P_T-\alpha_{0T})}$.

The output intensity of the chaotic laser is a series of irregularly spaced pulses having a spiky appearance, as evidenced in the numerical simulation of a loss-modulated solid-state laser in Fig. 1(a) and in similar experimental data such as Fig. 1(b), which are recorded at slightly different parameter values. Although the numerical simulation and the experimental data appear similar with respect to the irregularity of the intensity maxima, the temporal sequence of intensity maxima appears more regularly spaced in the experimental data than in the numerical simulation. We will return to this point, and to a more detailed description of the output intensity, in Sec. III.

The equations describing the receiving laser in which the encoded signal from the transmitter laser has been injected are given by

$$\frac{dE_R}{dt}=\gamma_c(G_R-\alpha_{0T}-\alpha_1\cos\Omega t)E_R+i\omega_R E_R+\sqrt{\epsilon_R}\eta_R-\kappa A_b\gamma_c\left(E_R-\frac{A_S}{A_b}E_T\right), \tag{2.2a}$$

$$\frac{dG_R}{dt}=\gamma_f[P_R-G_R(1+|E_R|^2)]. \tag{2.2b}$$

In the above equations all variables have the same meaning as for the transmitter. In addition, the modulated loss coefficient of the receiver, $\alpha_R(t)\equiv\alpha_{0R}+\alpha_1\cos(\Omega t)$ is operated at the condition for synchronization (i.e., $E_R=E_T$), $\alpha_{0R}=\alpha_{0T}+\kappa$. The quantity $\kappa\ll\alpha_{0T}$ is the coupling coefficient between the transmitting and receiving laser which also accounts for any losses in the transmission process [9].

The transmission coefficients A in Eqs. (2.2) describe the encoding of the signal on the external output of the transmitting laser. The output intensity of the transmitting laser is slightly attenuated by an external filter by a fixed bias factor A_b, so that the intensity at the receiver is given by $E_T'=\kappa A_b E_T$. This implies that synchronization is achieved when no signal is encoded at a setting of $\alpha_{0R}=\alpha_{0T}+\kappa A_b$. To encode a "1" bit, the transmission is increased a few percent to $A_S>A_b$, while to send a "-1" bit the transmission is decreased a few percent to $A_S<A_b$. Thus the message is encoded as small amplitude modulations of the spiky, high intensity output of the transmitting laser. To avoid encoding signals on the low intensity pulses, the pulses are monitored before attenuation and only those pulses whose intensity exceeds some predetermined, fixed threshold intensity are used for encoding.

In Eq. (2.2a) the signal difference term can be written as

$$-\kappa A_b\gamma_c\left(E_R-\frac{A_S}{A_b}E_T\right)=-\kappa A_b\gamma_c(E_R-E_T)+\kappa\gamma_c(A_S-A_b)E_T. \tag{2.3}$$

The first term $-\kappa A_b\gamma_c(E_R-E_T)$ is responsible for the synchronization of the transmitter laser to the receiver laser. For values of κ above some threshold, the damping is sufficient to drive the signal difference to zero, thereby synchronizing the receiver to the chaotic transmitter carrier wave. If $\kappa\gamma_c(A_S-A_b)E_T$ is small, the transmitter carrier wave plus signal is then entrained by the receiver laser. The signal can be deciphered precisely because it is a small perturbation of the carrier signal. As long as the κ is above some threshold value (which usually needs to be found empirically, see Fig.

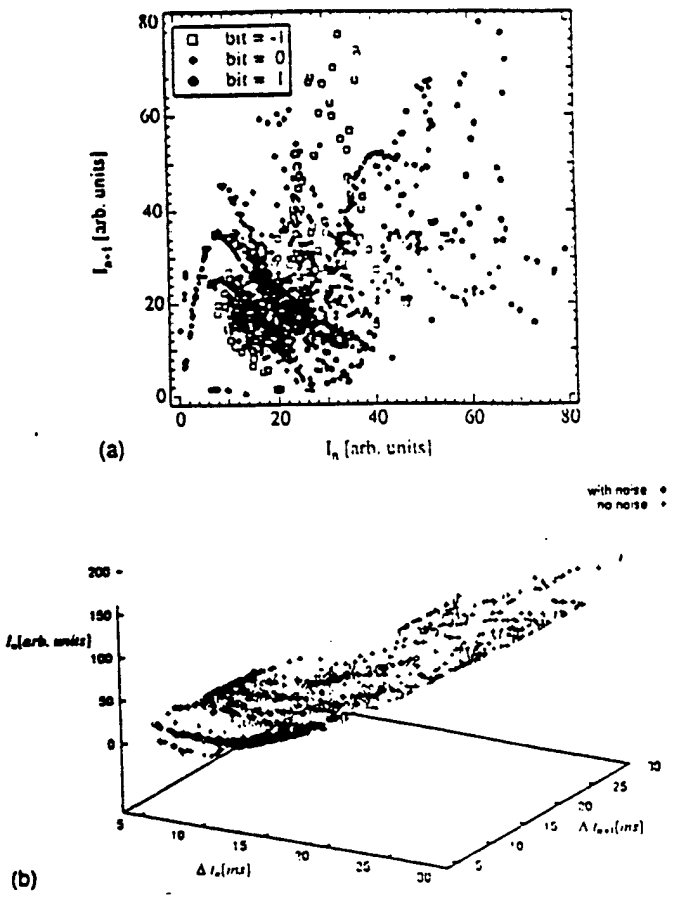

FIG. 2. (a) Plot of intensity maxima return map $I_T(n+1)$ vs $I_T(n)$ with data from Fig. 1(a); (b) same data plotted as intensity maxima $I_T(n)$ vs the interspike intervals $\Delta t_T(n+1)=t_T(n+1)-t_T(n)$ and $\Delta t_T(n)=t_T(n)-t_T(n-1)$.

2 in [6]) and the signal amplitude is small relative to the carrier wave, the carrier wave plus the encoded signal remains entrained by the output of the receiving laser.

The encoded signal can then be extracted as the integrated intensity difference M [6],

$$M=\int_{\text{pulse}}(|A_S E_T|^2-|A_b E_R|^2)dt. \tag{2.4}$$

The quantity M will equal zero when no signal is sent, $A_S=A_b$, and will have a strong positive (negative) value when a "1" ("−1") bit, $A_S>A_b$ ($A_S<A_b$), is being sent. Figure 2(a) shows a first return map of the numerically generated receiver intensity $I_R(n+1)$ vs $I_R(n)$, evaluated at the intensity maxima, when a signal has been encoded on the transmitter. The carrier wave maxima, and the "1" and "−1" bit are depicted by the diamonds, pluses, and squares, respectively. One sees that the encoded signal is seemingly inextricably mixed with the carrier wave. Higher dimensional intensity peak return maps, $I(n+1)$ versus $\{I(n),I(n-1),I(n-2),\ldots\}$, offer no additional help towards unraveling the signal from the carrier [8].

III. ANALYSIS VIA INTERSPIKE INTERVALS

A useful representation of the data occurs when one considers return maps based not solely on intensity maxima; but rather on a combination of the intensity maxima with the time intervals between intensity maxima, which we call the *interspike intervals* (ISI). In a recent paper, Sauer [10] proposed the use of interspike intervals as a means for attractor reconstruction from time series, in analogy with Takens' theorem [11]. In this work we use the interspike intervals to find a useful relationship between the ISI and the intensity maxima of a chaotic loss-modulated solid-state laser.

Figure 2(b) is a plot of numerically generated transmitter laser intensity maxima $I_T(n)$ of Fig. 1(a) occuring at time $t(n)$ versus the pair of interspike intervals $\Delta t_T(n+1)$ and $\Delta t_T(n)$, where $\Delta t_T(n+1)=t_T(n+1)-t_T(n)$. Here $\Delta t_T(n+1)$ is the time between the nth intensity maxima $I_T(n)$ at time $t_T(n)$ and the occurrence of the next intensity maxima at time $t_T(n+1)$. Similarly, $\Delta t_T(n)$ is the time between the nth intensity maxima $I_T(n)$ at time $t_T(n)$ and the previous intensity maxima at time $t_T(n-1)$. A reconstruction of the attractor solely using interspike intervals, i.e., $\Delta t_T(n+1)$ versus $\Delta t_T(n)$ and $\Delta t_T(n-1)$ reveals no added information over a reconstruction solely using intensity maxima, $I(n+1)$ versus $I(n)$ and $I(n-1)$. It is the combination of intensity maxima and interspike intervals as shown in Fig. 2(b) which uncovers structure, and a relationship between physical quantities.

Figure 2(b) shows results of the numerical simulation with noise ("+") and without the inclusion of noise (diamonds). The level of noise was chosen to be typical of that experienced in laboratory experiments (see Fig. 1 in [6]). Both the noise-free and noisy maxima fall on a nearly two-dimensional surface that is essentially planar. Figure 3(a) shows the intensity maxima of the noise-free simulation, while Fig. 3(b) shows the same plot from an edge-on view, that is $I_T(n)$ versus

$$\begin{aligned}\cos(\theta)&\quad(n+1)+\sin(\theta)\Delta t_T(n)\\ &=[\Delta t_T(n+1)+\Delta t_T(n)]/\sqrt{2}\\ &=[t_T(n+1)-t_T(n-1)]/\sqrt{2}.\end{aligned}$$

where the angle $\theta=\pi/4$ gave the optimal view. Here we clearly see an almost one dimensional structure of the return map. Figure 3(c) shows the noisy simulation with the similar, nearly one-dimensional structure in the return map, viewed edge on in Fig. 3(d). Note that the intensity maxima of the noisy simulation Fig. 3(c), fall on the same nearly two-dimensional surface of Fig. 3(a), but in that portion of the surface corresponding to lower intensity maxima. We return to this point shortly.

Figure 3(e) is an edge-on plot of the experimental data (diamonds) of Fig. 1(b). Because the experimental data was taken at parameter values slightly different from that of the numerical simulation, the temporal variation of the interspike intervals in Fig. 1(b) is on a finer scale. In fact, the data in Fig. 3(e) corresponds to the upper right-hand, high intensity maxima corner of the data of the numerical simulation, Fig. 3(c). However, even for this more uniform variation of the interspike intervals, a plot of the intensity maxima-ISI return map reveals structure and a relationship between physical variables. The experimental data is again essentially planar as evidenced by a global least squares fit of the experimental intensity maxima to the experimentally derived interspike

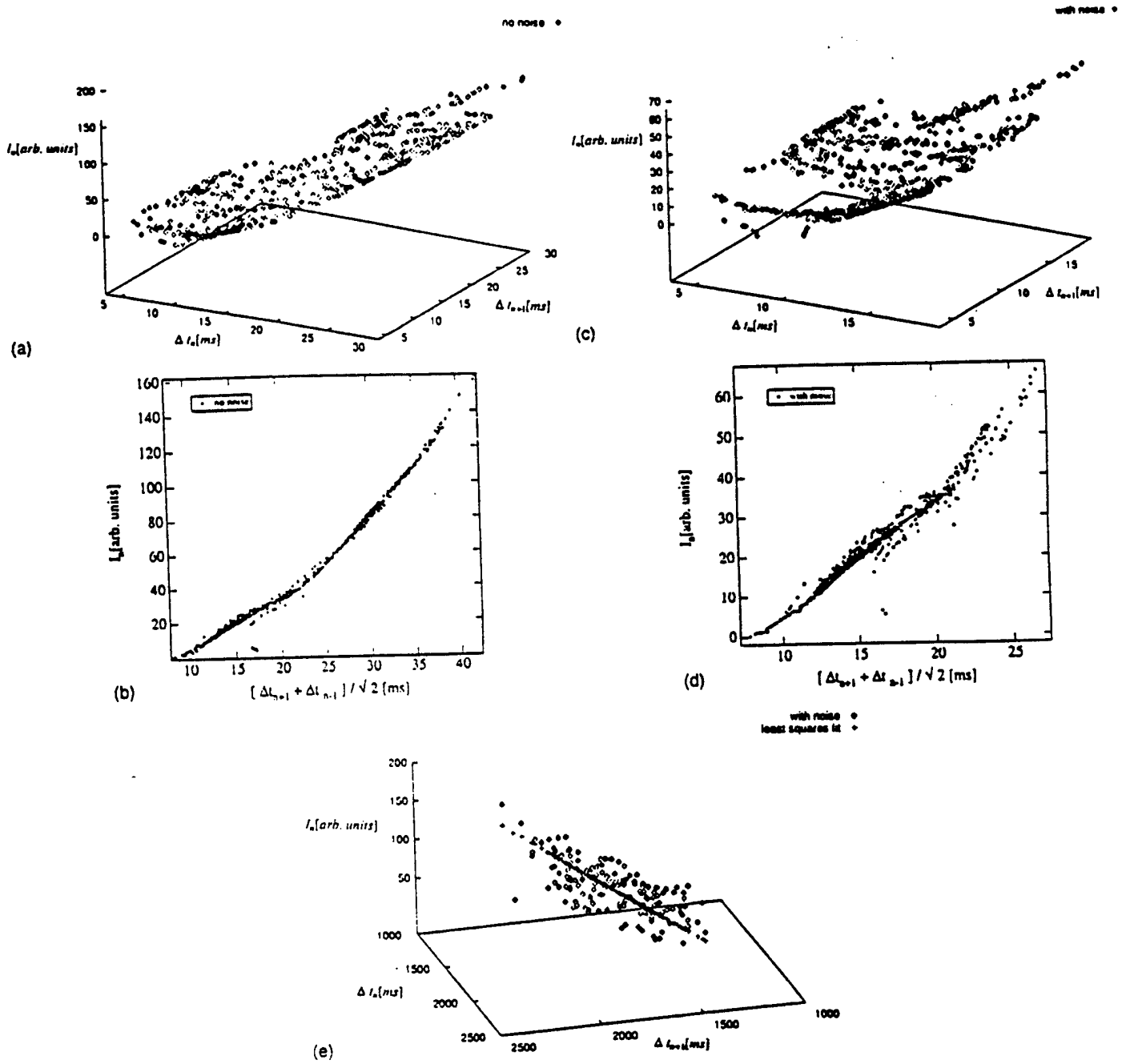

FIG. 3. Intensity-interspike intervals return maps of the transmitter laser: (a) $I_T(n)$ vs $\Delta t_T(n+1)=t_T(n+1)-t_T(n)$ and $\Delta t_T(n)=t_T(n)-t_T(n-1)$ corresponding to Fig. 1(a); (b) edge-on view of (a); (c) part (a), with noise, $\epsilon_T=\epsilon_R=8.33\times10^{-9}$ s^{-1}; (d) edge-on view of part (c); (e) edge-on view of experimental data (diamonds), Fig. 1(b), with global least square fit ("+") of intensity maxima $I_T(n)$ to $\Delta t_T(n+1)$ and $\Delta t_T(n)$. Note that this data corresponds to the upper right-hand corner (15–20 μs) of (c).

intervals $\Delta t_T(n+1)$ and $\Delta t_T(n)$. The plane of this least square fit of intensity maxima to ISI is shown in an edge-on view as the overlaid heavy straight line ("+") in the center of Fig. 3(e). One should note that it is not important in plotting these return maps to utilize the precise maxima of the intensity, which may be hard to resolve in an actual experiment. Any convenient threshold value on the intensity spike could be used to replace $I_T(n)$, and $\Delta t_T(n)$ would then be measured as the time between successive crossings of this threshold.

If one were to plot a three-dimensional return map of the interspike intervals alone, i.e., $\Delta t_T(n+1)$ vs $\Delta t_T(n)$ and $\Delta t_T(n-1)$, the result would be an unfolding of the attractor, topologically equivalent to an unfolding utilizing only the intensity maxima, $I(n+1)$ vs $I(n)$ and $I(n-1)$. The significance of the nearly planar (linear) structure of the intensity-ISI return maps in Fig. 3(a) [Figs. 3(b) and 3(e)] is that it implies that there exists a nearly linear relationship between the intensity maxima $I_T(n)$ and the interspike intervals $\Delta t_T(n+1)$ and $\Delta t_T(n)$.

Schwartz and Erneux [12] explored this loss-modulated laser system and found explicit representations for the Poincaré mapping between the (dimensionless) gain and the ISI applicable to the period 1 and 2 orbits. Though it is not the goal of this paper, Figs. 3 suggest that such a map might be found also in the chaotic regime. They analyzed the periodi-

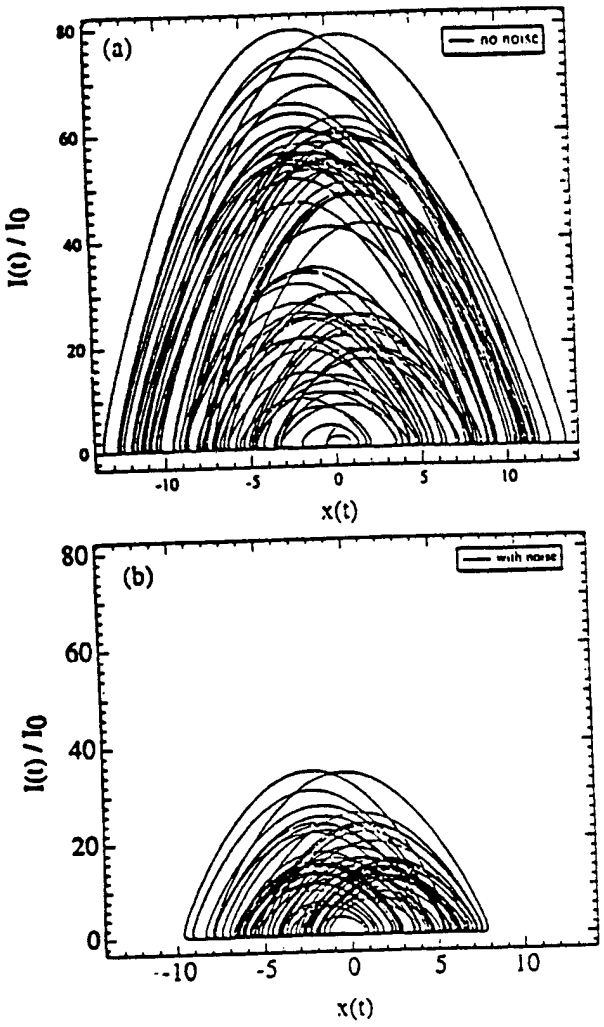

FIG. 4. Plot of scaled transmitter intensity $y(t) = [I_T(t) - I_{ss}]/I_{ss}$ vs the normalized gain $x(t)$ from Eq. (2.1): (a) no noise, (b) with noise. [I_{ss} is the steady-state intensity of the conservative system, which to lowest order approximates the system of equations in Eq. (2.1)]. The large intensity maxima occur when the previous intensity minima reach very low values.

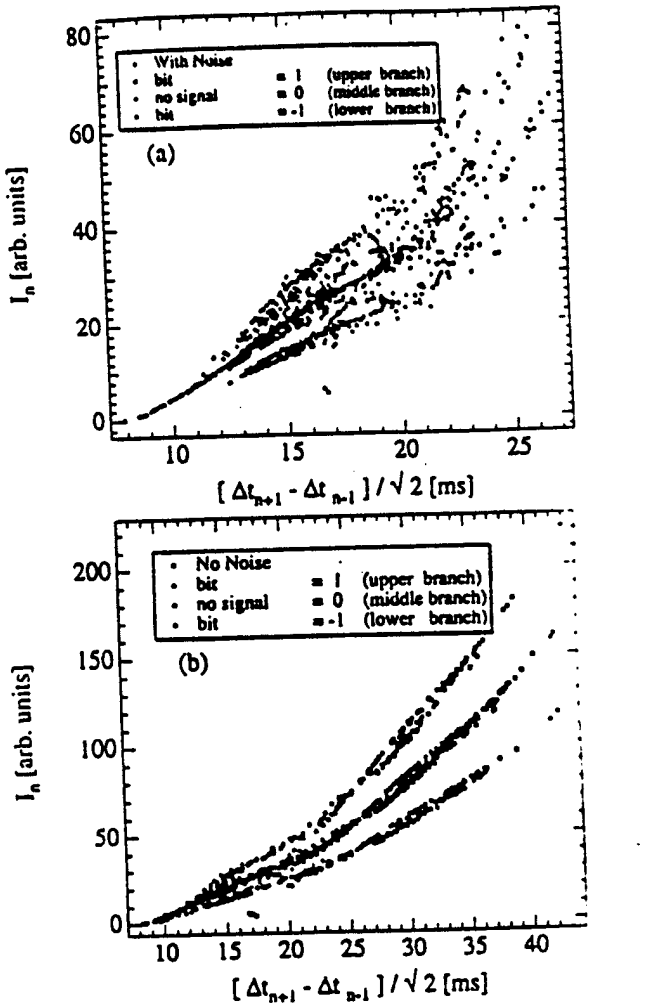

FIG. 5. Decoding of the signal hidden in the chaotic carrier of the transmitter laser by the return map of $I_T(n)$ vs $[t_T(n+1) - t_T(n-1)]/\sqrt{2}$. The transmitter laser has been modulated with $A_S = 1.0 \pm 0.15A_b$, with $A_b = 0.85$: Upper branch → "1" bit, middle branch → no signal, lower branch → "−1" bit. (a) no noise, (b) with noise.

cally driven laser system as a conservative system (to lowest order of approximation) plus small nonlinear terms. When dissipation is neglected, periodic orbits in the plane of the (dimensionless) gain x and intensity relative to the steady-state value of the conservative system $y = (I - I_{ss})/I_{ss}$, are rounded triangular closed orbits with a flat base parallel to the x axis at a value of $y \sim -1$ corresponding to zero intensity (see Fig. 4 and Fig. 5 in [12]). High intensity maxima correspond to the previous intensity minima reaching very low values, Fig. 4(a) where we plot the dimensionless intensity and gain $I_T(t)$ vs $G_T(t)$ from Eq. (2.1) as $y(t)$ vs $x(t)$. In the chaotic regime, the lowest order approximation of the laser system is still a conservative system, and this relationship between the height of the intensity maxima and period (and therefore ISI) is retained. With the inclusion of noise, Fig. 4(b), a minimum base line intensity is maintained, which correspondingly limits the maximum height of the intensity peaks. We see this in Fig. 3(a) where the noisy intensity maxima are restricted to the portion of the two-dimensional surface corresponding to smaller intensity peak heights and therefore, small values of the ISI.

IV. CONSEQUENCES FOR CHAOTIC COMMUNICATION

The regular structure of the intensity versus ISI return maps has important implications for communicating signals via a chaotic transmitter laser. As proposed by Colet and Roy [6], the transmitter laser encodes the signal by an amplitude modulation external to the laser. Since the transmitter is not intrinsically perturbed, Figs. 3 suggests that the intensity maxima-ISI return maps applied to the transmitter signal alone could be used to decode the signal. Figure 5(a) is a plot of the simulated transmitter intensity output maxima $I_T(n)$ vs the ISI combination $[t_T(n+1) - t_T(n-1)]/\sqrt{2}$, when the laser has been modulated with $A_S = 1.0 \pm 0.15A_b$ with $A_b = 0.85$, without the inclusion of noise. Signals were encoded only on intensity maxima with values approximately greater than 10. The middle branch is the no-signal maxima $A_S = A_b$, while the upper branch corresponds to a "1" bit $A_S = 1.15A_b$, and the lower branch corresponds to a "−1" bit $A_S = 0.85A_b$. Figure 5(b) is the corresponding simulation when noise has been included using a value of $\epsilon_T = \epsilon_R = 8.33 \times 10^{-9}$ s^{-1}, typical of actual experiments [6,9]. Even though the noise smears the branches out some-

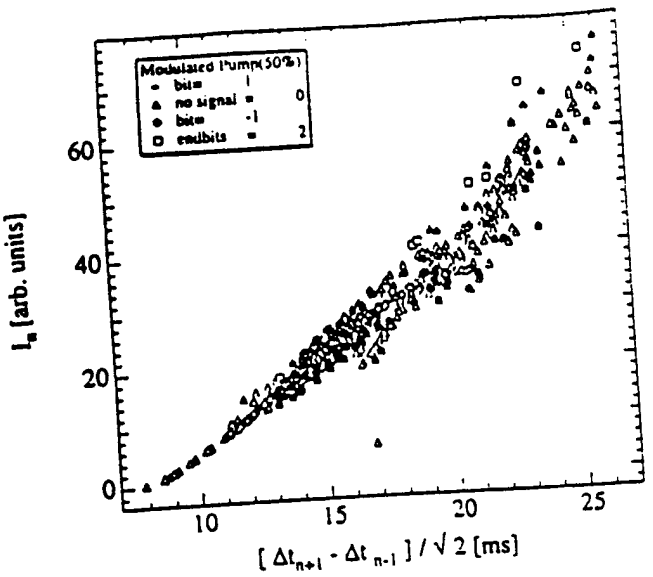

FIG. 6. The return map of the transmitter laser, $I_T(n)$ vs $[I_T(n+1)-I_T(n-1)]/\sqrt{2}$, when the transmitter laser pump has been modulated with $P_S = 1.0 \pm 0.50 P_T$, (no noise). Compared with Fig. 5(a), the signal branches corresponding to the encoded bits $\{1,-1\}$ have been merged with the no-signal branch.

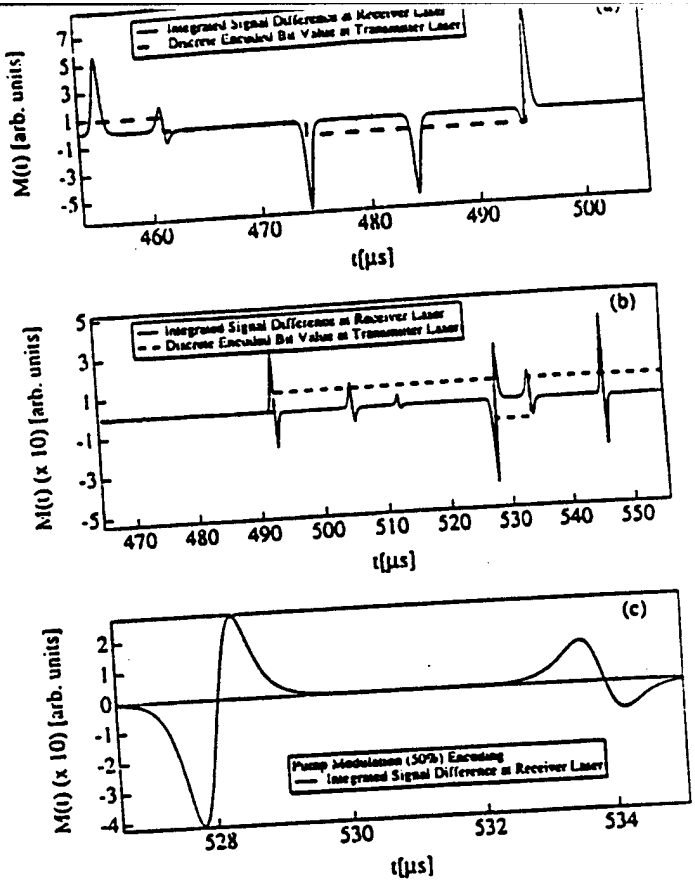

FIG. 7. The integrated signal difference $M(t) = |E_T'|^2 - |A_b E_R|^2$ vs time for the receiver laser: (a) external modulation of peak intensity, (b) pump modulation by 50%. The broken line is the discrete bit values encoded on the transmitter laser. For the pump modulation scheme (b), the signal is encoded in the difference between the positive and negative maxima of the integrated signal difference across the intensity maxima. (c) magnification of the region $525 < t < 535$ of part (b) showing the decoding of a "-1" bit (left) and "1" bit (right).

what, they are still clearly distinguishable. Plots at 5% encoding modulation for $A_b = 0.9$ show similar behavior of clearly distinguishable signal branches.

The signals embedded in the chaotic output of the transmitting laser were decipherable because of the inherent relationship between intensity maxima and interspike intervals exhibited in the intensity-ISI return maps. This encoding scheme, in which the transmitter laser intensity was modulated outside of the laser cavity, did not dynamically alter the relationship between intensity maxima and interspike intervals. Therefore, to encode and hide signals on the chaotic transmitter carrier we suggest that it would be more advantageous to have the encoding method fundamentally perturb the ISI. This can be achieved by modulating the transmitter pump across an intensity peak. The actual beginning and ending of the modulation could occur in the intensity troughs, as long as the pump change persists over the intensity peak. In Figure 6 we have simulated the intensity output of the transmitting laser when its pump has been modulated with $P_S = 1.0 \pm 0.50 P_T(t)$ and without the inclusion of noise. The resulting edge-on view of intensity-ISI return map for the transmitter shows that the attractor surfaces have been essentially merged together onto the no-signal surface. Even if we were to look at the logarithmic signal differences, our success rate of distinguishing a "± 1" bit from no-signal via the transmitter return maps is greatly diminished due to the severe overlapping of the surfaces. For smaller modulations or with the inclusion of noise, things only become more difficult. However, the signal *can* be decoded when the transmitting laser output is synchronized to the receiver and the integrated signal difference of Eq. (2.4) is utilized.

We point out an interesting feature of this encoding scheme that differs from the original encoding scheme in which the laser intensity is externally modulated. Figure 7(a) shows the decoded message bits (solid line) when the external intensity is used to encode the signal. The dashed line in this figure is the value of the discrete bits "± 1," encoded on the transmitter laser. Although it is drawn as a continuous line, the value of the encoded bit only has meaning across the intensity peak. In these figures we plot $M(t) \equiv |E_T'|^2 - |A_b E_R|^2$ vs t, where $|E_T'|^2$ is the intensity of the modulated transmitter laser at the receiver laser. Positive values of $M(t)$ can be associated with a transmitted "1" bit and negative values of $M(t)$ can be associated with a "-1" bit. Figure 7(b) shows a decoded message bit when the pump is modulated by $\pm 50\%$ to encode the signal. The signal is again decoded by the integrated signal difference $M(t)$ and the dashed line in this figure is the value of the discrete bits "± 1" encoded on the transmitter laser. The first two "blips" ($t < 490$) in Fig. 7(b) represent no signal encoded. The encoding of signals consisting of random values of "± 1" beginning at $t > 490$. Note that $M(t)$ in Fig. 7(b) is neither all positive nor all negative as is essentially the case when the signal is encoded by modulating $|E_T|^2$ outside the laser, such as in Fig. 7(a). Figure 7(c) shows a magnified view of the region $525 < t < 535$ of Fig. 7(b) where a "-1" (left pulse) and "1" bit were decoded from the signal. For the "1" bit the positive area is slightly larger than the negative area leading to an overall positive integrated area, while

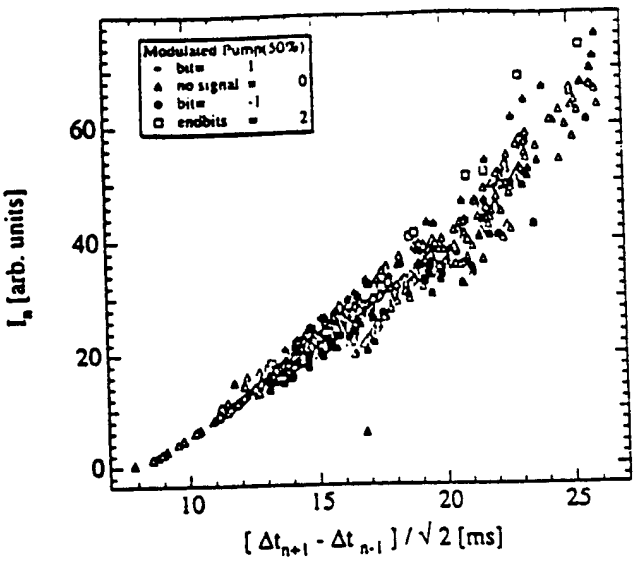

FIG. 6. The return map of the transmitter laser, $I_T(n)$ vs $[I_T(n+1)-I_T(n-1)]/\sqrt{2}$, when the transmitter laser pump has been modulated with $P_S=1.0\pm0.50P_T$. (no noise). Compared with Fig. 5(a), the signal branches corresponding to the encoded bits $\{1,-1\}$ have been merged with the no-signal branch.

what, they are still clearly distinguishable. Plots at 5% encoding modulation for $A_b=0.9$ show similar behavior of clearly distinguishable signal branches.

The signals embedded in the chaotic output of the transmitting laser were decipherable because of the inherent relationship between intensity maxima and interspike intervals exhibited in the intensity-ISI return maps. This encoding scheme, in which the transmitter laser intensity was modulated outside of the laser cavity, did not dynamically alter the relationship between intensity maxima and interspike intervals. Therefore, to encode and hide signals on the chaotic transmitter carrier we suggest that it would be more advantageous to have the encoding method fundamentally perturb the ISI. This can be achieved by modulating the transmitter pump across an intensity peak. The actual beginning and ending of the modulation could occur in the intensity troughs, as long as the pump change persists over the intensity peak. In Figure 6 we have simulated the intensity output of the transmitting laser when its pump has been modulated with $P_S=1.0\pm0.50P_T(t)$ and without the inclusion of noise. The resulting edge-on view of intensity-ISI return map for the transmitter shows that the attractor surfaces have been essentially merged together onto the no signal surface. Even if we were to look at the logarithmic signal differences, our success rate of distinguishing a "±1" bit from no-signal via the transmitter return maps is greatly diminished due to the severe overlapping of the surfaces. For smaller modulations or with the inclusion of noise, things only become more difficult. However, the signal *can* be decoded when the transmitting laser output is synchronized to the receiver and the integrated signal difference of Eq. (2.4) is utilized.

We point out an interesting feature of this encoding scheme that differs from the original encoding scheme in which the laser intensity is externally modulated. Figure 7(a) shows the decoded message bits (solid line) when the external intensity is used to encode the signal. The dashed line in this figure is the value of the discrete bits "±1," encoded on

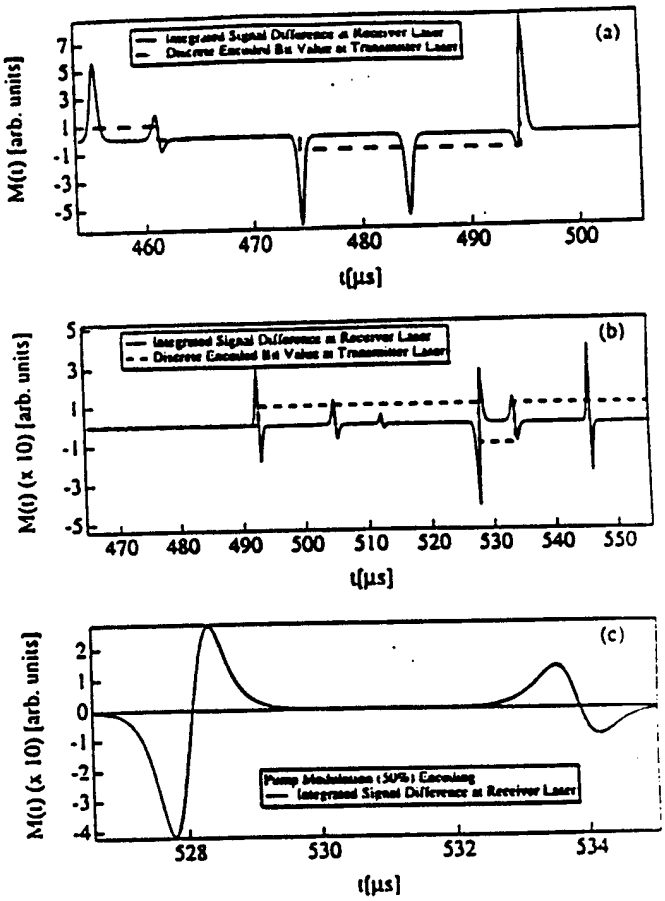

FIG. 7. The integrated signal difference $M(t)=|E_T'|^2-|A_bE_R|^2$ vs time for the receiver laser: (a) external modulation of peak intensity, (b) pump modulation by 50%. The broken line is the discrete bit values encoded on the transmitter laser. For the pump modulation scheme (b), the signal is encoded in the difference between the positive and negative maxima of the integrated signal difference across the intensity maxima. (c) magnification of the region $525<t<535$ of part (b) showing the decoding of a "-1" bit (left) and "1" bit (right).

the transmitter laser. Although it is drawn as a continuous line, the value of the encoded bit only has meaning across the intensity peak. In these figures we plot $M(t)=|E_T'|^2-|A_bE_R|^2$ vs t, where $|E_T'|^2$ is the intensity of the modulated transmitter laser at the receiver laser. Positive values of $M(t)$ can be associated with a transmitted "1" bit and negative values of $M(t)$ can be associated with a "-1" bit. Figure 7(b) shows a decoded message bit when the pump is modulated by $\pm50\%$ to encode the signal. The signal is again decoded by the integrated signal difference $M(t)$ and the dashed line in this figure is the value of the discrete bits "±1" encoded on the transmitter laser. The first two "blips" ($t<490$) in Fig. 7(b) represent no signal encoded. The encoding of signals consisting of random values of "±1" beginning at $t>490$. Note that $M(t)$ in Fig. 7(b) is neither all positive nor all negative as is essentially the case when the signal is encoded by modulating $|E_T|^2$ outside the laser, such as in Fig. 7(a). Figure 7(c) shows a magnified view of the region $525<t<535$ of Fig. 7(b) where a "-1" (left pulse) and "1" bit were decoded from the signal. For the "1" bit the positive area is slightly larger than the negative area leading to an overall positive integrated area, while

the reverse is true for the "−1" bit. Again, positive values of $M(t)$ can be associated with a "1" bit encoded on the transmitter laser and negative values of $M(t)$ can be associated with a "−1" bit. Net magnitudes of $M(t)$ clustered around zero can be interpreted as no signal sent. For the case of encoding the signal by pump modulation, the receiver is synchronized to the modulated transmitter laser in all regions outside of the area of the receiver intensity peak. Under the peak the transmitter and receiver intensities are slightly out of synchronization, yet still mutually entrained, with the receiver lagging the transmitter, leading to the double humped decoded signals in Figs. 7(b) and 7(c).

We note that when this pump modulation scheme is used to encode the signal onto the transmitting laser, an intensity return map $I_T(n+1)$ vs $I_T(n)$, is again useless in deciphering the hidden signal, having an appearance similar to that of Fig. 2(a). In addition, we also explored signal encoding with pump modulations of 10% and 90%. For both these modulation values, the intensity vs ISI return maps are similar in structure to Fig. 6, i.e., the encoded bit surfaces nearly coincide with the no-signal surface and they are all intertwined. The signals again could be decoded by an integrated signal difference at the receiver. However, for weak modulations values (e.g., 10%) decoded bit values could occasionally be misinterpreted because the difference between the positive and negative areas in Fig. 7(b) was small enough that a signal could be interpreted as a nonsignal.

On the other hand, for stronger modulation values (e.g., 90%) the decoding would occasionally fail, and decoded bits would be interpreted incorrectly. These instances would occur when perturbations to the transmitter carrier were enough to make it sufficiently dissimilar to the receiver that entrainment was momentarily lost for that signal pulse. As dicussed in Sec. II, the first term of Eq. (2.3) $-\kappa A_b \gamma_c (E_R - E_T)$ is responsible for the synchronization of the transmitter laser to the receiver laser. If the second term $\kappa\gamma_c(A_S - A_b)E_T$ is small with respect to the first term, the transmitter carrier wave plus signal can still be entrained by the receiver laser. However, for large pulse modulations this second term may, on occasion, not be small, and across this spiky peak entrainment is lost. In general, it appeared that intermediate values of the modulation (around 50%) produced the best results for reliably decoding the message at the receiver.

In a final numerical experiment, we explored the consequences of quasiperiodically modulating the loss coefficient of both the transmitter and receiver laser. The form of the modulation was modified to

$$\alpha(t) = \alpha_0 + \alpha_1[\cos(\Omega t) + a_2\cos(f_2\Omega t) + a_3\cos(f_3\Omega t)], \tag{4.1}$$

where the amplitudes $\{a_2, a_3\}$ and frequencies multipliers $\{f_2, f_3\}$ are fixed, but arbitrarily chosen constants. Again the receiver was operated at conditions for optimal synchronization $\alpha_{0R} = \alpha_{0T} + \kappa A_b$, and noise (typical for these lasers) was included in the calculations.

When a single additional frequency was used, ($a_2 \neq 0, a_3 = 0$ and $f_2 \neq 0, f_3 = 0$), the branches of the two-dimensional intensity-ISI return maps [as in Fig. 5(b)] *thickened and merged* as the amplitude a_2 approached unity. This thickening and merging effect was pronounced when two

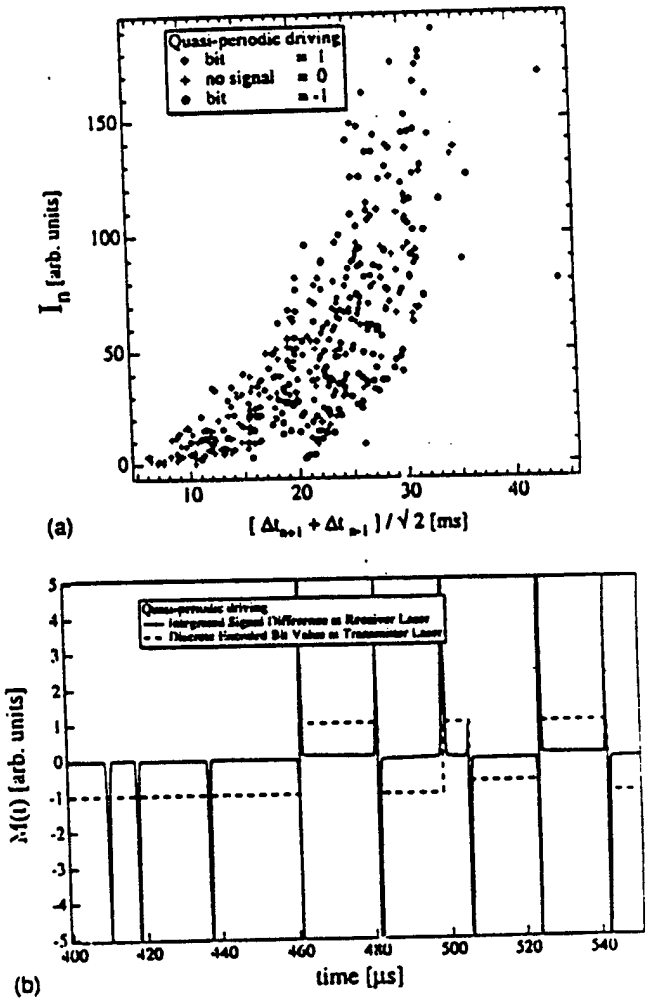

FIG. 8. Quasiperiodic driving of the loss coefficient of both the transmitter and receiver lasers: (a) intensity maxima vs ISI of the transmitter laser, (b) $M(t) = |E_T'|^2 - |A_b E_R|^2$ vs time for the receiver laser. The broken line is the discrete value of the decoded bit. By adding more driving frequencies (a), the signal branches of Fig. 5(b) are thickened and intermixed. However, the integrated signal difference at the receiver laser Fig. 8(b) can still decipher the hidden message.

additional frequencies were utilized. Figure 8(a) shows the intensity vs ISI return map for the transmitter laser for the case $a_2 = a_3 = 1$, with a choice of incommensurate relative frequencies $f_2 = \sqrt{2}$ and $f_3 = (\sqrt{5} - 1)/2$. Quasiperiodic driving led to an increase in the dimensionality of the attractor, exhibited by the thickening and merging of the intensity vs ISI map in Fig. 8(a). This renders the intensity vs ISI map ineffectual for deciphering the hidden message from the transmitter laser alone. The effect was qualitatively the same when additional commensurate frequencies were added to the driving. However, when utilizing commensurate frequencies, the remnants of the separate attractor surfaces for the encoded bits [as in Fig. 5(b)] could be inferred, if barely. However, the surfaces were thickened and merged enough, as in Fig. 8(a), to render the intensity vs ISI map ineffectual as a deciphering tool.

With no signal encoded, the transmitter synchronized effortlessly to the receiver laser. When the signal was encoded by amplitude modulation external to the transmitter laser (as in [6]), the signal could be decoded at the receiver laser by

means of an integrated signal difference, as evidenced in Fig. 8(b). Occasionally there were misinterpretations of the decoded bits for reasons similar to those discussed above for the case of encoding with pump modulations. We purposely increased the dimension of the attractor by adding more driving frequencies of arbitrary amplitude. Therefore, when a signal is impressed upon the transmitter carrier wave, it is occasionally different enough from the receiver signal so that the second term on the right-hand side of Eq. (4.1) perturbs the system enough so that entrainment is lost for this signal peak. The details of the modification of the local Lyapunov spectrum in the presence of multiple driving frequencies was not investigated, but would make for an interesting topic of exploration.

V. SUMMARY AND CONCLUSIONS

We have investigated the chaotic loss-modulated Nd:YAG laser and have found, both numerically and experimentally, that a return map utilizing intensity maxima and interspike intervals (ISI) reveals a regular, almost planar structure. This observation indicates that a simple relationship exists between the intensity maxima and the interspike intervals centered about that maxima, i.e., $I_T(n)=F[\Delta t_T(n+1),\Delta t_T(n)]$. In fact, by plotting the nth intensity maxima $I(n)$ versus the difference between the succeeding and preceding interspike intervals, i.e., $[\Delta t_T(n+1)-\Delta t_T(n)]/\sqrt{2} = [t(n+1)-t(n-1)]/\sqrt{2}$, we observe a nearly one-dimensional, one to one relationship between these variables, even in the presence of noise. This relationship was observed in numerical simulations as well as in experimental data taken at slightly different parameter values, leading to a variation of the interspike intervals on a much finer scale. However, even in this latter case, a plot of the intensity maxima-ISI return map reveals an almost planar structure and therefore a relationship between physical variables. Such a result would be useful, for example, in time series prediction of the future intensity maxima. In constructing the intensity-ISI return map it was not essential that the peak of the intensity be utilized. The ISI could have been defined relative to some arbitrary threshold value under the region of the peak and the return map then reconstructed.

The relationship between the the intensity maxima of the laser and the interspike intervals has consequences for the use of a transmitter-receiver pair of chaotic loss-modulated Nd:YAG lasers as a system to transmit encoded messages privately. By plotting the intensity-ISI return map of the transmitter laser alone, the message of "$\pm$ 1" bits, encoded by means of external cavity modulation, appears on surfaces above and below the no-signal surface. Even in the presence of moderate noise, the message can be deciphered.

As an alternative encoding scheme, we suggest encoding the signal by modulating the pump across the intensity maxima. This intrinsically perturbs the ISI of the transmitter laser, as opposed to the above externally modulated encoding scheme. The subsequent attempt to decode the embedded message by means of intensity-ISI return maps of the transmitter laser alone is unsuccessful because the *signal* attractor surfaces are merged onto the no-signal attractor surface. However, the message can still be decoded by means of driving the receiver laser with the output of the transmitter laser and extracting the message from an integrated intensity difference.

In addition, quasiperiodic driving of the loss coefficient of both the transmitter and receiver laser produced an increase in the dimensionality of the system. This led to a thickening of the intensity-ISI return maps with the merging of the individual surfaces corresponding to the $\{1,0,-1\}$ encoded bits. This rendered the intensity-ISI return maps ineffectual as means to decipher the signal from the transmitter laser alone. However, the signal could once again be extracted by means of an integrated signal difference at a receiver laser synchronized to the transmitter carrier wave.

Finally, the lessons learned in this study are twofold. First, an intensity-ISI or purely ISI return map can be a useful tool in the study of a pair of loss-modulated Nd:YAG lasers because of the implicit relationship between the intensity peak to the interspike intervals centered about that peak. Second, as applied to chaotic communications, the intensity-ISI return maps can be used to decipher the hidden message from the transmitter carrier wave alone. Care must be taken to intrinsically perturb the system or to increase the dimensionality of the system (though not high enough to void synchronization) so that the signal is safe from undesired deciphering by means of mapping techniques.

ACKNOWLEDGMENTS

The authors would like to thank the Maui High Performance Computer Center and the Albquerque Research Center for the use of their parallel computing facilities during this work. R.R. would like to acknowledge support from the Division of Chemical Sciences, Office of Basic Energy Sciences, Office of Energy Research; U.S. Department of Energy, and the Office of Naval Research.

[1] L. M. Pecora and T. L. Carroll, Phys. Rev. A 44, 2374 (1991); W. L. Ditto and L. M. Pecora, Sci. Am. (Int. Ed.) 269, 62 (1993); N. Gershenfeld and G. Grinstein, Phys. Rev. Lett. 74, 5024 (1995); E. Ott and M. Spano, Phys. Today 48, 34 (1995); L. Kocarez and U. Parlitz, Phys. Rev. Lett. 74, 5028 (1995); T. C. Newell, P. M. Alsing, A. Gavrielides, and V. Kovanis, Phys. Rev. E 51, 2963 (1995).

[2] K. M. Cuomo and A. V. Oppenheim, Phys. Rev. Lett. 71, 65 (1993).

[3] S. Hayes, C. Grebogi, E. Ott, and A. Mark, Phys. Rev. Lett. 73, 1781 (1994); S. Hayes, C. Grebogi, and E. Ott, *ibid.* 70, 3031 (1993).

[4] R. Roy and K. S. Thornburg Jr., Phys. Rev. Lett. 72, 2009 (1994).

[5] T. Sugawara *et al.*, Phys. Rev. Lett. 72, 3502 (1994).

[6] P. Colet and R. Roy, Opt. Lett. 19, 2056 (1994).

[7] C. R. Mirasso, *et al.*, IEEE Photonics Technol. Lett. 8, 299 (1996).

Dynamical Evolution of Multiple Four-Wave-Mixing Processes in an Optical Fiber

D. L. Hart, Arthur F. Judy, and Rajarshi Roy

School of Physics, Georgia Institute of Technology, Atlanta, GA 30332

and

James W. Beletic

European Southern Observatory, Karl-Sch-Str 2, D85748 Garching, Germany

Abstract

We present unique results of detailed experimental and theoretical investigations of the dynamical evolution of four wave mixing spectra in an optical fiber. The experimental measuremen*s probe the evolution of sidebands generated through four wave mixing as they co-propagate with the pumps along the fiber. We find that standard theoretical models are inadequate to predict the experimental results and that it is necessary to modify the approach to modeling the dynamics in two ways. The first modification is to include a pump laser input with multiple longitudinal modes. This reflects the fact that the pump laser fields may actually have internal structure that is not resolved by the spectrometer used and which is very small compared to the spacing of the central frequencies of the pump fields. Yet the evolution of the fields is dramatically altered for the sidebands generated by nonlinear processes in the fiber medium. The second is the inclusion of phase noise added along the propagation length; this causes damping of the sideband oscillations. These two modifications lead to excellent agreement of the measurements with numerical predictions of the sideband evolution.

I. Introduction

The study of wave propagation in a nonlinear dispersive medium, such as an optical fiber, is of interest in many areas of science and engineering. The past few decades have seen enormous growth in the use of optical fibers in communications systems. With this growth, engineers and researchers have been challenged with a wide range of physical phenomena associated with high intensity light waves propagating in optical fibers. Specifically, some of the interesting characteristics of silica glass, of which fibers are made, are low loss, dispersion, and especially nonlinearity. Since optical fibers have a relatively small cross section, a comparatively small amount of power is required to generate high intensities; thus, many nonlinear optical processes are easily observed in the medium [1].

Some of the earliest work in nonlinear fiber optics consisted of both experimental and theoretical investigations of such effects as stimulated Brillouin and Raman scattering [2]. This work stimulated the expansion of research to other nonlinear phenomena, such as four-wave-mixing [3], optically induced birefringence [4], self-phase modulation [5], and cross-phase modulation [6]. Advances in communications technology came when researchers realized that the nonlinearity in optical fibers could be exploited. In 1973, Hasegawa suggested that optical fibers would support soliton pulses in which the nonlinear effects balance the effects of dispersion [7]. Shortly thereafter, optical solitons were experimentally observed [8]. Technologies using solitons are promising for high bit rate optical communication systems [9]. Nonlinear fiber optics has found many uses beyond communications systems; for example, pulse compression [10] and sensor devices [11].

Until recently, communications systems using optical fibers supported one communication channel per fiber. To increase the information capacity of communications systems, engineers

have turned to wavelength division multiplexed (WDM) systems in which each communication channel is represented by a unique wavelength. The dominant nonlinear process which limits the information capacity of a WDM system is four-wave-mixing. The parameters that set this limit are the power coupled in the fiber and the frequency spacing between adjacent channels.

Nonlinear fiber optics is not only relevant to telecommunications; it is also of great interest in mathematics and physics. The equation which governs wave propagation in a single-mode optical fiber is a nonlinear second-order partial differential equation (the nonlinear Schrodinger equation). This particular equation has been studied extensively for its mathematical properties, for example, its analytic solutions give rise to the possibility of soliton propagation [12]. The nonlinear dynamics accessible in optical fibers is rich and varied and makes an excellent experimental system for the study of many nonlinear phenomena.

In this paper, the nonlinear dynamics of four-wave-mixing processes resulting from two waves copropagating in an optical fiber is investigated. Multiple waves at different frequencies copropagating in an optical fiber can interact through the nonlinear susceptibility of the fiber medium to generate new frequencies, sidebands, through four-wave-mixing (FWM). Two pump waves at ω_1 and ω_2 input to an optical fiber can generate first order sidebands at frequencies $\omega_3=2\omega_1-\omega_2$ and $\omega_4=2\omega_2-\omega_1$. Second order sidebands are found at $\omega_5=2\omega_3-\omega_4$ and $\omega_6=2\omega_4-\omega_3$. The number of sidebands generated is determined by the input power and frequency separation between the pumps, e.g. higher order sidebands may easily be generated by either increasing the pump power or decreasing the pump detuning.

We present detailed studies of the dynamical evolution of sidebands, generated from two input pump waves at ω_1 and ω_2, as they propagate along an optical fiber. Previous numerical studies

have shown that two critical parameters, the pump power and the frequency separation (detuning) between the pump waves, determine the dynamical evolution of power in the sidebands and the number of sidebands generated in a particular length [13]. Previous theoretical studies have shown interesting and sometimes complex dynamical evolution of the sidebands with length in the fiber [14,15]. Section II reviews the nonlinear dynamical equations used to study the evolution of FWM processes in the optical fiber. There were two sets of equations used throughout this research to model the system; the nonlinear Schrodinger equation (NLSE) [1] and a set of coupled amplitude equations derived from the NLSE [13]. Numerical simulations based on these models that show the sensitivity of the sideband dynamics on the input pump power and frequency detuning are presented. These simulations motivated the initial choice of parameter regimes to investigate in this research.

A unique set of experimental measurements of multiple FWM processes along an optical fiber were performed for this research. The experimental apparatus used to conduct the measurements is presented in Section III. The key elements of the system were two tunable dye lasers which were pumped by a frequency doubled Nd:YAG (neodymium doped yittrium aluminum garnet) laser, polarization maintaining optical fiber supplied by AT&T Bell Labs, a spectrometer, and a high resolution, low noise CCD (charge coupled device) camera supplied by Georgia Tech Research Institute (GTRI). The GTRI CCD camera was a critical instrument in the experiments. Standard CCD cameras would have been inadequate to detect very weak sidebands; the regime most of the experiments probed. The experimental results presented here are unique in two ways; first, the GTRI CCD camera allowed for detection of weak (<1% of the pump waves) sidebands and second, these are the only detailed measurements tracing the dynamical evolution of the sidebands along a fiber in existence at this time.

Section IV presents the experimental investigation of the dynamical evolution of multiple FWM processes in an optical fiber. Measurements tracing the power in the sidebands along a length of 50 meters of fiber are presented. These measurements were done at two input pump powers which yield different sideband dynamics. The power in the sidebands was observed to evolve periodically with fiber length. However, the periodic evolution appears to damp to a constant value of power for each sideband. Furthermore, each of the sidebands evolves along the fiber with different dynamics. Other studies in which the pump power was varied for a fixed length of fiber are presented as well. The initial growth of the sidebands in the first 5 meters of fiber was found to be fairly well predicted by the standard theoretical models. However, for longer lengths, the inadequacy of the models to predict the experimental observations is apparent.

Section V discusses the interpretations of the experimental results. To understand the measurements, the theoretical models are modified by including two effects previously not considered; a pump input with multiple longitudinal modes and phase fluctuations added to the waves as they propagate alo g the fiber length. The impact of a multimode input is examined and found to dramatically alter the dynamical evolution of the individual sidebands when compared with the standard theory using a single mode pump input. Weak stochastic phase perturbations, added to the copropagating waves are also included in the modeling and found to damp the periodic evolution of the power in the sidebands. Neither the relatively straightforward multimode input nor the phase fluctuations which were not so obvious have ever been considered when modeling multiple wave propagation in an optical fiber. Both effects are found critical to understanding and predicting the dynamics of the experimentally observed sideband evolution. This research has probed a very specific regime of a complex nonlinear system. The experimental research pointed to several inadequacies of the standard theoretical models to predict the experimental results. Section VI summarizes the conclusions of this research.

II. Theoretical Considerations

Propagation of optical pulses in single mode optical fibers is described by the well-known nonlinear Schrodinger equation [1]:

$$\frac{\partial U}{\partial Z} + \frac{\beta^{(2)}}{T_o^2}\frac{\partial^2 U}{\partial \tau^2} = i\gamma P_o |U|^2 U \qquad (1)$$

where U is the complex electric field envelope normalized to the absolute amplitude of the field $\sqrt{P_o}$, P_o is the total power in the fiber, τ is time normalized to the pulse width and measured in a reference frame moving with the group velocity of the pulse ($\tau = (t\text{-}z/v_g)/T_o$), T_o is the pulse width, $\beta^{(2)}$ is the group velocity dispersion (GVD) and is given by the second order derivative of β, the axial wavevector, with respect to the angular frequency ω_{ave}. The nonlinearity coefficient γ is given by the relationship,

$$\gamma = \frac{\omega_{ave}\, n_2^I}{cA_{eff}} \qquad (2)$$

where A_{eff} is the effective core area of the fiber determined by the size of the fundamental mode, n_2^I is the Kerr coefficient for the intensity dependent refractive index and ω_{ave} is the average angular frequency of the wave envelope [1].

In order to obtain the nonlinear Schrodinger equation (eqn. (1)), several assumptions are made. One assumption is an instantaneous nonlinear response of the medium. This is valid for pulses longer than 100 femtoseconds since the third order susceptibility of the medium, $\chi^{(3)}$, has electronic contributions on the 1 to 10 femtosecond timescale [1]. The experimental research used relatively long pulses ~5 ns. The slowly varying envelope approximation is also used where

the second order derivative of the field with respect to the length is neglected. This assumes that the change in slope of the field envelope over a distance of one wavelength is small compared with the slope of the field envelope itself. The optical field is assumed to maintain its polarization along the fiber, thus the scalar form of the NLSE (eqn. (1)). This is justified for the experiments presented here, since linearly polarized light from the lasers was propagated with the polarization aligned along one of the principal axes of a polarization preserving fiber (Section III). The axial wavevector, $\beta(\omega)$, is approximated by a Taylor series expansion. For wavelengths near the zero dispersion regime ($\lambda \sim 1.3$ microns), where $\beta^{(2)}$ approaches zero, higher order terms from the Taylor series need to be included. The experiments in this research were performed in the visible regime ($\lambda \sim 633$ nm) thus only terms up to $\beta^{(2)}$ were retained. The linear fiber loss is also assumed negligible. This is justified for the wavelength regime and fiber lengths ($L < 50$ m) investigated, since the loss is approximately 6 dB/km at ($\lambda \sim 633$ nm) which amounts to < 1% loss over 50 meters.

There are two wavelength regimes of interest in optical fibers; the anomalous dispersion ($\lambda > \lambda_o$) and the normal dispersion ($\lambda < \lambda_o$) regimes where the zero dispersion wavelength λ_o can range from 1.3μm to 1.58μm. The experiments presented here were performed in the normal dispersion regime. However, the integrability of the NLSE gives rise to interesting solutions in the form of solitons in both regimes. Soliton propagation occurs when the fiber nonlinearity balances the effect of dispersion and the pulse propagates without dispersive broadening. In the anomalous dispersion regime ($\beta^{(2)} < 0$) the fundamental soliton solution of the NLSE is in the form of hyperbolic secant pulses [1,12]. In the normal dispersion regime ($\beta^{(2)} > 0$) the fundamental soliton solution is in the form of a hyperbolic tangent, giving rise to dark solitons or dips in a continuous wave background [1,16]. In the context of the experiments presented, in the normal

dispersion regime with finite width pulses, a carrier pulse of finite width may support relatively stable propagation of dark pulses for short distances [16]. These are not 'proper' dark solitons however; the distance of stable propagation decreases with decreasing carrier width.

The split step Fourier method (SSFM), a pseudospectral technique, was used in this research [17]. Specifically, a symmetrized form of the SSFM was used [1], and the fast Fourier transform (FFT) routines were obtained from the IMSL mathematical libraries. An advantage of using the NLSE in the four wave mixing problem, is that integration is reduced to using the FFT. Modeling four wave mixing processes, for example, with a dual frequency input, the total complex field is represented by U, the field envelope, and all frequency components are propagated using the single NLSE. However, care must be taken under conditions where many orders of sidebands are generated. As the number of sidebands increases, the size of the FFT must necessarily be increased.

For long pulses or continuous wave input, assuming monochromatic waves, the coupled amplitude equations for the pump waves and sidebands derived from the wave equation [13] are written below, normalizing all of the complex field amplitudes to the absolute value of the total amplitude of the pumps with average frequency ω_{ave} (which has total power P_o at the input end of the fiber)

$$\frac{dU_j}{dz} = i\gamma P_o\left\{\left(|U_j|^2 + 2\sum_{k\neq j}|U_k|^2\right)U_j + \sum_{kmn} d_{kmn}U_kU_mU_n^* e^{\Delta\beta_{kmn}z}\right\} \qquad (3)$$

where j,k,m,n = 1,2,3,4... and k,m ≠ n. Here Σ_{kmn} denotes the permutations of the indices k, m and n such that $\omega_k + \omega_m - \omega_n = \omega_j$, and the quantity $\Delta\beta_{kmn} = \beta_k + \beta_m - \beta_n - \beta_j$ is the axial wavevector mismatch. The quantity d_{kmn} is a degeneracy factor that is unity when k = m and 2 when k ≠ m. The nonlinearity coefficient γ is given in equation (2). Comparing the coupled

amplitude equations (eqn. 3) with the NLSE (eqn. 1), the contributions to the evolution of the field U_j are now separated into three sets of terms. On the right side of eqn. (3), from right to left, the contributions are due to self-phase modulation (SPM), cross-phase modulation (XPM) and four-wave-mixing (FWM).

The linear mismatches $\Delta\beta_{klmn}$ are simplified using the approximation that the material part of the index difference dominates the mismatch and the waveguiding contribution can be neglected. This approximation is justified for the frequency separations in these experiments, since the v-number characterizing the single transverse mode changes by less than 1 percent over the entire range of frequencies considered. By using the frequency relationships between the peaks and expanding the propagation constants β_j in a Taylor series about average frequency, ω_{ave}, all the mismatches are found to be integer multiples of the quantity $\Delta\kappa = \Omega^2\beta^{(2)}$ where Ω is the frequency difference, or detuning, between the two pump waves and $\beta^{(2)}$ is the group velocity dispersion [18]. These amplitude equations can be solved numerically, and the power in each frequency component obtained as a function of distance along the fiber.

Choosing the scaled powers of the waves to be $\rho_m = |U_m|^2$, then in reference [18] it was shown that the equations (3) display power conservation, as is expected. It was also shown that another conserved quantity

$$C(z) = (\rho_1(z) - \rho_2(z)) + (\rho_3(z) - \rho_4(z)) + (\rho_5(z) - \rho_6(z)) \qquad (4)$$

is obtained for the multiple four wave mixing processes that occur within the fiber. It was shown in [18] that the conservation of power and equation (4) are the only two conservation relations that involve linear combinations of the powers in the different frequency components. This

relation holds at any distance, z, of propagation in the nonlinear medium, and connects the asymmetries of the pump waves and sidebands. A more generalized form of equation (4) has been derived from the NLSE and is presented in reference [19]. Equation (4) has been verified experimentally for relatively short fiber lengths of less than 2 meters (see ref. [19]). The conservation of asymmetry (eqn. (4)) was used in all of the experimental measurements as a sensitive test for other competing processes not included in the models, for example, stimulated Raman scattering.

The initial parameter regime chosen for the experiments came from numerical simulations of the equations presented above. The dynamics of these equations for multiple waves copropagating in a fiber have been studied numerically for long fiber lengths [14,20]; however, experimental work has been limited to a few meters [13,15]. As the sidebands evolve along the fiber, there is exchange of power between the pumps and sidebands, the dynamics of which, are determined by the phase mismatch between the copropagating waves. The two key experimental parameters, for a given optical fiber and wavelength regime, that determine the dynamics of the power exchange are the pump detuning and the total input power. This can be seen in eqns. (3) where all terms on the right side of the equations are multiplied by P_o and the FWM terms include oscillating terms with the argument proportional to Ω^2. The FWM strength and dynamics are very sensitive to the pump detuning as well as γ and $\beta^{(2)}$. The values used for $\beta^{(2)}$ and γ are same throughout this research, $\beta^{(2)} = 55$ ps^2/km and $\gamma = 0.019$ W^{-1}m^{-1}, and are consistent with the experimental regimes explored later in this paper.

To investigate the dependence of the evolution of the power in the first order sidebands ($\rho_3(z)$ and $\rho_4(z)$) on the pump power and detuning, the coupled amplitude equations are numerically solved using a fourth order Runge Kutta algorithm [21]. A comparison between the power in

the sidebands predicted by the NLSE and the coupled amplitude equations was made as a check on the numerical simulations. Simulations based on the NLSE with a continuous wave (CW) input and the coupled amplitude equations were performed and compared. The comparisons yielded the same predictions for the evolution of the power in the sidebands. However, comparison of the NLSE using a Gaussian pulse input with either the continuous wave input or the coupled amplitude equations showed a discrepancy between the models. The power generated in the first order sideband was found to be higher using the CW input than with the pulse input. It was found necessary to include a scale factor in the CW models, where $\gamma P_o \rightarrow \zeta \gamma P_o$ with $\zeta = 0.735$. The value of ζ was determined by comparing predictions from the NLSE for a Gaussian pulse input with a continuous wave input. Intuitively, as the pulse width approaches infinity, the CW and pulse inputs should agree. However, there is no analytic form for estimating this scale factor. Independent studies have also been performed comparing various pulse shapes input to the NLSE with the cw input, confirming the discrepancy between the two types of input.

The sensitivity of the sideband dynamics on the pump power is illustrated in Figure 1. The first order sideband evolution along 100 meters of fiber for a detuning of 300 GHz and different input pump powers is plotted in Figure 1, (a) 2 W, (b) 6 W and (c) 50 W. The coupled amplitude equations were truncated to six waves, including up to second order sidebands. In Figure 1 (a) the input power is low, generating relatively weak first order sidebands, and the pumps and sidebands exchange power periodically along the fiber. Using an undepleted pump approximation, eqns. (3) have an analytic solution which shows the power in the first order sidebands evolves as a sinusoid as a function of length [22]. In Figure 1 (b) and (c), as the pump input power is increased, higher order sidebands are generated and the power exchange between the pumps and sidebands becomes increasingly complex. In fact, the equations when truncated to include just a few orders of sidebands exhibit chaotic dynamics at high pump powers [13].

However, the NLSE is integrable, and does not exhibit chaos. In the case of the coupled amplitude equations the apparent chaos is induced by truncating the equations to include only a few frequency components [14].

Doubling the pump detuning to Ω = 600 GHz, the phase mismatch is increased by a factor of four. As the phase mismatch increases the efficiency of power conversion from the pumps to the sidebands decreases. The evolution of the first order sidebands with length in the fiber for a detuning of 600 GHz is shown in Figure 2 with pump input power levels of (a) 2 W, (b) 6 W and (c) 50 W. Comparing the evolution with a pump input of 2 W, by doubling the detuning the maximum power in the first order sidebands is decreased by a factor of 10 (Figure 1 (a) and Figure 2 (a)). The period of the power exchange between the sidebands and pumps has also increased. In Figure 2(b) and (c), it takes much higher powers to generate higher order sidebands that impact the dynamics of the first order sidebands. Thus, increasing the detuning decreases the efficiency of the four wave mixing power conversion. Increasing the pump power increases the number of sidebands generated, and thus the dynamics becomes more complex.

III. Experimental Apparatus and Technique

The entire experimental set up used to study multiple four wave mixing processes along a length of optical fiber is shown in Figure 3. The laser system consists of two Littman type tunable dye lasers, pumped by the second harmonic of a Q-switched frequency doubled Nd:YAG laser. Pulses that are ~5 ns (FWHM) in length are generated. The outputs from the two dye lasers (λ ~ 633 nm) are amplified and then passed through the appropriate delays to ensure temporal overlap of the pulses at the input to the optical fiber. The telescope in the path of one laser controls the spot size and, thus, the coupling efficiency so that the relative power of the two lasers coupled into the fiber can be adjusted to the desired value. The two apertures ensure nearly colinear propagation of the two beams. The light is coupled into a single mode polarization maintaining optical fiber, after passage through a polarizer and half wave plate. The polarizer at the input to the fiber produces linearly polarized light while the half wave plate rotates the polarization of the light to coincide with a principal axis of the birefringent fiber. The fiber chosen for the experiments was developed by AT&T as an experimental fiber. The fiber is single mode at 633 nm and polarization maintaining. The AT&T fiber achieves high birefringence by deforming a circular fiber preform so that it is rectangular in shape, the cladding is elliptical, and the core is circular [23]. This fiber has a core diameter of 4 μm with a birefringence of 2.7×10^{-4}.

A beamsplitter cube, at the fiber output, is used to direct half of the light to an optical power meter to monitor the power in the pulses while the other half is input to a grating spectrometer. A computer controlled video camera is mounted on an output port of the spectrometer with a variable neutral density filter (VNDF) placed at the input port to regulate the amount of light incident on the camera. Spectra for individual pulses are digitized and stored in the memory of a microcomputer and a video monitor is used to display each spectrum.

For the experiments presented in this paper, images of the fiber output spectra were captured using a system based on advanced high speed, low noise, and high resolution charge coupled device (CCD) technology. The system uses a scientific CCD device developed by MIT Lincoln Laboratories [24]. The CCD device is backside illuminated with 420 x 420 pixels/frame. To increase the readout rate, there is a separate frame storage region which allows one image to be read as the next one is integrated. Each pixel has a dimension of 27 μm x 27 μm with a full well depth or charge holding capacity of 100,000 electrons. Pixel nonuniformity has been measured to be 6% peak to peak for similar backside illuminated devices made by MIT Lincoln Laboratories [25]. The advantage of illuminating the CCD from the backside is that the quantum efficiency (QE) is high, for this device the peak QE is 90% near 600 nm. The CCD chip incorporates an on-chip readout amplifier which is the dominant source of noise in the device.

The camera system was built at Georgia Tech Research Institute (GTRI) for use in low light level astronomical imaging [26]. External to the CCD chip is a 14 bit A/D and controlling electronics for the CCD which run at a maximum rate of 1 Mpixel/sec. Using the full 420 x 420 array this translates to ~5 frames/second. The external electronics incorporate low noise design techniques such that the system noise is limited by the readout noise from the amplifier on the CCD chip. The CCD is liquid nitrogen cooled to -50°C, reducing the dark current to 0.04 electrons per pixel (at room temperature the dark current ~700 electrons per pixel). The minimum readout noise from the on-chip amplifier is 7.2 electrons per pixel rms at -50°C [26].

The camera system is controlled using a Macintosh computer running Labview control software. This software controls a Pulse Instruments PI5800A data generator. The PI5800A generates signals on 16 parallel programmable lines which control the camera. From the camera there is a fiber optic data link which transmits up to 8.3 MBytes per second. The data is then stored in a high speed 32 MByte ram buffer. From the buffer the data may be either stored on a high speed

video recorder which runs as fast as 4 MBytes per second, or, for small files it may be stored to a hard disk which is limited by the I/O of the computer system. Programs in Labview were developed with the capability to select a subarray at any location on the chip. For example, in the experiments presented here, a subarray of 10 x 256 pixels near the center of the chip was chosen. This decreases the size of required data storage and increases the maximum number of frames per second. In these experiments the frame rate is limited to the 10 Hz repitition rate of the Nd:YAG laser system. To achieve the slow rates the camera hardware is programmed to run at 10 Hz and a clock signal is generated which is used to control the laser system through the oscillator sync input. The resolution of the camera-spectrometer system is approximately 43 GHz and is limited by the resolution of the CCD.

The data acquisition method used in this research was to collect output spectra using the GTRI CCD. The pump lasers fluctuate from shot to shot. For statistical analysis, a total of many spectra for each data point are collected. Typically, 400 independent spectra are captured for each pump propagating alone in the fiber and the two pumps copropagating (FWM). The power in the individual sidebands is measured as a fraction of the total power, normalized to unity, in the fiber, and the total input power is determined based on measurements of each individual pump propagating alone in the fiber. Quantitative measurements are then made of the power in the pumps and sidebands, generated by FWM. Prior to data acquistion a set of "dark" frames (a set of frames with no light incident on the detector) is collected. An average "dark" frame is found and then subsequently used to remove the camera bias from the data frames using pixel by pixel subtraction. The power in each frequency component is distributed symmetrically about a central peak for that component. To calculate the power in the pumps and sidebands, we developed software to find the locations of the peaks in the spectrum and the power in each frequency component in two ways. The first is to take a linear cross-section along one row and integrate the power in each frequency component. The second is to integrate the power in the full

distribution for each component. The second method is insensitive to horizontal misalignment of the CCD detector with respect to the spectrometer. Both methods were employed in this research and agreed closely throughout. Quantitative values were obtained of the FWM pump and sideband power as well as the statistics. It will be seen later that the statistical information obtained played a crucial role in confirming the physical interpretation of the experiments.

The 14 bit dynamic range of the camera system allows for weak FWM signals to be detected. A typical linear cross-section of a FWM spectrum is shown in Figure 4 (a) linear scale and (b) logarithmic scale. The spectrum is plotted first on a linear scale which is comparable to the type of spectrum that would be obtained from a standard 8 bit video camera. The uniqueness of the GTRI CCD camera is shown in Figure 4 (b) where the spectrum is plotted on a log scale, the highest peaks in the spectrum are approximately four orders of magnitude above the noise. This spectrum shows many orders of sidebands, the highest orders just above the noise with a power less than 1% of the total pump power. The two central peaks are the pump waves at ω_1, higher frequency (blue-shifted), and ω_2 lower frequency (red-shifted). The first order sidebands are located on either side of the pumps at $\omega_3=2\,\omega_1-\omega_2$ and $\omega_4=2\,\omega_2-\omega_1$. The detection of weak FWM sidebands at the fiber output presented here would not have been possible without the exceptional performance of this CCD camera system.

IV. Experiments

The measurements of the dynamical evolution of four-wave-mixing processes along a length of single mode polarization maintaining optical fiber were performed using two different values of the pump power, 2.1 W and 5.5 W. The frequency separation between the pumps was held constant throughout the measurements at $\Omega = 366$ GHz. The experiments began with 50.39 meters of AT&T birefringent optical fiber [23]. Starting at this initial length, measurements of the FWM spectrum at the output of the fiber were made using the GTRI CCD camera. From these measurements, conservation of total power and asymmetry (eqn. (4)) were tested for each data set. To check the conservation of these quantities, the total power and asymmetry in the single pumps propagating were calculated and compared with the power and asymmetry of the copropagating pumps. Data sets were accepted and kept if the conservation laws were preserved. In some cases, the presence of weak stimulated Raman scattering (SRS) was detected through the asymmetry relation. In the experiments tracing the evolution of the four wave mixing spectra along the fiber length no SRS was detected. After the initial measurements were made at the two input powers (2.1 W and 5.5 W), 1 to 1.5 meters of fiber was cut and cleaved. The fiber was cut and cleaved at the output side of the fiber, to maintain approximately constant pump coupling to the fiber throughout the experiments. This process was repeated until the four-wave-mixing spectrum had been traced along the full 50.39 meters of fiber for the two input power levels.

Figure 5 and Figure 6 show three dimensional plots of the average FWM output spectrum along the length of single mode birefringent optical fiber. The vertical axis represents the intensity, normalized to the peak power in one of the pumps, plotted on a logarithmic scale. The pump frequencies are centered on $\pm\Omega/2$, and the fiber length is increasing into the page. In Figure 5 the input power to the fiber is 2.1 W and first order sidebands are clearly seen. Plotted on a log scale

the evolution of the power in the sidebands appears to evolve periodically with increasing fiber length. Figure 6 shows the evolution of the FWM spectrum for a pump input of 5.5 W. First order sidebands are generated as well as 'weak' second order sidebands. The first order sidebands appear to evolve periodically initially, and, with increasing fiber length, evolve to a constant value.

A clearer picture of the evolution of the first order sidebands is obtained by plotting the power in the sidebands as a function of length along the fiber. Figure 7 shows the evolution of the first order sidebands as a function of length. The two first order sidebands are plotted separately, where Figure 7 (a) shows the evolution of the blue sideband (blue-shifted from the pumps) and Figure 7 (b) shows the red sideband (red- shifted from the pumps). The solid line in the figure is generated by numerically solving the coupled amplitude equations truncated to six waves. The parameters $\beta^{(2)}$ and γ were determined by finding the best fit of the numerical simulations to the experimental data. The values obtained were $\beta^{(2)} = 55$ ps^2/km and $\gamma = 0.019$ m^{-1}W^{-1}, both well within the regime expected for a central wavelength of 633 nm [1]. The measured sideband power, normalized to the total power in the fiber, is periodic with length, but it appears to be damping to a constant value. Also, the first minimum of the blue sideband trajectory occurs at a shorter distance than the first minimum for the red sideband. This contradicts the predictions of the coupled amplitude equations (ODE) and NLSE. The models predict essentially the same evolution for each sideband. The other difference between the two sidebands is the magnitude of the first maximum. The blue sideband has a larger maximum than the red sideband.

The apparent damping of the periodic sideband trajectory is seen more dramatically in Figure 8 which shows the evolution of the first order sideband power along the fiber for an input power of 5.5 W. Again the two first order sidebands (blue and red) evolve with different trajectories. Furthermore, they also appear to damp to a constant value at a faster rate than for the case with a

pump input power of 2.1 W. Both sets of experiments are compared with the numerical simulations in Figure 7 and Figure 8. The standard theoretical models do not account for either the damping of the sideband power or the different trajectories of the blue and red sidebands.

The FWM spectrum in Figure 6 shows that first order sidebands as well as weak second order sidebands for a pump input power of 5.5 W. Figure 9 shows the evolution of the power in the second order sidebands with propagation length. The blue and red shifted sidebands are plotted separately and the power is normalized to the total input power. The measured sideband power has a maximum of 0.2% of the total input. The 14 bit A/D used in the camera system limits the resolution to 1/16384 = 0.07%. Figure 9 shows a complex evolution of the sidebands. The sidebands are weak and just above the limits of resolution imposed by the detection system. Comparison is made using simulations based on the nonlinear Schrodinger equation. The NLSE is used in these simulations because it was found necessary to include higher order sidebands (>second order) to model the dynamics.

A first set of experiments was performed using 20 meters of the AT&T birefringent fiber. In these earlier measurements, the evolution of the sidebands was traced along the fiber using an input power of 2.1 W and a pump detuning of 366 GHz. A direct comparison between the sideband power along the length of 20 meters of fiber with the sideband evolution along the 50.39 meters of fiber was made. The two sets of data were found to yield the same results. Thus, the observations of the damping of the sideband trajectory and the different evolutions of the individual sidebands are repeatable.

Another perspective on the evolution of the sidebands is gained through investigation of the sideband power dependence on the pump power [13]. Measurements were made of the sideband power as a function of pump power at a length of 50.39 meters for two different values of the

pump detuning. Figure 10 shows the power in the first order sidebands as a function of input power using a pump detuning Ω = 366 GHz. The blue and red sidebands are plotted separately, Figure 10 (a) and (b) respectively. The input power was varied from approximately 2 W to 15 W, and the procedure outlined above was used for data collection. Pump depletion due to stimulated Raman scattering (SRS) was observed for pump powers greater than 10 W. For both the blue and red sideband, the measurement peaks around 12 W and then begins to decrease with increasing pump power. This decrease can be attributed to significant pump depletion associated with Raman scattering. The solid lines in Figure 10 were generated by numerically solving the coupled amplitude equations truncated to six waves using $\beta^{(2)} = 55\ ps^2/km$ and $\gamma = 0.019\ m^{-1}W^{-1}$. The numerical solutions yielded quite different dynamics than those observed experimentally.

The pump detuning was maintained at 366 GHz throughout the experiments probing the evolution along the fiber length. Prior to cutting the fiber, a series of measurements of the sideband power dependence on the pump power were performed with a detuning twice as large: Ω = 722 GHz. Doubling the detuning resulted in a smaller conversion of power from the pumps to the sidebands. Figure 11 shows the results of these measurements. Only first order sidebands were detected for the range of pump powers explored. Consequently, essentially periodic dynamics were predicted by the theoretical models. As in the 366 GHz detuning case, the sideband power steadily increased with pump power until stimulated Raman scattering began to deplete the pumps. The numerical simulations again showed oscillations in the sideband power with increasing pump power, in marked contrast to the dynamics seen in the experiments.

To check some of the observed dynamics, a series of sideband power dependence measurements were performed at a length of 5.52 meters with a detuning of 366 GHz. Figure 12 shows the sideband power as a function of input power. Raman scattering was observed for pump powers

greater than 25 W. Comparison of the experimental measurements with numerical simulations shows very close agreement for pump powers less than 25 W. Thus, as the sidebands initially grow in the fiber, the numerical models can accurately predict the sideband dynamics. However, for longer fiber lengths the standard theory fails to predict the dynamical evolution of the pumps and sidebands as the pulses propagate through the fiber.

So far, only the dynamical evolution of the power in the sidebands has been discussed. It is also worth discussing the experimental FWM spectral envelope, which, resembles a hyperbolic secant shape at the output of 50.39 meters of fiber. The hyperbolic secant is an ubiquitous shape in nonlinear fiber optics and arises in the context of soliton propagation in fibers. Soliton propagation in the form of a hyperbolic secant pulse shape is found in the anomalous dispersion regime ($\beta^{(2)}<0$) [12,27]. However, the experiments in this research were performed in the normal dispersion regime. In the normal dispersion regime, dark-pulse solitons of the form of a hyperbolic tangent are predicted and have been observed [16].

Figure 13 shows some of the experimental FWM output spectra at a fiber length of 50.39 meters, detuning Ω = 366 GHz, with a range of input power levels (a) 2.1 W, (b) 5.5 W, (c) 8.3 W, and (d) 17.4 W. The solid line represents the experimental data and the dashed line is a curve fit to the spectral envelope. The curve is fit by $y(\omega)=A\,\mathrm{sech}(B\omega)$ where A and B are the fit parameters. The values used to generate the plots in Figure 13 are: (a) A=3.85, B=0.36, (b) A=2.26, B=0.27, (c) A=1.56, B=0.23, and (d) A=0.81, B=0.20. Figure 13 shows close agreement between the hyperbolic secant shape and the experimental spectral envelope. For the lower input powers, the peaks in the spectra are distinct. However, as the input power increases, the peaks broaden and the spectrum begins to fill in.

In Figure 13 (d) with an input power of 17.4 W, the pumps are depleted by Raman scattering. Furthermore, close examination of the spectrum shows an asymmetry even though the initial conditions on the pump waves were symmetric, i.e. $\rho_1(0)= \rho_2(0)$. As the waves copropagate in the fiber, photons from the band of frequencies generated through four wave mixing will be down-shifted by spontaneous and stimulated Raman scattering. The Raman gain spectrum ranges from 0 to tens of terahertz frequency shift from the pumps. For silica glass, maximum Raman gain occurs at a down-shifted frequency of 13.2 THz (several orders of magnitude larger than the pump detuning) [1]. However, the Raman gain is nonzero near zero frequency shift. Thus, in Figure 13 (d), the observed asymmetry in the spectrum arises from strong stimulated Raman scattering.

These experiments exposed several discrepancies in the comparison of experiment and theory and illustrated the inadequacy of the standard theoretical models to predict the observed dynamics over the full length of fiber investigated. The next section will present modifications to the theoretical models, to allow a quantitative comparison of experimental observations and numerical simulations. The key aspects of the experiments to be addressed are (1) the damping of the periodic sideband trajectories with length and (2) the difference between the red and blue sideband trajectories.

V. Theory vs. Experiment

This section develops a theoretical description which includes two effects which had not previously been considered. We consider the effect of a multimode pump laser at the fiber input and investigate the resulting dynamical evolution of the sidebands. By modeling one of the pump lasers as two closely spaced longitudinal modes, the subsequent dynamical evolution of the sidebands is altered dramatically. By introducing this asymmetry in the mode structure of the pump input, the resultant dynamics for the blue and red sidebands begin to approach the sideband dynamics observed in the experiments. However, the damping of the periodic trajectories seen in the experiments is still not explained with the simple multimode structure at the input. Building on the multimode analysis, one then introduces weak phase fluctuations to the pump waves propagating along the fiber. The combination of both the multimode pump input and weak phase perturbations along the fiber is found necessary to accurately predict the experimental observations. Excellent agreement is thus finally obtained on comparing predictions based on the stochastic multimode model with experiments.

V.I Multimode Pump Input

As mentioned previously, the dye laser systems used in the experiments were designed for narrowband operation. However, the resolution of our instrumentation limits the ability to measure the linewidth of the lasers and distinguish single versus multiple mode operation. Thus, either of the dye laser outputs may have consisted of several longitudinal modes. We examine the impact of multimode operation on the dynamical evolution of the sidebands by introducing a multimode pump input to the theoretical models. The sideband evolution predicted from numerical solutions of both the NLSE and the coupled amplitude equations with a multimode input is found to exhibit similar dynamics, when compared with the experimental observations.

To model wave propagation in the fiber using a multimode pump input, both the nonlinear Schrodinger equation and the coupled amplitude equations discussed earlier can be used. The NSLE requires only a modification of the input pulses. The input spectrum can be set for one, two, three, etc., modes in each pump laser. Thus, a variety of initial pump conditions can be investigated. Starting with the simplest case, Figure 14 shows an example (a) Gaussian input pulse and (b) corresponding spectrum, to the NLSE, with two modes in the blue shifted pump and one mode in the red shifted pump. In Figure 14 (b) the spectrum is plotted with the pump detuning normalized to unity and the pumps centered about zero frequency shift. The input is a Gaussian pulse modulated by the pump detuning and the longitudinal mode spacing. The longitudinal mode spacing (Δv) were chosen to be 0.5 GHz, consistent with the expected spacing from the experiments, and the pump detuning is 366 GHz. The initial conditions on the pumps were chosen so that the conservation relation for the asymmetry (eqn. 2.3) is zero, i.e. $\rho_1 = \rho_2$. Figure 15 shows the FWM output spectrum generated from the multimode input. The sidebands and pumps now consist of many frequencies. To estimate the relative power in the pumps and sidebands, the power in the band of frequencies centered around the primary frequency is summed and then normalized to the total power in the spectrum, for example the blue pump power, ρ_1, is calculated from summing the power in the frequency components located between zero and one. For consistency the same notation used throughout this paper is retained to represent the power in the pumps and sidebands, e.g. ρ_3 represents the relative power in the blue first order sideband even though now it consists of multiple frequency components.

The split step Fourier method is used to propagate the pulses along the fiber [1]. Figure 15 shows a schematic representation of the FWM output spectrum after propagation through a length of fiber with the multimode input. The evolution of the four wave mixing processes is now more complex, not only is there mixing between the distantly spaced pump frequencies but

there is mixing between the closely spaced longitudinal modes. A difficulty of using the NLSE to model the multimode input is the size of the FFT which must be computed. Since the longitudinal mode spacing is several orders of magnitude smaller than the pump detuning the number of points necessary to represent the pulse spectrum is large $>=2^{15}$. The computation algorithm sets limits on the number of points used to represent the spectrum and the spectrum will necessarily be truncated. In general, the NLSE with single mode inputs yields the ability to work with a broad spectrum consisting of many orders of sidebands, a definite advantage over the coupled amplitude equations.

Extending the modeling of the multimode input to the coupled amplitude equations, the general form of the equations given in eqn. (3) is used to generate a new set of coupled amplitude equations. The frequencies in these equations now include the longitudinal mode spacing. Thus, the wavevector mismatch will now be proportional to $(\Omega \pm \Delta v/2)^2$, $(\Omega \pm 3\Delta v/2)^2$, etc, whereas in the single mode model, the mismatch was proportional to Ω^2. The number of frequency components necessary to model the FWM dynamics, including up to second order sidebands, results in at least 100 terms in each equation. Using equation (3), a 'C' program was written to find the allowed combinations of k, m and n. The multimode four waving mixing equations were then stored to a file in a subroutine format to be called from the integration programs.

For simplicity, the case of two longitudinal modes in the blue pump and one in the red pump is considered. The blue pump was initially chosen to be multimode because the fluctuations in experimental measurements of the linewidth were larger than those in the red pump. The single mode input standard model consists of 6 complex coupled field equations which includes the pumps, first order sidebands, and second order sidebands. Terms up to second order sidebands were included since they were observed in the experiments for a pump input of 5.5 W. With the

exhibited by the blue and red sidebands with this model are significantly different. Within the first 10 meters, the model follows the evolution quite well, and yet the damping observed in the experimental measurements with increasing length makes comparison difficult. Overall, the multimode model yields promising results for predicting the dynamical evolution of the sidebands. The modeling of the damping of the sideband trajectories will be discussed in the next section.

As another comparison of the multimode input model with experiment, Figure 18 shows the evolution of the second order sidebands with propagation distance. Terms including up to at least third order sidebands must be included in the model to properly predict the dynamics of the second order sidebands. The coupled amplitude equations including only up to second order were found inadequate. Thus, the nonlinear Schrodinger equation was used to easily include higher order sidebands. Comparison of the second order sideband and predictions based on the NLSE with a multimode input shows close agreement. The second order sidebands are weak and yet for fiber lengths less than 20 meters the simulations follow the experimental measurements closely. However, beyond 20 meters the blue second order sideband (Figure 18 (a)) appears to be damping to a constant value.

As mentioned earlier, the model can be extended to include various combinations of pump inputs, for example, three modes in one of the pumps and two or one in the other pump. No significant difference was found in the first order sideband evolution for the different combinations of asymmetric multimode input, for the parameter regimes investigated; L_{max} = 50.4 m, $P < 6W$, $\Omega = 366$ GHz, and $\Delta\nu = 0.5$ GHz. As the fiber length increases beyond 50.4 meters, differences in the trajectories arise between the various asymmetric combinations for the input. Referring to Figure 15, the spectrum broadens around the central frequency components due to FWM between the longitudinal modes. The longitudinal mode spacing used in these

simulations is small compared to the pump detuning. Furthermore, since the mode spacing is small, the FWM processes between adjacent modes will evolve with a period much longer than the fiber lengths considered in this research. Subtle differences in the sideband evolution will arise for different mode structures as the fiber length increases due to the different dynamics between adjacent modes. Only the simplest case of multimode input was considered for comparison with these experiments.

V.II Stochastic Phase Fluctuations

The previous theoretical analyses presented have been limited to deterministic models. We now turn to modeling of stochastic processes along the fiber length as well as including stochastic initial conditions on the pump inputs. The latter are included in the modeling to closely imitate the conditions present in the experiments. The former examines the impact on the dynamical evolution of the four wave mixing processes when weak fluctuations are added to the phase of each of the waves copropagating along the fiber. These phase fluctuations are found to damp the sideband periodic trajectories to a constant value. Comparison with the experimental observations is made and excellent agreement is found.

Consider a physical process which acts to perturb the phase of the waves propagating along the fiber. The physics of this phase noise could arise from a number of sources, such as; fiber medium inhomogeneities [29,30], Brillouin scattering, or Raman scattering [1]. In the experiments, there was no indication that these sources were present. However, the existence of these processes could have been lost in the background noise of the instrumentation. Identification of the physical process generating the noise through both experiments and modeling is a promising area for future research. A strong candidate for the source of phase noise is stimulated Raman scattering that builds up from a spontaneous noise background. Recalling the experiments probing the sideband power dependence on the pump input power, for

a 50 meter length of fiber significant Raman scattering was detected for pump inputs greater than 10 W. Thus, it is highly likely that very weak (< 4 orders of magnitude down from the pumps) Raman scattering was present in measurements.

There are two theoretical models which may serve as the core set of equations to model the nonlinear wave propagation along with stochastic processes in the fiber. The multimode coupled amplitude equations, developed previously, were used for the stochastic modeling in this research. A model incorporating the phase noise into the nonlinear Schrodinger equation is desirable as well. However, algorithms to properly include the necessary stochastic terms in the NLSE are not available at this time. Thus, the remainder of the research will use the coupled amplitude equations. Integration of the amplitude equations proceeded as follows. After the initial conditions on the input were set, the multiple waves were propagated in the fiber using a fourth order Runge-Kutta integration [21] with a step size Δz (typically 10^{-3} meters). After each integration step, the complex field amplitudes were converted to intensity and phase. The phase, ϕ_j, of each wave at frequency, ω_j, was modified according to:

$$\phi_j(z+\Delta z) = \phi_j(z) + \delta\phi_j \qquad (5)$$

where the phase fluctuations are represented by $\delta\phi_j$. The intensity and phase were then converted back to the complex field amplitudes. The field was then propagated another step Δz and the process repeated for each integration step.

Since the exact source generating the noise is not known, the phase fluctuations are taken to be delta correlated along the fiber and are considered to be independent sources for each wave. The Box-Muller algorithm was used to generate Gaussian deviates from computer generated uniform deviates [21,31]. The fluctuations are given by:

$$\delta\phi_j = \sqrt{-2\sigma_{\phi_j}\Delta z \ln(r_1)}\cos(2\pi r_2) \qquad (6)$$

and,

$$\delta\phi_{j+1} = \sqrt{-2\sigma_{\phi_{j+1}}\Delta z \ln(r_1)}\sin(2\pi r_2) \qquad (7)$$

where r_1 and r_2 are uniformly distributed random numbers on the interval (0,1) and σ_{ϕ_j} is the standard deviation of the phase fluctuations for a given frequency component. For simplicity in the numerical computations, the phase fluctuations were added to only the frequency components associated with the two pump waves. However, computations were also performed adding phase noise to all components; there was no detectable difference in the resulting sideband dynamics for the parameters investigated. This is reasonable in the regime of primary interest, since for pump powers less than 6 W, the pump intensities are much larger than the sidebands and thus make the strongest contribution to the FWM dynamics. Typically, the noise strengths σ_j, were chosen to be of the same order of magnitude for each pump.

V.III Stochastic Initial Conditions

Previous studies showed that fluctuations in the initial conditions of the pumps could have a significant impact on the dynamics of the FWM processes in the fiber [13,18]. To model the initial conditions of the experiments, measurements of pump fluctuations were included in the input to the integration of the equations. To measure the pump fluctuations, each pump was propagated alone in the fiber for each fiber length and pump power. The mean intensity, normalized to unity, and standard deviation were calculated from the output spectra. The intensity in the pumps was found to be Gaussian distributed. Figure 19 shows the measured standard deviation in the normalized pump power as a function of length along the fiber. The blue and red pump standard deviations are plotted separately. The blue laser has a higher mean intensity fluctuation than the red, this is probably associated with multiple longitudinal modes in the blue pump. The experimental measurements over the full length of optical fiber were

performed over a long period of time (approximately one year). As can be seen from Figure 19, the pump intensity standard deviation varied with time.

The numerical simulations were performed with fluctuations in the input pump intensity as well as fluctuations in the detuning. The measured frequency fluctuations had a magnitude of less than 1 GHz, several orders of magnitude smaller than the pump detuning of 366 GHz. Including the frequency fluctuations in the simulations was found to have no measurable impact on the resulting dynamical evolution of the sidebands. However, the pump power fluctuations were large (~10%) and could not be neglected. The pump input was of the form:

$$U_j(0) = \sqrt{\rho_j(0)}e^{i2\pi r_j} \tag{8}$$

where ρ_j is the intensity and r_j is a uniformly distributed random number in the interval (0,1), which selects a nonzero initial phase. For completeness r_j is included here. However, randomizing the initial phase had no measurable impact on the resulting evolution of the power in the waves. The pump intensity input to equation (8) for each component in the dual mode pump was set according to,

$$\rho_{1k}(0) = \tfrac{1}{2}\rho_{ave} + \tfrac{1}{2}\delta\rho_1 \tag{9}$$

where k represents each mode and for the single mode pump,

$$\rho_2(0) = \rho_{ave} + \delta\rho_2 \tag{10}$$

where ρ_{ave} is typically set to unity for both pumps and $\delta\rho$ are the fluctuations in the pumps and are generated using the Box-Muller algorithm [21]. The fluctuations are generated using the measured values of the standard deviation in the pump intensities (see Figure 19) and, are given by, for the blue pump,

$$\delta\rho_1 = \sqrt{-2\sigma_{\rho_1}^2 \ln(r_1)}\cos(2\pi r_2) \tag{11}$$

and for the red pump,

$$\delta\rho_2 = \sqrt{-2\sigma_{\rho_2}^2 \ln(r_1)}\sin(2\pi r_2) \qquad (12)$$

Computations with the multimode model (for the dual mode pump) used the same noise strength for each longitudinal mode. The next section will discuss the specific values used in the numerical simulations and compare with the experiments.

V.IV Numerical Simulations

The numerical simulations were performed using the multimode coupled amplitude equations along with the stochastic conditions discussed above. A complication arose when adding the phase fluctuations to the waves which resulted in a "noise-induced" drift [32]. This is a feature of multiplicative noise sources in which the noise added causes the sidebands to grow with propagation. Even though the noise is additive to the phase, the equations are cubic in the complex field and, thus, the phase noise is multiplicative when coupled back into the field equations. Including phase noise in the FWM calculations resulted in trajectories for the sideband power with length which were damped periodic trajectories with an increasing slope. To remove this artifact of the computations, a linear loss term, $-\alpha U_j$, was added to each of the complex field equations. The loss coefficient, α, was then set by finding the value which removed this increasing slope. In theory, the mathematical form of α can be derived from the equations and is a function of the noise strength [32]. However, the size of the system of coupled propagation equations made the technique for estimation intractable, even for the simplest approximate form of the equations.

The strength of the phase noise used in all of the following simulations was determined by fitting the simulations to the experimental data. The values found to give the best fits were $\sigma_{\phi_1} = 0.0067\ m^{-1}$ and $\sigma_{\phi_2} = 0.005\ m^{-1}$ and $\alpha = 0.0046\ m^{-1}$. For comparison with the experiments

tracing the evolution of the sidebands along the fiber, the simulations were the result of two calculations, one from 0 to 20 meters and the other from 0 to 50.4 meters. The calculation from 0 to 20 meters replaces the first 20 meters of the 0 to 50.4 meter simulations. This was necessary since the initial conditions on the pump fluctuations were larger (due to the laser adjustments for the measurements, which took several months) for lengths less than 20 meters (see Figure 19). The fluctuations in the pump intensities were set at $\sigma_{\rho_1} = 0.20$ (blue) and $\sigma_{\rho_2} = 0.11$ (red) to generate the curves from 0 to 20 meters and $\sigma_{\rho_1} = 0.12$ and $\sigma_{\rho_2} = 0.05$ to generate the curves from 20 to 50.4 meters. The other parameters were set at $\beta^{(2)} = 55$ ps^2/km, $\gamma = 0.019$ W^{-1}m^{-1}, $\Omega = 366$ GHz, $\delta\nu = 0.5$ GHz. The numerical simulations compute both an average and standard deviation from 50 trajectories. Simulations were done for 100 trajectories and it was determined that accurate statistics (the standard deviation was less than 5%) were obtained for as few as 50 trajectories. Thus, to reduce computation time the statistics are calculated from 50 runs.

Figure 20 (a) and Figure 21 (a) show the blue and red sideband trajectories, respectively, for an input power of 2.1 W. The experimental data are plotted with the numerical solution of the multimode coupled amplitude equations including both phase noise at each integration step and fluctuating the pump inputs. The multimode model with the inclusion of stochastic initial conditions and, most importantly, phase fluctuations along the fiber length, results in predictions which are very close to the experimental observations of the dynamical evolution of the sidebands. Figure 20 (b) and Figure 21 (b) show the measured standard deviation in the sideband power along the fiber length for the blue and red sidebands, respectively. The standard deviation was also calculated from the numerical simulations. Excellent agreement is found between the model and experimental measurements. Throughout the course of this research, many stochastic models have been investigated and this model is the only one found that reproduces the evolution of both the average power and fluctuations in the sidebands.

For an input power of 5.5 W, Figure 22 and Figure 23 show comparison between the numerical simulations and experimental data for the blue and red sidebands, respectively. The red sideband trajectories in Figure 23 show excellent agreement between the numerical model and experiment. The power in the red sideband from numerical solutions is periodic and appears to be damping at the appropriate rate. However, the blue sideband power trajectory shown in Figure 22 (a) does not reproduce the experimental measurements as closely. The numerical simulations at this pump power result in a blue sideband power evolution which does not damp as quickly as the experimental observations. However, the fluctuations measured in the experiments are fairly well predicted by the numerical simulations as shown in Figure 22 (b) and Figure 23 (b) for both the blue and red sidebands, respectively. The discrepancy in the damping seen between the experiment and model of the blue sideband power evolution could arise from several effects. The strength of the phase noise was the same for both the 2 W and 5.5 W calculations. Many simulations have been performed to optimize the values used for the phase noise strengths. The values used in these simulations were optimized in the sense they gave the best fit to the experimental data. A better approach would be, to identify the physical phenomena generating the phase fluctuations and with this knowledge, the magnitudes of σ_{ϕ_1} and σ_{ϕ_2} could be estimated from the physics. Another benefit of identifying the physics of the phase noise, the noise could be properly included in a model based on the nonlinear Schrodinger equation.

As a confirmation of the multimode model with phase noise, numerical simulations were performed examining the sideband power dependence on the input power at a length of 50.4 meters. Figure 24 and Figure 25 show the power in the sidebands as a function of input power for a pump detuning of 366 GHz and 722 GHz, respectively. The experimental measurements of the sideband powers are represented by closed circles in Figure 24 (a) and Figure 25 (a), blue sideband, and closed squares in Figure 24 (b) and Figure 25 (b) red sideband. The results of numerical simulations are represented by the open circles in Figure 24 (a) and Figure 25 (a) and

open squares in Figure 24 (b) and Figure 25 (b). The numerical simulations follow the general trend seen in the experiments. A large deviation occurs for pump powers >10 W where the pumps begin to be depleted by stimulated Raman scattering. Below 10 W, the experimental measurements of the red sidebands tend to be higher than the simulations, this increase arises from weak scattering of the blue photons to the red. With the smaller detuning (366 GHz), care must be taken to account for all orders of sidebands and for powers greater than 6 W probably third and fourth order sidebands are generated. However, with this model, including only up to second order sidebands, yields predictions in close agreement with experimental measurements especially when compared with the predictions based on the deterministic single mode input coupled amplitude equations.

We have presented a new approach to modeling the dynamical evolution of four wave mixing processes along an optical fiber. This modeling was motivated by the standard theoretical models inability to predict the results of experimental measurements presented in Section III. The two critical features of the model were a multimode pump input along with phase fluctuations added along the fiber length. The multimode pump input was found to alter the resulting sideband dynamics significantly. Due to an asymmetry introduced in the input, the blue and red sidebands evolved with different trajectories along the fiber. Furthermore, by adding weak phase fluctuations to the copropagating waves, the periodic sideband trajectories were found to damp out. Figure 20 through Figure 25 show comparisons between the experimental measurements of the sideband dynamics and the stochastic multimode model. The experimental observations brought to light several questions regarding the dynamics of the four wave mixing processes in the fiber.

VI. Conclusions

The dynamical evolution of four wave mixing (FWM) processes in an optical fiber has been investigated. This research consisted of experimental, theoretical, and numerical computations. The focus of this work was to experimentally trace the evolution of the sidebands, generated through FWM, along a length of optical fiber. Previous theoretical work suggested that, in certain parameter regimes, the sidebands exchange energy with the pumps periodically [13,14]. Specifically, in the undepleted pump regime [28], the sideband power evolves as a sinusoid with fiber length. Previous experiments had probed the dynamics for short fiber lengths (< 2 m) [13], however, the periodic evolution had never been directly verified.

The FWM spectral evolution along 50 meters of fiber for two input pump power regimes was investigated. The experimental work consisted of measuring the FWM mixing spectrum output from an optical fiber at different lengths in the fiber. Specifically, a low noise, high resolution CCD camera made at Georgia Tech Research Institute, was used [26] to detect weak (<1% of the power in the pumps) sidebands. With this resolution, measurements of the power in the first order sidebands for input pump powers (2.1 W and 5.5 W) were made using a pump detuning of 366 GHz. In the case of a pump input of 2.1 W, the sideband power evolution is expected to follow a sinusoid along the length of the fiber. Experiments showed that the power in the sideband evolved periodically, but that the evolution followed a damped sinusoid. The experiments also found that the two first order sidebands (blue and red shifted from the two pumps) had different evolutions along the fiber. Neither the damping nor the different evolutions were predicted by theory. Using a pump input power of 5.5 W the evolution of both first and second order sidebands was also measured. For a pump input of 5.5 W the damping in the first order sidebands appeared to occur faster than in the 2.1 W case.

Experiments probing the dependence of the sideband power on the input power for two different values of the detuning (366 GHz and 722 GHz) were also performed at the output of 50 meters of fiber. With a detuning of 366 GHz, the sideband power for pump inputs ranging from 2 W to 17 W was measured. Comparison of theoretical predictions with the measurements showed a large discrepancy both quantitatively and qualitatively. The measurements of the sideband power as a function of pump input power with 722 GHz detuning showed the same discrepancies with the theoretical models as the 366 GHz detuning case. Another set of measurements were performed at a length of 5 meters with a pump detuning of 366 GHz. Comparisons of the measured sideband powers with theoretical predictions, for this case, showed excellent agreement up to a pump input power of 25 W. For higher powers, the deviation between experiment and theory was due to other competing processes (stimulated Raman scattering) not accounted for in the theoretical model. The results of the measurements show that the initial evolution of the FWM spectrum in the fiber is modeled well by the standard theory. However, beyond the initial growth of the spectrum the models do not predict, even qualitatively, the experimental observations.

Three dimensional plots of the evolution of four wave mixing spectrum in the fiber, indicate that the spectrum was evolving to a stable profile. Since, in the anomalous dispersion regime, soliton propagation in the form of a hyperbolic secant shape is known to be supported in an optical fiber [12], the envelope shape of the experimental FWM spectrum was investigated. It was found that at the output of 50 meters of fiber the spectral envelope could be fit by a hyperbolic secant shape. However, these experiments were performed in the normal dispersion regime, where the fundamental soliton shape is predicted to be a hyperbolic tangent. Furthermore, in the normal dispersion regime, true solitons are essentially dips in a continuous wave carrier. Theoretical and experimental research indicates that soliton-like pulses can be supported on carrier pulses where the length of stable propagation in the fiber is determined by the length of the carrier [16]. Further studies need to be done to determine if the FWM processes in the fiber evolved to a train

of stable soliton dips in the long pulse background for the fiber lengths investigated in the experiments [33].

The experimental results pointed to the need to modify the approach to the theoretical modeling of the four wave mixing processes. The experimental measurements tracing the sideband evolution along the fiber length, showed that the different first order sidebands evolved with different dynamics. This observation was not accounted for in the standard theoretical models. By imposing an asymmetry on the spectral structure of the pump inputs, the sidebands were found to follow different dynamical evolutions. Specifically, one of the pump inputs was modeled to consist of two closely spaced longitudinal modes. It is worth emphasizing that the inter-mode spacing is very small compared to the difference in wavelength of the two pump lasers, and is not resolvable with the spectrometer system used and had to be resolved with a higher resolution wavemeter. This multimode input was found to alter the sideband dynamics dramatically.

The experimental measurements of the sideband power with length along the fiber indicated that there was damping of the periodic evolution of sideband power with increasing fiber length. Again, this was not accounted for by the standard theory. One interpretation that gives insight to the damping of the sidebands is that the exchange of power between the pumps and sidebands copropagating in the fiber can be thought of as a coherent process. The experimental measurements showed the damping of sideband power, indicating that there was a mechanism along the fiber acting to remove the coherence of the power exchange between the pumps and sidebands. This mechanism was modeled by adding weak phase fluctuations to the waves as they propagated along the fiber, using the continuous wave model (coupled amplitude equations). These phase fluctuations were found to account for the damping of the sideband power evolution along the fiber. However, the physical source of these phase fluctuations has yet to be

determined and is an area for future research. Numerical simulations using the new approach, including a multimode input and phase fluctuations along the fiber length, were performed for the parameters of the experiments, and excellent quantitative and qualitative agreement was found.

Acknowledgements: D.L.H. and R.R. acknowledge support from the Division of Chemical Sciences, Office of Basic Energy Sciences, the Office of Naval Research and National Science Foundation grant NCR-961225. We thank Patrick O'Shea for his comments on the manuscript. D.L.H. thanks Jerry Zadnik for his assistance with the GTRI CCD camera.

Figure Captions

Figure 1: Dynamical evolution of first order sidebands as a function of fiber length; Ω = 300 GHz, and input pump powers of (a) 2 W, (b) 6 W, and (c) 50 W. Note the different scales of each vertical axis.

Figure 2: Dynamical evolution of first order sidebands as a function of fiber length; Ω = 600 GHz, and input pump powers of (a) 2 W, (b) 6 W, and (c) 50 W. Note the different scales of each vertical axis.

Figure 3: Experimental setup used to investigate four-wave-mixing in an optical fiber.

Figure 4: Experimental FWM output spectrum (a) plotted on a linear scale and (b) plotted on a logarithmic scale.}

Figure 5: Evolution of the FWM spectrum along the fiber from experiments, P=2.1 W, Ω = 366 GHz.

Figure 6: Evolution of the FWM spectrum along the fiber from experiments, P = 5.5 W, Ω = 366 GHz.

Figure 7: Comparison between the experimental measurements (symbols) and the standard theoretical models (solid line), of the sideband evolution as a function of fiber length; P=2.1 W, Ω = 366 GHz. Dynamical evolution of the (a) blue shifted sideband and (b) red-shifted sideband.

Figure 8: Comparison between the experimental measurements (symbols) and the standard theoretical models (solid line), of the sideband evolution as a function of fiber length; P=5.5 W, Ω = 366 GHz. Dynamical evolution of the (a) blue shifted sideband and (b) red-shifted sideband.

Figure 9: Comparison between the experimental measurements (symbols) and the standard theoretical models (solid line), of the second order sideband evolution as a function of fiber length; P=5.5 W, Ω = 366 GHz. Dynamical evolution of the (a) blue shifted sideband and (b) red-shifted sideband.

Figure 10: Comparison between the experimental measurements (symbols) and the standard theoretical models (solid line), of the sideband power versus pump input power; L=50.39 m, Ω = 366 GHz. Power in the (a) blue shifted sideband and (b) red-shifted sideband.

Figure 11: Comparison between the experimental measurements (symbols) and the standard theoretical models (solid line), of the sideband power versus pump input power; L=50.39 m, Ω = 722 GHz. Power in the (a) blue shifted sideband and (b) red-shifted sideband.

Figure 12: Comparison between the experimental measurements (symbols) and the standard theoretical models (solid line), of the sideband power with pump input power; L=5.52 m, Ω = 366 GHz. Power in the (a) blue shifted sideband and (b) red-shifted sideband.

Figure 13: Experimental FWM output spectrum (solid line) and hyperbolic secant envelope fit (dashed line) for pump input powers of: (a) P=2.1 W, (b) 5.5 W, (c) 8.3 W, and (d) 17.4 W. Fiber length L=50.39 m and detuning Ω =366 GHz.

Figure 14: Multimode pulse input to the NLSE, (a) input pulse in the time domain and (b) input spectrum.

Figure 15: Multimode output spectrum from the NLSE after propagation through several meters.

Figure 16: Comparison between the experimental measurements (symbols) and the multimode model (solid line), of the sideband evolution as a function of fiber length; P=2.1 W, Ω = 366

GHz, $\Delta\nu$=0.5 GHz, γ=0.019$W^{-1}m^{-1}$, and $\beta^{(2)}$ = 55ps^2/km. Dynamical evolution of the (a) blue shifted sideband and (b) red-shifted sideband.

Figure 17: Comparison between the experimental measurements (symbols) and the multimode model (solid line), of the sideband evolution as a function of fiber length; P=5.5 W, Ω = 366 GHz, $\Delta\nu$=0.5 GHz, γ=0.019$W^{-1}m^{-1}$, and $\beta^{(2)}$ = 55ps^2/km. Dynamical evolution of the (a) blue shifted sideband and (b) red-shifted sideband.

Figure 18: Comparison between the experimental measurements (symbols) and the multimode model (solid line), of the second order sideband evolution as a function of fiber length; P=5.5 W, Ω = 366 GHz, $\Delta\nu$=0.5 GHz, γ=0.019$W^{-1}m^{-1}$, and $\beta^{(2)}$ = 55ps^2/km. Dynamical evolution of the (a) blue shifted sideband and (b) red-shifted sideband.

Figure 19: Measured input pump power standard deviation as a function of fiber length, (closed circles) blue shifted pump and (open squares) red shifted pump.

Figure 20: Comparison between the experimental measurements (symbols) and the stochastic multimode model (solid line), of the blue sideband evolution as a function of fiber length; P=2.1 W, Ω = 366 GHz, $\Delta\nu$=0.5 GHz, γ=0.019$W^{-1}m^{-1}$, and $\beta^{(2)}$ = 55ps^2/km. Dynamical evolution of (a) the power in the blue shifted sideband and (b) the measured fluctuations.

Figure 21: Comparison between the experimental measurements (symbols) and the stochastic multimode model (solid line), of the red sideband evolution as a function of fiber length; P=2.1 W, Ω = 366 GHz, $\Delta\nu$=0.5 GHz, γ=0.019$W^{-1}m^{-1}$, and $\beta^{(2)}$ = 55ps^2/km. Dynamical evolution of (a) the power in the red shifted sideband and (b) the measured fluctuations.

Figure 22: Comparison between the experimental measurements (symbols) and the stochastic multimode model (solid line), of the blue sideband evolution as a function of fiber length; P=5.5

W, Ω = 366 GHz, $\Delta\nu$=0.5 GHz, γ=0.019$W^{-1}m^{-1}$, and $\beta^{(2)}$ = 55ps^2/km. Dynamical evolution of (a) the power in the blue shifted sideband and (b) the measured fluctuations.

Figure 23: Comparison between the experimental measurements (symbols) and the stochastic multimode model (solid line), of the red sideband evolution as a function of fiber length; P=5.5 W, Ω = 366 GHz, $\Delta\nu$=0.5 GHz, γ=0.019$W^{-1}m^{-1}$, and $\beta^{(2)}$ = 55ps^2/km. Dynamical evolution of (a) the power in the red shifted sideband and (b) the measured fluctuations.

Figure 24: Comparison between the experimental measurements (closed symbols) and the stochastic multimode model (open symbols), of the sideband power versus pump input power; L=50.39 m, Ω = 366 GHz. Power in the (a) blue shifted sideband and (b) red-shifted sideband.

Figure 25: Comparison between the experimental measurements (closed symbols) and the stochastic multimode model (open symbols), of the sideband power versus pump input power; L=50.39 m, Ω = 722 GHz. Power in the (a) blue shifted sideband and (b) red-shifted sideband.

[19] D.L. Hart, A. Judy, T.A.B. Kennedy, R. Roy, and K. Stoev, Phys. Rev. A **50**, 1807-1813 (1994).

[20] Y. Chen, J. Opt. Soc. B, **7**, 43-52 (1990).

[21] W.H. Press, S.A. Teukolsky, W.T. Vetterling, and B.P. Flannery, *Numerical Recipes in C: The Art of Scientific Computing*, (Cambridge University Press, 1992).

[22] D. A. Marcuse, J. Light. Tech. **9**, 121-128 (1991).

[23] R.H. Stolen, W. Pleibel, and J.R. Simpson, J. Light. Tech. **2** , 639-641 (1984).

[24] B.E. Burke, R.W. Mountain, P.J. Daniels, D.C. Harris, Opt. Eng., **26** (1987); B.E. Burke, R.W. Mountain, D.C. Harris, M.W. Bautz, J.P. Doty, G.R. Ricker, and P.J. Daniels, IEEE Trans. Electron. Devices **38** (1991).

[25] J.C. Twichell, B.E. Burke, R.K. Reich, W.H. McGonagle, C.M. Haung, M.W. Bautz, J.P. Doty, G.R. Ricker, R.W. Mountain, and V.S. Dolat, Rev. Sci. Instrum. **61**, 2744 (1990)

[26] J.A. Zadnik, *The Use of Charge Coupled Devices in Astronomical Speckle Imaging*, Georgia Institute of Technology, PhD Dissertation, 1993.

[27] A.C. Newell and J.V. Moloney, *Nonlinear Optics*, (Addison Wesley, 1992).

[28] D. Marcuse, *Theory of Dielectric Optical Waveguides*, 2nd ed. (Academic Press, San Diego, 1991).

[29] F. Reitmayer and E. Schuster, Appl. Opt. **11**, 1107-1111 (1972).

[30] J.M. De Freitas and M.A. Player, Appl. Phys. Lett. **66**, 3552-3554 (1995).

[31] G. Vemuri and R. Roy, Opt. Comm. **77**, 318-324 (1990); R.F. Fox, I.R. Gatland, R. Roy, and G. Vemuri, Phys. Rev. A **38**, 5983 (1988).

[32] H. Risken, *The Fokker-Planck Equation*, (Springer-Verlag, 1989).

[33] C.S. West and T.A.B. Kennedy, Phys. Rev. A **47**, 1252-1262 (1990). T.A.B. Kennedy, Unpublished Work.

Fig 1

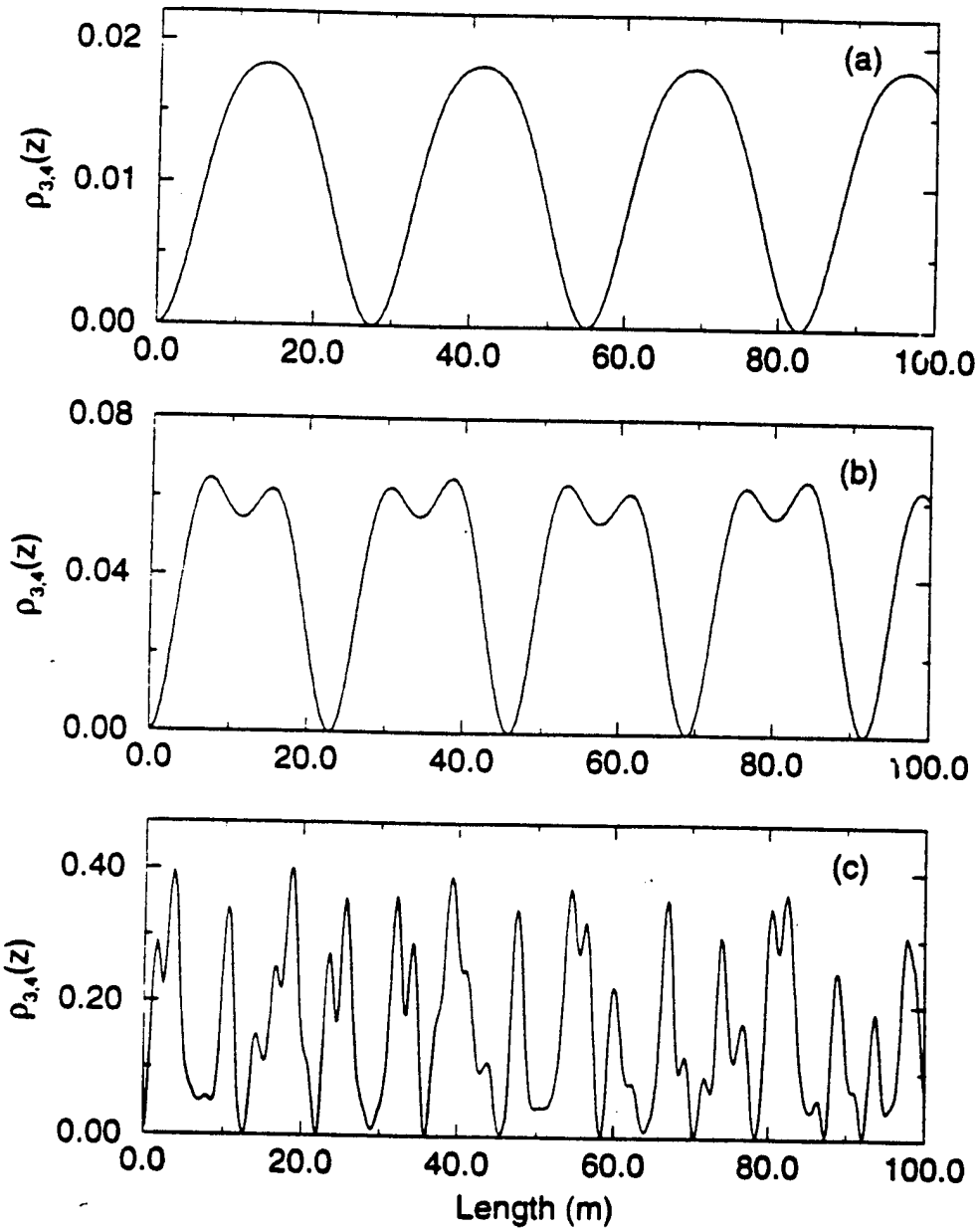
0.02
0.01
0.00
$\rho_{3,4}(z)$
(a)
0.0
20.0
40.0
60.0
80.0
100.0
0.08
0.04
0.00
$\rho_{3,4}(z)$
(b)
0.0
20.0
40.0
60.0
80.0
100.0
0.40
0.20
0.00
$\rho_{3,4}(z)$
(c)
0.0
20.0
40.0
60.0
80.0
100.0
Length (m)

Fig 2

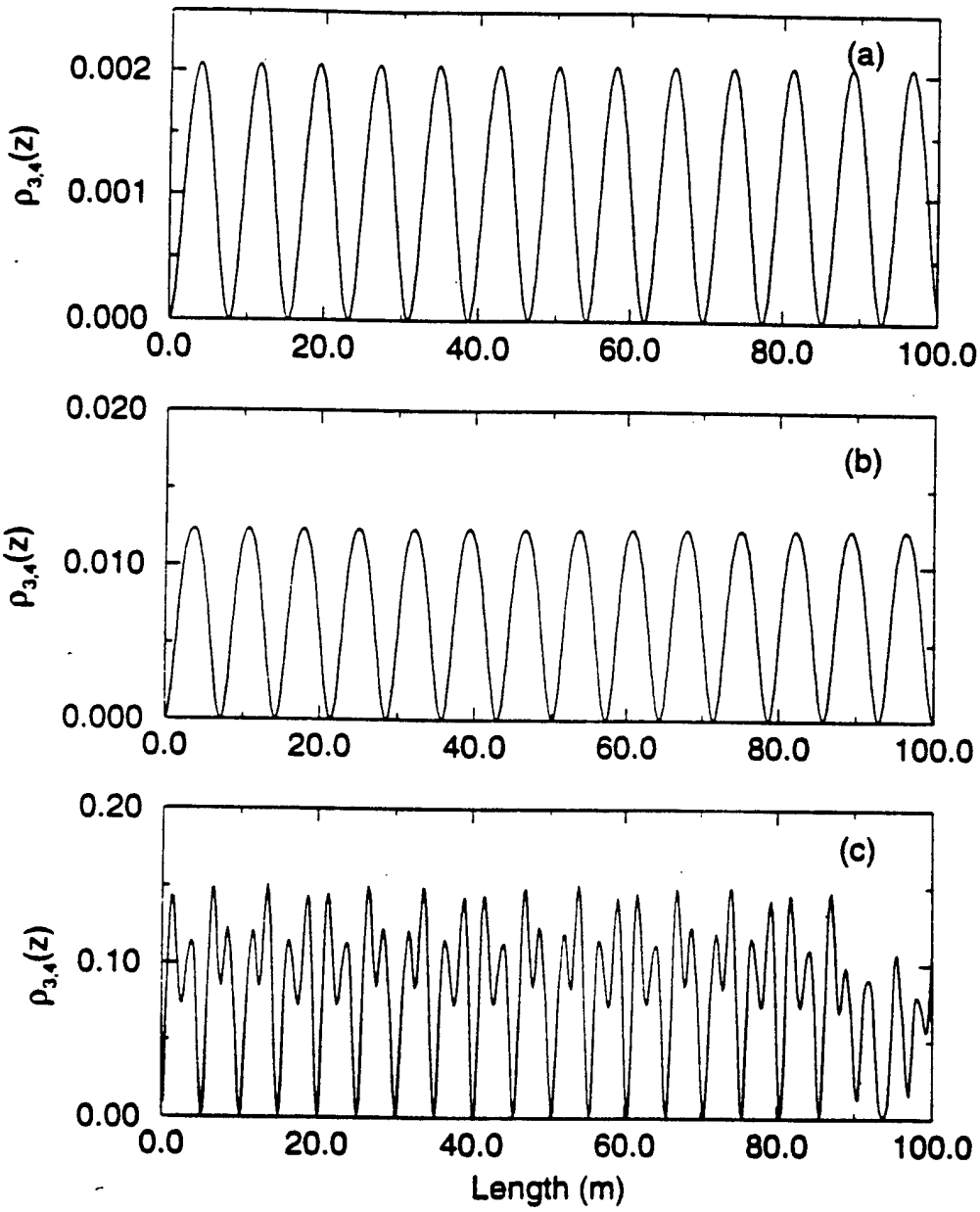
(a)
0.002
0.001
0.000
$\rho_{3,4}(z)$
0.0
20.0
40.0
60.0
80.0
100.0
(b)
0.020
0.010
0.000
$\rho_{3,4}(z)$
0.0
20.0
40.0
60.0
80.0
100.0
(c)
0.20
0.10
0.00
$\rho_{3,4}(z)$
0.0
20.0
40.0
60.0
80.0
100.0
Length (m)

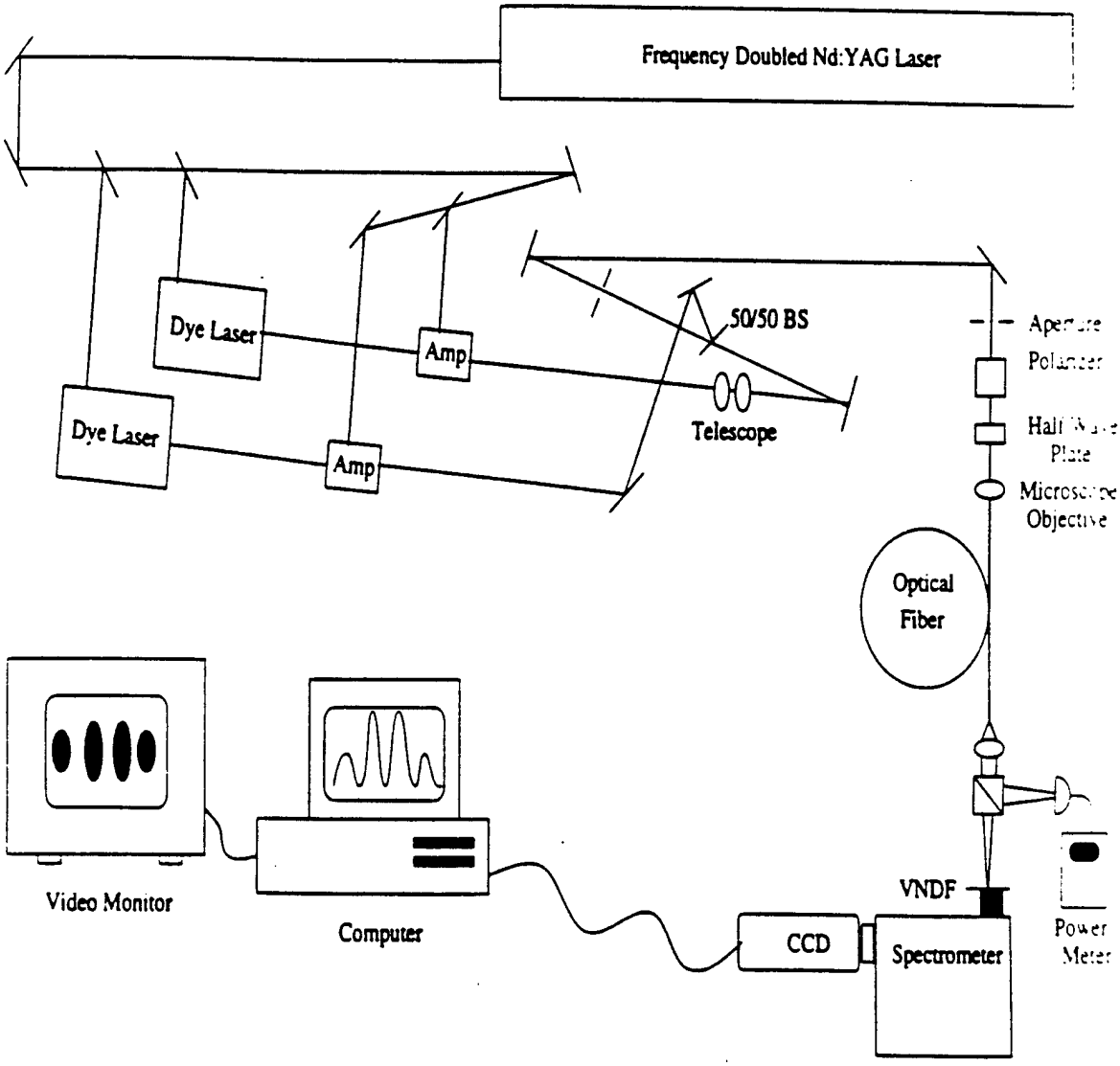
Frequency Doubled Nd:YAG Laser
Dye Laser
Amp
Dye Laser
Amp
50/50 BS
Telescope
Aperture
Polarizer
Half Wave Plate
Microscope Objective
Optical Fiber
VNDF
Video Monitor
Computer
CCD
Spectrometer
Power Meter

Fig 4

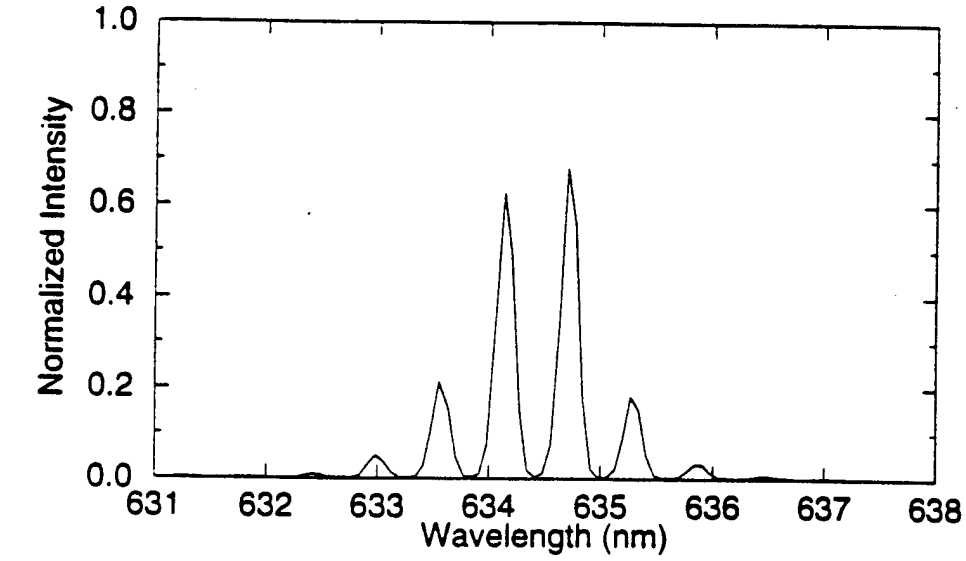
1.0
0.8
0.6
0.4
0.2
0.0
Normalized Intensity
631
632
633
634
635
636
637
638
Wavelength (nm)

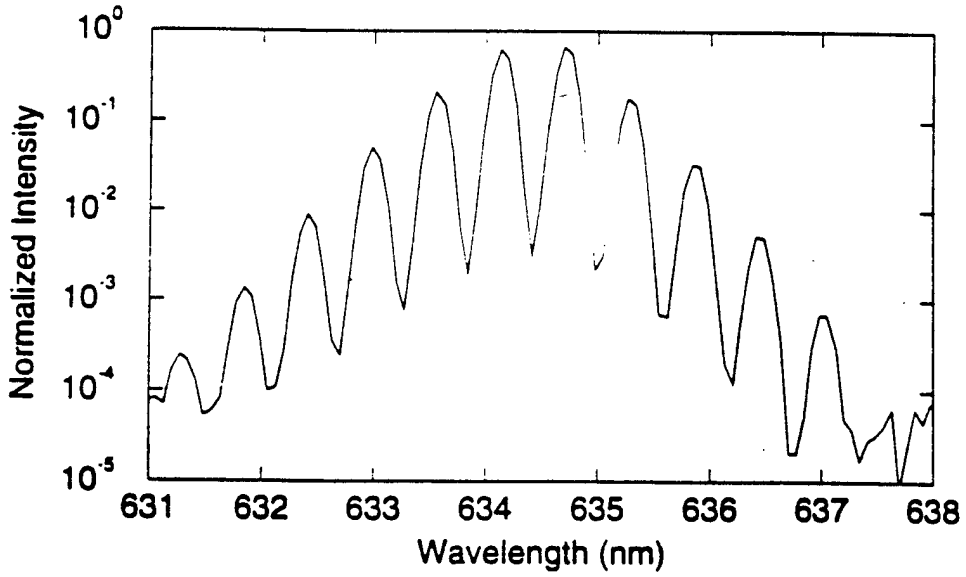
10^{0}
10^{-1}
10^{-2}
10^{-3}
10^{-4}
10^{-5}
Normalized Intensity
631
632
633
634
635
636
637
638
Wavelength (nm)

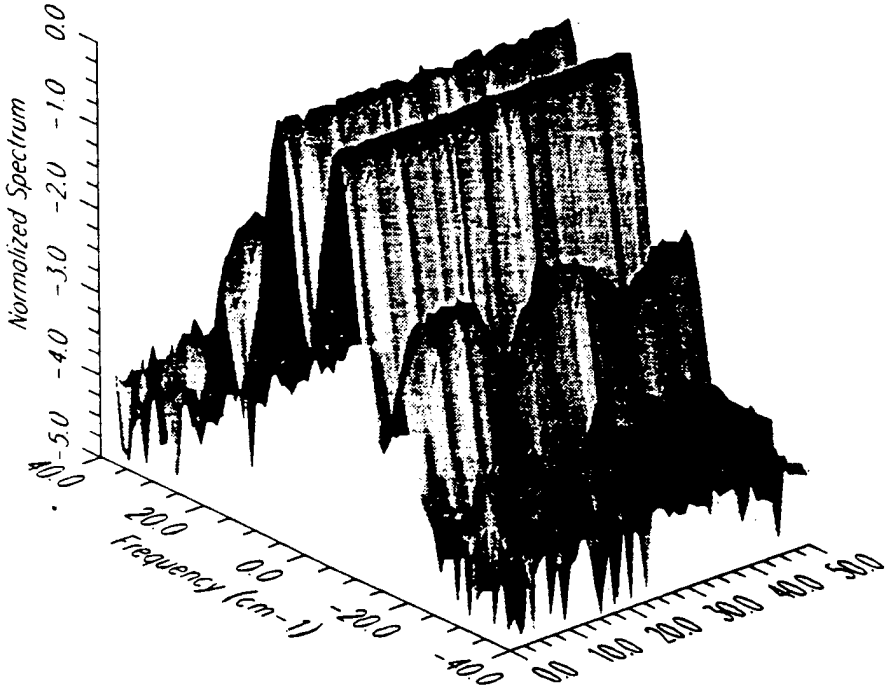
Normalized Spectrum
0.0
-1.0
-2.0
-3.0
-4.0
-5.0
40.0
20.0
0.0
-20.0
-40.0
Frequency (cm-1)
0
100
200
300
400
500

Normalized Spectrum
0.0
-1.0
-2.0
-3.0
-4.0
-5.0
40.0
20.0
0.0
-20.0
-40.0
Frequency (cm-1)
0
100
200
300
400
500

Fig 7

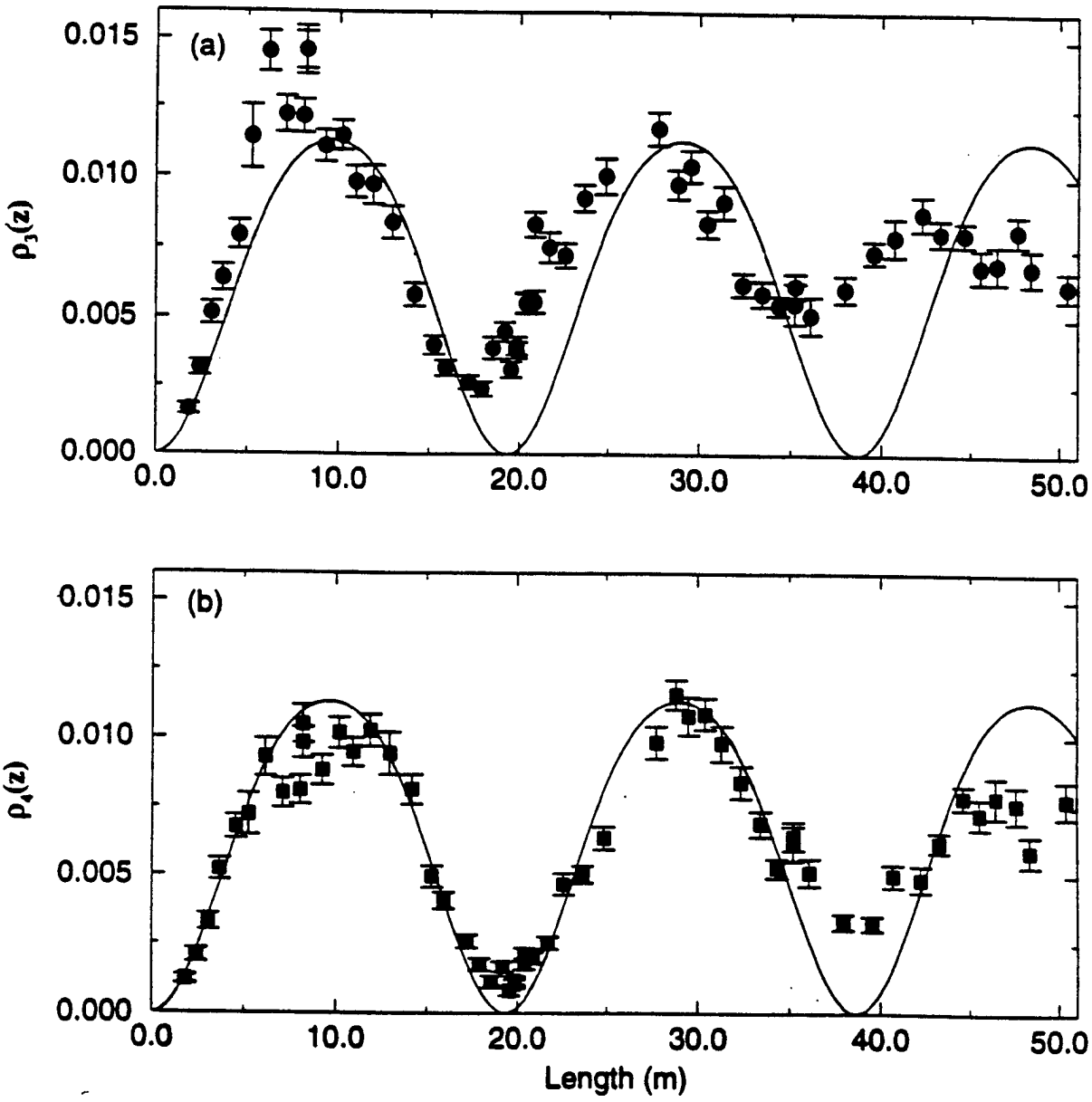
(a)
0.015
0.010
0.005
0.000
$\rho_3(z)$
0.0
10.0
20.0
30.0
40.0
50.0
(b)
0.015
0.010
0.005
0.000
$\rho_4(z)$
0.0
10.0
20.0
30.0
40.0
50.0
Length (m)

Fig8

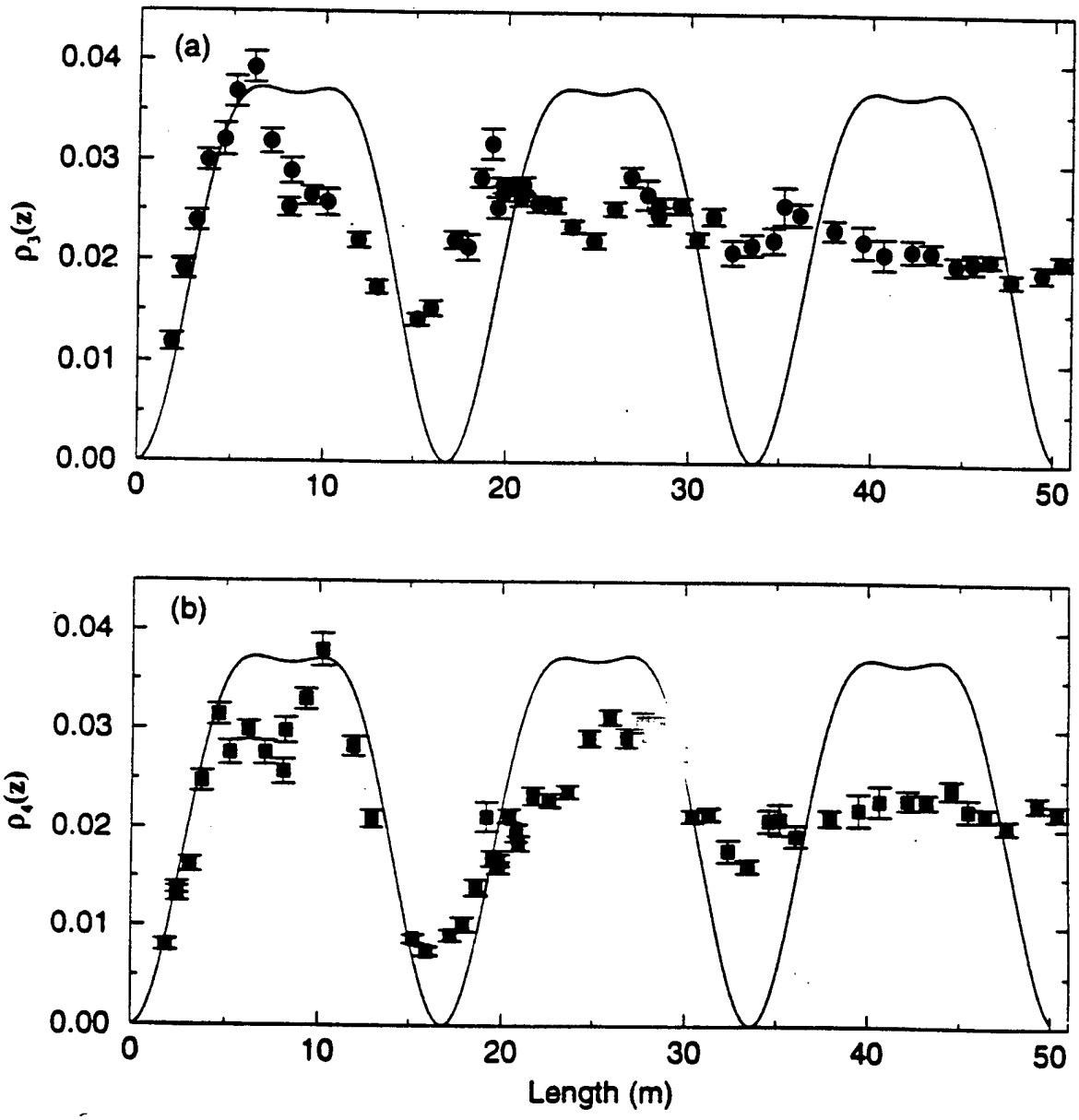
(a)
0.04
0.03
0.02
0.01
0.00
$\rho_3(z)$
0
10
20
30
40
50
(b)
0.04
0.03
0.02
0.01
0.00
$\rho_4(z)$
0
10
20
30
40
50
Length (m)

Fig 9

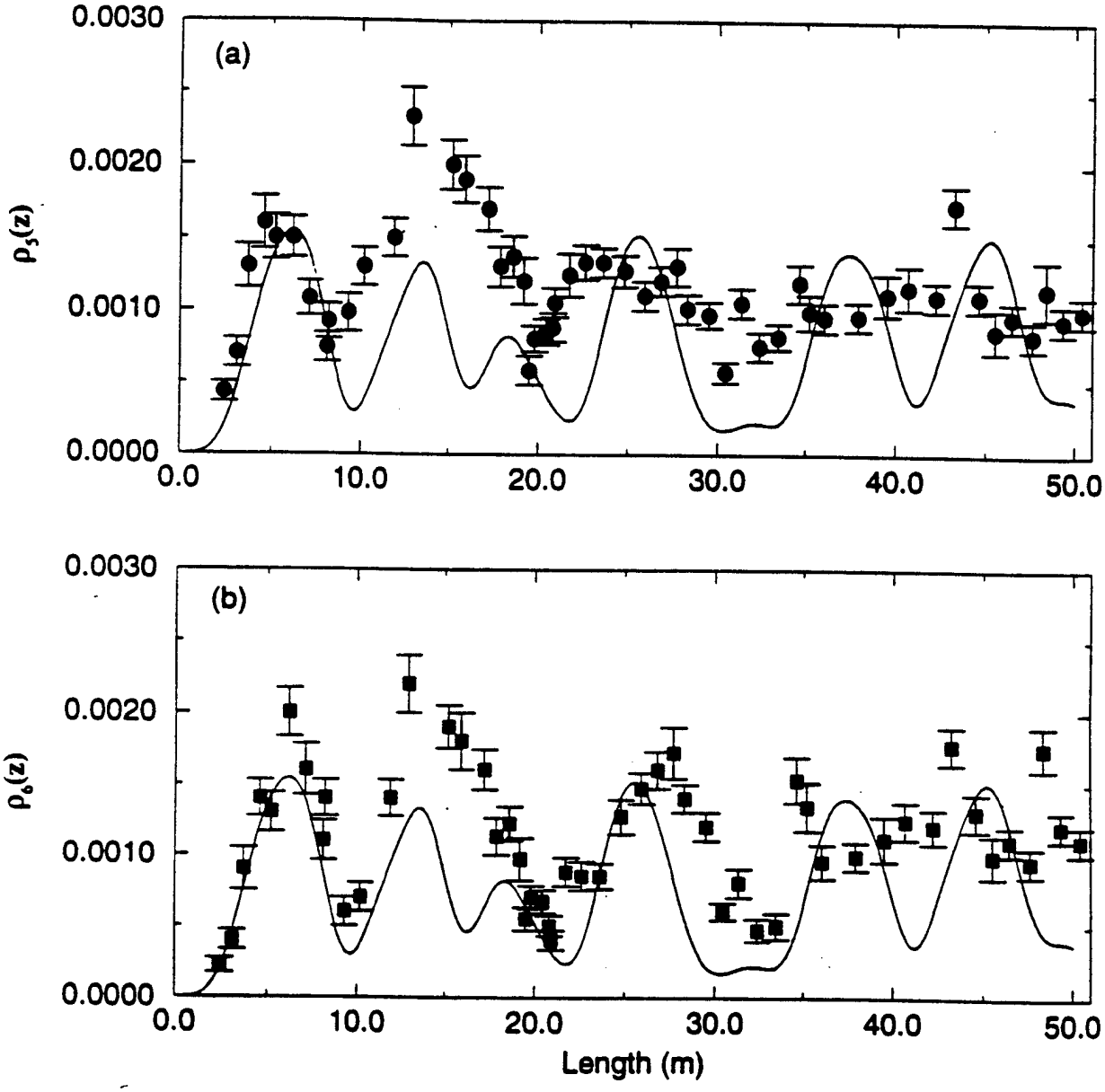
(a)
(b)
$\rho_s(z)$
$\rho_o(z)$
0.0030
0.0020
0.0010
0.0000
0.0
10.0
20.0
30.0
40.0
50.0
Length (m)

Fig 10

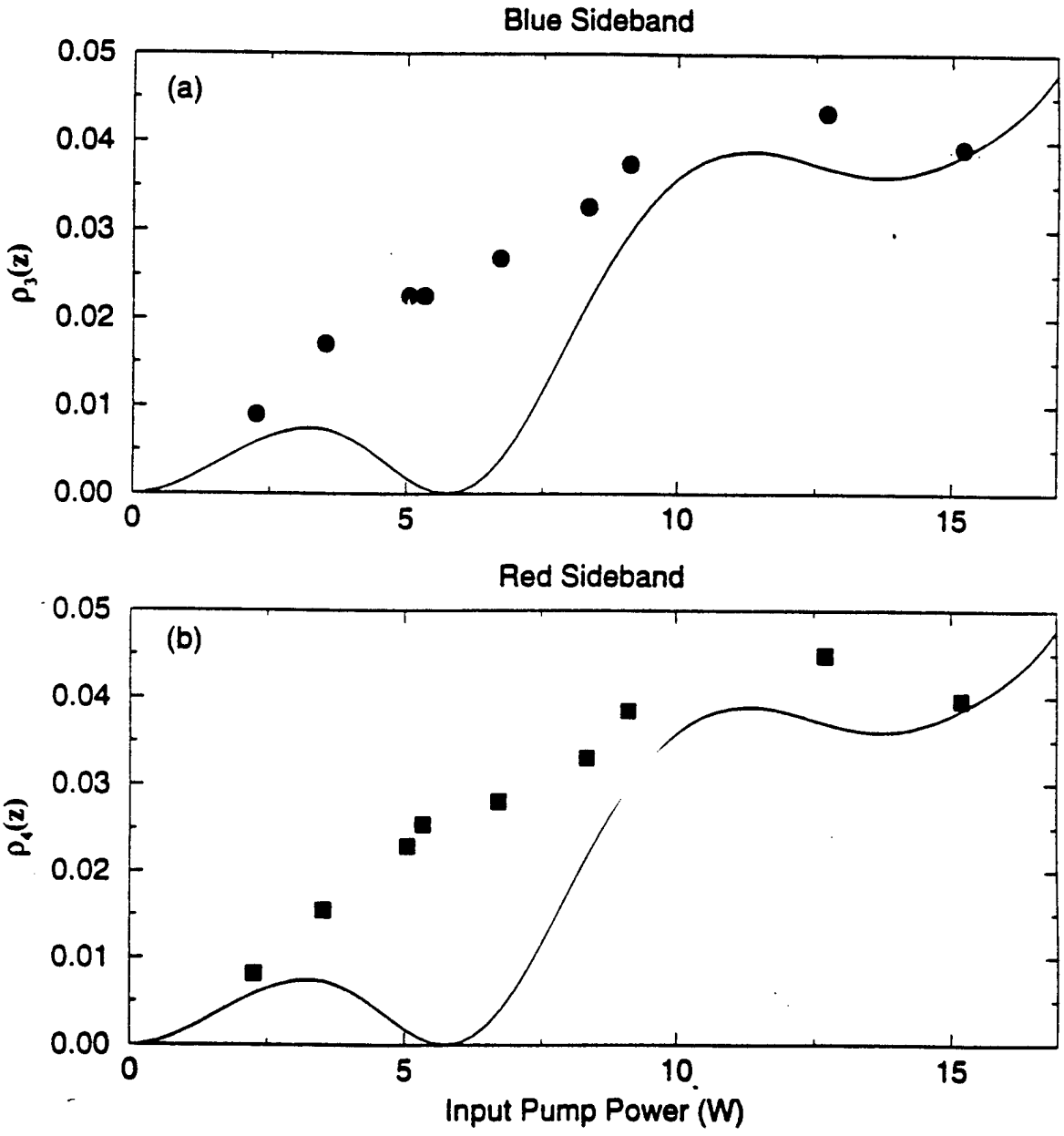
Blue Sideband
(a)
0.05
0.04
0.03
0.02
0.01
0.00
$\rho_3(z)$
0
5
10
15
Red Sideband
(b)
0.05
0.04
0.03
0.02
0.01
0.00
$\rho_4(z)$
0
5
10
15
Input Pump Power (W)

Fig 12

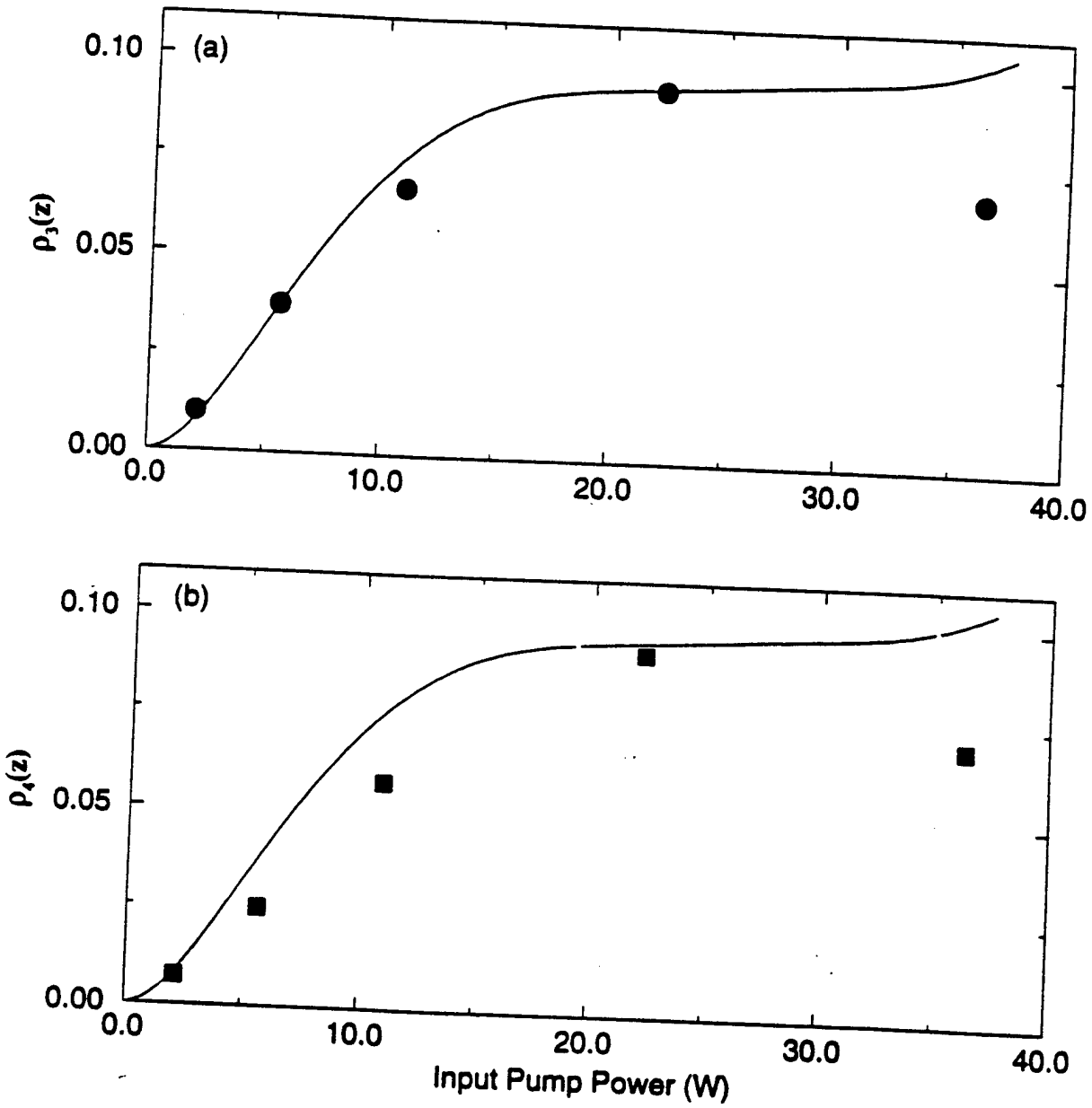
(a)
0.10
0.05
0.00
$\rho_3(z)$
0.0
10.0
20.0
30.0
40.0
(b)
0.10
0.05
0.00
$\rho_4(z)$
0.0
10.0
20.0
30.0
40.0
Input Pump Power (W)

Fig13

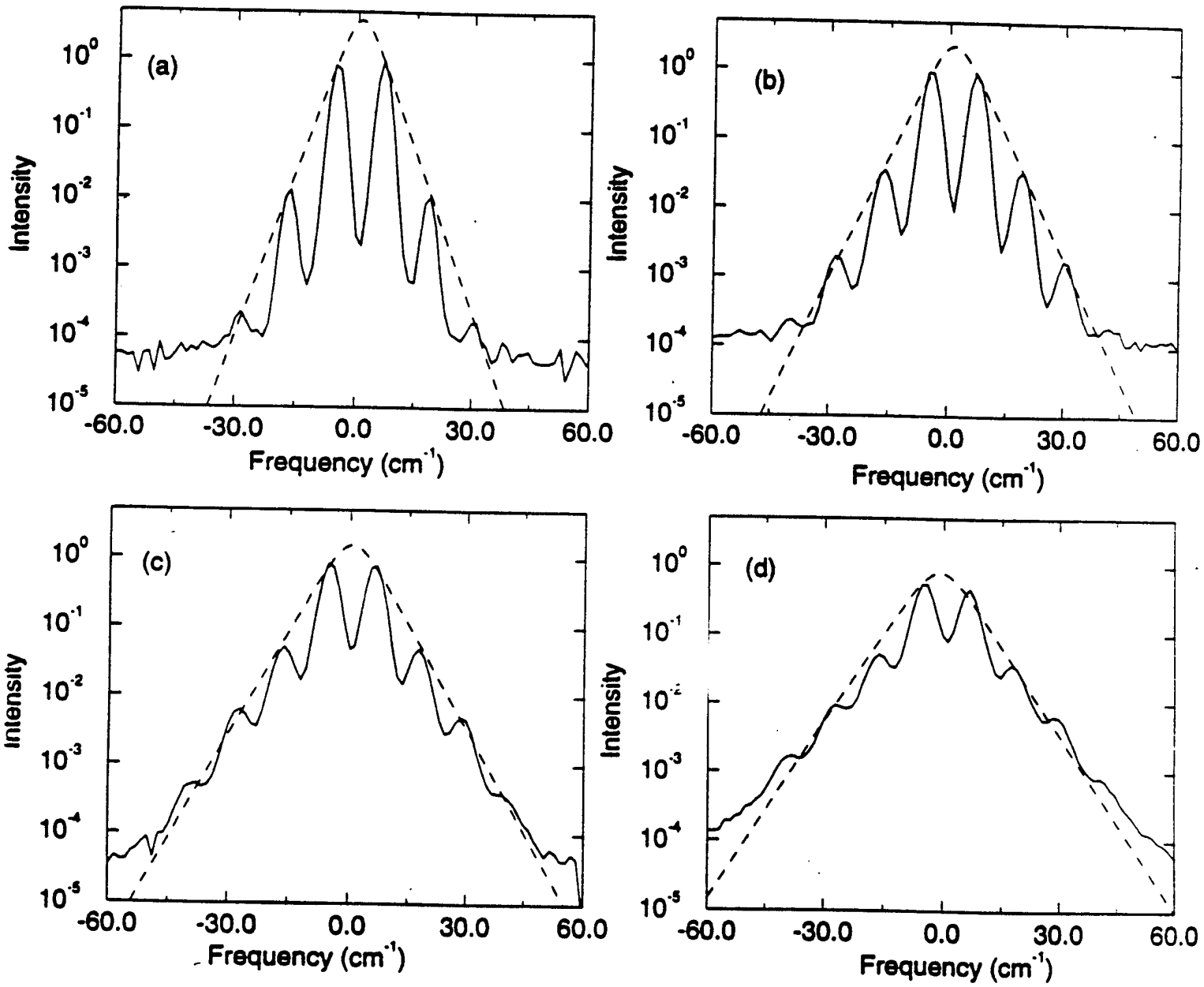
(a)
(b)
(c)
(d)
Intensity
Frequency (cm^{-1})
10^{0}
10^{-1}
10^{-2}
10^{-3}
10^{-4}
10^{-5}
-60.0
-30.0
0.0
30.0
60.0

Fig14

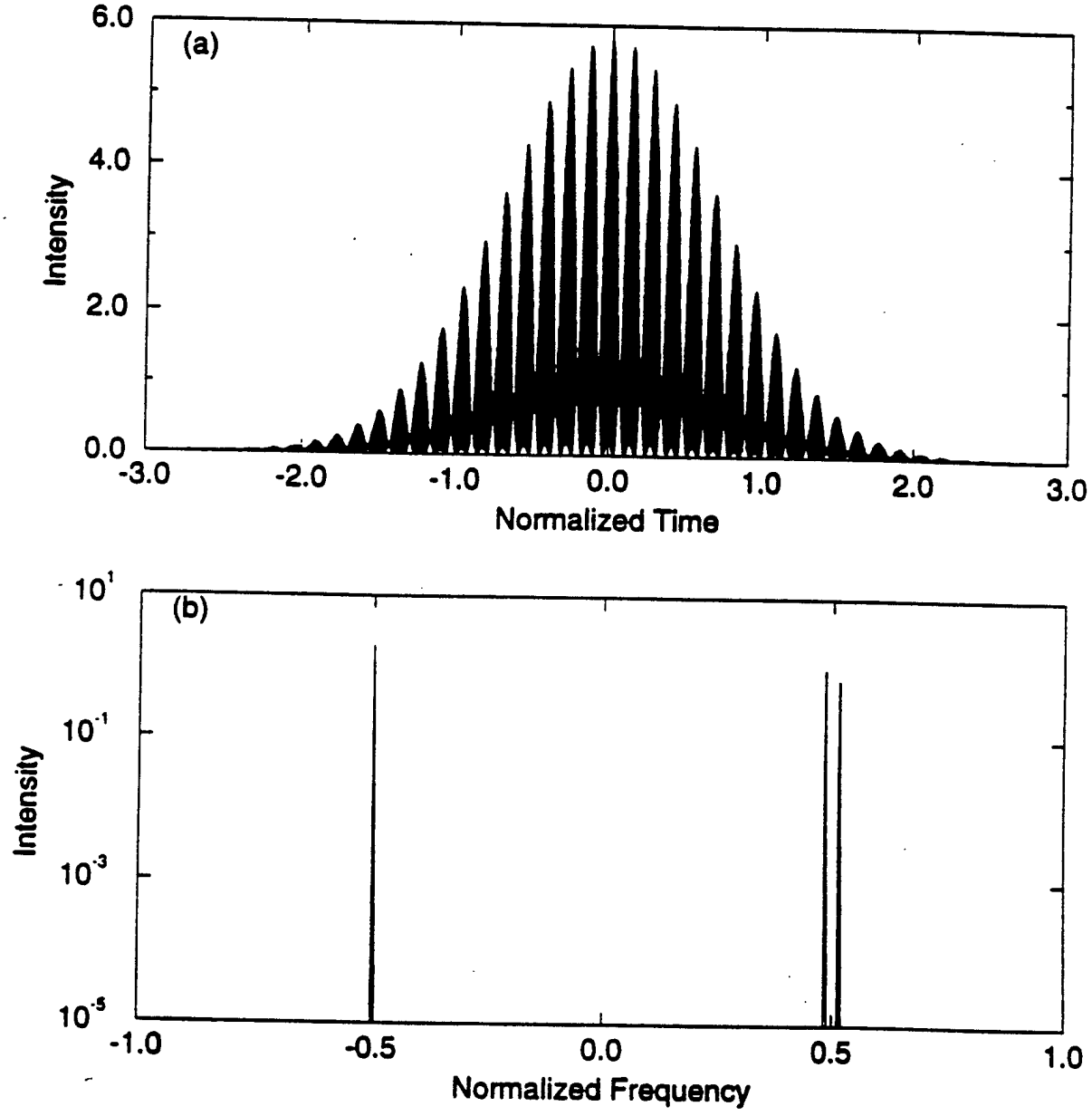
(a)
6.0
4.0
2.0
0.0
Intensity
-3.0
-2.0
-1.0
0.0
1.0
2.0
3.0
Normalized Time
(b)
10^{1}
10^{-1}
10^{-3}
10^{-5}
Intensity
-1.0
-0.5
0.0
0.5
1.0
Normalized Frequency

Fig 15

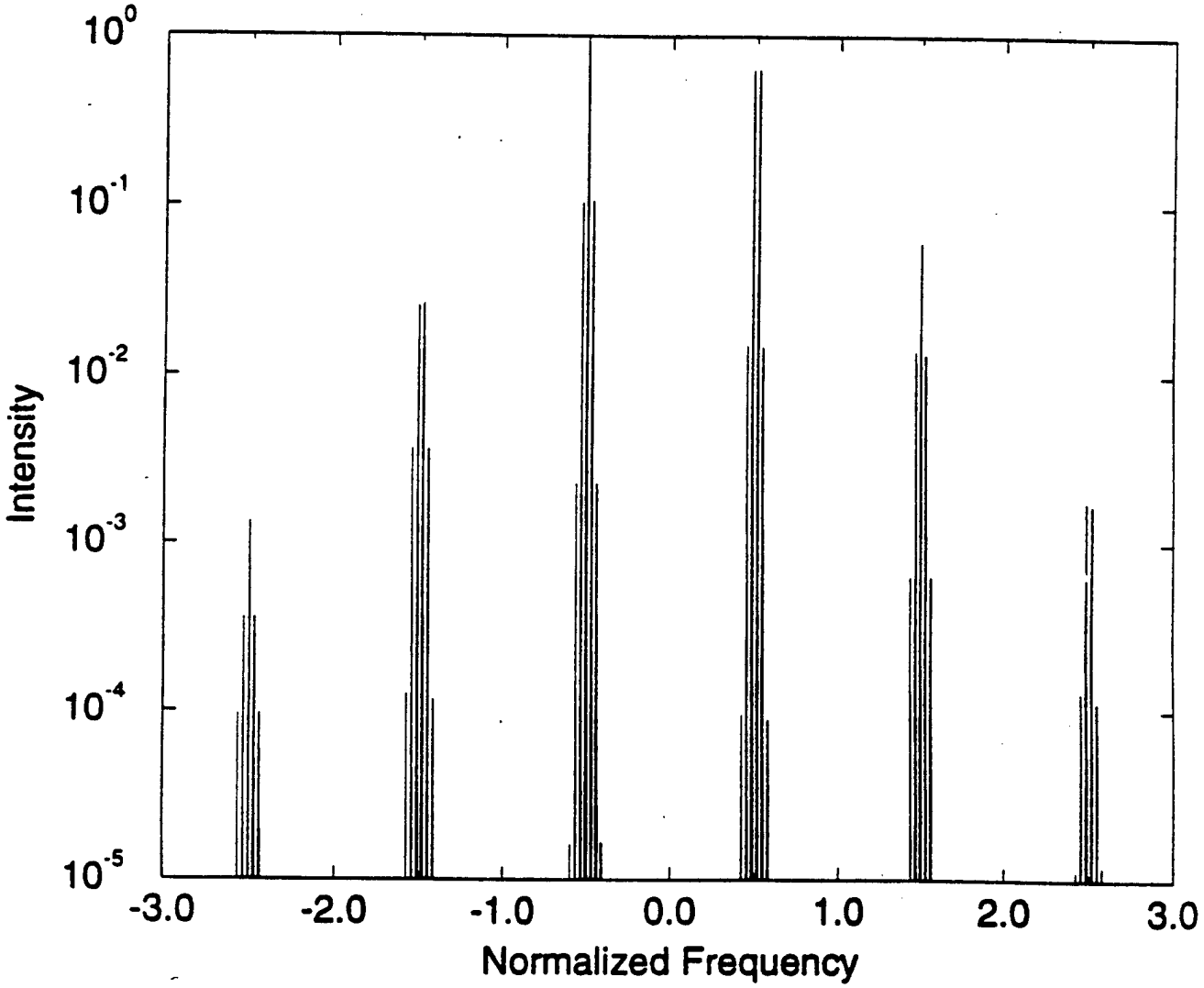
Intensity
10^{0}
10^{-1}
10^{-2}
10^{-3}
10^{-4}
10^{-5}
-3.0
-2.0
-1.0
0.0
1.0
2.0
3.0
Normalized Frequency

Fig16

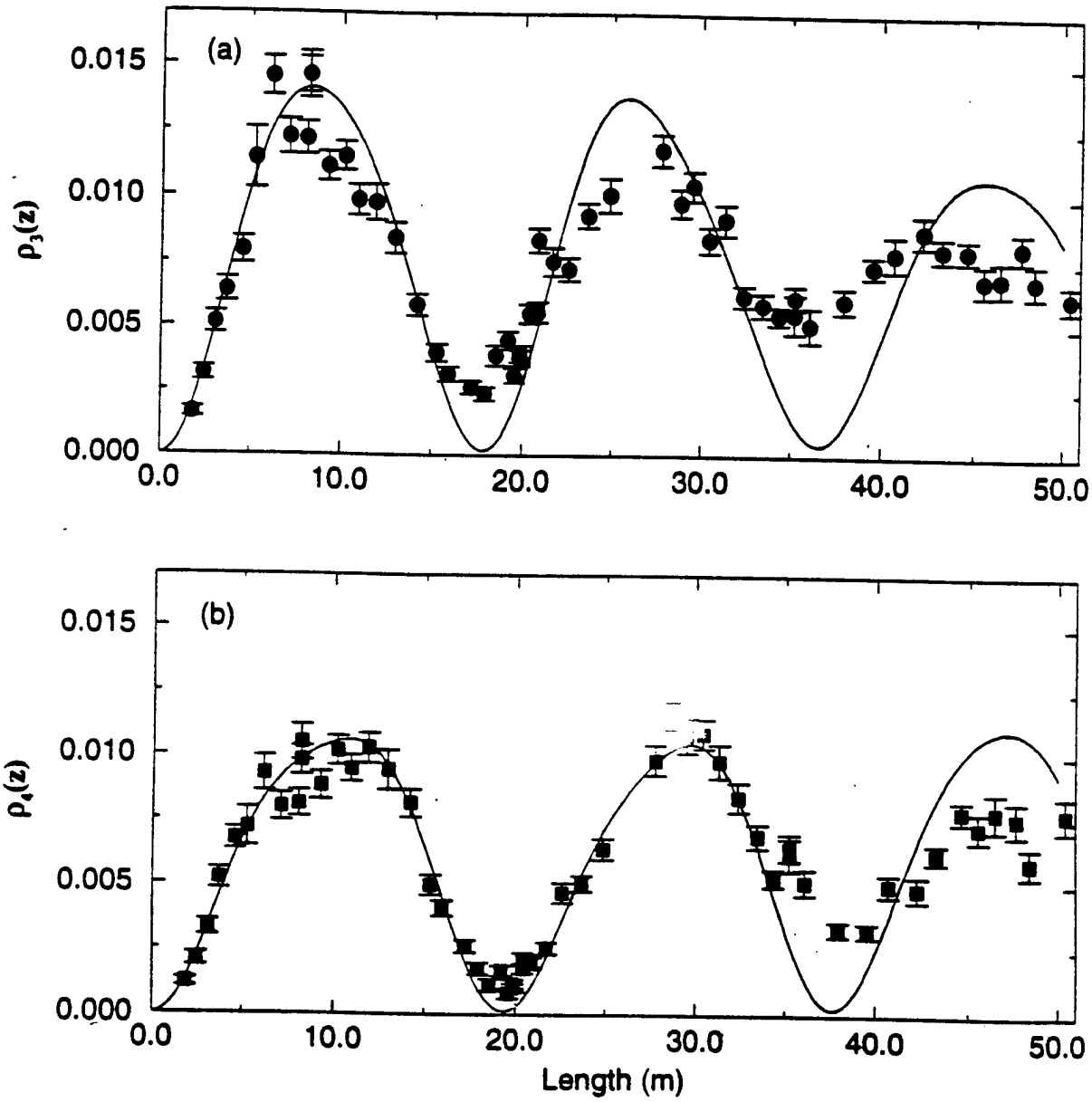
(a)
0.015
0.010
0.005
0.000
$\rho_3(z)$
0.0
10.0
20.0
30.0
40.0
50.0
(b)
0.015
0.010
0.005
0.000
$\rho_4(z)$
0.0
10.0
20.0
30.0
40.0
50.0
Length (m)

Fig 17

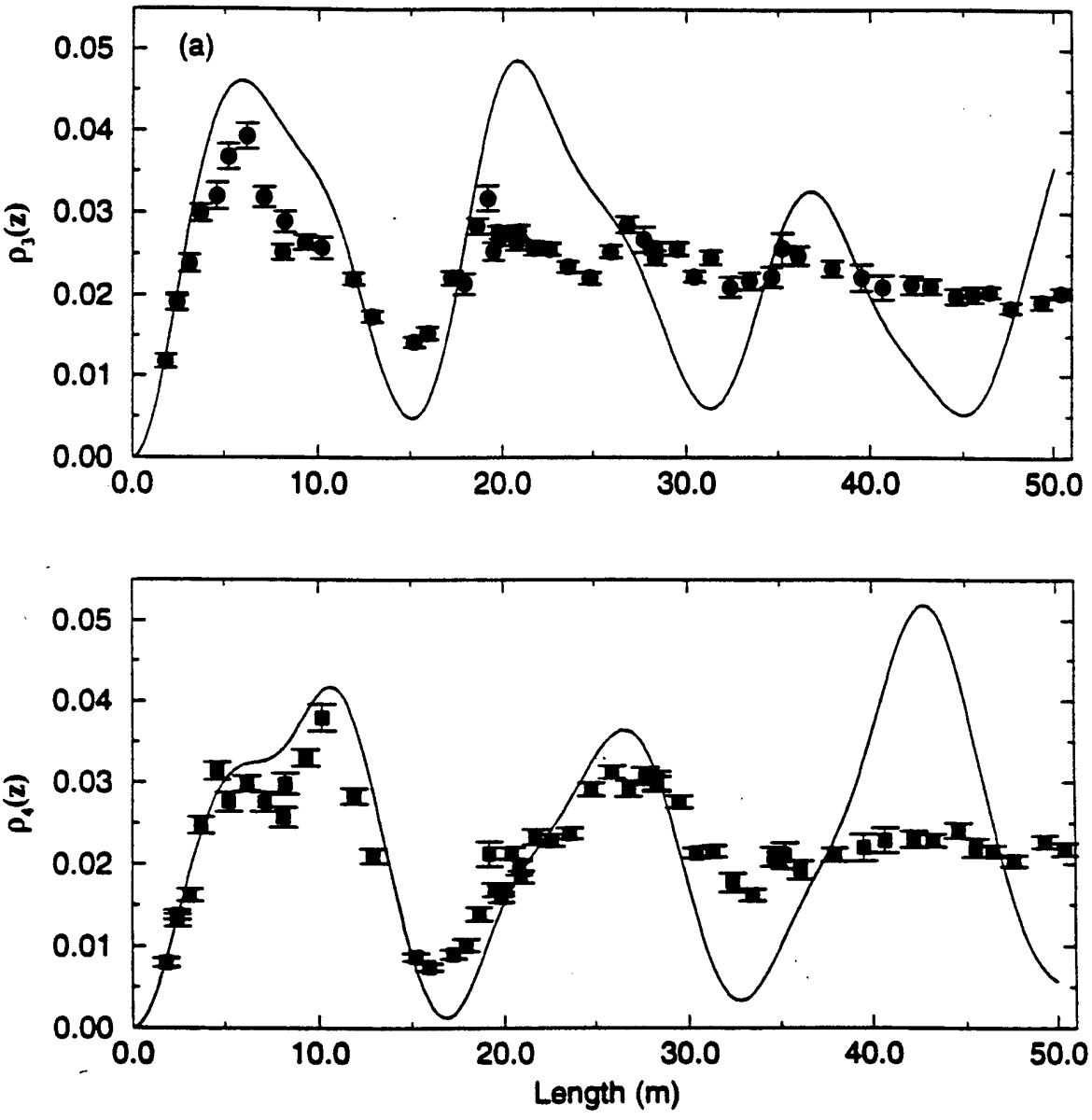
(a)
0.05
0.04
0.03
0.02
0.01
0.00
$\rho_3(z)$
0.0
10.0
20.0
30.0
40.0
50.0
$\rho_4(z)$
Length (m)

Fig 18

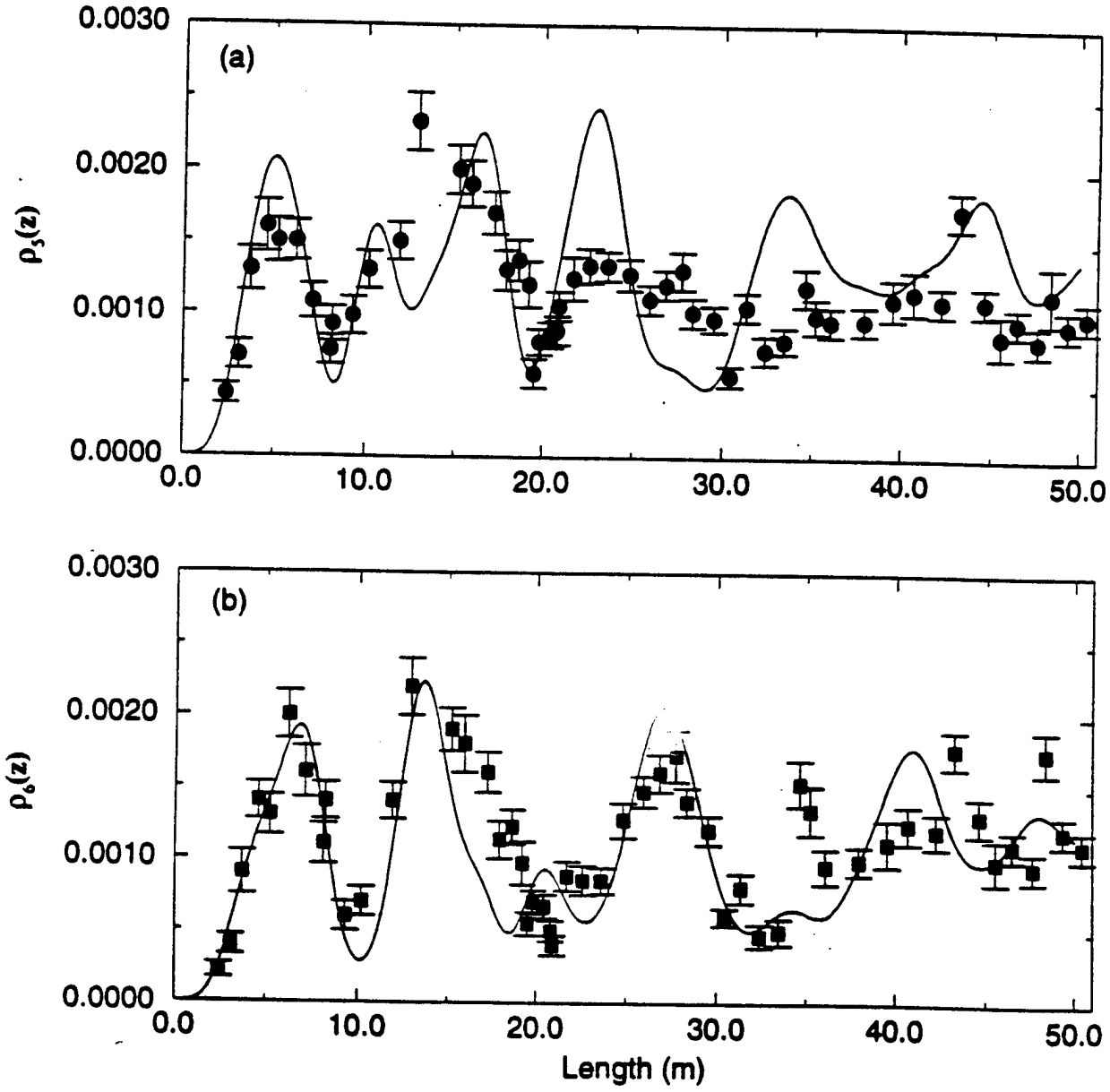
(a)
(b)
$\rho_s(z)$
$\rho_b(z)$
0.0030
0.0020
0.0010
0.0000
0.0
10.0
20.0
30.0
40.0
50.0
Length (m)

Fig 19

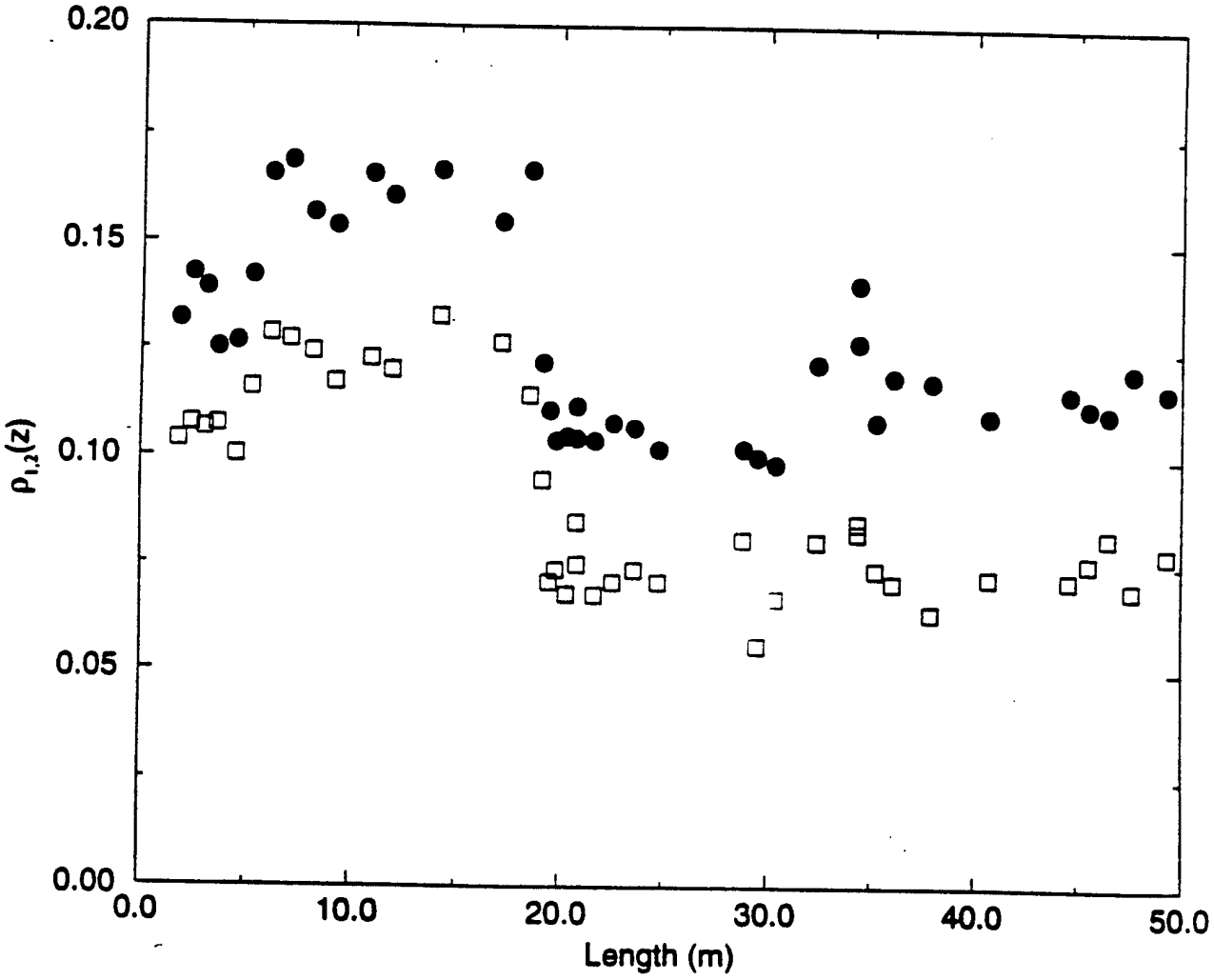

Fig 20

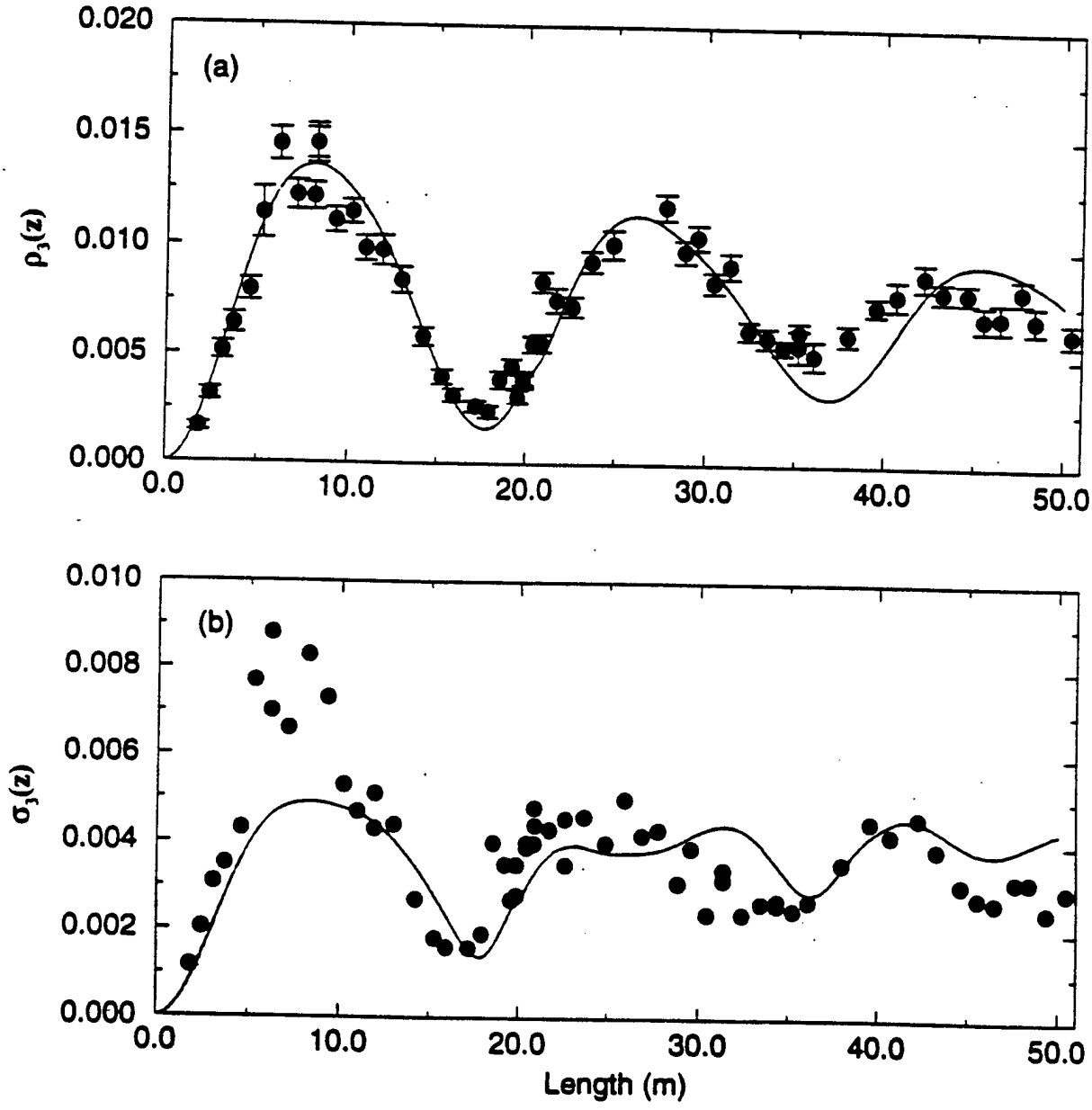
(a)
0.020
0.015
0.010
0.005
0.000
$\rho_3(z)$
0.0
10.0
20.0
30.0
40.0
50.0
(b)
0.010
0.008
0.006
0.004
0.002
0.000
$\sigma_3(z)$
0.0
10.0
20.0
30.0
40.0
50.0
Length (m)

Fig 21

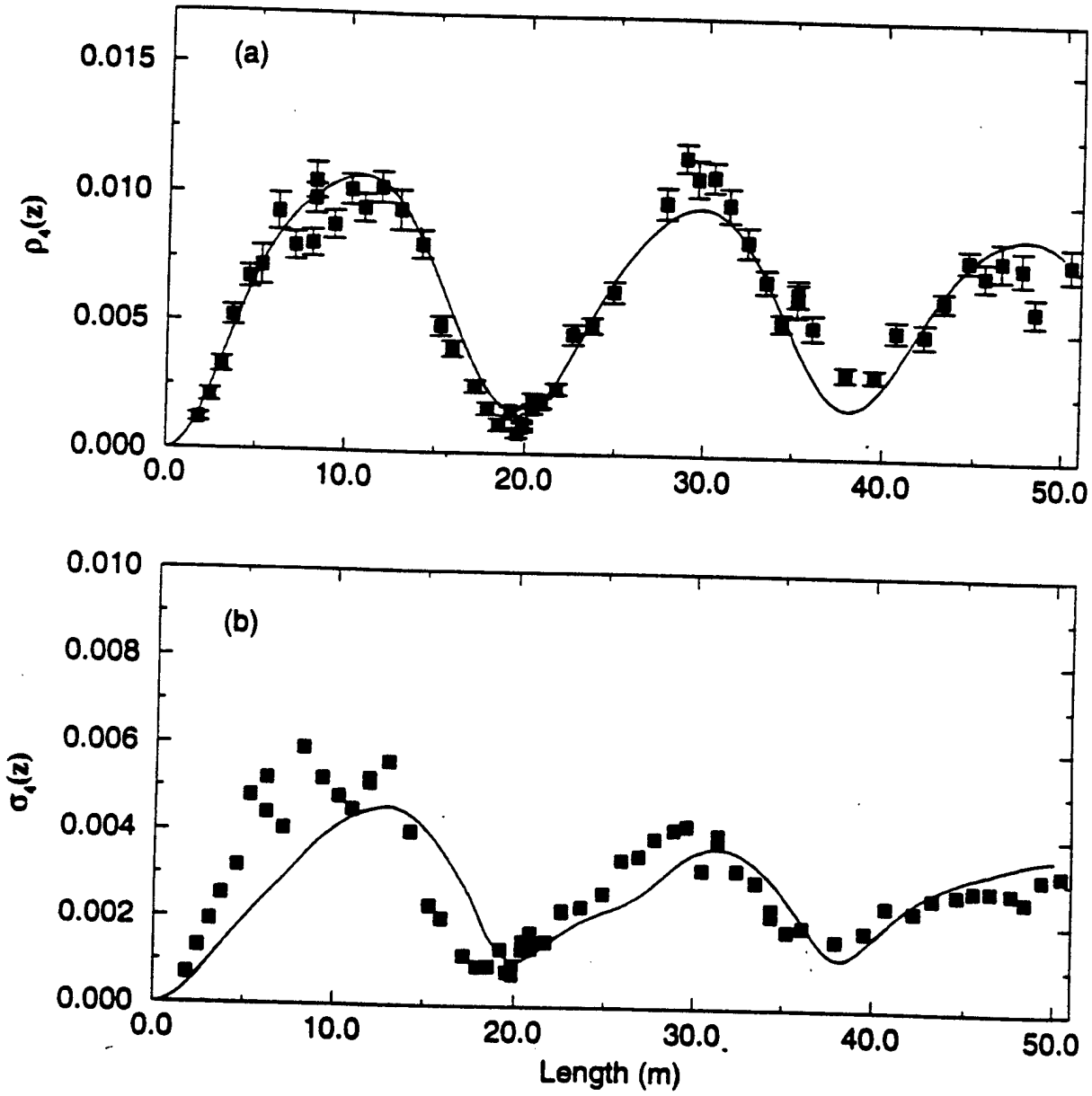
(a)
0.015
0.010
0.005
0.000
$\rho_4(z)$
0.0
10.0
20.0
30.0
40.0
50.0
(b)
0.010
0.008
0.006
0.004
0.002
0.000
$\sigma_4(z)$
0.0
10.0
20.0
30.0
40.0
50.0
Length (m)

Fig 22

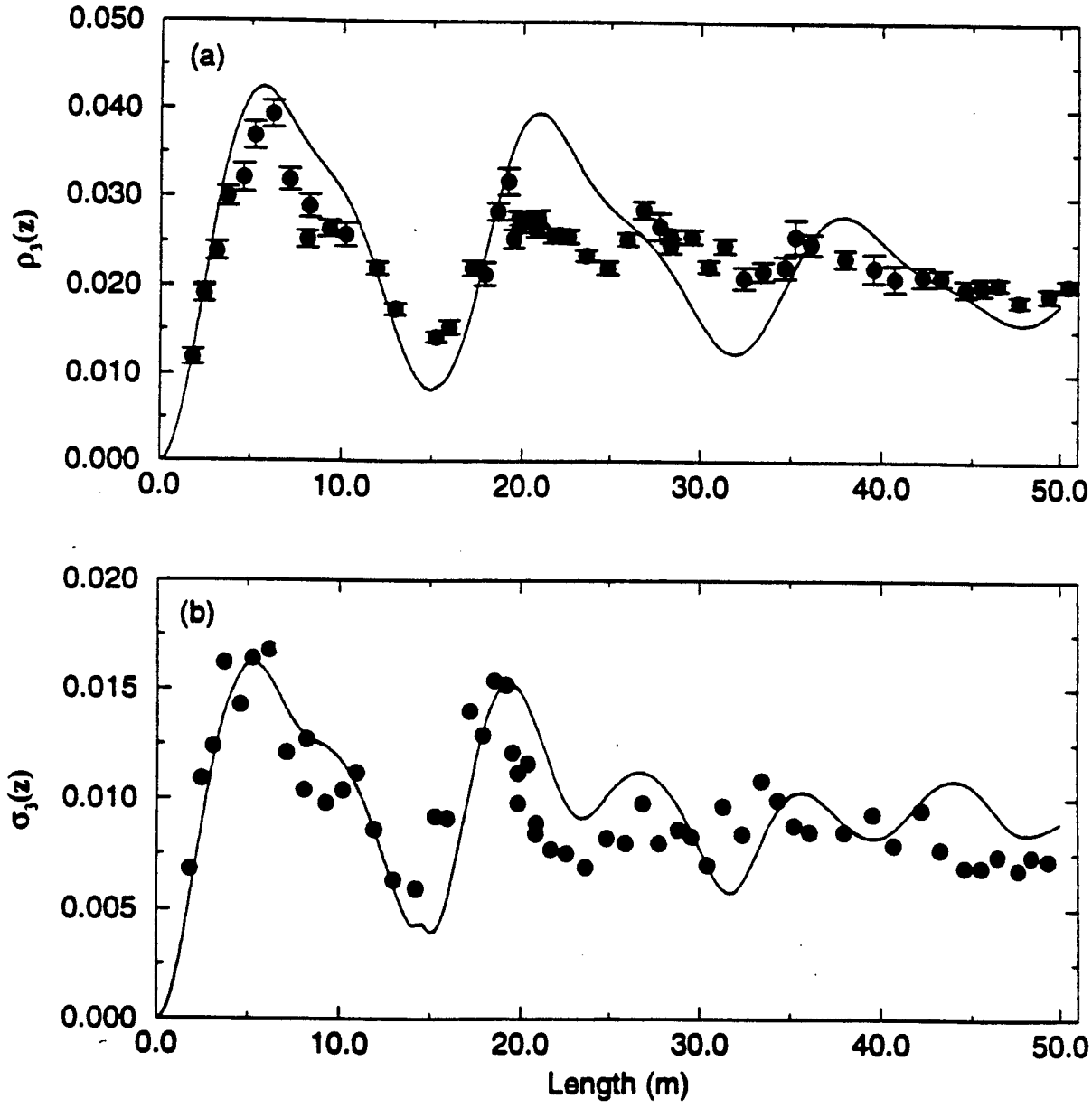
(a)
$\rho_3(z)$
0.050
0.040
0.030
0.020
0.010
0.000
0.0
10.0
20.0
30.0
40.0
50.0
(b)
$\sigma_3(z)$
0.020
0.015
0.010
0.005
0.000
0.0
10.0
20.0
30.0
40.0
50.0
Length (m)

Fig 23

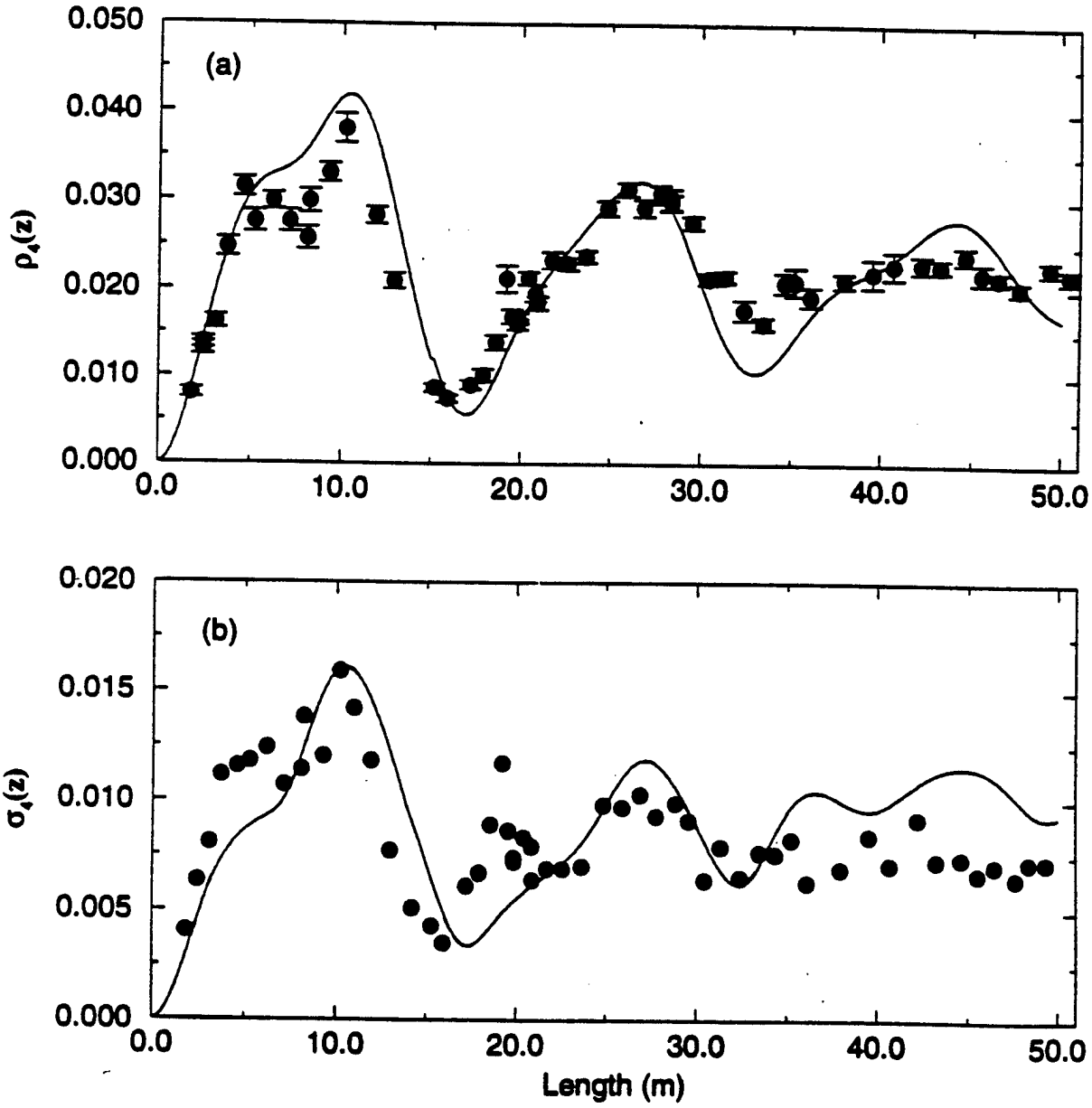
(a)
$\rho_4(z)$
0.050
0.040
0.030
0.020
0.010
0.000
0.0
10.0
20.0
30.0
40.0
50.0
(b)
$\sigma_4(z)$
0.020
0.015
0.010
0.005
0.000
0.0
10.0
20.0
30.0
40.0
50.0
Length (m)

Fig 24

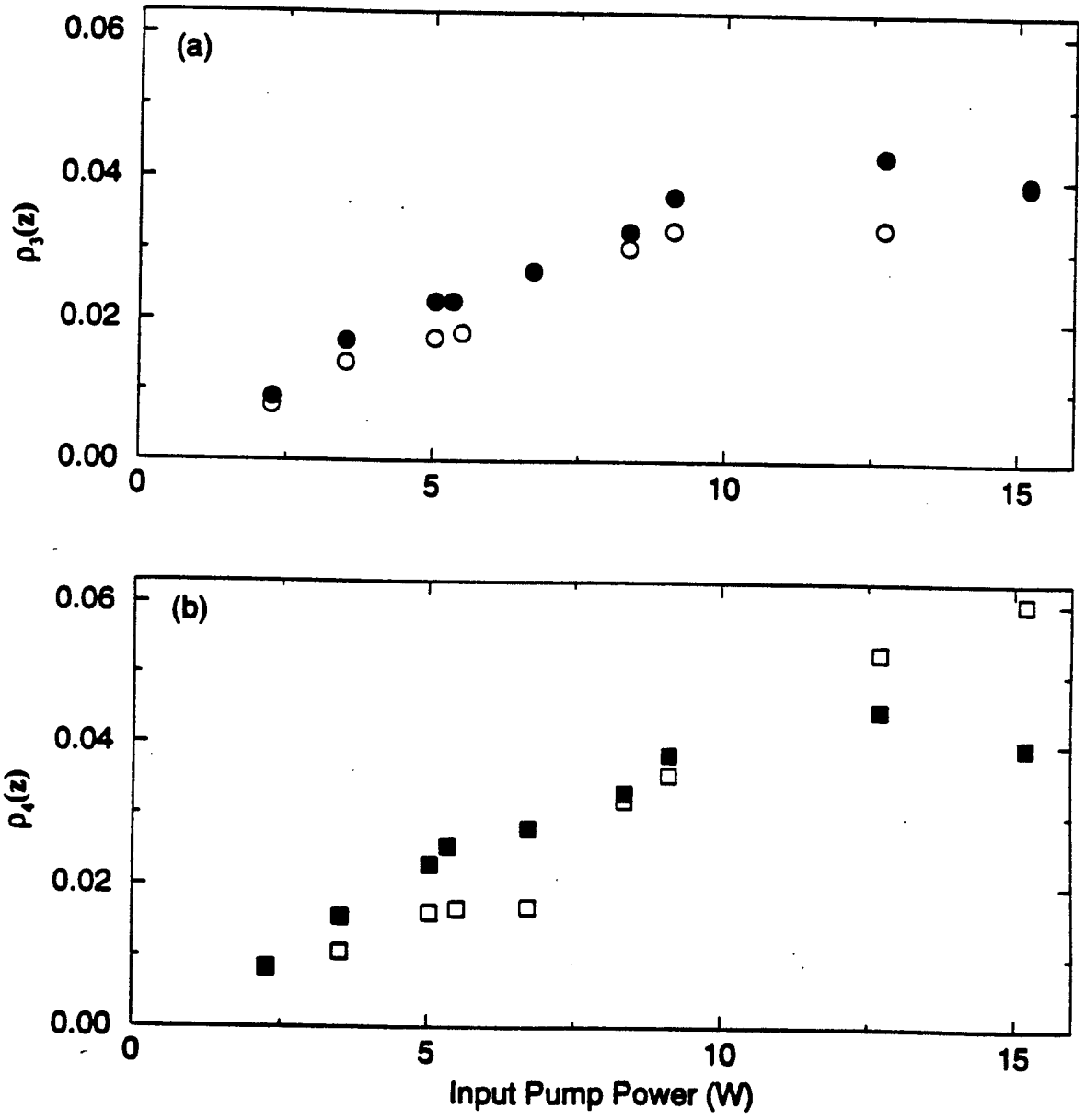
(a)
0.06
0.04
0.02
0.00
$\rho_3(z)$
0
5
10
15
(b)
0.06
0.04
0.02
0.00
$\rho_4(z)$
0
5
10
15
Input Pump Power (W)

Fig 25

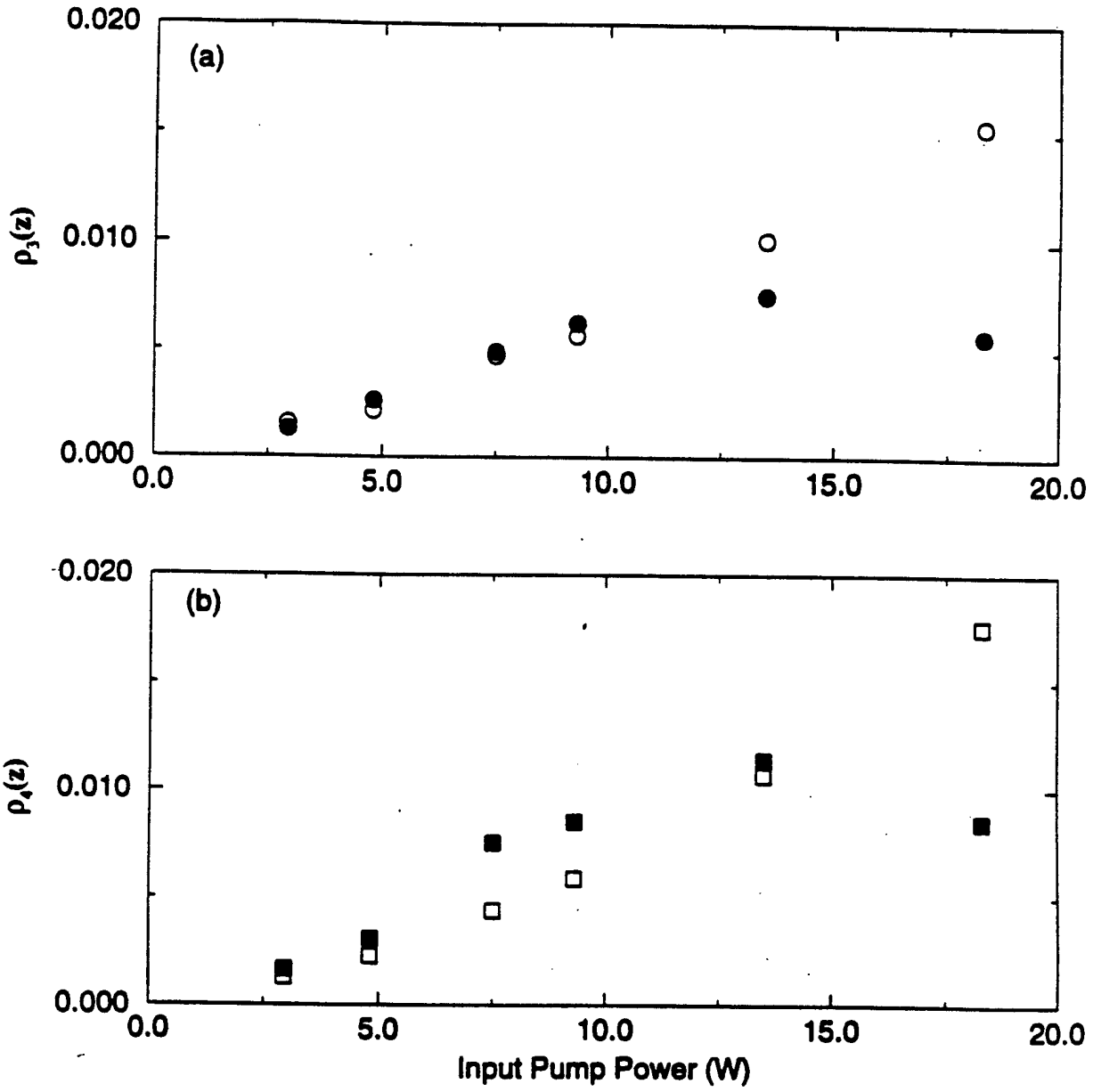
(a)
0.020
0.010
0.000
$\rho_3(z)$
0.0
5.0
10.0
15.0
20.0
(b)
0.020
0.010
0.000
$\rho_4(z)$
0.0
5.0
10.0
15.0
20.0
Input Pump Power (W)

REPORT DOCUMENTATION PAGE

Form Approved
OMB No. 0704-0188

1. AGENCY USE ONLY (*Leave Blank*)	2. REPORT DATE	3. REPORT TYPE AND DATES COVERED
	10/17/97	Annual Performance Report 10/1/96-9/30/07

4. TITLE AND SUBTITLE
Nonlinear Dyanmics of Coupled Laser Systems

5. FUNDING NUMBERS
N00014-96-1-0045

6. AUTHORS
Rajarshi Roy

7. PERFORMING ORGANIZATION NAME(S) AND ADDRESS(ES)
Dr. Rajarshi Roy
School of Physics
Grorgia Institute of Technology
Atlanta, GA 30332-0430

8. PERFORMING ORGANIZATION REPORT NUMBER

9. SPONSORING / MONITORING AGENCY NAME(S) AND ADDRESS(ES)
Michael Shlesinger
ONR Code 1112
800 N. Quincy St.
Arlington, VA 22217-5000

10. SPONSORING / MONITORING AGENCY REPORT NUMBER

11. SUPPLEMENTARY NOTES

12a. DISTRIBUTION / AVAILABILITY STATEMENT

12b. DISTRIBUTION CODE

13. ABSTRACT *(Maximum 200 words)*
see attached

14. SUBJECT TERMS

15. NUMBER OF PAGES

16. PRICE CODE

17. SECURITY CLASSIFICATION OF REPORT	18. SECURITY CLASSIFICATION OF THIS PAGE	19. SECURITY CLASSIFICATION OF ABSTRACT	20. LIMITATION OF ABSTRACT

Summary

We have investigated the stability properties of two and three element laser arrays that are nearest neighbor coupled. A novel form of generalized synchronization has been discovered, where the outer elements of the three laser linear array are synchronized identically, but the middle one is not synchronized with the outer ones. Experiments on fiber ring lasers have lead to a model that employs delay equations coupled to a differential equation to describe the fast (nanosecond) dynamics of the polarized light output from these lasers. Four wave mixing of light beams at detuned frequencies has been studied both experimentally and theoretically and a uniques set of measurments has been analyzed. Phase fluctuations of the light play an important role in the propagation of the sidebands through the fiber. The first experiments on optical communication with chaotic fiber lasers have been performed.